THE DESIGN, MANUFACTURE & TESTING OF A PODDED PROPULSOR INSTRUMENTATION PACKAGE

JAMES ANDREW MACNEILL

THE DESIGN, MANUFACTURE & TESTING OF A PODDED PROPULSOR INSTRUMENTATION PACKAGE

BY

© JAMES ANDREW MACNEILL, B.ENG.

A thesis submitted to the
School of Graduate Studies
in partial fulfillment of the
requirements for the degree of
Master of Engineering

Faculty of Engineering and Applied Science
Memorial University of Newfoundland
May 2011

St. John's   Newfoundland   Canada

To Jennifer, Aaron & Rebecca

ABSTRACT

This body of work encompasses the documentation of the design, manufacture and initial testing of a unique piece of instrumentation. This instrumentation package attempts to measure a number of parameters related to the field of azimuthing podded propulsion, a type of marine propulsion for vessels.

During the course of the design process, as many measurement capabilities as possible were included in the same setup, in addition to providing the ability to easily allow geometry changes.

The measurement capabilities include: propeller torque and thrust measured at the propeller hub, propeller thrust measured at the pod interior end of the propeller shaft, pressure between the opposing faces of the propeller hub and pod shell end at five different radius values, the potential to measure blade angle position, outer pod shape drag force, and global loads of the pod unit relative to the test carriage.

The geometry change capabilities include: propeller and propeller hub taper angle, pod shape, and adjustment of the gap distance between the propeller hub and pod shell end.

When instrumentation manufacturing was completed, the instrumentation was assembled, calibrated and tested for the first time to assess its ability to measure the parameters it was designed to measure.

ACKNOWLEDGEMENTS

A great many people contributed to the success of this project. Beginning with those from Memorial University of Newfoundland, and with deep gratitude, the author would like to start his acknowledgements by thanking Dr. Brian Veitch. At the very beginning of the project it was he who provided the author with the necessary background information to start the design process. Throughout the project, his knowledge, guiding input and direction made it possible to carry out a very complex set of tasks. He also provided the author with the unique opportunity to travel to Europe and meet with two world experts in the field of model testing with podded propulsors. He introduced the author to Mr. Fredrick Mewis of HSVA in Hamburg Germany and Mr. Jan Holtrop of Marin in Wageningen Netherlands. Having the once in a lifetime experience to sit down and converse with them on issues related to the topic and to tour their facilities was extremely interesting and beneficial to the author's personal development in understanding this topic and advancing the designs carried out in the project.

The author also acknowledges the important discussions he had with Dr. Neil Bose, also from MUN. His outlining and alerting to the author the inherent problems that arise when attempting to measure such things as gap pressure and shell drag, and the isolation of propeller hub thrust from the effects due to gap pressure, played a pivotal role during the early stages of the project. Without these initial conversations and insights the author would not have been able to get off to as smooth a start as he did.

The author is deeply indebted to graduate student Rocky Taylor. His help with the unit dynamometer design as well as taking care of the lift elevator and wave shroud in entirety was a key factor in getting everything ready for testing.

The author would also like to say a special thanks to Jim Gosse, who gave freely of his time during the often irregular and late hours when the author needed access to the tank or needed the test carriage operated. His help during the installation and calibrations, and advice throughout the project were most appreciated and contributed to the author getting through one of the more difficult stages of the project.

Also from MUN and during the initial phase of the project, Susan Molloy carried out the important task of researching the various full scale geometries of various podded propulsors and compiled the initial model scale envelope necessary to develop the maximum dimensions that the pod instrumentation package could occupy. Without this necessary information the author could never have proceeded with the design phase of the instrumentation.

Acknowledgement of the expert craftsmanship by the technicians from the electronics and mechanical divisions of MUN Technical Services is also of most importance. The level of competence and ability carried out by all was absolutely essential in getting everything done successfully. Their help was immeasurable near the end when time was just simply running out.

From IOT the author acknowledges Dr. Pengfei Liu, who designed the propeller for the project and Tony Randell who created the CAD model of the propeller and integrated it with the hub design. The author thanks John Bell as well, who along with Mr. Randell and Dr. Liu, provided valuable design feedback for the propeller hub, pressure sensing system and shell drag measurement systems. Also of IOT, the author thanks Howard Mesh and Spence Butt, who aided in the selection of the pressure transducers and provided valuable information throughout the span of the project on the issue of pressure transducers, their calibration and interpretation of the voltage output traces.

From Thordon Bearings the author thanks Jeff Butt and others from the engineering department who aided in the design of the water lubricated bearing and provided valuable feedback as to the configuration of this detail.

From Oceanic, the author is especially grateful to Dr. Dan Walker for allowing the author time to work on the project during the design, manufacturing and testing phases.

At this time the author also acknowledges the financial support provided to the project by the Natural Sciences and Engineering Research Council of Canada (NSERC).

The author would also like to thank Dr. Michael Hinchey. Dr. Hinchey started supervising the author in the fall of 1996 and has been there ever since. His guidance, suggestions and patience have kept the author from quitting many times. At this time the author must simply say a heart-felt thank-you for everything he has done.

Last of all, the author must thank his family. To Jennifer, I say thank-you for your support, patience and encouragement over the span of this project and completing the thesis. To Aaron and Rebecca, I say thank-you for all the times I needed to be away from you, especially at bedtime. Thoughts of your smiling faces and laughter, especially while listening to the 'Jawbahrish' song, will be forever etched in my mind when I think of this thesis.

CONTENTS

CHAPTER 1 – PODDED PROPULSION HISTORY & PROJECT GOALS

CHAPTER 2 –LITERATURE REVIEW

CHAPTER 3 - INSTRUMENTATION DESIGN

CHAPTER 4 - INSTRUMENTATION MANUFACTURE, SETUP & CALIBRATIONS

CHAPTER 5 – INSTRUMENTATION TESTING

CHAPTER 6 – EXPERIMENTAL RESULTS

CHAPTER 7 – CONCLUSIONS & RECOMMENDATIONS FOR FUTURE WORK

List of Figures

List of Tables

List of Symbols

$c_{0.7}$, propeller chord length measured at r/R = 0.7

c_o, outer radius of propeller shaft gauge area

c_i, inner radius of propeller shaft gauge area

D, test propeller diameter

D_P, 1% test propeller diameter

GF, gauge factor

CFN, command frequency number

CFN_{MAX}, maximum value for command frequency number

G, shear modulus for torsion

GBR, gear box ratio

J, propeller advance ratio coefficient, *and* polar moment of inertia

n, propeller rotation rate in revolutions per second (rps)

r, propeller radius of interest

R, radius of test propeller

Re, Reynolds number

r/R, propeller radius ratio

Q, propeller torque

T, twisting torque as used to calculate shear stress

V_A, propeller speed of advance in metres per second (m/s)

V_{ex}, excitation voltage

V_{out}, sensor output voltage

γ, shear stress for torsion

ε, tensile strain

$\mu\varepsilon$, microstrain (μm/m, μin/in,)

τ, shear strain for torsion

ν, viscosity of water (1.01×10^{-6} m^2/s)

CHAPTER 1 – PODDED PROPULSION HISTORY & PROJECT GOALS

INTRODUCTION

Podded propulsion is the fitting of a propeller to a motor that is supported on a strut outside the hull of a ship. This propeller and motor arrangement can rotate through 360° of continuous motion to provide both a thrust force for the ship as well as steering. This setup simultaneously erases the need for a traditional rudder setup and propeller shaft, and lends itself well to revolutionary layouts of new ships for machinery, accommodations and cargo spaces.

Podded propulsion has only been around for a little over 20 years, and first gained popularity in the mid 1990's. The following sections briefly outline some of the history as well as the problems that have resulted from the rapid development of this technology.

1.1 History of Podded Propulsion

Podded propulsion developed from the need for ice breaking vessels to be able to break out of existing ice channels to allow merchant ships to pass. Such a need requires that the propulsion system be able to direct thrust in any direction. This idea became a reality in the late 1980's when, as a result of a research & development project, the Finnish Maritime Administration owned vessel, Seili, was converted to the world's first podded propulsion system. The power output of this first system was 1.5 MW and continues to operate today without fault.

Over the next several years Kvaerner Masa-Yards and ABB, both of Finland, agreed to jointly develop and market this propulsion unit under the name *Azipod*. As a result of the partnership, several other ships were converted to this type of propulsion. The power output at this point in time increased to 11.4 MW.

In 1995 Carnival Cruise Lines of The United States chose the Azipod propulsion unit for its two ships *Elation* and *Paradise*. These ships were fitted with two 14 MW units each. This choice of propulsion greatly influenced future cruise liner propulsion concepts [1].

Such an example of a modern cruise liner fitted with podded propulsion is the *Queen Mary 2*, shown in figure 1.1 [2]. This vessel is equipped with 4 Rolls-Royce *Mermaid* units. All four units are depicted in figure 1.2 [3]. The two forward units are fixed while the aft units are able to rotate, or azimuth, allowing the ship to be steered. A close-up view of this propulsion device is shown in figure 1.3 [4], while a cutaway view appears in figure 1.4 [5].

With the rapid advancements and use of podded propulsion systems have come several problems, briefly outlined in the following section. These problems have caused severe failures while in service, resulting in the loss of confidence in this type of propulsion system in addition to the loss of revenue and customer base for companies owning ships fitted with podded propulsion [6].

Figure 1.1 – The Queen Mary 2, an example of a modern day ship fitted with podded propulsors.

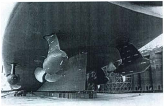

Figure 1.2 – The Rolls-Royce *Mermaid* propulsion units as installed on the Queen Mary 2.

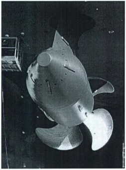

Figure 1.3 – A close-up of the podded drive unit.

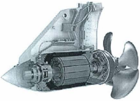

Figure 1.4 – A cut-away view of the pod unit.

1.2 Problems & Advancements with Podded Propulsion

In general, problems with podded propulsion can be described as those related to the reliability of the system and those related to the hydrodynamic performance. The reliability problems stem from those that can be categorized as electrical and mechanical in nature. Hydrodynamic performance issues are those resulting from hull, strut, pod housing and propeller interactions in water flow.

One of the larger electrical problems associated with pod systems is the transmitting of power across slip rings that allow azimuthing. Components in the power transmission across rotating joints have to be subjected to rigorous maintenance schedules to ensure trouble free operation and maximum energy transfer to the pod motor [7]. Another electrical issue is the energy density of the motor. This governs the physical size of the pod and thus has a direct effect on its hydrodynamic performance [8]. In recent years there have been ongoing research and development activities towards producing high temperature super-conducting motors. This will both decrease the pod size and increase power output [9].

As pod units grow in rated capacity, the issue of efficiently and safely controlling the propulsion energy will dictate advances in motor control technology. Pod motors are driven by alternating current and thus are controlled by motor drives that vary the output frequency to control the speed. In recent years advances in semiconductor technology and control strategies have allowed improved performance and higher power handling for podded propulsion applications. An example is the drive technology developed by ASIRobicon, utilized by the Royal Dutch Navy vessel *Johan De Witt*, which is fitted with pods developed by *Schottel* [10].

Mechanical problems with pods include bearing and seal failures, as well as vibrations. Due to the nature of the motor arrangement, high gyroscopic forces are generated even during normal use. This can lead to bearing and seal damage. Such damage is compounded by the fact that debris and water in the lubrication oil is circulated after initial damage, reducing its service life and performance as well as damaging the internal components of the pod unit. This has led to the development of monitoring systems, such as the one developed by ABB, which can continuously monitor the lubrication oil for signs of water contamination [11].

Issues related to hydrodynamic performance include propeller, strut and pod housing design and use, all of which to some degree are influenced by the motor design and size as well as the manner in which the pod operates. The propeller on a pod unit often is exposed to flow angles up to 90° to its axis of rotation, causing vibrations during maneuvering. Such sustained flows are not usually the case for conventional arrangements. Of additional importance is the distribution of pressures that leave the propeller and continue on in the wake field and impinge upon the strut. These pressure pulses can lead to damaging vibrations, especially when the pod is used in tractor or pulling mode, whereby the propeller is situated ahead of the pod unit as it propels the ship. It is important therefore to understand issues related to geometry, hence the reason for many studies on the topic. This now leads the discussion to the current project.

1.3 Project Information & Goals

This project is entitled "Systematic Investigation of Azimuthing Podded Propeller Performance", and is a Natural Sciences and Engineering Research Council (NSERC) funded project. The applicant is Dr. Brian Veitch, a professor of Naval Architectural Engineering at Memorial University of Newfoundland.

There are four partners in this project. They are:

1. Memorial University of Newfoundland (MUN)
2. The Institute for Ocean Technology (IOT)
3. Oceanic Consulting Corporation (OCC)
4. Thordon Bearings Limited

The goals set forth for this project were ambitious and many. The original goals evolved to include the following:

1. Development of the ability to manufacture high quality model scale propellers
2. Development of new methods of instrumentation design
3. Integrate industry with research institutions
4. Enhancement of the manufacturing capability within the research community
5. Carrying out a systematic study of pod and propeller related geometries with the newly designed instrumentation
6. Correlate the model tests with those obtained by numerical methods

Because instrumentation and equipment for use in scale model tests of ships fitted with podded propulsors is still under development, advances in instrumentation design must occur to allow advanced studies of the issues with this type of propulsion.

The author became involved with the project through working with Oceanic Consulting Corporation, a company that provides marine evaluation services. He was listed as one of the design engineers for the project. As soon as it became apparent that the level of involvement would be quite extensive, the author decided to make it the topic of this thesis and switch from the field of corrosion. His previous work experiences and masters work in the field of corrosion greatly influenced the design tasks carried out for this thesis.

1.4 Scope of Work

The author's scope of work was to design the instrumentation, oversee its manufacture, assemble and calibrate the instrumentation and run a series of tests to check its measuring ability. The scope of work also included the delegation of tasks to several work term and graduate students throughout the project.

The intent of this work was to create a facility that could measure both local and global loads. Local loads are generated in the pod whereas global loads result from the pod acting on the ship. In model testing, differences exist between these loads because of factors such as friction. The instrumentation designed in this project measured local loads using load cells, pressure transducers and torque strain gauges, whereas the global loads were measured using a dynamometer connected to the pod. A dynamometer is a multi axis load sensor that when calibrated can measure loads at specific locations for comparison to loads measured locally. For example, thrust local load has two components: one is the thrust generated by the propeller and the other is the drag load generated by the flow of water around the pod shell. This facility was designed to measure these loads separately. It was also designed to allow quick changes to pod and propeller geometry to see how they influenced the local and global loads. Figure 1.5 shows the final instrumentation design and where the loads are referenced.

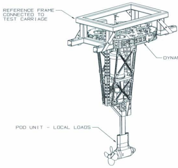

Figure 1.5 – Schematic of final instrumentation design.

1.5 Project Personnel

This project was very much a team effort. From each of the partners mentioned in 1.3, there were key people who all contributed to the overall success of the project.

The discussion now turns to the literature review.

CHAPTER 2 – LITERATURE REVIEW

INTRODUCTION

Designing and manufacturing the instrumentation that enables scale model testing of podded propulsors and models fitted with podded propulsors is a complicated task. The level of knowledge and effort required, as well as the cost to develop these devices is quite high. Because of the uniqueness of each aspect of the overall problem, most institutions and companies that undertake this work are reluctant to release the details of such designs or indeed any results that may diminish any advanced abilities over their competitors. Thus, much of the information remains proprietary.

1.1 Project Information Sources

During the design phase of this project, nearly all the critical design goals came about as a result of a relatively small number of sources of information. *The Propulsion Committee's* final report and recommendations to the 23rd International Towing Tank Conference (ITTC) [12] is one source that served as a summary of issues in regards to testing with model pods. In section 4 of this report, the issues of how to predict the performance of ships fitted with azimuthing thrusters and how to conduct the model testing required to obtain the data for predicting full scale performance is outlined. Two parameters discussed are that of the gap that exists between the strut housing and unit dynamometer, and the gap between the rotating propeller hub and the end of pod housing. The result of this work is an interim procedure entitled *Podded Propulsor Tests and Extrapolation* [13], particularly in which recommended procedures are outlined on how to set up and conduct model experiments with instrumented podded propulsors. This procedure is recognized as one that will evolve over time as procedures become more defined for these types of experiments.

In addition to the information from ITTC publications, the author relied very much so on personal conversations for the review of the state-of-the-art on model podded propulsion units. Conversations with Dr. Brian Veitch [14] and Dr. Neil Bose [15] of Memorial University of Newfoundland, St. John's Newfoundland, made the author aware of many of the current areas of focus in regards to experimental testing with instrumented podded propulsors. Conversations with Veitch and Bose laid the framework for the understanding required to start the design tasks.

In April 2002, the author was very fortunate to travel to Europe with Dr. Veitch to visit and converse with two leading world experts in podded propulsion testing. Conversations with Mr. Friedrich Mewis [16] of Hamburgische-Versuchanstalt (HSVA), Hamburg, Germany and Mr. Jan Holtrop [17] of the Maritime Research Institute Netherlands (MARIN), Wageningen, Netherlands were extremely important to the author's understanding of test parameters such as propeller thrust and torque, and the effect that measurement position has on each. Gap pressure and its effect on measured thrust, in addition to unit thrust and shell drag were also discussed in depth. These conversations were key in guiding the author in his design of the instrumentation measurement systems.

After the design, manufacturing and testing phases of the project had been completed, the author attended a conference, entitled "T-POD, First International Conference on Technological Advances in Podded Propulsion", at the University of Newcastle in Newcastle, UK between April 14-16, 2004. The topics of the conference were widely varied and represented a large number of topics related to podded propulsion. The author presented a paper on the design of the instrumentation used in this project and was the only such one that represented this aspect of podded propulsion testing [18].

The relatively short nature of this literature review reflects the fact that there was little available information on podded propulsor instrumentation design at the time the design phase of this project was carried out. The discussion now shifts to the detailed design stages of the instrumentation used in this project, presented in Chapter 3 following.

CHAPTER 3 - INSTRUMENTATION DESIGN

INTRODUCTION

The instrumentation for this project was designed to enable several sets of experiments to be carried out that measure the performance effect that geometry changes have on podded propulsors. Thus stated, the design tasks became threefold in order to accomplish this overall goal. *First* was the task of designing a system that allowed such geometry changes to be accomplished in a short period of time. Very often, experimental procedures are prone to time delays caused by changing certain parameters or the introduction of errors while changing parameters that are mechanically difficult to attempt. Easily changing geometry allows the collection of large amounts of experimental data in a relatively short period of time. The *second* task was to design instrumentation to measure a number of parameters as they changed (or not) with a change in geometry. For example, torque and unit thrust are typical parameters measured in many commercial model test programs employing podded propulsion. The instrumentation had to register these parameters at a minimum. *Thirdly*, the techniques used in the design of the instrumentation systems were implemented as an attempt at trying to improve instrumentation designs for the study of podded propulsors. During the author's initial consultations with other experts the following questions were posed:

- Can shell drag force be measured?
- How different is the measured propeller thrust depending upon where the force sensor is located in the mechanical system?
- Does the placement of the propeller relative to the pod have an effect on measured thrust and/or the pressure developed in the gap between these two components of the pod system?

These questions led directly to the development of the measurement techniques in the instrumentation systems for this project.

3.1 The Design Process

The design process was completed by jointly considering each of the three major design tasks while taking into account the general practicalities of designing, manufacturing and assembling an instrumentation package of this complexity.

3.1.1 Project Design Criteria

The design criteria for this project were numerous and a challenge to implement in one package. Figure 3.1 shows the design criteria requirements that served as inputs to the design process. These are listed as geometry, instrumentation and experimental apparatus inputs to the design process. Each item listed had to be considered and resulted in a series of design tasks. These are listed in figures 3.2, 3.3 and 3.4. The constraints on design parameters are listed in figure 3.5.

GEOMETRY REQUIREMENT INPUTS

PROPELLER GEOMETRY CHANGES

1. LEFT ROTATING
2. RIGHT ROTATING
3. PULL CONFIGURATION
4. PUSH CONFIGURATION
5. DIFFERENT HUB TAPER ANGLES

PROPELLER GAP DISTANCE CHANGES

1. MINIMUM GAP
2. MAXIMUM GAP
3. CONTINUOUS LINE OF TANGENCY ACROSS THE GAP BETWEEN PROPELLER HUB AND POD SHELL OUTER PROFILES

OUTER POD SHELL CHANGES

1. MINIMUM POD SHELL LENGTH
2. MINIMUM POD DIAMETER
3. INTEGRATION WITH PROP HUB GEOMETRY

INSTRUMENTATION REQUIREMENT INPUTS

INSTRUMENTION TO MEASURE ALL QUANTITIES

1. PROPELLER TORQUE AT PROPELLER
2. PROPELLER THRUST AT PROPELLER HUB
3. PROPELLER THRUST AT SHAFT END
4. PRESSURE AT INTERFACE BETWEEN PROPELLER HUB AND POD SHELL END
5. POD SHELL DRAG FORCE
6. INSTRUMENTATION PACKAGE UNIT GLOBAL FORCE DYNAMOMETER

EXPERIMENTAL APPARATUS REQUIREMENT INPUTS

FEATURES NECESSARY TO RUN EXPERIMENTS

1. DRIVE MOTOR & CONTROL
2. POWER TRANSMISSION SYSTEM
3. ELEVATOR LIFT SYSTEM TO FACILITATE GEOMETRY CHANGES
4. DATA AQUISITION SYSTEM
5. WATER-TIGHT ENVELOPE FOR ALL INSTRUMENTATION SYSTEMS

Figure 3.1 – Geometry, Instrumentation & Experimental Apparatus Requirement Inputs to the design process.

GEOMETRY DESIGN TASK OUTPUTS

UNIVERSAL PROPELLER HUB ADAPTER

1. UNIVERSAL PROPELLER HUB THAT ALLOWS MULTIPLE PROPELLERS WITH MULTIPLE PROPELLER HUB TAPER ANGLES TO BE MOUNTED
2. LOAD CELL INSTRUMENTATION TO FIT INSIDE
3. HUB TO BE WATER-TIGHT

GAP DISTANCE ADJUSTER MECHANISM

1. EASY GAP ADJUSTMENT
2. MINIMUM / MAXIMUM GAP RANGE DICTATES DRIVE GEAR AND THRUST MEASUREMENT DESIGN
3. DICTATES CHANGEABLE POD SHELL END DESIGN (GAP FILLERS)

SPLIT SHELL DESIGN

1. UNIVERSAL MOUNTING POSITIONS
2. UNIVERSAL INTERIOR SPACE DESIGN
3. WATER TIGHT INNER INSTRUMENTATION PACKAGE
4. MINIMIZATION OF WATER FLOW BETWEEN SHELL COMPONENTS AND INNER INSTRUMENTATION
5. MINIMIZATION OF WATER VOLUME BETWEEN COMPONENTS
6. DEVELOPMENT OF METHOD OF GENERATION OF ALL POD SHELLS
7. IMPLIMENT GAP FILLER ADAPTOR DESIGN ON SHELL USED IN INSTRUMENTATION COMMISIONING

Figure 3.2 – Geometry design task outputs generated.

INSTRUMENTATION DESIGN TASK OUTPUTS

PROPELLER TORQUE & THRUST

1. DESIGN PROPELLER SHAFT WITH STRAIN GAUGES LOCATED AT PROPELLER HUB
2. DESIGN TORQUE TRANSMITTING CONNECTION BETWEEN PROPELLER HUB AND SHAFT
3. DESIGN SECURING METHOD TO KEEP PROPELLER ATTACHED TO SHAFT
4. DESIGN PROPELLER THRUST LOAD CELL MOUNT AS AN INTEGRAL PART OF THE PROPELLER SHAFT
5. DESIGN ELECTRICAL CABLE INSTALLATION FEATURES

POD THRUST

1. DESIGN LOAD CELL MOUNT AS INTEGRAL PART OF GAP ADJUSTMENT MECHANISM
2. DESIGN TORQUE TRANSMITTING CONNECTION BETWEEN PROPELLER SHAFT AND DRIVE GEAR
3. CONSIDER WIRING ROUTES

GAP PRESSURE

1. LOCATE PRESSURE TRANSDUCERS AT INTERFACE
2. LOCATE PRESSURE TRANSDUCERS AT DIFFERENT RADIUS VALUES
3. DESIGN CHAMBER TO ALLOW ATMOSPHERIC VENTING OF TRANSDUCERS
4. CONSIDER WIRING ROUTES

SHELL DRAG

1. DESIGN MOUNTS TO MEASURE SHELL DRAG FORCE LOAD
2. CONSIDER WIRING ROUTES AND WATERPROOFING OF LOAD CELL

UNIT THRUST

1. DESIGN 6 COMPONENT DYNAMOMETER
2. DESIGN COMPONENTS TO CONNECT POD UNIT TO DYNAMOMETER
3. CONSIDER WIRING ROUTES FOR ALL SYSTEMS

Figure 3.3 – Instrumentation design task outputs generated.

EXPERIMENTAL APPARATUS DESIGN TASK OUTPUTS

EXPERIMENTAL APPARTUS SUPPORT SYSTEMS DESIGN

1. DRIVE MOTOR & CONTROLLER SELECTION
2. POWER TRANSMISSION SYSTEM DESIGN
3. ELEVATOR LIFT SYSTEM DESIGN
4. DATA AQUISITION SYSTEM SELECTION
5. ELECTRICAL SYSTEM DESIGN & CABLE ROUTES
6. MAIN DRIVE CASE, SLIP RING, AND HUB SEALING METHODS

Figure 3.4 – Experimental Apparatus design task outputs generated.

CONSTRAINTS

MIN/MAX GEOMETRIC CONSTRAINTS

1. MAXIMUM INSTRUMENTATION DIAMETER
2. MAXIMUM INSTRUMENTATION LENGTH
3. MINIMUM/MAXIMUM PROPELLER GAP SETTING
4. PROPELLER DESIGN DIAMETER
5. MINIMUM HUB TAPER ANGLE
6. DEPTH OF PROPELLER DEPLOYMENT DURING TESTING

INSTRUMENTATION LOAD CONTRAINTS

1. MAXIMUM PROPELLER TORQUE = 34 Nm (300.9 in-lb)
2. MAXIMUM PROPELLER THRUST = 890 N (200 lb)
3. MAXIMUM DYNAMOMETER THRUST = 2 X PROPELLER THRUST = 1780 N (400 LB)
4. MAXIMUM DIFFERENTIAL PRESSURE IN GAP = 48.3 kPA (7 psi) (SENSOR RATING ONLY)
5. MAXIMUM UNIAXIAL SHELL DRAG = 222.4 N (50 lb)

DEPLOYMENT CONTRAINTS

1. INSTRUMENTATION PACKAGE TO FIT MUN TOWING TANK & IOT TOWING TANK
2. PROPELLER MUST BE LOCATED IN AT LEAST 1.5 X PROPELLER DIAMETER OF WATER

Figure 3.5 – Constraints.

Several aspects of the design were iterative and subject to design reviews by the project group. After input from each in the project group had been expressed, and after a significant and extended effort, the author arrived at the final design.

3.1.2 Using Readily Available Parts

To speed the design process along and increase the serviceability of the instrumentation, as many parts as possible were sourced as commercially available. Items such as bearings, seals, o-ring cord stock, ball elements, the gear box, the drive coupling, load cells, slip rings and brushes, fasteners, clips and other items such a hardened and ground round stainless steel rods were used. The drive belt was the only custom ordered piece in the system. Even so, the tooth profile was of a standard design such that the drive gear mounted on the output shaft of the gearbox could be ordered as a stock item blank and finish machined to final design specifications.

3.1.3 Material Considerations

As with any exercise in mechanical design, the choice of which material to use in each component was thought through very carefully. For this project, the main considerations governing material selection were:

- *strength*
- *ease of machining*
- *mass*
- *corrosion resistance*
- *availability*

3.1.4 Manufacturing Considerations

The use of CNC machining techniques allowed the freedom to design parts utilizing complex combinations of lines and arcs for their form, either as 2 ½ D parts or surfaces. Thus, the component designs were not restricted to the relatively simple shapes capable of being produced by traditional milling or turning techniques. In some cases however, the consideration of using combinations of CNC machining followed by conventional methods were used in design process. In particular, the propeller shaft and drive gear are two pieces. In the latter case, one manual step (turning the blank) and one manual step in conjunction with a CNC step (milling each drive belt tooth profile, followed by a rotation with an indexing head) were the steps considered as the fabrication process required to produce the part. Also, the fact that it is practically very difficult to machine an inside right angled corner caused the design of the drive gear to be an assembly that required material to be machined away in one step, and then put back with the added assembly of a secondary part. The correct end geometry was thus designed as a union of two boundaries, both practical and simple to manufacture. This is how the drive gear guide rings for the drive belt were produced.

Some components required the use of a fixture design, especially the dynamometer live end upper and lower plates. This is often the case with a larger component that is subject to natural deflection due to its own mass. In the case of the dynamometer live upper and lower plates, the material chosen was ½ inch (12.7 mm) plate. This sheet stock usually has a natural deviation in terms of flatness that is dictated by such factors as ambient temperature, past handling characteristics and method of separation from the 4'x8' standard sheet size. For these components the method of support that would be required for the machining stage was considered during the design phases. The individual design of each system is now discussed.

3.2 Propeller Hub Thrust Measurement

There are several key functional highlights of the hub mechanical and electrical design. *First* is the ability to convert propeller thrust force into a stable electrical signal. There were two options to consider when designing this aspect of the pod subassembly. The first option was to design a hub that utilized strain gauged thrust load bearing components designed specifically for this application. The second option was to design the hub to use a factory ready force sensor. Given the complexity anticipated by the author coupled with the high probability of a large thrust range expected with numerous test setups, it was decided to use a commercially available stock load cell as the force sensor. Designing the hub to accept a factory piece would allow several propeller thrust ranges to be tested, given that many force sensors are available with several ranges for the same geometric package. This could potentially avoid the situation of measuring a small load with a force transducer having too large a range, compromising resolution.

The second option as a choice of sensor also gave the advantage of allowing for pre-amplification of the signal, given that load cells are available as high output units. In this case, a manufacturer was sourced that produces a high output load cell with several load ranges available in the same geometric package. The output is 200 mV (with 15 VDC excitation) at a full scale loading of 890 N (200 lbs) (see **Appendix A** for specifications). As a comparison, using a properly designed load element gauged with a strain gauge having a typical gauge factor of 2.1, the output would only be 20-30 mV with a full scale loading. One can immediately see a gain factor advantage of nearly 10. This pre-amplification reduces the signal to noise ratio as the thrust signal is conducted through the slip rings of the rotating subassembly. It also reduces the gain setting required at the input to the data acquisition system card for this channel. Thus it was decided early in the design phase to use a readily available load cell for the thrust measurement.

Once a scheme for converting thrust to an electrical signal had been chosen, the *second* aspect of the design could commence. The following points describe the mechanical requirements of the design:

- Lowest possible friction loss in the thrust direction
- Maximum torque transmission through the joint
- Limited water leakage and maximum mitigation of the effects of a leak
- A design that was achievable in terms of both ease of component machining and final assembly
- The design had to occupy the smallest possible volume to facilitate the mounting of different propellers without disturbing the thrust instrumentation

Each of these in turn dictated specific component selections and material choice.

To lower friction it was decided to use a rolling assembly that consisted of hardened stainless steel ball bearing elements and shafting between the moving and fixed parts of the hub. In essence this creates a linear bearing type assembly.

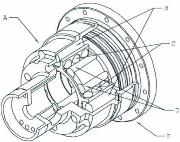

Figure 3.6 – Prop hub torque transmission drive component arrangement.

The layout in Figure 3.6 shows the rod and ball arrangement in a sectioned view of the final propeller hub design. The moving or live portion of the hub (A) is the component that connects directly to the propeller. The first set of rods (B) are inserted into holes in the live end of the hub (note that two inner rods have been omitted to allow a clearer view of inner components) and contact the balls (C) which in turn contact a second set of rods (D) which are inserted into holes in the reference part of the hub (E). With this arrangement, the input torque to the joint causes a force to be passed through the balls to allow propeller rotation, without any restraint in the thrust direction. This setup has a low rolling friction, but necessitated the use of hard materials to prevent the balls from imbedding into the rod surfaces. By using hardened rods and balls, the other components could be machined from type 303 stainless steel, which is relatively soft. Specifications for type 303 stainless steel can be found in **Appendix B**. Note that there are five such sets of three drive balls and rods arranged in three parallel planes. This reduces the load force per ball due to torque, and stabilizes the joint.

The material for the rods and ball elements was chosen to be type 440C. These off-the-shelf components are heat treated after their manufacture to a range of Rockwell C58-C65 hardness. To ensure that the hardness of the purchased components was as specified, the author had several samples mounted and tested, as shown in figure 3.7.

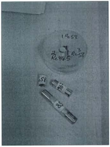

Figure 3.7 – Hardness check of 440C stainless steel and alternate P7 rods.

The test value was C58 hardness, which was within specification, although at the lower end of the range. Because of its dimensional accuracy, a sample of P7 drill rod was also tested. A hardness test yielded a value of C46.5. This sample was tested as a potential substitute material if the type 440C stainless steel rod was not as hard as specified. Specifications of 440C stainless steel is listed in **Appendix B**.

The ball elements were located as far as possible apart in the radial direction to maximize torque transmission and minimize individual ball load. The final position was a result of an iterative process that involved the propeller hub design. Although intertwined, the propeller hub design is covered separately in the next section. Figure 3.8 outlines the final rod and ball placement geometry. Based on a design torque of 34 N·m and the final ball and rod positions, each ball supports a normal force loading of 134.12 N (30.15 lb).

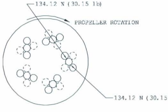

Figure 3.8 – Ball and rod layout geometry with maximum ball loading.

Note that for each direction of propeller rotation, the line of force on each ball element passes through two points of contact. The other two rods are used during the opposite rotation.

Once the layout of the mechanism allowing a maximum torque value to be transmitted while allowing freedom to translate in the axial direction had been finalized, the next aspect of the hub instrumentation design commenced. The factory load cell that registers the thrust force of the propeller was mounted directly into the end of the propeller shaft. This decision was made to eliminate one potential mechanical coupling that might vibrate loose during operation. The live end of the load cell was located such that it connected directly to the component that the propeller mounts on. This arrangement allows a simple mechanical link between the propeller and the propeller shaft in terms of thrust transmission, while allowing the de-coupled torque transmitting components to be arranged around the load cell and propeller shaft end. Figure 3.9 illustrates the location of the load cell.

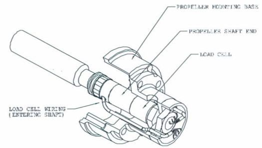

Figure 3.9 – Load cell position between propeller mount and shaft.

Note that there are jam nuts on only one stud of the load cell. This prevents torsional loading of the load cell body due to minute relative movements during loading of the propeller.

The next step in the design process of the hub instrumentation consisted of creating a water tight seal that protects the load cell while the pod unit is deployed in water. To mitigate the effects of a possible leak, it was decided to use all stainless steel components. Very often, the mistake is made of assuming that a leak in this type of instrumentation will not likely occur. The author chose to assume that it would leak at some point in time, mostly likely due to improper assembly, or damage during operation. In the case of a leak, the damage would be limited to the electronics of the load cell, and not the torque transmission components. In the event of a leak, a new load cell can be purchased and installed.

There were several issues to deal with in terms of minimizing water leaks. The first was the seal between the propeller hub and the hub instrumentation. It was decided to use o-rings seals at both ends of the hub because of the relatively frequent change of propellers. Gaskets were ruled out because although superior (in the author's view), they are not easily changed and new ones must be used each time. O-rings are superior in the case of frequent disassembly. It was thus decided to make the inner bores of the propeller hub part of the water-tight container that protects the propeller hub thrust load cell. By not having a completely sealed hub mounting assembly for the propeller, one component was eliminated (an outer canister) and the torque capacity increased because of an increase in potential radial space for the ball and rod arrangement. A disadvantage that was considered is the fact that the unit cannot be deployed in water without either a propeller or a dummy hub.

The o-ring seals for the propeller hub were designed with an approximate squeeze value of 28%. The o-ring diameter was chosen to be 1.78 mm (0.070") to keep the cavities holding the o-ring to a minimum. The final cross sectional dimensions for each o-ring groove was 2.54 mm (0.100") in width and 1.27 mm (0.050") deep. Figure 3.10 shows the final o-ring seal configuration for the propeller hub.

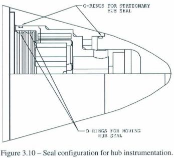

Figure 3.10 – Seal configuration for hub instrumentation.

The next issue that had to solved in terms of keeping the hub instrumentation sealed was the fact that under load, there would be a relative movement between the live end (and its attached propeller) and the reference end at the propeller shaft. Making the assumption that all other components in the hub are infinitely stiff and that the load cell would be the only part deflecting under load, the relative movement would be approximately the 0.076 mm (0.003") specified deflection of the load cell under maximum load. Thus, the seals had to seal the moving end to the fixed end *and* allow relative movement without adding a significant amount of stiffness to the system.

To accomplish this sealing problem, a unique solution was proposed by the author. A set of o-rings would be used in a non-conventional way to allow the relative movement.

This was accomplished by having the o-ring seal squeezed between two parallel surfaces with a greatly exaggerated lateral clearance value. As well, the squeeze value was reduced to a final value of just 10%. This would allow the two parallel surfaces to move relative to each other with the o-ring *rolling* between them. Two seals at one joint were utilized to compensate for the relaxed fit. The final squeeze value was determined experimentally by machining a test piece and assembling a dummy hub to the seal adaptor. The test assembly was then held under water and the two moving components actuated as it would be in operation. Two minor adjustments were made to the initial geometry as designed. One was to move the position of the lateral clearance to a position that would allow the relative sliding to occur during assembly without pinching the seal material, and the second was an adjustment of the gap between the seal containment surfaces. The original distance was 1.525 mm (0.060"). This value had a tendency to bind the joint under extreme lateral movements. The value was finalized to be 1.600 mm (0.063") and this value proved to be effective at allowing free movement and no water leakage. Figure 3.11 shows the final seal arrangement for the moving seal. Figure 3.12 shows the seal test piece used in the experimental development of the seal. The final geometry is in the right of the photo.

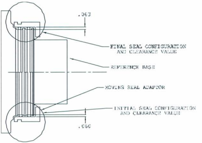

Figure 3.11 – Moving seal arrangement.

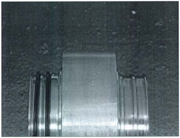

Figure 3.12 – Moving seal test piece.

The final design issue with the hub thrust measurement was the setup clearance values that would need to be implemented during assembly. Also of importance were considerations as to how the thrust measurement could be truly isolated from any effects of pressures in the space between the rotating face of the propeller hub and the stationary face of the pod end.

The initial design thinking in terms of isolating the effects of gap pressure influencing the propeller thrust measurement was to consider the propeller hub cross section as a trapezoidal shape (omit the propeller nose cone). The larger face of the hub at the gap interface would need to be stationary and rigidly fixed to the propeller shaft. The other three faces would therefore need to be mobile relative to the first face. The complexities of the design hinged on the details of how the interface between these two sets of faces would be arranged to minimize the introduction of unknowns, and some simplifying assumptions and recognition of some errors that would have to be included due to the limitations of the machining processes and a desire to produce parts that made assembly relatively simple. Indeed, the entire instrumentation package would ultimately have to be rugged enough to stand up to the initial testing and subsequent use.

The author settled on a geometrical compromise for the issue of gap pressure isolation. The sides of the propeller hub ended with an intersection to a line parallel to the end of the pod shell, perpendicular to the axis of rotation. After this face there is a ring of clearance that is just 0.254 mm (0.010"). This value was decided upon because it is larger than the maximum specified deflection of the load cell, and assuming no other component flexes, there would be ample clearance at full load to ensure that mechanical interference does not limit the load measurement capacity of the load cell. After this gap is a ring whose outer surface is tangent to the hub taper angle of the propeller. This ring is fixed to the propeller shaft via a connection with the propeller reference base. A hub taper angle adaptor must be machined to accommodate each hub taper angle change. The length of this adaptor along the direction of the propeller axis was kept as short as possible. Any drag due to this short rotating ring will be measured by the propeller shaft thrust load cell, but *not* by propeller hub thrust load cell. This will introduce an error due to the differing surface areas of the hub, depending on which load cell is registering it. The error due to this geometry must be assumed to be small. An alternative that was considered was to have the hub surface end with an intersection with a conical surface subtended by the outer surface. The end result would have been a sharp edge at the end of the propeller hub. There would have to be an axial clearance of about 0.254 mm (0.010") and another adaptor that would have the same taper angle as the inner conical taper angle. The author chose not to go this route for several reasons. The first is the consideration that for such an arrangement, as the propeller moves though water there might be a tendency to scoop water up, depending on the direction of pod travel. Also, the end of the hub would be in the same general area as the gap, thereby opening the possibility of gap pressure influence. Lastly, the resulting sharp edge of the propeller hub would have been very fragile and, while not impossible to machine, it would have been undesirable. An adaptor with this feature could have been designed, but this would add yet another machining task to the already time consuming endeavor of machining the propeller. Thus, it was decided to go the route of a thin ring having the same taper angle as the propeller hub and accepting any error this may introduce. It is left to the reader to contemplate or investigate the effects of this choice. Figure 3.13 shows a comparison of the two considered geometries.

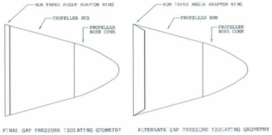

Figure 3.13 – Alternate geometries for isolating gap pressure effects on hub thrust.

3.3 Propeller Hub Design

Aside from the outer geometry of the propeller hub there were several design issues as follows:

- final geometry as a function of propeller diameter
- method of attachment of propeller to hub instrumentation
- method of attachment of propeller nose cap to hub
- integration with propeller blade geometry

To accommodate the mounting of a large electric motor in the body of a podded propulsion unit, the hub of a propeller used on a podded drive is typically larger than a traditional shaft driven propeller. In the case of this project it was desired to have a hub diameter to propeller diameter ratio of 0.26:1. The base geometry was calculated for a 15° hub taper angle. Using a propeller diameter of 270 mm (10.630"), a cylindrical hub would therefore be 70.2 mm (2.764") in diameter. By rotating the cylindrical profile at the midpoint, this yielded the final leading and trailing edge diameters of the propeller hub. For a 20° hub taper angle, the hub profile line was rotated about the smaller endpoint of the profile instead of the midpoint. This ensured that the mounting design could remain the same for both of these propellers and others in the future.

Attaching the propeller to the hub instrumentation presented several design challenges. The first was that the method had to be simple, and the second was that the process of installing the propeller had to be one such that no excessive forces would be applied to the hub instrumentation during installation or removal.

The final attachment method was by the use of 8 #10-32 machine screws arranged in 4 sets of two holes spaced at 90° intervals. The plane of the mounting holes was near the small end of the propeller, at the opening, to allow easy access. Having 8 fasteners allows for redundancy since only 4 are actually required to evenly hold the propeller in place at full load. This way up to 4 fastener locations can have the threads stripped (due to improper fastener mounting or wear) in the stainless steel propeller mounting component of the hub instrumentation without disabling the pod unit. Using 8 screws with a thread pitch of 32 threads per inch (approximately 0.8 mm thread pitch) allows the propeller to be easily installed over the hub instrumentation while compressing the o-ring seal. A 15° bore entrance taper at the hub of the propeller allows this. The torque required to complete this assembly sequence is thus far below the rated capacity of the torque instrumentation, even if the screws are tightened without holding the propeller, allowing the reaction torque to be supplied by the pod drive system.

A propeller removal method was also a design feature of the propeller hub. There are 4 jacking holes, each with a # 8-32 thread. These are located in the spaces between the mounting holes. These allow the installation of at least two machine screws, located opposite each other, to pull the propeller off the hub with a minimum amount of applied force from tools. Figure 3.14 details the mounting features of the propeller hub.

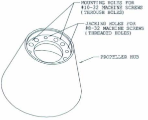

Figure 3.14 – Propeller hub mounting details.

The propeller nose cap design features a screw-on method of attachment and an o-ring seal. The threads for the nose cap are machined on the propeller hub instrumentation. The thread pitch is 28 threads per inch (approximately 0.9 mm pitch) to ensure that the nose cap can be installed by hand without the use of any tools. Installing the nose cap hand tight will ensure that it will not come off during testing. In addition, a design of this nature has no discontinuities or other blemishes in the surface such as those made by counter-bored mounting holes. Figure 3.15 shows the nose cap threaded connection details.

Once all of the hub features had been designed, the geometry was integrated with the propeller blades. The propeller blade foil sections were designed by Dr. Pengfei Liu of the Institute of Ocean Technology (IOT) in St. John's Newfoundland Canada. Once the blade section data had been defined by Dr. Pengfei, the surfacing was carried out by Mr. Tony Randell, also of IOT. Using the hub geometry, the blade root fillets were also completed by Mr. Randell. The complete propeller CAD model was then ready for manufacturing.

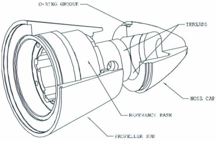

Figure 3.15 – Nose cap mounting details.

3.4 Propeller Shaft Thrust Measurement & Gap Adjustment Mechanism Design

The thrust of the propeller is measured internally at the end of the propeller drive shaft. The system has a dual function in that it has to allow movement of the propeller plane relative to the pod end *and* measure thrust for all positions. As with the propeller hub thrust, the torque had to be de-coupled from the load cell body and a mechanism had to be designed to allow the transmission of torque while allowing the free movement of the propeller shaft system in the thrust direction. The free movement in the thrust direction allows the thrust force to be registered by the load cell as well as an axial movement of the propeller shaft relative to the entire assembly during adjustment of the gap distance. The design process for this aspect of the pod instrumentation started with the torque transmission joint. An approach similar to the propeller hub instrumentation torque transmission joint was used. In this case, four sets of 4 balls and 4 rods were used for a total of 16 balls whereas the hub joint has 15 balls. The radial arrangement of the torque transmission joint for the shaft thrust was calculated to match the capacity of the hub. This led to a slightly more compact arrangement and less machining for the same torque capacity (4 sets of parts versus 5). Figure 3.16 shows the arrangement of the torque transmission drive joint.

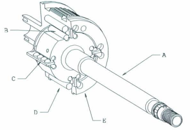

Figure 3.16 - Drive gear torque transmission joint drive component arrangement.

In this case, the moving or live portion of the arrangement is the propeller shaft (A) and is the component that connects to the propeller via the hub instrumentation. The first set of rods (B) are inserted into holes in the propeller shaft base (note view is sectioned at arrow) and contact the balls (C) which in turn contact a second set of rods (D) which are inserted into holes in the drive gear (E). As with the propeller hub instrumentation, the input torque to the joint causes a force to be passed through the balls to allow propeller shaft rotation, without any restraint in the thrust direction.

The next step in the design process was to design a mechanical connection between the propeller shaft and the load cell that *would not* transmit any torque. This was accomplished by the inclusion of a thrust bearing in the end of the propeller shaft that is connected to another shaft (termed the thrust shaft) that carries the thrust load to the load cell. The thrust bearing along with a needle roller bearing are arranged in a cavity in the propeller shaft end that is located in the torque transmission joint. In essence, the propeller shaft rotates around the thrust shaft and transmits thrust *only* to the load cell. The thrust and needle roller bearing cavity is fitted with its own seal arrangement so that in the event of a leak in the hub instrumentation, water will not likely get into the main pod instrumentation cavity through the hollow section of the propeller shaft. Figure 3.17 shows the arrangement of the thrust and needle bearings, and the thrust shaft. Note that the thrust shaft is held in place by the use of a common mechanical retainer termed a 'keeper'. This type of retention relies on the mechanical arrangement of parts and an external force to keep the assembly from falling apart. In this case it is the propeller shaft cover that carries out this task.

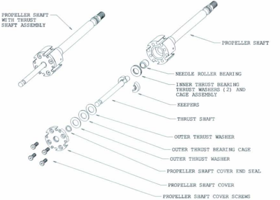

Figure 3.17 - Thrust and needle bearings, and thrust shaft arrangement.

Next, the load cell mount was designed in such a manner that its relative axial position could easily be changed to adjust the gap distance at the propeller end of the pod instrumentation. The mechanism designed to carry out this task is a stand alone subassembly that can be removed from the pod assembly with a minimum amount of effort. This was done to enable the load cell to be changed relatively easily in the case of water or other damage. The route for the load cell signal cable was also incorporated in the design. In this case the design process was less involved in that the wiring was not part of a rotating assembly. The cable from the load cell simply includes a strain relief loop and then proceeds through the housing for the slip rings and meets up with a terminal block.

The gap change mechanism is designed such that to change the gap setting, all one has to do is loosen a lock nut and then rotate another shaft (termed position setting shaft) clockwise or counterclockwise to move the propeller in the axial direction. The mechanism was also designed to prevent any torque from reaching the load cell body from the fixed end of the load cell. Figure 3.18 shows the arrangement of the gap adjustment mechanism and load cell mount. Sealing of the thrust position shaft was

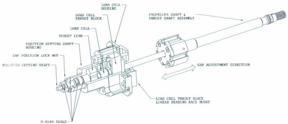

Figure 3.18 - Gap adjustment mechanism and load cell mount arrangement.

accomplished with a dual o-ring arrangement at all points of potential leaks. The components that make up the various housings are sealed with gaskets and bolted joints that evenly distribute the clamping force on the gasket.

The range of gap adjustment was set after considering the 2002 ITTC interim standards on pod testing [13], which states that the propeller gap should be set at 1% of the propeller diameter. In this case the project propeller is 270 mm (10.630"). This means that the gap adjustment mechanism had to accommodate a gap setting of 2.7 mm (0.106") plus be adjusted to lower and higher values. After some consideration, the minimum gap setting was set at 0.254 mm (0.010") and a maximum of about 7.250 mm (0.285"). This range can be increased with some minor modifications to the adjustment mechanism, as the actual travel of the propeller shaft system is nearly 10 mm. To do so would require the removal of position shaft housing and replacement of the thrust link with a longer version. The two photos in figure 3.19 show the unrestrained range of movement that

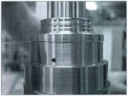

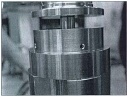

Figure 3.19 – Unrestrained gap distance range is approximately 0.254 -10 mm (0.010-0.394").

results when the load cell is not connected. Before ending the discussion on the thrust measurement aspect of this section's design, it should be noted that mechanical friction from a number of sources will influence the thrust measurement, in addition to the effect of the gap distance. The effects of the two sets of seals as well as the three sets of bearings will be minimized by way of the instrumentation's calibration procedure. The propeller torque measurement design is discussed next.

3.5 Propeller Torque Measurement Design

Early in the design thinking it was decided to measure the propeller torque as close to the propeller as possible. This decision simplified a number of issues including the testing and calibration process, given that if the torque measurement occurs at the propeller location, then the effects of seal or bearing friction need not be considered. It also simplified the design of the propeller shaft and drive gear arrangement in that by locating the torque measurement transducer in a space close to the propeller, the shear strain could be maximized without making the component overly delicate, thereby maximizing electrical output from the torque sensor.

The sensor in this case is a carefully designed segment of the propeller shaft that is instrumented with torsional strain gauges. To compensate for temperature, axial and bending strains, the gauges were configured as a full bridge type sensor circuit. A full bridge sensor circuit is one that employs a configuration known as a Wheatstone Bridge circuit, in which all resistors are active strain gauge elements. Having a full bridge sensor also maximizes the electrical output for a given torsional strain due to the propeller torque. Figure 3.20 shows a typical wheatstone bridge circuit. Referring to the figure, the excitation voltage in this case is 10 VDC (V_{ex}) and the output voltage sensed by the data acquisition system is V_{out}. Both the excitation and signal currents were conducted through slip rings. The issue of slip rings and their selection is discussed in section 3.11.

Figure 3.20 – Wheatstone Bridge circuit with four active gauge elements.

The gauges chosen were manufactured by Micromeasurements Group Incorporated and have a gauge factor of approximately 2.06. **Appendix C** has the specifications for the selected gauges, including any tolerances. Without justification, the equation relating strain (ε), gauge factor (GF), input (V_{ex}) and output (V_{out}) for a bridge containing 4 active elements is:

$$\frac{Vout}{Vex} = -GF * \varepsilon \qquad \text{- Equation 3.1}$$

To maximize the longevity of the sensor, the shaft section that registers the torque is designed to have an induced strain value of 1200 microstrain (μm/m, μin/in, με) for an applied torque of 34 N·m (303.01 in·lb). The shear modulus and modulus of elasticity for type 303 stainless steel are 77.2 GPa (11200 ksi) and 193 GPa (28000 ksi) respectively. **Appendix B** has the specifications for type 303 stainless steel. Equations 3.2 and 3.3 display the relationship between torsional strain (γ) and stress (τ), and stress, torque (T) and polar moment of inertia (J) respectively as follows:

$$\gamma = \frac{\tau}{G} \qquad \text{- Equation 3.2}$$

$$\tau = \frac{Tc}{J} \qquad \text{- Equation 3.3}$$

The polar moment of inertia for a hollow cylindrical shaft is given in equation 3.4 as:

$$J = \frac{\pi}{2}(c_o^{\,4} - c_i^{\,4}) \qquad \text{- Equation 3.4}$$

where:

c_o = shaft gauge area outer radius
and
c_i = shaft gauge area inner radius

Equation 3.4 is used because the shaft must have a central hole to carry the wiring from the strain gauges as well as the propeller hub thrust load cell. For practical deep drilling purposes, a hole diameter of 6.35 mm (0.250") was chosen for the passageway through the shaft, thus c_i is set to 6.35 ÷ 2 = 3.125 mm (0.250 ÷ 2 = 0.125"). To arrive at a value for c_o, equation 3.4 is substituted into equation 3.3 and then combined with equation 3.2. Setting this result equal to the value for maximum torsional strain leads to the following expression (using imperial units):

$$1200 \times 10^{-6} = \frac{301.01 c_o}{\pi \frac{11200000}{2}(c_o^{\,4} - 0.125^4)} \qquad \text{- Equation 3.5}$$

Iterating this expression allows a final value for c_o, to be selected, as shown in table 3.1. Note that the upper and lower limits of the iteration were selected based on the maximum shaft diameter and an arbitrary value larger than the central hole.

d_O (inches)	c_O (inches)	Torsional Strain (in/in, mm/mm)	
0.700	0.350	0.000406	
0.675	0.338	0.000454	
0.650	0.325	0.000510	
0.625	0.313	0.000575	
0.600	0.300	0.000653	
0.575	0.288	0.000747	
0.550	0.275	0.000859	
0.525	0.263	0.000997	
0.500	***0.250***	***0.001168***	0.0012
0.475	0.238	0.001383	
0.450	0.225	0.001660	
0.425	0.213	0.002026	
0.400	0.200	0.002524	
0.375	0.188	0.003235	
0.350	0.175	0.004316	
0.325	0.163	0.006136	

Table 3.1 – Iterated values converging on final value for c_o.

From table 3.1, the calculated strain value for c_o = 6.35 mm (0.250") is 1168 $\mu\varepsilon$, which is just under the maximum value of 1200 $\mu\varepsilon$. The resulting diameter of 12.7mm (0.500") allows ample room for mounting the gauges and terminal strip.

In the case of measuring torque, the strain is determined by using gauges that have the grid pattern at a 45° angle. The total strain in the bridge is therefore equal to twice the strain measured in one gauge at 45°. If one substitutes this value, the gauge factor and excitation voltage into equation 3.1 the result is 0.0241 V. This yields a sensitivity of 2.41 mV/V at full scale torque loading.

The final configuration for the gauge area of the shaft is shown in figure 3.21.

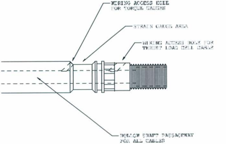

Figure 3.21 – Final gauge area for propeller shaft.

Once the issue of designing the shaft to register the expected torque load had been completed, the method of transmitting the torque from the propeller shaft to the propeller hub instrumentation was dealt with. There are several methods typically employed for such a situation. One is by the use of a shaft keyway. Normally this method would have been adequate, but the requirement of having a water-tight joint at the propeller shaft/hub interface meant that the method used to machine a keyway would not have allowed this to be possible. A splined connection was also considered, however the tooling required and machining procedures would have been beyond the time capabilities of the project, especially since the internal spline of the hub would need to be blind.

To accomplish this aspect of the project, a unique geometry was employed by the author. An octagonal shaped drive interface was designed. The 8 sides of the drive connection were filleted with a 1.5875 mm (1/16") to ensure that this feature could be machined on both parts. A diametral clearance of 0.0254 mm (0.001") was used between the mating parts. To provide a water-tight seal, one o-ring seal was included between the shaft and the propeller hub reference base. Figure 3.22 shows the details of the octagonal drive segment of the shaft while figure 3.23 shows a cut-away of the o-ring seal detail. The design of the gap pressure measurement instrumentation is discussed next.

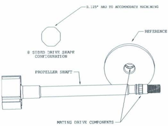

Figure 3.22 – Octagonal drive feature of the propeller shaft.

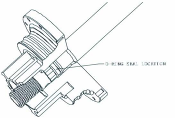

Figure 3.23 – O-ring seal detail between shaft and reference base.

3.6 Propeller/Pod Interface Gap Pressure Measurement Design

Designing instrumentation for the measurement of the gap pressure proved to be quite challenging. There were several main issues that had to be thought through during the design phase of this aspect of the pod instrumentation. These include:

- the orientation of the orifices measuring the gap pressure
- the number of orifices measuring gap pressure
- the sensor type to use to measure this parameter

During the initial thinking on this part of the instrumentation, it was decided to set-up the sensors in a horizontal plane, and employ 5 in total, each at a different radial position relative to the propeller shaft axis of rotation. This choice of orientation was made with the desire of perhaps measuring any potential pressure distributions across the face of the pod end. Figure 3.24 shows the radial distances to each pressure measuring orifice.

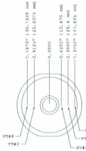

Figure 3.24 – Radial location of the five pressure transducers.

The sensor type chosen is a high output device with a differential measuring range of ±5 psi (34.5 kPa). **Appendix D** lists the specifications. At the maximum pressure level the output is approximately 245-250 mV, depending on the individual transducer. This type of device has the specific requirements of having a vent on the opposite side of the pressure sensing element at atmospheric pressure, and it must have no direct contact with water. In anticipation of operating the sensors in silicone oil to avoid water contact, they were ordered with no protective screens in the sensor body tubing to lower the probability of entrapment of air bubbles, which hinders both response time and accuracy of their readings.

To accommodate the atmospheric venting parameter, the design necessitated a common chamber to which all vent tubes could exit at atmospheric pressure. This issue was relatively simple to solve, however machining considerations has to be made to allow tooling choices. The layout of the chamber includes a water tight passageway though the center for the propeller shaft (which is surrounded by water) to pass through, an exit spigot for both the pressure transducer wiring and PVC tubing that allows the chamber to be vented at atmospheric pressure, and gasket sealed joints. Figure 3.25 shows the layout of the chamber.

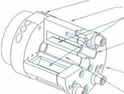

Figure 3.25 – Atmospheric pressure chamber.

To keep water from contacting the pressure sensing element, silicone based oil was used as an intermediate medium between the pressure measuring orifice and the sensor. To arrive at this decision, the author drew upon the experiences of IOT test programs for the measurement of propeller wake pressure measurements. In particular the author is grateful for the advice given to him by Mr. Howard (Bud) Mesh of IOT. His explanation of the experimental setup and use of such sensors in a water environment was extremely insightful as well as aiding in the selection of the sensor itself for this application.

The arrangement of the sensor in the pressure measurement face of the gap pressure measuring instrumentation is shown in figure 3.26. The placement was designed in the following manner. The sensor mounting hole is a standard # 10-24 threaded hole, with threads flush to the flat surface. This allows the o-ring of the sensor to contact the mounting component and effectively seal the passageway that holds the body of the sensor. At the end of the mounting hole is a cylindrical passageway that houses the tube of the sensor. This passageway extends beyond the sensor tube and leads into the small

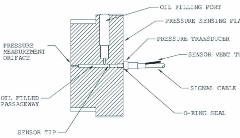

Figure 3.26 – Pressure transducer mounting arrangement.

diameter passageway that leads to the orifice at the gap interface. A vertical passageway then intersects the main passageway that leads from the sensor to the orifice. This vertical passageway is termed the *oil filling port*, and its function is to allow the introduction of silicone oil into all passageways connected to the pressure transducer, as well as allowing air to be purged from the system. The bottom portion of the oil filling port is threaded to allow a bleeder screw to be installed. This component is essentially a valve that is operated with a hex key wrench and allows air bubbles to escape from the system.

The theory of operation and set-up of the gap pressure measurement is as follows. Once the sensor is installed, the passageway is filled with silicone oil through the oil filling port. Once filled to overflowing, the bleeder screw is tightened after a short time to allow air to rise out of the system. This process is repeated for all five transducers and carried out while the face of the pressure measurement plate is angled slightly upwards. During operation of the pod unit, as pressure acts on the area of the orifice, the pressure change is carried to the sensor by the oil. A large assumption at this point is that not too much of the oil will be lost through the orifice either due to gravity or displacement and loss due to a pressure drop. During the design phase the passageway was made as long as possible to ensure that the oil volume was maximized.

The last design detail that had to be addressed was the issue of ensuring that no water flows existed between the propeller gap and the propeller shaft support bearing. The bearing is a water lubricated bearing, supplied by Thordon Bearings Ltd., one of the four project partners. Being a water lubricated bearing, the definition implies that there would be a water flow between the inner bearing surface and the propeller shaft outer surface. Although ideally there should be a water flow present for cooling and lubrication, the fact that pressure measurements would be taking place during operation necessitated that no flows exist in this region other than those due to the propeller, pod and gap setting geometries as water flowed around the propeller and pod assembly. Thus, there had to be a seal present that would stop any flow of water through the bearing, but allow the axial movement of the propeller shaft as it moved due to thrust loading, as well as gap distance adjustments. This issue was solved by using a hydraulic piston cup seal with the inner o-ring removed. This allows for a seal that has a minimal impact by way of adding another friction component to the thrust measurement instrumentation. The issue of supplying ample cooling and lubrication water was determined to be a non-issue by design engineers at Thordon Bearings Ltd. [20], given that there would be relatively cold water present in the space between the pod instrumentation and the outer shell. Operating such a bearing with essentially no flow was deemed to be non-detrimental to the application in this case. The correct operating tolerances were determined by the Thordon Bearings engineering department and then manufactured and supplied to the project. The author then included the correct space for the bearing and incorporated the anti-flow seal mounting area in the pressure measurement plate. Allowances for bearing installation using a shrink-fit with liquid nitrogen was incorporated into the design. Figure 3.27 shows the seal and bearing mounting details.

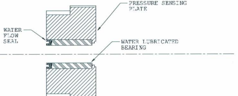

Figure 3.27 – Seal and water lubricated bearing mounting details.

The discussion now turns to the issue of designing instrumentation to measure the drag force on the outer pod body.

3.7 Shell Drag Measurement and Pod Shell Design

The issue of possible measurement of the drag force on the pod shell moving through water was presented to the author early in the design phase. Without justification, the load estimate was given to be less than about 220 N (50 lbs). It was decided to use a 50 lb (222.68N) load cell to give a suitable range and sensitivity, and one was sourced as a high output unit. **Appendix A** has the specifications for this load cell.

There arose several difficulties in attempting to measure such a quantity. The *first* was how to load the force transducer while restraining the shell geometry with enough rigidity so as not to cause undue vibrations or lack of geometrical integrity. The *second* was the problem of preventing an inflow or indeed a *flow through* of water between the shell and inner instrumentation package while allowing shell drag force measurement to occur. The *third* was that the design had to have the capability of allowing the outer shell geometry to be easily changed for studies relating to pod shell/strut/propeller geometry interactions. Lastly, a *fourth* difficulty that had to be overcome was compensating for change in surface tangency alignment that would occur between the propeller hub taper surface and the end of the pod at the propeller gap interface as the gap distance was adjusted [14].

The author began the shell drag measurement design by realizing that any shell geometry would have to be attached to the pod unit by splitting it along a vertical plane of symmetry. Also, after an initial conceptual design had been attempted, consisting of a 6 component shell drag dynamometer, the force resolution was instead limited to a uni-axial loading case only, parallel to the line of rotation of the propeller. This solution would take up the least amount of space, given that the dimensions of the smallest pod shape desired to be tested had been established, however only loads with an azimuth angle of 0° would be measured. For oblique angles, only the component parallel to the shaft line would be measured.

The design thus began with thoughts on a method of attaching the pod shell to the instrumentation package inside it. The pod shell material was selected to be Renshape® 460, a prototyping material with desirable machining characteristics and a low water absorption coefficient. The properties of this material are given in **Appendix E**. The author settled on an arrangement of 4 attachment points, located symmetrically at the same elevation as the propeller shaft. For redundancy, there are 2 fastener locations at each attachment position to allow for mounting thread damage that is to be expected over time with multiple pod shell change-outs. The fasteners chosen are #10-24 stainless steel socket head cap screws. This allows each screw in turn to be mounted on a tee-handle hex wrench and then inserted into the appropriate mounting location in the pod shell component. Given that this operation would be taking place while one is physically situated in an awkward position on the test carriage, having the provision of being able to insert the fastener into a threaded mounting position using the installation tool makes for a simpler installation process.

With a layout of the mounts completed, the design focus was on how to minimize any friction and what method to use to allow a free movement in the pod drag direction. It was decided to use miniature instrument grade stainless steel linear bearings and guide rods to support the shell mounts. The material for the shell mount itself was then selected to be 316 stainless steel. Using these components and the material selection made it possible to *not* have to consider water-proofing the mounting point components. The final design of the shell mount was then completed. There were two shell mounts designed, one served as the mount for the shell only, the other served as the mount for the pod drag force load cell live end mount in addition to the shell mount. This was done for several reasons. The first is that due to limited space, it was easier to locate the load cell off the central axis of the pod unit. This choice opened up the possibility of using just one load cell, or two if desired. The author recommends only one however, because the shell and its mounting method are sufficiently stiff to not be deflected due to the asymmetrical reaction force on it due to the shell drag load cell, as well as the fact that unless both are set up exactly, one could preload the other when they are both connected to the shell. A second reason to mount the load cell in one of the shell mounts is that the instrumentation could be set up and calibrated once to design specifications and then as long as each shell was manufactured in the same way, it would be guaranteed to fit correctly. If the load cell was mounted in any other position, it would have meant that another mount would have to be made to accommodate the live end-to-shell connection, and this would lead to a rather complex issue of having to restrain the live end mount so that the forces sustained during connection of the load cell would not damage it. Figures 3.28 and 3.29 show the two shell mounts as designed.

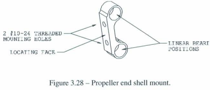

Figure 3.28 – Propeller end shell mount.

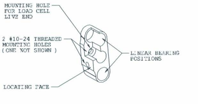

Figure 3.29 – Load cell end shell mount.

One last detail on the shell mounts to be discussed is the fit of the bearings in the shell mount. To ensure that no amount of binding of the bearings occurred due to installation, the bores in the shell mounts were drilled and reamed to the correct installation size. This ensured that a sliding fit would exist between the components as well as a minimum amount of friction that would occur during the drag loading of the shell. Retaining the bearings was accomplished with a retaining compound. The retaining compound specifications are found in **Appendix F**.

The design of the pod shell mounting system was completed with the design of the mounting positions of the bearing race rods. The positions were located in the atmospheric pressure chamber, drive gear housing and the load cell housing faces in such a way as to be convenient for machining and to allow for easy assembly of the respective components. Figure 3.30 shows a side & top view of the final shell mounting system design. Figure 3.31 shows an alternate view angle.

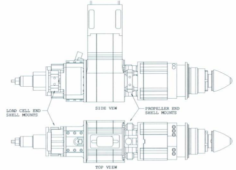

Figure 3.30 - Side & top views of shell mounting system.

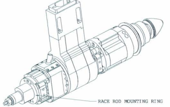

Figure 3.31 – Alternate view of shell mounting system.

There were two issues left to consider before the shell drag force measurement system design was finished. Both of these issues are related to preventing unwanted flow effects that could potentially influence the measured shell drag force, as well as influence the gap pressure measurement system discussed in the previous section.

The ***first*** of the two to be contemplated was the issue of keeping a continuous line of tangency between the propeller hub and the pod shell end as the gap distance was changed. This issue is important for several reasons and its solution solves two sub-issues. The first sub-issue of importance is that as with the propeller hub thrust, it was necessary to attempt to isolate the effects of the gap pressure on the drag force of the pod shell, or alternatively stated, geometry related to the opposing gap faces had to be isolated from geometry related to the shell drag force. This meant that the end face of the pod shell had to be separate from the outer surface of the shell. The author's solution was to create a very thin ring whose outer surface would be a small length of the outer shell.

The second sub-issue is that to allow the gap geometry change to be achieved, a mechanism or adaptor had to be designed to allow this to happen. Having a removable ring would serve as an adaptor that could be changed as the propeller gap changed. For each setting of the gap, a new pod end surface was created so that its outer surface had a common line of tangency across the gap. This solution introduces two small errors that again have to be assumed to be small. The first error is that as the gap distance increases, the projected area for propeller end of the pod increases, which one would assume to have some finite influence on the drag force reading. The second error is that the small portion of the ring whose tangential surface is not part of the shell would not contribute to the drag force reading. It is left to the reader to interpret the importance of these errors.

The ***second*** flow issue to be dealt with was in preventing a flow of water through the interior space of the pod unit during testing. Having a flow through the interior space of the pod would almost certainly influence the drag force measurements. The solution to this issue was to provide a rolling o-ring seal similar to the one as developed for the propeller hub thrust measurement seal arrangement. Given that there would be water on both sides of the seal (the pod shell interior space floods and is not intended to be water tight) it was decided to use the same 10% squeeze value and lateral clearance values, but to keep the friction as low as possible, only one seal was used. The o-ring seal cord stock was the same 1.778 mm (0.070") diameter as the seals used in the propeller hub thrust assembly. The arrangement of the seal components is shown in figure 3.32.

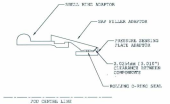

Figure 3.32 – Shell drag o-ring seal detail.

To ensure that the components could be assembled and removed easily and quickly, each component was produced as a two piece ring. Also, to allow the gap fillers to be attached to the pod, a ring adaptor was designed that is held in place by a groove in the inner shell surface geometry. Each half of the gap filler is then attached to this shell ring adaptor with three stainless steel countersunk screws. The end of the pod, which forms the face opposite of the propeller hub end, is formed by an additional stainless steel adaptor, named the pressure sensing plate adaptor, also shown in figure 3.32. This adaptor completes the seal and is also designed as a two piece ring. These two parts connect to the pressure sensing plate. Figure 3.33 shows the general layout of this design.

At this point in time materials were considered to minimize corrosion effects as well as the machining time and complexity. Type 316 stainless steel was selected as the material for the pressure sensing plate adaptor and shell ring adaptor. Aluminum was chosen for the gap filler adaptor. The author chose aluminum in this case because it would make the machining time shorter than if stainless steel had been used, given that the part was of a relatively large diameter with most of the interior removed. Although the gap filler adaptors are directly attached to the stainless steel ring adaptor, they are both electrically isolated from the pod assembly and carriage, thus the corrosion rate of these components due to the driving potential between them and the tank water would be minimized. In the case of the pressure plate adaptor, the component had to be made from stainless steel.

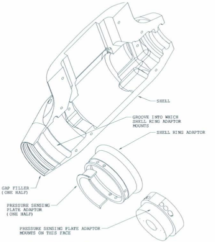

Figure 3.33 – Gap filler and pod adaptor design layout.

To complement the adjustment of the gap distance, another ring adaptor was designed for the pod shell end opposite the propeller. This ring adaptor was also mounted in a groove in the pod shell geometry. This allows the ring adaptor to be clamped tightly in place when the shell is assembled. The end of the pod was effectively cut off at the point of the location of the adaptor and using a threaded connection, an aluminum pod end was designed that simply threaded onto this adaptor. This allowed the gap adjustment lock nut and position shaft to be changed during gap distance adjustments without taking the shell off, thereby speeding up the process. Figure 3.34 shows this adaptor layout.

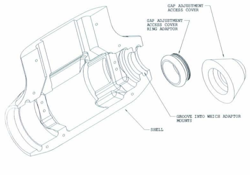

Figure 3.34 – Gap adjustment access shell adaptor

In summary, the gap filler and adaptor assembly serve to isolate the effects of the gap pressure on the end of the pod shell, compensate for the position change of the line of tangency between the propeller hub and pod shell end, and prevent a flow of water between the inner pod shell surface and the instrumentation package within. This completes the discussion on the design of the shell drag measurement instrumentation. To allow the successful completion of tests with this system, a method for manufacturing the outer pod shells had to be devised. This is discussed in the following section.

3.8 Design of the Outer Pod Shell Generation & Production Process

The author includes this work, as it was necessary to allow the design of the pod used in the tests conducted by the author as well as other experimental work. Once the process was finished, it became easy to generate any pod shape required, and test it on screen in a CAD system of choice to ensure that it could be manufactured.

This design was a complete *method* that allows each shell shape to be generated in minutes, ready for final machining. The first step was to model a volume that encompassed the entire volume of the instrumentation package, plus a clearance value. The clearance between any extremity of the pod instrumentation and the inner surface of a shell was set at 2mm (0.078"). This minimized the volume of water between the inner shell boundaries and the outer surface of the pod instrumentation. Figure 3.35 shows the complete pod unit (including the strut), while figure 3.36 shows a rendered view of the completed inner volume shape, including the 2 mm clearance allowance.

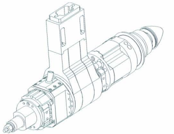

Figure 3.35 – The complete pod unit, including strut.

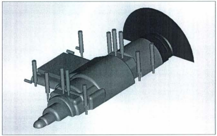

Figure 3.36 – Rendering of inner pod clearance volume, complete with seal and adaptor trimming geometry as well as fastener holes.

To test the fit of the generated shape, a test piece was machined from high density insulation foam. This material was utilized because of its desirable machining characteristics and dimensional stability. Turn around time for this material was very quick, allowing machining and testing of the pod unit for fit to occur in less than 2 hours. Figure 3.37 shows the foam test piece clearance volume.

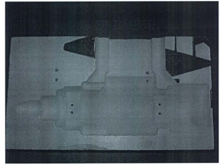

Figure 3.37 – Foam test piece clearance volume.

Once the test fit was deemed to be satisfactory, the pod shell was modeled by rotating the appropriate profile around the propeller shaft axis, adding in the extruded profile of the strut in the correct location relative to the propeller plane and then creating a union of the two separate solids to form one entity. The shell outer form was then completed by filleting the intersection. The inner volume was then subtracted from the pod shape volume. The alignment between the inner volume and the pod shell is the absolute end of the pod profile line, at the central axis of rotation. When the inner volume is inserted into the shell form file and subtracted from the outer pod shell shape, it automatically trims the shell to include space for the ring adaptor and clearance value. Note that included in the subtraction volume is a clearance space that allows the PVC venting hose carrying the cables from the pressure transducers as well and the main harness carrying the torque and two thrust signals from the pod. Note also that the cable from the shell drag is taped to the inner strut and clearance has been allowed for this cable route. Figure 3.38 shows a rendered view of the completed pod shell form.

Figure 3.38 – Rendering of completed pod shell form.

To complete the shell generation for the tests carried out by the author, the final shell had two additional trimming operations carried out to allow mounting of the gap fillers and adaptor, as well as the gap distance adjustment lock nut and position shaft access adaptor. In addition, the attachment fastener locations for the shell mounts were added to the CAD solid model as well as the fastener locations that keep the port and starboard shell components together. The port and starboard pieces are mirror images of each other. Note that one shell portion has blind threaded holes and the other has through holes complete with countersinks of the correct depth to allow fasteners to be used without any modifications such as being cut to length. The final shell rendering is shown in figure 3.39. The drive system design is discussed next.

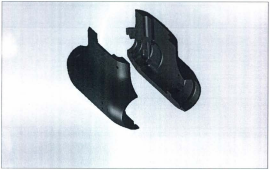

Figure 3.39 – Final shell rendering, including allowances for gap filler and gap distance adjustment access.

3.9 Drive System Design

Several aspects of the drive system had to be considered. These included:

- motor power, current type (AC versus DC) and frame configuration
- controller type
- speed ratio between output shaft of motor and propeller shaft
- torque transmission system
- feedback system for speed to data acquisition system

The motor power requirement was given to be approximately 3.7 kW (5hp). Given the size of the motor unit capable of delivering this power level, careful consideration had to be given to the mounting configuration and its impact on the overall drive system design. It was decided that due to limited space on the live end of the instrumentation package unit thrust dynamometer, the motor would have to be mounted such that its output shaft was perpendicular to the propeller shaft and the components completing the torque path would have to be selected and/or designed to accommodate this.

As a result of this decision, the motor chosen had a face mounting flange and main armature bearings that could support this orientation.

The motor current supply was selected as AC current as it was the author's experience that AC drive systems are cheaper, easier to work on, and delivery time for components is reasonable. In addition, past experience with AC drive systems revealed no negative impacts on data acquisition systems in terms of radio frequency (RF) noise. Using an AC system setup also allows the selection of a motor that is designed as a standard speed unit.

The motor speed can be successfully controlled with an AC controller that is properly configured.

The final motor selection was a Baldor™ 5 hp (3.7 kW) AC motor. **Appendix G** has the specifications for this motor. Photos of the installed motor can be viewed in chapter 5.

The speed ratio was also considered in the drive system design. The maximum propeller speed needed is approximately 900 rpm (15 rps). Given that the drive motor had a speed rating of 1875 rpm, a drive ratio was determined to be 2:1. Because the motor is mounted in a vertical manner and that the speed ratio was now set at 2:1, a right angle gearbox having this speed ratio was selected. Figure 3.41 shows the gearbox. The selected gearbox also had the added feature of a separately lubricated input shaft bearing, given that it is elevated above the level of the internal gear lubricant. The grease nipple is shown on the upper bearing housing in figure 3.40. This design feature had to be specified when ordered. **Appendix H** has the gearbox specifications.

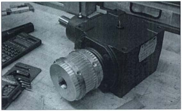

Figure 3.40 – Gearbox featuring vertical input shaft and separate bearing lubrication.

There were two drive systems considered to deliver the driving torque from the gearbox to the propeller. The first choice was a transmission system consisting of gears and shafting. This mechanism would have been compact and easily able to deliver the power from the motor, but sourcing the gears with the necessary mechanical features proved difficult. Given that gear manufacturing is quite complex, it was decided not to design and build custom gears of the type having intermeshing teeth.

The second choice for a transmission system consisted of a timing belt and gear drive. This choice was attractive because the tooth profile for timing belt gears could easily be chosen to take up very little radial space, and once selected would be easy to manufacture. In addition, the material choice for timing belt gears is much broader than conventional gears. Thus, early in the design phase the choice of aluminum for the timing gear was made. Also, given that the torque transmission joint for the thrust measurement and gap adjuster mechanism had to occupy the same region in the instrumentation package, the choice of using an aluminum timing gear made it easy to incorporate the gear teeth in the drive system components.

The belt selection was next completed. A high strength polyurethane belt that is reinforced with steel tensile cords was selected. This belt has a typical strength rating of 118 N/mm (84 lbs per 1/8") of belt width. For a timing pulley having a diameter of 75.5 mm (2.972") diameter, and a torque capacity requirement of 34 Nm, the maximum continuous pull strength required is 900.7 N (202.53 lbs). For a 25mm belt width

(0.984"), the tensile strength of the belt is 2950 N (661.25 lbs). Thus, the safety factor with regards to torque transmission is approximately 3.28:1.

The gear tooth profile selection followed the belt type selection. A tooth profile was chosen that was capable of being machined by a 3.175mm (1/8") diameter flat end mill. This led to a selection of a 5mm pitch and a "T" profile. The geometry of a T5 timing gear profile is shown in **Appendix I**. This profile is used in high strength, high accuracy applications. In this case, the belt and gear tooth profile combination gave good operational characteristics such as high strength, low stretch, low profile (least radial space required), ease of machining, and a good minimum belt bending radius value. This parameter was important because it allowed the inner strut member tube to be at a minimum width, given that the belt wrap angle for the drive gear in the pod unit was maximized by the use of two idler pulleys, the diameter of which was slightly larger than the minimum belt bending radius.

The drive system design was finished with thoughts on the final belt length, drive gear support bearing selections, belt tensioning system, upper drive gear pulley design and a method to keep the opposing teeth of the drive belt from locking during operation. According to ITTC recommendations, the minimum recommended propeller depth is 1.5 times the propeller diameter. This value, in addition to the positions of the motor, gearbox and coupling was used to calculate the final belt length. A belt having 400 teeth was required and a company was sourced through KINECORE (in St. John's

Newfoundland), that could manufacture a belt with 400 teeth, a T5 profile and a width of 25 mm.

Because the drive gear does not support any thrust loads, radial load and installation space only was considered for the bearing selection. Very thin radial ball bearings were sourced for this application, which also kept the maximum pod housing diameter to a minimum. The specifications for the drive gear bearings are in **Appendix J**. The housing into which these bearings mount has several design features to make installation and removal relatively easy. The bearing bores each have an entrance relief on the diameter to allow the bearing to be easily installed. To make the removal easier upon disassembly, there are 4 jacking holes in the drive gear housing at the slip ring end of the pod. Because the fit on the drive gear is tighter than the opposite drive gear housing, the bearing will most likely be removed with the drive gear when it is extracted from the housing. In the event that it stays in the housing, there is ample relief under the inner race to allow the use of an inside jaw puller.

To allow optimum driving characteristics, the belt has to be tensioned correctly upon installation and after an initial period of operation. A tensioning system was designed to allow the initial belt tension to be set as well as periodic adjustment during operation. The tensioning system consists of two sets of idler pulleys. The first set is located in the pod unit, and keeps the belt wrapped around the circumference of the drive gear beyond 180°. These idler pulleys are not adjustable. These pulleys are also designed to be machined from one piece of material and run on needle roller bearings in the mounting positions in their respective housing. These bearings have a high load and speed capacity and their specifications also appear in **Appendix J**. The integrally machined flanges allow the belt to keep the pulleys tracking in a central location within the pod drive system. The second set of pulleys is located on a set of pivoting arm assemblies, positioned at the top of the inner strut assembly. A set screw and lock nut assembly pushes each arm out in such a way as to push on the belt and increase its tension. The pulley itself is simply a large diameter ball bearing that is supported in position by a spigot in its inner race. The outer race acts as a flat pulley, over which the flat side of the belt rides.

The upper drive gear pulley design utilizes timing gear blank stock that could be simply purchased with the 5T profile pre-machined. To complete the design, a bore and keyway matching the output shaft of the gearbox was designed, in addition to retaining set-screws and belt guide rings. As with the pod unit drive gear, the belt guide rings were simply designed as a ring that was then split and fitted with mounting holes to keep it retained to the gear. For ease of machining brass was selected as the guide ring material.

An important detail of the drive system to be determined at this point in time was a method to keep the opposing sides of the drive belt loop from contacting each other during operation. As with any belt setup that has a relatively long distance between the two timing gears, and a high rate of speed of operation, there exists the potential for vibration of each length of the belt. If the amplitude is significant, and the clearance between the belt lengths small enough, the teeth could potentially contact causing noise and/or tooth damage. To keep the two sides of the belts from contacting, a separator made from 3.175 mm (1/8") Teflon™ sheeting was located between them. This belt separator was designed to fit exactly into filling slots in the bottom portion of the strut tube pod mount block and the upper gearbox plate support mount (to be pre-machined before welding into the strut assembly). The belt separator has a retainer that was designed to keep it in place once installed. Figure 3.41 shows the drive system setup, including the belt separator. Figure 3.42 shows a close-up of the drive gear, including the pockets used to mount the terminal block printed circuit boards that allow electrical connections between the drive gear and propeller shaft.

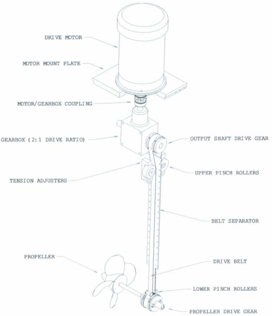

Figure 3.41 – Drive system setup.

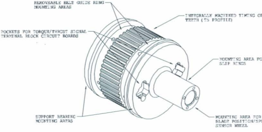

Figure 3.42 – Final drive gear configuration.

One last detail to be designed was a method of providing propeller shaft rotational speed and blade position feedback to the data acquisition system. There were actually two systems proposed and planned for, however because of time limitations only one was fully implemented. The first was a combination speed and blade angle position sensor system. This essentially was an indexing wheel with 36 positions indicated for one full revolution. Although this provides a relatively low resolution for blade angle, it does give a marker point every 10° to which all data can be referenced to. Thoughtful post processing of test data could yield good interpolations. An emitter/detector sensor was selected with an adequate response time for this application in conjunction with a high speed counter module for the data acquisition system. The parts were designed such that the indexing wheel mounted on the back end of the drive gear, and the sensor mounted on the bottom access cover to the slip ring housing. This setup fit in the space available, as no commercial sensor of this type could be sourced to fit in the required space. A layout of the blade position/speed sensor setup is shown in figure 3.43.

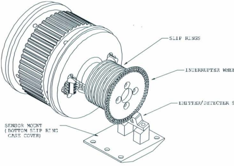

Figure 3.43 – Blade position/propeller shaft speed sensor setup.

The second system to be proposed for propeller shaft speed was more of a traditional analogue design. A mount was designed to allow a tachometer generator to be connected to the second gearbox output shaft with a timing belt. This method provides for good speed monitoring, but does not resolve blade position. This was the system used however as time did not allow for the setup of the blade position sensor. A photo of the installed tachometer generator can be found in Figure 7.9. **Appendix K** has the specifications for the tachometer generator selected for speed monitoring.

The discussion now moves to the design of the global load measurement dynamometer.

3.10 Global Load Measurement Design

A global force dynamometer is required to resolve the forces and torques applied to the test carriage as a result of both turning the propeller with its drive motor and its movement through the water in the test tank. In this case, the dynamometer is also the mounting platform that serves as an interface from the pod instrumentation to the test carriage. The drive motor is also mounted on the dynamometer frame.

The design of the global unit dynamometer started with determining a safety factor for the system. It was decided to use 2 as the safety factor and thus the straight ahead (azimuth angle of 0°) design thrust value was 1778.8 N (400 lbs). The task of designing the dynamometer then became subject to several geometric constraints. These were:

- the instrumentation had to be portable and thus capable of being mounted in the MUN towing tank as well as either of the ice tank or towing tank at IOT
- the MUN towing tank had the most restrictive mounting geometry of the two facilities so the relative positioning of the motor and live end was critical, as was the necessity of having an elevation system for the dynamometer and pod unit

Detailed measurements of the mounting position on the test carriage at MUN were carried out to allow the design process to begin. Assisting with this task was Mr. Rocky Taylor, then a fast track Masters student in the project. Once the detailed measurements were complete the author then met with Mr. Taylor for several months, once a week to go over the design strategy for dynamometers. These meetings were a mentoring process for Mr. Taylor in term 8 of his undergraduate engineering degree, as a design project, of which the global dynamometer was the subject of the course. Under the author's supervision Mr. Taylor completed the calculations for the preliminary positions of the 1000 lb (4447 N) load cells as well as the design of the reference and adaptor frames of the dynamometer. The adaptor frame is the component that allows the global dynamometer to be mounted to the MUN test carriage as well as either test carriage at IOT. During this time period he also completed the design of the lift elevator, an essential element in making fast geometric changes of the instrumentation's pod unit, given that unlike IOT, the test tank at MUN doesn't have a test frame elevator. A brief description of this work is given in section 3.11.

With the adaptor and dynamometer reference frame designs complete, the author completed the detailed design of the live end of the global force dynamometer as well as the flex links and their mounts. There were several factors that needed to be considered while completing the design of the dynamometer from a performance and manufacturing point of view. These were:

- Material choice of the main components of the instrumentation and the weight that the dynamometer must carry in addition to the loads generated by testing
- Stiffness of the main dynamometer frames
- Ease of component manufacture with respect to work envelope of machine tools

- The flex link material choice had to be made to allow a high stiffness in the direction of loading but much lower 90° to the direction of loading

The material of choice for most of the components in the dynamometer was mild steel plate and thin walled square tubing. This was necessary to allow each component to be as strong as possible. Thus stated, lightening holes were used wherever practical to keep all components as light as possible, in addition to using aluminum components with lightening holes and cutouts. Utilizing structural sections of standard dimensions also kept fabrication times down and simplified the manufacturing. The overall design philosophy of the live end components was to keep the stiffness as high as possible while minimizing the total mass. This ensured that the load capacity of the 3 vertical load cells in the assembly was not diminished too much by the weight of the overall assembly. Also, to contribute to the ease of the fabrication of the dynamometer components, it was decided to use bolted connections exclusively. This way each component could be fabricated separately and then added to the assembly by the use of screws. Using this method has several benefits. It ensures the geometrical accuracy of the assembly, a factor which is needed during analysis of testing results. It can avoid distortions caused by stress relaxation, which often happens with welded structures consisting of multiple parts. Another benefit is that multiple complex machining setups can be avoided when machining the different faces. This can keep the fabrication process located on machines of smaller envelopes.

The flex link material was selected to be 17-4 PH stainless steel. Specifications for this material can be found in **Appendix B**. The flex links were the only components that required heat treating to achieve the desired performance characteristics. Essentially, in the direction of loading this component needed to be capable of carrying the rated load of the load cell. A factor of 20% was applied during the design calculations to allow the failure strength to be approximately 5439.7 N (1200 lbs). This was done to ultimately make the dynamometer stronger than the pod unit. Should a catastrophic event cause the pod instrumentation to be damaged, then the dynamometer stands a greater chance of event survival. In the direction 90° to loading, the flex link is relatively flexible. This allows the transverse motion of the dynamometer to occur when deflection of the load cells and flex links occurs. To minimize cross-talk, the length of the flex link was made as long as possible. Long flex links minimize cross talk because as the dynamometer is loaded in one direction, the relative geometrical changes in the flex links at 90° to the load is minimized, hence the minimum induction of loading 90° to the true load. To prevent failure by buckling, the flex link was furnished with a middle section of considerable diameter. To keep the flex link from being damaged by accidentally applied torque loads, each end had a hex pattern designed so that during installation the portion of the flex link that is being installed has a reaction torque generator, created by using a second wrench as the lock nuts are tightened. Figure 3.44 shows the flex link features.

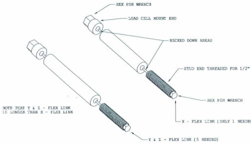

Figure 3.44 – Flex link features.

This point leads to several other considerations that needed to be addressed during the design phase. Such considerations as those following allow for the successful assembly of the dynamometer and calibrations required before use:

- The relative positions of the live and reference ends of the dynamometer had to be set without having any flex links and load cells installed
- All flex links and load cell assemblies required the characteristic of being installed or removed independently of the others
- The subassemblies had to be designed such that when put together, the final reference dimensions for analysis could be guaranteed.
- There needed to be provisions for future adaptations of the dynamometer
- The dynamometer had to be relatively simple to assemble
- Procedures required to assemble and calibrate the dynamometer had to be considered for interference problems, order-of-assembly problems and functionality

The following paragraphs discuss briefly some of these listed items.

During the design phase both the reference frame and the bottom of the lower live plate had faces provided that would be machined during manufacturing to allow the setup of the relative spacing between these components. The faces were produced by machining oversized blocks (pads) of material that were added to the frame during welding in the case of the frame, and by machining material away from the thickness of the plate in the case of the lower live plate. Figure 3.45 and figure 3.46 show the location and a close-up view of this alignment system respectively. Photos of the setup of this system can be found in Chapter 5.

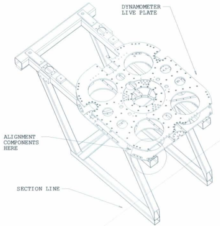

Figure 3.45 – Vertical alignment system component location.

To complete the design of this system, standard ground pins and a machined spacer is used to support the live plate until the load cells and flex links are installed. When installation is complete, the spacer is simply pulled out, rolling on the pins.

To ensure the maximum geometrical accuracy by not disturbing the placement of the live end relative to the reference frame by the process of installation, the load cell mounts, load cells and flex links were all designed to allow independent installation. Each component had sufficient installation and adjustment provisions to allow this to be accomplished.

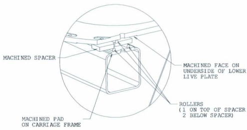

Figure 3.46 – Close-up view of vertical alignment components.

The load cell mounts were designed as a threaded adaptor machined from steel hex stock. The adaptor threads over the stud of the load cell and then the assembly is threaded into a larger threaded hole in the dynamometer reference frame. Because the threaded hole is much larger than the load cell threads, the adaptor is very robust and not likely to ever be damaged during use or installation. If for some reason the load cell threads are damaged, or stripped during installation, a new adaptor can simply be manufactured for replacement. After the load cell is installed, the flex link is installed into position in the live plate assembly. The installation position is designed as an oversize hole such that the flex link can be inserted at an angle to clear the load cell stud. When all three are installed, the live plate is free to move around in the X-Y plane to allow the installation of the lower live plate adaptor. This adaptor effectively couples the lower portion of the flex link to the live plate. There are six screws that keep the adaptor in place and then the two lock nuts on the flex link stud can be tightened. More on this procedure is found in section 5.1.2.4. This design allows the live plate to be accurately positioned in the X-Y plane with the correct Z height. Figure 3.47 shows the Z-direction flex link and load cell mounts.

In the case of the X and Y flex links, the mounts were designed in a similar manner. The threaded holes in the reference frame were furnished with an adaptor into which the load cell and then the flex link is installed. The live end mount was designed to slide into position, attached to the lower live plate and then be firmly attached to the flex link stud with two lock nuts. More on this procedure is also found in **Appendix N**, section 1.1.2.4. Figure 3.48 shows the X and Y direction flex link and load cell mounts.

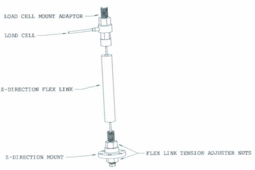

Figure 3.47 – Z-direction flex link, load cell and their mounts.

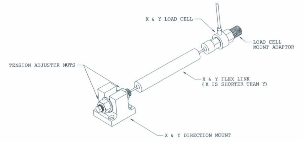

Figure 3.48 – X and Y direction flex link, load cell and their mounts.

To ensure that the distances between the propeller shaft and the load cells were maintained during assembly, a system of alignment between components was devised. Essentially, to maintain alignment in the X-Y direction at the joint between the dynamometer and the upper strut mounts, a small clearance value was used between the center spacer of the live end of the dynamometer and the inner spacer that sits on the mast assembly. Although there are no bearings at this rotating joint, provision was supplied by having the design such that the inner spacer could be modified to accept two large diameter angular contact radial ball bearings. These bearings would support the radial forces as well as supporting the weight of the instrumentation package. To keep the bearings in place all one has to do is machine a snap ring groove on the ID of the dynamometer center spacer. This snap ring would then carry the weight of the assembly instead of the face-to-face contact that is present now. In the event that dynamic rotary motion is desired, the installation of bearings would allow a correctly installed servo motor system to easily control this axis. To keep the Z distances correct at this joint, the components that install below the live plate are all referenced to the machined relief on the underside of the lower live plate. Each component has faces machined to keep X,Y and Z distances correctly maintained, independent of the fastener locations. At the joint between the inner strut assembly and the two support masts, there are keyways and tangs machined to keep the components correctly aligned. Figure 3.49 shows this alignment feature.

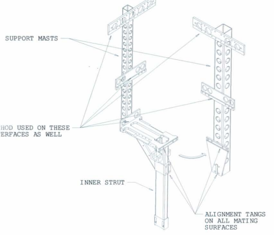

Figure 3.49 – Alignment method between inner strut and support masts.

Each component of the system was light enough as designed to be manipulated and assembled by hand. The procedure envisaged by the author in regards to final installation into the tank was that the dynamometer would be installed as a subassembly, then the pod unit subassembly would be connected to the dynamometer by the two masts and support brace assemblies. The support braces were designed as separate components that would make this procedure possible to be carried out, in addition to keeping the structure as stiff as possible. Strength of the strut/mast assembly is important, particularly at oblique testing angles. The philosophy of a multiple subassembly system reduces the risk of damage to the system during installation. All joints and order of assembly scenarios were thought through during the design phase to ensure that everything would work as planned. Figure 3.50 shows an overview of the completed dynamometer sub-assembly designs.

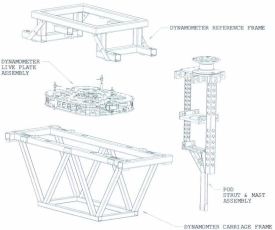

Figure 3.50 – Dynamometer subassembly designs.

3.11 Elevator Lift System Design

As mentioned in the previous section, this system was designed by Mr. Rocky Taylor under the author's supervision. Two main design points worth mentioning is that the author suggested to Mr. Taylor that the system be supported in a hanging mode by four synchronized lead screws. Hanging avoids having to account for buckling loads in the design of the lead screws, and can be sufficiently provided for by generous section sizes in the support structure of the elevator. The synchronous motion of the lead screws was provided by one long timing belt driven by an AC motor and controller. Mr. Taylor fully carried out the detailed design of the various components of the lift system to a very successful result. The author is very grateful for the effort extended on this aspect of the project by Mr. Taylor.

Some aspects of the electrical system design are now discussed.

3.12 Electrical System Design

The electrical system design consisted of designing all components such that wiring could be installed in a straight-forward manner. Very often the running of cables in electro-mechanical systems and other types of instrumentation systems is not well planned or even considered. For this instrumentation system there are several design features that were considered for the successful installation of the cables carrying the signals to the data acquisition system. One was the segmenting of the routes into sub-wiring harnesses. Each major mechanical component was designed with a wiring route such that the cable occupying that part of the route is essentially a stand alone harness segment. At each end of the segment was a provision for connection to the next segment via a terminal block. Each wiring segment was designed to be prepared with the following features:

- cable end tinning or terminal block detail
- strain relief where necessary
- mechanical shielding where necessary
- electrical RF shielding

Another design feature was the machining of the various passageways and holes for the cabling. For instance, the propeller shaft is hollow to allow the thrust and torque signal cables to be installed. There were three printed circuit boards designed and provisions for their mounting in the drive gear, propeller hub and pod wiring exit hatch. Figure 3.51 show mounting details of the PC boards to which the terminal blocks mount.

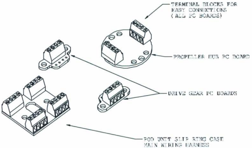

Figure 3.51 – PC board details.

To accommodate the passing of supply currents and sensor signals across rotating joints, one set of slip rings was employed in the design. These were located directly on the drive gear and consisted of an off-the-shelf unit with 8 individual conducting rings. The diameter chosen was done so to reduce the surface velocity of the brush/ring interface. The specifications are given in **Appendix L**. As a final comment on this issue, using slip rings for such an application has been used for decades by such companies as Kemph and Remmer (K&R) of Hamburg Germany (now owned by Cussons technology UK). In these units, un-amplified torque signals are transmitted across slip rings and successfully used in many types of experimental work. The author expected similar results by using slip rings in this project design.

To prevent RF interference the cable choice was one with a shield and twisted pair construction where possible. Also, where possible cable bundles were routed through one of the mast tubes and in all cases the cables were laid out on the test carriage as far as possible from the AC motor controller. Photos of the various cables can be found in the assembly sections of chapter 5.

The last design detail to be briefly discussed is the wave shroud.

3.13 Wave Shroud Design

Completed near the end of the design and fabrication phase of the instrumentation, this effort was carried out by the author, Mr. Taylor and Mr. Matthew Garvin, a work term student hired by the project. The system was designed as a two piece unit that would allow the wave shroud to be rotated away from the pod unit to allow the elevator to lift the system out of the tank. The purpose of the shroud is to keep the inner strut from registering any drag force on the global force measurement dynamometer. A device such as that designed is recommended in ITTC procedures.

Installation of the wave shroud was facilitated by two threaded rods per portion of the assembly. The threaded rods allowed the positioning of the components to be carried out after all other components had been installed into the tank. Photos of the wave shroud can be seen in Chapter 6.

The discussion on manufacturing of the components now starts in Chapter 4.

CHAPTER 4 – INSTRUMENTATION MANUFACTURE, SETUP & CALIBRATIONS

INTRODUCTION

This chapter outlines the lengthy process that was required to take the design from concepts to a working experimental apparatus. The details of these activities are documented separately in attached appendices.

4.1 INSTRUMENTATION MANUFACTURE

The author has extensive experience in the related fields of programming and operating computer numerically controlled (CNC) machining equipment as well as computer aided design (CAD) engineering. This experience aided the instrumentation manufacture in that each component was designed with a specific manufacturing process in mind. Having experience in CNC technologies and manual metal working techniques allowed a further advantage of being able to plan machining set-ups and order of manufacturing operations for each piece. In addition, the author had the extreme fortune of access to state-of-the-art manufacturing equipment and operating personnel to allow the successful manufacturing of each part such that the various assemblies functioned correctly. The expertise and equipment located at MUN technical services were pivotal in accomplishing the manufacturing of all parts of the instrumentation for this project.

4.1.1 Part Manufacturing Processes

Many of the parts were produced in parallel and required the use of multiple machine tool types and setups. Both manual and CNC milling machines and lathes were used as well as various drill presses and surface grinding equipment.

4.1.2 Use of CAD & SAT part files for direct manufacturing using CNC

The majority of parts were produced using a standard ACIS text (SAT) output file format exported from the design CAD software, CADKey. The SAT files represented the exact part size required. The CNC milling machines used in the fabrication achieved the dimensions required using standard setups. For example, if a part required a fit with a tolerance of 2 inches +0.000/-0.003 inches, then the SAT file was provided with a size of 1.997 inches. If a tighter fit had been required, then the dimension in the SAT file would be 1.999 inches. The machining capability of the HAAS milling machines installed at MUN technical services is +/- 0.0002 inches. As long as the machining setups, tool lengths and sharpness, feed-rates, spindle speed and material properties were accounted for in the generation of the machining numerical control (NC) code, then the tolerances were not difficult to keep. The NC code was produced with MasterCAM™, a computer aided manufacturing software (CAM) package. Parts produced on the CNC lathe employed the same philosophy, however more checks were carried out during turning as it is often the case that the production of "one-off's" on a CNC lathe still require a diligent application of skills and practices that are typical of those used in manual part turning.

4.1.3 Manual Machining Techniques

A combination of using CNC machining techniques with manual indexing as well as totally manual methods were used for the production of some parts. In some cases, such as producing the propeller drive gear teeth, the program was written without the use of CAM software for one tooth and then the part was rotated manually in a dividing head for the production of the remaining teeth.

Some components, such as the pressure sensing plate, were produced entirely using manual milling and turning operation. These machines were used with great skill and reflect immensely on the capability of the machinists. All tolerances required were achieved and made assembly of the instrumentation as trouble free as possible.

4.1.4 Implementation of Tolerances and QC Checks

Throughout the manufacturing process, checks of each piece were made by both the author and the machinist to ensure that the dimensions produced would be compatible with the function of the part. This aspect of the fabrication was not left to chance. The documentation of the manufacturing process is presented in **Appendix M**. This document should serve as a resource for those involved in the designing of similar instrumentation.

The instrumentation assembly is discussed next.

4.2 EXPERIMENTAL SETUP

The experimental setup was carried out as two activities. One was the apparatus setup, the other was the data acquisition setup.

The apparatus setup consisted of assembling the two main subassemblies: the pod instrumentation and the global dynamometer. During this phase the mechanical and electrical transducers were physically put together and adjusted to allow calibrations to be carried out. Later, the newly calibrated instrumentation was installed into the tank, which is covered in chapter 5. The forward thinking during the design phase regarding the installation of wiring allowed for a successful assembly.

The data acquisition setup consisted of setting and adjusting all electrical parameters for each channel of the instrumentation systems. The gains were set and channels labeled in the data acquisition software. All electrical connectors were soldered and final cable routings that interfaced the instrumentation with the data acquisition system were determined.

Because the procedures for the experimental setup are long, they have been documented separately in **Appendix N**. All assembly procedures for the instrumentation, including bolt tightening sequences are listed. Gains and jumper settings are also outlined.

Calibrations are discussed next.

4.3 CALIBRATIONS

Before the equipment could be used in any experimental work it had to be calibrated. Equipment calibration consists of a process of applying known quantities such as force, torque and pressure loadings to the instrumentation systems that allow the various sensors to respond with a series of output voltages. As a result of generating these output voltages, a mathematical relationship can be established such that when placed into service, the unknown loads from the experiments can be computed from the voltages generated and collected by the data acquisition system.

In most cases, a linear response is the desired relationship to be gained from a calibration procedure. However, even a sensor that generates an apparently linear equation can have non-linear characteristics at the extremes of its sensing capability. Getting the correct relationship requires extreme care during calibration procedures and an in-depth knowledge of sensor electronics. Also, the expected ranges of exposure that the instrumentation will experience during testing can influence the choice of calibration procedure.

The mechanical design of the supporting components and the amount of friction, deflection, vibrations, temperature differentials, radio frequency interference and other sources can influence the calibration outcome or indeed reduce its accuracy, especially if the calibrations are carried out under one set of conditions and the testing carried out under another. Bearing this in mind, it is up to the experimenter to try and mitigate as many of these factors as possible prior to conducting the experiments. In most cases, compromises must be made based on some necessary assumptions about the experimental test conditions, and indeed realistic constraints such as time and/or resources. In the case of the initial set of tests with the new equipment, there were a few assumptions and compromises that were made in order to allow the testing to be conducted for a first look at the instrumentation function. These are briefly explained next.

The first assumption is that the temperature would have a minimal effect on the system after calibration. This assumption was made and based on three factors. One, in the case of the force and pressure transducers, was the trust that the temperature compensation electronics of the purchased sensors would function correctly, even though these devices would be in a colder environment than the compensation temperature range listed by the manufacturer. The second, in the case of the torque transducer, is that utilizing a full bridge configuration would negate any temperature effects. The third, in the case of the data acquisition system, is the knowledge that the exposure temperature would not significantly change between the calibration procedure and tests, given that the system would always be in the same local atmospheric conditions and at the same relative elevation in the test facility. This assumption on temperature effect had to be made to allow the tests to commence. The alternative would have been to carry out tests to determine the effect temperature would have on the system sensors and data acquisition electronics, an exercise that was beyond the time constraints allowed.

The second major assumption to be made was that the calibration procedures envisaged by the author during the design stage would perform as planned. This assumption was based on the detailed knowledge of the mechanical and electrical systems derived from the design and manufacturing exercises of the project. The planned calibration procedure for the entire instrumentation package consisted of the following:

- each measurement system would be subjected to its own calibration procedure
- each measurement system is a separate subassembly that once calibrated would then be assembled to the unit dynamometer to form the fully assembled instrumentation package

This method was planned as an alternative to carrying out all calibrations for a completely assembled instrumentation package *in-situ*. Such an exercise would have required much more time to allow the design and manufacture of the necessary frames and setups to allow an in-situ calibration to occur. In addition, if there had been a problem with either of the pod unit systems, then disassembly would have been much more time consuming. This method paid off in the case of the propeller torque. During the initial calibrations it was determined that the wiring for the bridge had been completed incorrectly, resulting in zero output for all applied torque values. The pod unit had to be partially disassembled and the wiring corrected before proceeding.

Another important factor that contributed in making this assumption on the validity of the calibration procedures is, in the case of the propeller thrust and torque, designing and manufacturing the equipment to allow a dynamic calibration of the rotating hub instrumentation, either in-situ or as a separate uninstalled pod unit would have required much more time and effort to carry out. The assumption was thus made that the fully assembled pod unit could be statically calibrated as an assembled sub-assembly as initially planned.

In the case of the global dynamometer, the knowledge that the interfacing geometry of the apparatus was designed to allow positive alignment between the pod unit subassembly and the global unit dynamometer, and that the dynamometer had been assembled to defined relative geometric placements allowed the assumption that the distances used in the calculations for unit thrust were reasonably accurate.

The final overall assumption made was that test conditions would follow a pattern of a transient period during acceleration (both of the test carriage and propeller rotation) that lead to a static test state, followed by another transient as the system decelerated. This guided the author to decide to carry out a calibration over the expected loading ranges of the instrumentation with emphasis on generating a linear calibration mapping function instead of a detailed calibration that included any non-linearity at very light or heavy loadings.

A discussion of the calibration procedures for each measurement system is documented in **Appendix O**. The final calibration constants for the system are present in table 4.1

Final Calibration Constants for Experimental Data Analysis	
CHANNEL	SLOPE
T_{PROP}	470.306 (N/V)
T_{POD}	539.375 (N/V)
Torque, Q	+13.795 (Nm/V)
Shell Drag	104.658 (N/V)
Pressure Transducer #1	133.123 (Pa/mV)
Pressure Transducer #1	174.961 (Pa/mV)
Pressure Transducer #1	143.578 (Pa/mV)
Pressure Transducer #1	129.830 (Pa/mV)
Pressure Transducer #1	173.231 (Pa/mV)
Propeller Shaft Speed	-6.533 (rps/V)
Carriage Speed	0.982 (m/s/V)
Global Unit Dynamometer (X-Axis Only)	-1142.404 N/V

Table 4.1 – Summary of calibration constants used for experimental analysis.

The test program is presented in the following chapter.

CHAPTER 5 – INSTRUMENTATION TESTING

INTRODUCTION

This chapter outlines the first set of tests carried out with the newly assembled and calibrated instrumentation. The first step was installation of the equipment into the MUN test tank.

5.1 Installation into the Test Carriage

Installation of the instrumentation package started with lifting the global dynamometer into the test tank at MUN. The dynamometer was lifted over the rail of the tank with a forklift and then secured to the overhead crane. Slings were then used allow connection of a lifting beam to the dynamometer and tank overhead chain hoist. This rigging arrangement was used to prevent the dynamometer from becoming distorted during installation. After lifting the dynamometer free of the forks of the forklift, it was moved to a position slightly offset from the center of the tank. The dynamometer was then lowered to two work platforms that are suspended over the tank. The rigging was disconnected and the carriage moved back so that the dynamometer could be reconnected and lifted into position up through the test carriage. Figure 5.1 shows the dynamometer sitting on the platforms with lifting beam in place. Figure 5.2 shows the dynamometer being lifted up through the test carriage to its test rails.

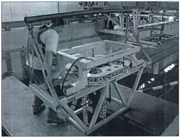

Figure 5.1 – Dynamometer sitting on platforms.

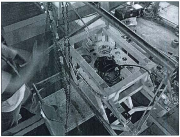

Figure 5.2 – Lifting the dynamometer from the platforms into position on the carriage test rails.

Once the dynamometer was in position, the lifting elevator was installed in a piecewise fashion. The synchronous lead screw system was then installed along with the drive belt. The belt was then tensioned and the lead screws aligned. The installed components are shown in figure 5.3. After installation, the elevator was used to lift the reference frame and live end of the dynamometer up from its operational position. At this point the pod unit subassembly could be installed.

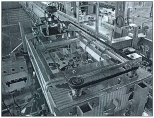

Figure 5.3 – Synchronous drive system of the elevator lead screws.

The fully assembled pod unit was carefully secured by a sling and then lifted over the test carriage guide rail to the platforms below. Figure 5.4 shows the pod unit connected to the chain hoist. Once securely on the platforms, the carriage was moved into position and a hand powered cable hoist was used to lift the pod unit into position. The keys of the support masts were matched to the pod unit strut and then several bolts installed to keep the unit from falling. The motor mount plate was then installed and all securing bolts tightened. Prior to these steps, safety rods were installed on the dynamometer live end. These safety rods prevent the assembly from dropping should either of the Z-axis flex links break.

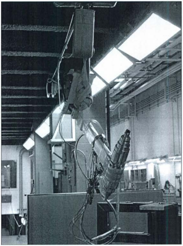

Figure 5.4 – Pod unit subassembly being lifted into the test tank.

Next the motor was installed into position along with the drive coupling and securing bolts. The gearbox was then subjected to a final alignment to allow the belt to track on center when the drive pulley was rotated through multiple rotations. All bolts on the gearbox mounting plates were then tightened and the upper cross bracing installed. The belt tensioners were then adjusted. Figure 5.5 shows a view of the installed pod unit. After adjusting the belt tension, the shaft speed tachometer generator was installed as shown in figure 5.6. The timing belt for this unit was also tensioned before a final tightening of its mounting bolts. At this point the lower cross-bracing was installed.

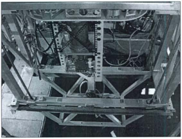

Figure 5.5 – Installed pod unit, with gearbox aligned and belt tensioned.

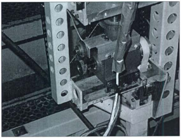

Figure 5.6 – Installed shaft speed tachometer generator.

The next step was to run the cabling to the data acquisition system signal distribution box. The cables were taped to the support masts initially, although eventually they were

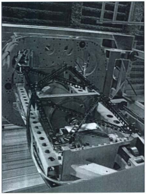

Figure 5.7 – View of cabling from bottom of dynamometer.

installed in the center of the mast tubes to provide a greater RF shielding effect. Figure 5.7 shows a view of the cabling from the bottom of the dynamometer. After the two main wiring harnesses from the pod unit had been run up the masts, the data acquisition system was mounted to the carriage. It was located as far away as possible from the drive motor. Figures 5.8 and 5.9 show the data acquisition system layout and main cable bundle run to the instrumentation. Figure 5.10 shows the signal distribution box labeling. Figure 5.11 shows the installed signal distribution box with all channels plugged in. Note that the harness for the torque and thrust signals was then connected to an air dryer, also shown in figure 5.11. The outer PVC hose through which the cables run, seen in figure 5.12, serves as a passageway for air from this device. Note that open end of tee is plugged with silicone sealant. This dryer was designed to allow dry air to be pumped into the pod unit to prevent condensation from forming inside on surfaces that are cooled as a result of the unit being immersed in water that is lower than room temperature.

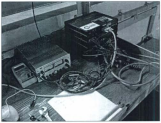

Figure 5.8 – Data acquisition system installed on test carriage.

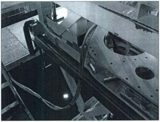

Figure 5.9 – Main cable bundle leading to instrumentation.

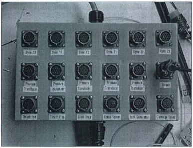

Figure 5.10 – Signal distribution box labeling for all channels.

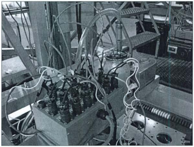

Figure 5.11 – Installed signal distribution box with all channels installed.
Note air dryer in background.

Note that the distribution box and air dryer are both supported by an aluminum c-channel that is mounted to the reference frame of the dynamometer. This is to prevent any unintentional mass changes from being registered by the global dynamometer. These could be caused by shifting components during acceleration of the test carriage.

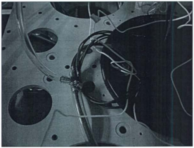

Figure 5.12 – Junction of cabling and dry air supply to pod unit.

When all cabling had been installed and secured, the data acquisition system was powered up for the first time with all systems connected. All channels were then monitored in meter mode of the DaqView data acquisition software. The systems were then tested for responsiveness by gently moving the live components. The thrust systems were tested by pushing and pulling on the propeller hub mount. The torque system was tested by gently twisting the hub and watching the voltage output for that channel. The shell drag system was tested by pushing in both directions on the instrumented shell mount. In each case the response changed polarity as it should have. The dynamometer was tested by gently pushing in each of the X, Y and Z directions. The pressure transducers could not be tested until immersed in water, but the voltage outputs at this point in time were as expected.

At this point in time the instrumentation package was considered to be completely installed and ready to outfit for a test program. The following sections outline the experimental test plan and basic procedures used to conduct the first set of experiments.

5.2 Experimental Test Plan

Where possible, known procedures were used for the first set of tests, in particular the ITTC Recommended Procedure for Podded Propulsor Tests and the IOT standard for propeller open water tests. Given that the instrumentation designed for this project was of a new and unique design, there were some instances where the test procedures had to deviate.

According to the mentioned procedures, the revolution rate of a propeller should be chosen such that the minimum value of the local Reynolds Number (Re) at 0.7 r/R does not fall below 3.5×10^5 at the various advance speeds (V_A) used during the experiments. This ensures that the flow of water over the blades is not laminar, a condition needed if any resulting test data will be used to predict full scale characteristics of the propeller or pod unit. The equation (5.1) for calculating the value of Re for these experiments is taken as:

Equation 5.1
$$\mathrm{Re} = \frac{c_{0.7}\sqrt{V_A^{\,2} + (0.7\pi\, nD)^2}}{\nu}$$

Where:

V_A	Speed of Advance (m/s)
n	Propeller rotation rate (revolutions/second)
ν	Viscosity of water (1.01×10^{-6} m^2/s)
D	Propeller Diameter (270mm (10.630 inches))

And:

$c_{0.7}$	Propeller chord length measured at r/R = 0.7 (Shown in Figure 5.13)

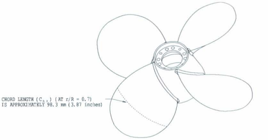

Figure 5.13 – Depicts the chord length at r/R = 0.7.

The selected propeller rotation rates appear in table 5.1. The rationale for these speeds is explained in more detail in section 5.4.9.

Propeller Shaft Speed (rps)
$n_1 = 3.5$
$n_2 = 7$
$n_3 = 9$
$n_4 = 12$
$n_5 = 14$

Table 5.1 – Shaft speed number and corresponding Propeller rotation rate.

Once the rotation rates had been selected, the advance speeds (V_A) were calculated to correspond to a range of *advance coefficients* (J) from 0.1 to 1.4 as defined by the following equation (5.2), solved for V_A (5.3):

Equation 5.2 $$J = \frac{V_A}{nD}$$

thus:

Equation 5.3 $$V_A = JnD$$

The calculated advance speeds for all shaft speeds are presented in table 5.2 below.

	J	Shaft Speed Number				
		n_1	n_2	n_3	n_4	n_5
Advance Speed V_A (m/s)	Bollard	0	0	0	0	0
	0.1	0.095	0.189	0.243	0.324	0.378
	0.2	0.189	0.378	0.486	0.648	0.756
	0.3	0.284	0.567	0.729	0.972	1.134
	0.4	0.378	0.756	0.972	1.296	1.512
	0.5	0.473	0.945	1.215	1.620	1.890
	0.6	0.567	1.134	1.458	1.944	2.268
	0.7	0.662	1.323	1.701	2.268	2.646
	0.8	0.756	1.512	1.944	2.592	3.024
	0.9	0.851	1.701	2.187	2.916	3.402
	1.0	0.945	1.890	2.430	3.240	3.780
	1.1	1.040	2.079	2.673	3.564	4.158
	1.2	1.134	2.268	2.916	3.888	4.536
	1.3	1.229	2.457	3.159	4.212	4.914
	1.4	1.323	2.646	3.402	4.536	5.292

Table 5.2 – Calculated advance speeds for the selected propeller rotation rates.

The resulting advance speeds were then substituted into equation 5.1 and the Reynolds number calculated for all cases. The resulting Reynolds numbers for each the shaft speeds over the range of J from 0.1 to 1.4 are presented in Table 5.3. It can immediately be seen that from a standpoint of adhering to test standards, the first shaft speed of 3.5 rps is not adequate. However, from a standpoint of starting up a mechanical system for the first time, the speed selection is justified as an attempt to approach the startup with caution in mind. Had the instrumentation been destroyed in the first instance of startup, no data collection would have been possible.

	J	Shaft Speed Number				
		n_1	n_2	n_3	n_4	n_5
Reynolds Number	Bollard	2.02E+05	4.05E+05	5.20E+05	6.93E+05	8.09E+05
	0.1	2.02E+05	4.05E+05	5.21E+05	6.94E+05	8.10E+05
	0.2	2.03E+05	4.06E+05	5.22E+05	6.96E+05	8.12E+05
	0.3	2.04E+05	4.08E+05	5.25E+05	7.00E+05	8.17E+05
	0.4	2.06E+05	4.11E+05	5.29E+05	7.05E+05	8.22E+05
	0.5	2.07E+05	4.15E+05	5.33E+05	7.11E+05	8.30E+05
	0.6	2.10E+05	4.19E+05	5.39E+05	7.19E+05	8.39E+05
	0.7	2.12E+05	4.25E+05	5.46E+05	7.28E+05	8.49E+05
	0.8	2.15E+05	4.30E+05	5.53E+05	7.38E+05	8.61E+05
	0.9	2.19E+05	4.37E+05	5.62E+05	7.49E+05	8.74E+05
	1.0	2.22E+05	4.44E+05	5.71E+05	7.62E+05	8.89E+05
	1.1	2.26E+05	4.52E+05	5.82E+05	7.75E+05	9.05E+05
	1.2	2.30E+05	4.61E+05	5.92E+05	7.90E+05	9.22E+05
	1.3	2.35E+05	4.70E+05	6.04E+05	8.06E+05	9.40E+05
	1.4	2.40E+05	4.80E+05	6.17E+05	8.22E+05	9.59E+05

Table 5.3 – Calculated values of Reynolds number for all shaft speeds and J values.

With the propeller shaft speeds selected and advance speeds calculated, the last parameter needed to plan the tests was the gap distance settings.

Originally, it had been planned to carry out an extensive array of gap distances in an attempt to see if the instrumentation was capable of measuring small changes in this variable. However, there was not enough time to allow the machining of all the gap filler components. Thus, nearing the end of the machining stage for all parts of the instrumentation, it was decided to chose several gap distances to reflect the range of what the instrumentation was capable of being adjusted to as well as one reflecting the 1% D_P recommended by ITTC standards. The largest gap filler that was complete at the time of selection was 5.25 mm (0.2067 inches), thus this was the largest gap selected for testing. All other selected gap filler components were then machined to completion. Table 5.4 shows the gap filler number and distance. Note that the instrumentation is designed for a setting of up to 7.25 mm (0.285 inches). As noted in chapter 3, larger gap settings are possible with additional thrust shaft components and setup. Note also that although the smallest design gap setting is 0.25 mm (0.0098 inches), this value could not be attained due to one threaded hole not being tapped deep enough. This was discovered during the final setup and testing of the range of adjustability. As noted in section 5.4.1.4, the smallest gap setting is 0.83 mm (0.033 inches). If one desires, the lower design value can be attained easily by correcting the applicable components.

Gap Filler Number	1	6	11	16	21
Gap Distance (mm)	0.25	1.50	2.75	4.00	5.25
Gap Distance (inches)	0.0098	0.0591	0.1083	0.1575	0.2067

Table 5.4 – Gap filler numbers and distances.

Once considerations had been given to test standards, propeller shaft speed, and gap adjustability, the test plan could be completed. The following points summarize the test plan:

1. Carry out a bollard test in pull mode to evaluate the drive system
2. Carry out a series of tests while varying:
    a. Propeller Advance Speed
    b. Propeller Rotational Speed
    c. Gap distance setting

A series of runs were planned based on these parameters. Each run consisted of a series of tests that kept a constant shaft speed as well as the gap distance setting. The J value was altered for each test and in the case of the lower values of J, several values were carried out in that test. The runs carried out reflected the overall initial performance of the drive system, which is covered in section 5.3.9. Thus stated, the test plan evolved over the course of three days in the MUN test tank and reflected what the author thought best at the time to carry out given the performance of the overall system. The experiment test procedure is discussed next and explains what was necessary to ready the instrumentation initially, now that it was assembled and calibrated, as well as changes that were necessary during the runs.

5.3 Experiment Test Procedure

The following steps outline the procedure required to conduct a series of tests with podded propulsors.

5.3.1 Setting Experimental Parameters

Five main parameters are discussed in this subsection.

5.3.1.1 Pod Direction

The test carriage at the MUN tank is capable of 5 m/s in the forward direction and 2 m/s in the reverse direction. To test the pod unit in pull mode, it was installed such that the propeller would travel in pull mode in the 5 m/s direction. This ensured that the carriage could reach the higher speeds in table 5.2. Note that this is an *important* consideration in planning any tests as the global dynamometer must be installed in the correct direction to allow the test to be carried out.

5.3.1.2 Propeller Depth

The design depth for the pod unit was 1.5 D_P, as indicated as the minimum in the test standards. This distance was selected because it minimized the effective moment arm length in the global dynamometer, in particular with respect to the Z-axis load cells. In addition, the mounting rails of the MUN test tank are not easily adjustable, thus the absolute distance from this elevation was set as non-adjustable and utilized the position that was most common for test setups (including setup to mount the propeller opens boat, used to evaluate propeller operation characteristics). Filling the tank to the correct level is thus essential in achieving the correct propeller depth. The depth is verified by using a tape measure from the propeller shaft axis to the free surface to verify that the distance is 1.5 times the propeller diameter. If larger diameter propellers are designed to be used in the future, the wave shroud and strut extension will have to be modified to allow a deeper absolute tank depth. Using smaller propellers will not present a problem.

5.3.1.3 Propeller Speed

The propeller speed command is a calculated number that was entered into the control software running the motor. To calculate the command frequency number, the following equation was used:

Equation 5.4
$$CFN = \left(\frac{60n}{1750}\right)(CFN_{MAX} \bullet GBR)$$

Where:

CFN	Command Frequency Number
n	Desired shaft speed in rps
CFN_{MAX}	60 (maximum speed command number which corresponds to 100% motor speed)
GBR	Gear box ratio, which is 2:1

Table 5.5 lists the command frequency number calculated for the test shaft speeds. These numbers were entered into the dialogue box of the control software. Once set, the start and stop tabs were clicked to control the motor operation.

Propeller Shaft Speed (rps)	Command Frequency Number
$n_1 = 3.5$	14.40
$n_2 = 7$	28.80
$n_3 = 9$	37.03
$n_4 = 12$	49.37
$n_5 = 14$	57.60

Table 5.5 – Command Frequency Numbers for the test shaft speeds.

5.3.1.4 Gap Distance

The initial gap setting was number 11, or 1% D_P. This distance was set prior to installing the gap fillers, propeller or pod shell, however the following procedure is explained from the point of view of changing this parameter while conducting a series of tests.

Setting the desired gap distance first required stacking a series of feeler gauges that added up to the required gap distance. Figure 5.14 shows gap filler number 11 and the distance required for these components. Figure 5.15 shows the stacked feeler gauges. The thickness was verified by using a set of digital calipers.

Figure 5.14 – Gap filler number 11 components and setting distance.

Next the position shaft lock nut access cone cover was unscrewed from the pod shell. Figure 5.16 shows the cone installed while figure 5.17 shows the cover removed, revealing the lock nut.

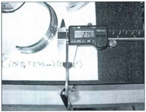

Figure 5.15 – Stacked feeler gauges and calipers verifying thickness.

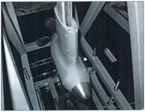

Figure 5.16 – View of position shaft lock nut access cone cover.

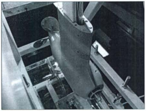

Figure 5.17 – View with cone cover removed, exposing lock nut.

The lock nut was loosened by using a 3/4 inch (19.05 mm) wrench. The thread is right hand, thus while looking towards the propeller, the nut was rotated CCW (counter-clockwise) to loosen. Next a ¼ inch socket driver was used to rotate the position setting shaft. Again, looking towards the propeller, the position setting shaft was rotated CCW to increase the gap distance such that it was slightly greater than the desired gap distance. The previously stacked selection of feeler gauges was then inserted into the propeller gap and the position shaft rotated clockwise to decrease the gap until the feeler gauges were gripped but could be moved with a slightly noticeable drag feeling. Figure 5.18 illustrates the insertion of the feeler gauges as well as the use of the socket driver to adjust the gap distance. Note that while rotating the position shaft for this operation one should attempt to keep the position setting shaft from rotating out of the lock nut. One

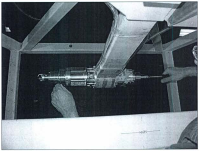

Figure 5.18 – Using feeler gauges and a socket driver to adjust the gap distance.

can do this by holding the nut with a thumb and index finger while the socket driver is being rotated with the grip provided by the other fingers and palm of the hand. This way the lock nut and shaft are rotated in unison. If during this operation some slight relative motion occurs between these two components, simply rotate the lock nut to pull the position setting shaft in, thereby decreasing the gap distance. When the gap distance had been set, the lock nut was tightened firmly, but not too tight.

After setting the gap distance, the gap filler needed to be changed, as described in 5.4.3. Figure 5.19 illustrates shows a view of the gap before initiating a change. Figure 5.20 shows a view of the gap after the gap filler has been changed, but before the matching gap distance change has been carried out. Note that changing the gap filler components before the gap distance does not affect the end result. Note also the discontinuity between the hub and pod surfaces. Figure 5.21 shows the gap with the feeler gauges in place after the adjustment has been carried out. Figure 5.22 shows the maximum gap distance tested.

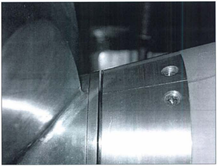

Figure 5.19 – View of gap before change (Gap distance of 1.50 mm).

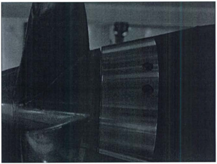

Figure 5.20 – The discontinuity after changing the gap filler & before changing the gap distance.

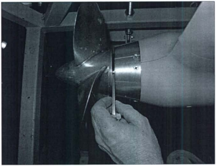

Figure 5.21 – Final checking of gap distance after adjustment (Gap distance of 4.00mm).

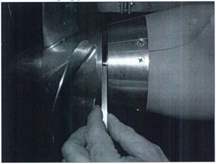

Figure 5.22 – Maximum gap distance tested (Gap distance of 5.25 mm).

As mentioned in section 5.3, the smallest gap setting is 0.84 mm (0.033 inches). This was the minimum gap distance tested. Note that one should refer to section 5.4.2 for the procedure of installing the gap fillers.

5.3.1.5 Carriage Speed

Setting the carriage speed consisted of advising the carriage operator of the current test speed prior to starting the test. In the case of lowest speeds of advance, several possible speeds were given to the operator on paper so that if one speed was successfully carried out, then another could be conducted in the same test. The number was dialed up on the carriage speed controller as was an acceptable acceleration rate, determined by the carriage operator. For higher speeds, the acceleration rate was increased to allow the time at speed to be as long as possible, since the distance lost during acceleration and deceleration became significant at higher speeds. The carriage speeds given to the operator were taken from table 5.2. The controller is capable of accepting the speed command with three significant figures after the decimal, but is not capable of delivering the actual speed to this accuracy.

5.3.2 Installing the Gap Fillers

Installing the gap fillers, or more importantly the gap filler ring adaptor was the first step in outfitting the instrumentation for testing. This adaptor was installed first as it cannot fit over the propeller hub taper angle adaptor or propeller if either of these components is installed. Note that section 1.1.1.9 in **Appendix N** gives the procedure for installing the gap fillers for the purpose of adjusting the shell drag instrumentation load cell. The procedure for installing the gap fillers is thus only briefly described here.

The ring adaptor was first placed over the hub instrumentation and onto the pod unit atmospheric pressure chamber. At this point note that it just sits here until the other components align it to the final installed position. Figure 5.23 shows the ring sitting in position.

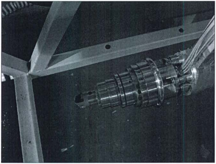

Figure 5.23 – Ring adaptor in position.

Next the bottom portion of the pressure plate adaptor was installed. Note that it was best to insert the center fastener screw into this adaptor and while keeping the tip of a Philips head screwdriver in place, then lift the adaptor up into place until the screw could be guided to the correct hole in the bottom of the pressure sensing plate. The screw was then fully installed and gently tightened. Note that ceramic anti-seize compound was used here to prevent the two stainless steel components from sticking together. The remaining two screws were then installed.

Next the rolling o-ring seal was installed by slipping it over the hub instrumentation. A view of this is shown in figure 5.24, complete with the lower installed pressure plate adapter.

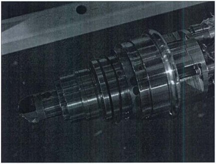

Figure 5.24 – Lower pressure plate adaptor and rolling o-ring seal installed.

Next the upper pressure plate adapter was installed by slipping it under the top portion of the o-ring. This prevents the seal from being stretched. Note that as described in chapter 3, this o-ring does not necessarily provide a 100% seal, but rather prevents a large inflow of water between the outer pod shell and the instrumentation within. A view of the installed upper pressure plate adaptor is shown in figure 5.25. A view of this setup with the pod shell and propeller installed is shown in figure 5.26.

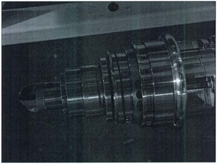

Figure 5.25 – Upper pressure plate adapter installed.

To complete the gap filler installation, each half is installed such that the o-ring is centered in the recess at the inner end closest to the propeller. This is shown in figure 5.27 in which the first half has been installed. Note that the ring adaptor has been oriented such that the parting lines of the pressure plate adapter pieces and the gap filler pieces are 90° apart. The second gap filler half was then installed to complete the installation. This ends the discussion on gap filler installation.

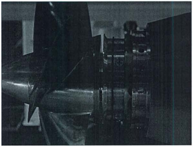

Figure 5.26 – Both pressure plate adaptor pieces installed with o-ring in position.

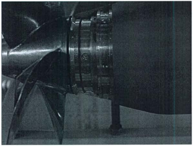

Figure 5.27 – O-ring positioning relative to the gap filler component.

5.3.3 Propeller Installation

Prior to installing the propeller, the hub taper angle adaptor was installed. This consisted of sliding it over the hub instrumentation and rotating it to align the mounting holes with the threaded holes in the reference base. Next 11 of the 12 mounting screws were installed to retain this adaptor. One hole has a broken tap that remains in place as the author though it was not worth the risk of damaging the part trying to extract it. Figure 5.28 shows the hub instrumentation before the adaptor is installed. Figure 5.29 shows the installed component.

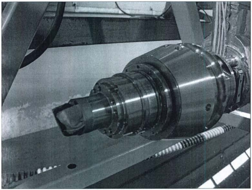

Figure 5.28 – Bare hub instrumentation.

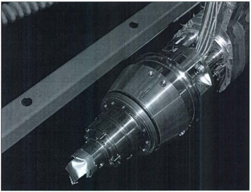

Figure 5.29 – Hub taper angle adaptor installed.

The propeller installation consisted of placing it over the hub instrumentation and gently pushing it in until the o-ring stopped the movement. At this point the propeller was rotated until the installation holes were aligned with the threaded holes in the hub instrumentation. Next all 8 of the Philips head stainless steel installation screws were threaded into their respective mounting holes. Care was taken not to cross thread them as the pitch of these fasteners is fine. Then the screws were successively tightened in a crossways pattern to gently pull the propeller over the o-ring such that it could be compressed by the tapered entrance machined into the propeller inner bore. During this process 1 half turn on each fastener was required before progressing to the next. Only one fastener from each group of two was used for this operation, as the others could be quickly tightened after the propeller was fully seated. Figure 5.30 shows the fully seated propeller. Note that because of the way this mounting is designed, very little thrust or torque is applied to the instrumentation and also that the screws need only to be gently tightened as the fine pitch gives more than adequate holding force.

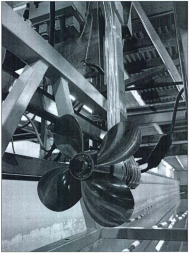

Figure 5.30 – Fully installed propeller.

After the propeller had been mounted, the nose cap was threaded into position. Again, because of the fine thread pitch, only hand force was necessary to install this component. The machined taper in the propeller bore at the nose cone end ensures that little torque and no thrust has to be applied to compress the o-ring seal. Figure 5.31 shows the propeller with the nose cap installed.

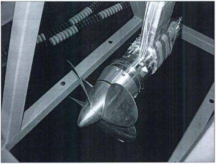

Figure 5.31 – Propeller with installed nose cap.

5.3.4 Installing the Pod Shell

Pod shell installation started with mounting a pod shell half to the instrumented shell mount side first. This is starboard side as viewing the pod in pull mode. Starting with the instrumented shell mount first ensured that the previously installed gap filler ring and gap fillers (if installed at this point in time) were aligned correctly. Note that the correct gap filler operational clearance was previously setup in section 1.1.1.9 of **Appendix N**.

Installing the shell half consisted of fitting it first over the ring adaptor of the gap filler assembly and then moving it in to enclose the instrumentation. While looking in from port side, the forward (un-instrumented) shell mount was jogged into position with a screwdriver such that when looking through one could see light through the hole, indicating that it was aligned. A fastening screw was then inserted into the top mounting hole of this position and almost fully installed. Next a fastening screw on the aft starboard side shell mount (instrumented) was inserted and the entire shell half moved forward and aft until the screw fit into the threaded hole. At this point both fasteners were then fully tightened. All others were then installed and tightened. Figure 5.32 shows a view with the first half installed. Note that the threaded adaptor for the position shaft lock nut access cone cover has been installed by placing it in the mounting groove in the first half.

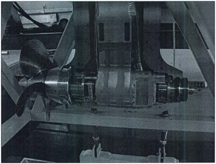

Figure 5.32 – First half of pod shell installed.

At this point the assembly clearance was checked to ensure that during experimentation, no obstructions existed that would hamper the movement of the shell during loading. Next the second half of the shell was installed. This was accomplished by mounting the piece into position on the port side of the unit and installing all fasteners into their respective threaded mounting holes. To complete the pod installation, the position shaft lock nut access cone cover was threaded onto its mounting adaptor which is gripped by the two pod shell components. Figure 5.33 shows a view of the completed installation. Note that the strut extension is held onto each portion of the pod shell by 4 long threaded rods with nuts on the top end. These are visible in figure 5.33 as well.

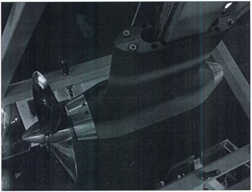

Figure 5.33 – Completed pod shell installation.

5.3.5 Installing the Wave Shroud

Installing the wave shroud consisted of inserting the two threaded rod mounts for each section into the corresponding holes in the lower member of the carriage frame. Once the threaded rods were inserted, one nut on each threaded rod was installed on top of the member. Note that one nut and washer had been previously installed on each rod prior to inserting them into position. The top nuts were then used to jack up the wave shroud to a position that was close to the final elevation required. Figure 5.34 shows the two wave shroud assembles installed, ready for final adjustment, which is described next.

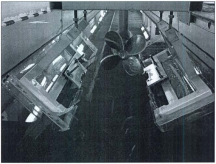

Figure 5.34 – Installed but not yet adjusted wave shroud.

Using the procedure in section 5.4.6, the pod unit was lowered to allow final positioning of the wave shroud. Note that the tank water level had been dropped for this procedure. When the pod unit had been lowered to the final position, the starboard side wave shroud portion was rotated on it mounts until it was level. A rope was tied to the shroud half and secured to the frame to allow the final elevation adjustment to take plate. Once it had been adjusted, the pod unit was raised and the port side half was adjusted to the first. The two were then clamped together for a final check on alignment. Figure 5.35 shows the adjusted wave shroud with the pod in the raised position. They were then opened, the pod unit lowered, then closed and clamped to test for fit and obstruction of the global dynamometer function. Figure 5.36 shows a view of the lowered pod and closed wave shroud.

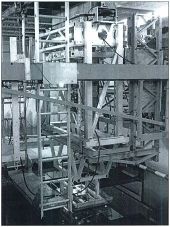

Figure 5.35 – Closed and adjusted wave shroud with pod unit raised.

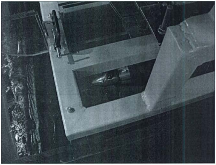

Figure 5.36 – Fully installed and adjusted wave shroud with pod unit lowered.

5.3.6 Lowering the unit into Water

This task began by first ensuring that all cabling was clear of the mating pads of the reference and carriage frames. Next it was ensured that the wave shroud was fully opened and restrained with ropes to prevent accidental closure. Next the power cable for the elevator lift motor was plugged in. Note that it is essential to keep this motor unplugged when not required for use to prevent accidental damage or injury to test personnel. The acme threads of the lift mechanism are non-self-overhauling which means they will not allow the elevator to lower even if the main synchronizing drive belt breaks or is removed altogether.

Once plugged in, the motor controller was turned on and the direction switch turned to the down position. The start button was then pressed and the speed gradually increased with the speed potentiometer. As the elevator was lowered careful attention was paid to the pod unit components to ensure that they did not get snagged, especially in the restraining ropes used to keep the wave shroud open. When the elevator had reached a level where the pads were only a few centimeters apart, the speed was decreased to a rate where one could comfortably observe all four contact pads in a short period of time. When the pads were in full contact, the motor was stopped and then unplugged. The direction switch was then changed so that when the motor was started again, it would already be traversing in the correct direction.

5.3.7 Securing the Dynamometer Reference Frame

Once the dynamometer was in the lowered position, a visual check was carried out to verify that all mating pads between the reference frame and carriage frame were indeed in full contact. Then, referring to figure 180 in **Appendix N**, the bolts were installed and tightened before a test was conducted. Note that after securing the reference frame it was ensured that the safety rods were removed from the live end assembly. Failure to remove these will cause the dynamometer not to register the test forces correctly.

5.3.8 System Power-Up

Energizing all systems started with turning on the power supplies and data acquisition unit, preferably several hours before any testing was to occur to allow the power supply voltages to stabilize. Each sensing system (except the gap pressures) was then tested by gently applying a force by hand to see if the channels were responding.

5.3.9 Configuring the Motor Controller & Belt Guide Rings

The information on configuring the motor drive in this section is brief, as the topic of AC motor controllers is quite involved and not necessary to understand completely in this context. Should the reader be interested in the specifics of the Allen Bradley Poweflex 70 AC Drive then one can find all information in the user manual.

Configuring the motor controller was carried out prior to starting the pod system for the first time. Essentially, the configuration consisted of setting the control parameters to give good low speed control to allow for tarring of all the channels, and a relatively long acceleration and deceleration rate to limit the torque and resulting belt tension that would be applied during spool up of the propeller. It was during this task that the pod unit drive system was tested for the first time. Prior to this task the tank water level was adjusted to the correct depth and the pod unit lowered. The wave shroud was not closed at this time to allow a clear view of the pod unit under water.

Upon starting, the speed of the propeller was gradually increased. The top target speed was 15 rps. Several minutes into the test a loud cracking sound was heard from the pod unit. The pod unit was immediately shut down and raised out of the water. Next about 12 hours of reasoning and investigation resulted in the author concluding that the belt was not perfectly aligned, despite having gone through a thorough alignment procedure for the gearbox. It was decided that to mitigate the problem, one of the guide rings on the gearbox output shaft would have to be modified to keep the belt from tracking off to one side. The belt guide ring was redesigned, manufactured and installed late the next day. The fact that the guide rings were removable facilitated the ability to carry out this task. The ring was installed on the side that the belt preferred to wander to and in fact did keep the belt tracking correctly. Note that the misalignment was between the two pulleys of the drive system and not the pod alignment relative the dynamometer, nor the relative alignment of the pod unit to the motor position. At a later date after the initial testing, the pod strut assembly was remounted in the CNC milling machine and corrected. A new series of holes for the gearbox mounting plate was drilled in between the existing holes and the alignment was corrected. Subsequent test programs affirmed that the belt alignment had indeed been fixed.

Figure 5.37 shows the original guide ring setup on the gearbox output pulley. Note that the guide ring on the problematic side has been removed. Figure 5.38 shows the newly designed and manufactured guide ring being slit using the same jig as used in producing all other guide rings.

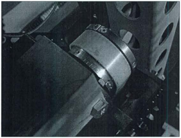

Figure 5.37 – Original belt guide ring setup with one removed.

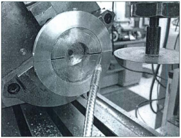

Figure 5.38 – Newly designed guide ring being cut in half with a slitting saw.

Figure 5.39 shows one half of the new guide ring installed on the drive pulley. Figure 5.40 shows the fully installed guide ring. Figure 5.41 shows the degree to which the belt was damaged during the initial startup. There was concern that the decreased effective width of the belt would cause it to fail at higher shaft speeds and lower speeds of advance.

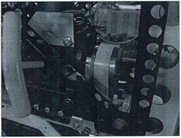

Figure 5.39 – One half of the new guide ring installed.

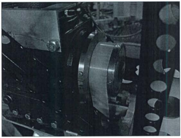

Figure 5.40 – Completely installed guide ring.

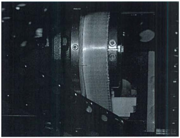

Figure 5.41 – Belt damage.

This damage severely hampered the initial testing and was the main reason for selecting lower test speeds. All tests were subject to the constraint of avoiding belt failure and with much caution the commissioning tests were completed without such an event.

Once the guide ring had been replaced, a startup was attempted again. A top speed of 14 rps was the limit determined to be safe. Most testing was conducted at lower speeds however because although the belt did not break, there was a tendency for the fractured edge to ride up on the face of the newly installed guide ring. Thus the new guide ring did extend the possible range of tests that could be carried out with a damaged belt.

After fixing the problem with the belt, a second major problem was encountered during startup. The problem was the tendency for the motor controller to cut out after seemingly random lengths of time of operation. The controller had been configured to allow good low speed characteristics, however after a short period of time it would trip out. After nearly two days of conversing with experts on AC drives, the author arrived at his own solution of changing the carrier frequency for the control signals to its maximum. This stopped to problem and finally allowed testing to begin.

In terms of the goal of assessing the functionality of the drive system, the author was satisfied with its operation despite the problems encountered.

5.3.10 Organizing the test data by way of File Nomenclature

The basis for the nomenclature for the files containing the test data is tables 5.1 and 5.4. These made up the beginning and end of the file name respectively. The advance speed that was tested was recorded on paper and assigned a letter value for that particular test, starting with 'a' for the first test in the run and then carrying on with sequential letters. The letter could stand for only one advance speed, or several if they could be carried out. This structure allowed for flexibility during testing. An example follows.

The file name for the first test of a run series carried out with a shaft speed of 3.5 rps and a gap distance of 2.75 mm would be assigned the following file name:

n1_a_gf11

In this case, it was recorded that the test had 4 advance speeds tested. Even without the record of the advance speeds, determining the advance speeds is carried out as part of the analysis because the target J value differs slightly from the actual value. This structure was used successfully for the entire test program.

5.3.11 Test Run Procedure

The test run commenced by entering the filename for the test (as per 5.4.10) into the data acquisition software and logging the parameters of that test and any other info on paper. The carriage was backed into position and the correct speed that corresponded to the test advance coefficient dialed up on the carriage speed controller. The shaft speed controller frequency number was then entered on the controller PC.

Next the data acquisition system was set into data collection mode with manual trigger. The trigger was actuated with the enter key and the system began collecting data. The main drive motor was then started by pressing the start key. With the motor accelerating, the carriage was started. The propeller was not allowed to develop full bollard thrust before starting the carriage because of the danger of destroying the drive belt. The entire system was then closely monitored while accelerating and traveling at the set speed. When the carriage was nearing the end of its travel, deceleration was initiated and at this point in time the main drive motor stopped. Again, this was to limit the belt tension force developed by the gearbox torque. When the carriage and drive motor had stopped the data acquisition process was ceased and all data was then automatically saved to the destination file.

Each test in the run series was conducted in a similar manner until all desired advance speeds had been tested, or as was often the case, it was felt that reducing the advance speed for a particular shaft speed was going to cause the drive belt to break. Initially the tests were conducted with an increasing J value, but near the middle of testing it was decided to test the higher speeds first and work down to the lowest speed possible. At the end of a run the pod unit was lifted out of the water and the gap distance and gap filler components changed. This procedure continued until the author was at the end of the tank time allotted. The instrumentation was then removed from the test tank by essentially following a reverse of the procedure used to install it. Once removed, a post calibration process was carried out to see how the effect of running in the instrumentation had affected its ability to be calibrated. Note that during the removal from the tank and post calibration procedures, it was determined that no water leaks had occurred during the commissioning tests.

Figures 5.42 to 5.45 present several of the more interesting photos obtained during testing.

The results of the initial tests are presented in the following chapter.

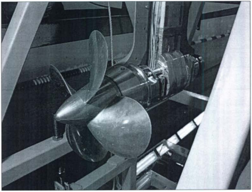

Figure 5.42 – View of the propeller and one shell half installed.

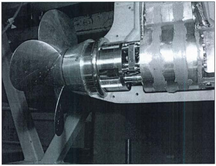

Figure 5.43 – A clear view of the clearance between the inner pod unit and shell interior.

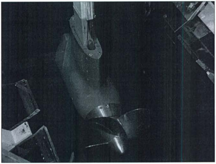

Figure 5.44 – A view of the pod underwater.

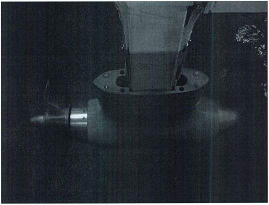

Figure 5.45 – A view of the pod running underwater.

CHAPTER 6 – EXPERIMENTAL RESULTS

INTRODUCTION

This section presents some of the initial measurement data from the various measurement systems. The reader is cautioned that these results are from a newly designed, calibrated and tested instrumentation package. Thus, it would be unwise to place emphasis on the results other than judging the functionality and operational success of the instrumentation as a result of looking at the data.

6.1 Discussion

Table 6.1 outlines the final tests that were carried out. The missing lower J values in the later runs reflect the increasing drive belt degradation and the subsequent torque limiting that had to follow. The sound of the instrumentation was a guiding factor in deciding how low to allow the J value to decrease. Each run series started at the high J values first and decreased until the author felt there was a danger of belt failure.

Run Series Number	Shaft Speed	Gap Distance Setting	Advance Ratio Range (J)
1	n1	GF11	0.1 - 1.4
2	n2	GF11	0.1 - 1.2
3	n3	GF11	0.1 - 1.2
4	n3	GF06	0.2 - 1.2
5	n4	GF06	0.9 ONLY
6	n3	GF01	0.3 - 1.2
7	n4	GF01	0.7 - 0.9
8	n3	GF16	0.4 - 1.2
9	n4	GF16	0.7 - 0.9
10	n3	GF21	0.5 - 1.1
11	n4	GF21	0.7 - 0.9

Table 6.1 – Final test parameters carried out.

6.2 Data analysis procedure

As stated in previous chapters the intent was to automate the data analysis process as much as possible, but spreadsheets were used in the end. A spreadsheet template was developed and used for each experiment analyzed. The final value for each channel in a run was then inserted into a summary sheet to allow plots to be developed for a particular set of parameters.

6.2.1 Determining Stable Data Ranges

Determining stable data ranges involved locating a segment of data from the entire sample where as many transients as possible had settled out. This step determined an average voltage for each transducer, which in turn allowed calculation of the parameter of interest for each test run. For this set of experiments, the stable data ranges were determined by first plotting the propeller shaft speed, carriage speed, the two thrusts, torque and the 5 pressure transducers in combination or separately to view the extent of the transient periods. In particular, the propeller shaft speed and carriage speeds were used to determine a possible useable range of data for the two thrust signals. When viewing the thrusts in this range, it could then be determined where they were stable. The range defined in this manner then became the sample region for the experiment from which the average voltage could be calculated for all channels. Torque was the most trouble free parameter to look at and was stable if the other signals were stable. A value for the tare was also obtained by a combination of plotting parameters to determine where the signal was most stable. For many instances, all five pressure transducer signals along with the propeller shaft and carriage speeds were plotted to determine the best region to obtain a tare value.

During the initial phase of testing, each test was conducted by starting the propeller shaft motor from rest, but after some time it was suggested that the motor be kept running at the slowest possible speed. As a result, for the first few experimental runs a tare value while all systems are at rest and one when the shaft is turning at a very slow speed can be taken. The change in torque, the two thrusts, shell drag and dynamometer channels exhibited no great change in the averaged value between these two states. The pressure transducers did however exhibit a change in value. The change was not predictable or the same each time the shaft was started. This caused a great deal of trouble when trying to obtain a good tare value for the pressure transducers. Sometimes the tare region of data was reasonably stable before the shaft started, and other times it was better to get the tare data from the region before the shaft rotation was started. The propeller shaft tachometer generator signal was not tared as this would give a speed lower than the actual speed value. The tare value for propeller speed was thus set to zero in the spreadsheets. The carriage speed channel had a 55 mV offset that was nearly consistent throughout the tests, so it was tared out. In general, it seems the pressure transducers exhibited the most inconsistency, drift and erratic voltage output over the duration of the tests.

6.2.2 Applying calibration equations to obtain test values

Once average values had been obtained for the tarring and stable sections of the test, the voltages were converted to engineering units. This was done by deducting the tare value from the stable region average value then multiplying the result by the calibration constant for each channel. The results were tabulated for all test conditions.

6.3 Sample plots

In the following sections, sample plots are presented that are a representative of the typical results encountered during the initial tests with the instrumentation. One must note that the sample times for some stable regions are much less than the ITTC recommended time, and reflects the author's concern that loading for an extended time period and magnitude would increase the likelihood of breaking the drive belt. Note also that the plots are presented in volts, only the values from the test were tabulated in engineering units.

6.3.1 Carriage & Propeller Shaft Speed with Torque

Figures 6.1 through to 6.4 show some typical results for carriage and propeller shaft speeds, as well as propeller torque. The x-axis is the time scale in milliseconds and the y-axis is the output voltage of the transducers. Note that one can get a sense of the timing of events for each run from these plots.

Figures 6.1, 6.2, 6.3 and 6.4, show the entire advance speed range for propeller speed 1, which was 3.5 rps (note that gap distance is set to 1% D_P). This run is unique in that the entire range was covered in just these few tests.

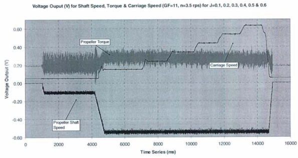

Figure 6.1 – Carriage speed, propeller shaft speed & torque voltage outputs from RUN1, J=0.1, 0.2, 0.3, 0.4, 0.5 and 0.6.

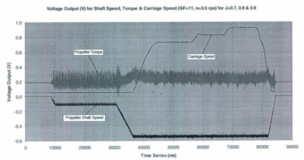

Figure 6.2 – Carriage speed, propeller shaft speed & torque voltage outputs from RUN1, J=0.7, 0.8 and 0.9.

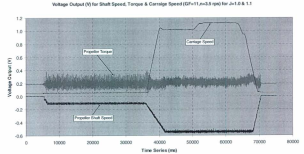

Figure 6.3 – Carriage speed, propeller shaft speed & torque voltage outputs from RUN1, J=1.0 and 1.1.

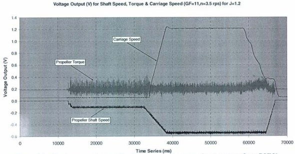

Figure 6.4 – Carriage speed, propeller shaft speed & torque voltage outputs from RUN1, J=1.2.

In general, the torque signal is low for a shaft speed of 3.5 rps, which makes sense. When a plot of a higher shaft speed is completed, the voltage signal is easier to visualize, as shown in figure 6.5. This result is taken from RUN 7 where the shaft speed is 12 rps and J=0.7. One can see the effect of the propeller speed and carriage speed acceleration on torque. Note the timing of starting the propeller and carriage. Torque is successfully limited below maximum for the stable region for all time during the test. In all of these plots one can see that the propeller shaft speed and carriage speed are well behaved signals.

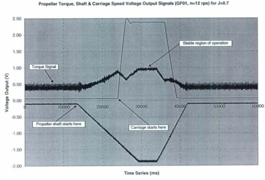

Figure 6.5 – Carriage speed, propeller shaft speed & torque voltage outputs from RUN7, J=0.7 and propeller speed of 12 rps.

The discussion now changes to hub and pod propeller thrusts.

6.3.2 Hub & Pod Propeller Thrusts

Plots of the two thrust signals were essential in determining the stable data ranges. Upon studying the responses of the thrust signals, it was observed that the hub thrust response time sometimes slightly lags the pod thrust. In many instances, this reduced the range of stable values that could be used for analysis, even though both the carriage and propeller shaft speeds had stabilized. Thus, each range had to be carefully looked at to determine the final useable data range. Figure 6.6 shows the responses of the two thrust signals, along with the carriage and propeller shaft speed for the first four advance ratios from RUN 3, where the propeller speed is 9 rps. One can see the lagging response times. Note that the shaft speed acceleration is uniform. Figure 6.7 shows the same plot with the shaft speed removed for clarity. Note that for J=0.1, the hub thrust signal only stabilizes at the very end of the range.

Figure 6.8 shows the thrust signals for J=1.0. Here the thrust signals are stable and well timed with the carriage speed. Figure 6.9 shows thrusts for J=1.2. The range of stable data for all channels is between the vertical lines. Note that figure 6.1 to 6.9 have a shaft speed of 0 rps at the start of data collection.

Figure 6.10 shows the thrust signals from RUN 7, with J values of 0.7. The propeller speed is 12 rps. Here the propeller is moving slowly at the beginning of the test.

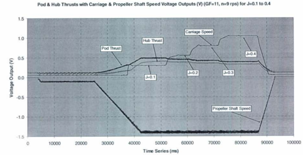

Figure 6.6 – Pod and Hub Thrust voltage outputs from RUN3, J=0.1 through to 0.4.

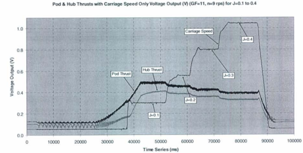

Figure 6.7 – Pod and Hub Thrust voltage outputs from RUN3, (with Propeller Shaft Speed Removed), J=0.1 through to 0.4

Pod & Hub Thrusts with Carriage & Propeller Speed Voltage Outputs (V) (GF=11, n=9 rps) for J=1.0

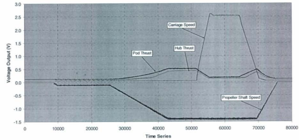

Figure 6.8 – Pod and Hub Thrust voltage outputs from RUN3, J=1.0.

Pod & Hub Thrusts with Carriage & Propeller Speed Voltage Outputs (V) (GF=11, n=9 rps) for J=1.2

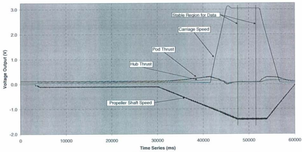

Figure 6.9 – Pod and Hub Thrust voltage outputs from RUN3, J=1.2.

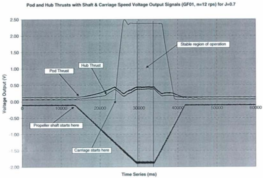

Figure 6.10 – Pod and Hub Thrust voltage outputs from RUN7, J=0.7.

The discussion now shifts to the shell drag system.

6.3.3 Shell Drag

Figures 6.11 through to 6.13 show some typical results from the shell drag measuring system. The idea for shell drag measurement was to compare its value to the global thrust value and propellers thrusts. The voltage traces seen in the plots indicate a logical response; a distinct change in shell drag value for changing advance speed is seen. In addition, when looking at individual plots, one can see how the shells drag responds to different events during each particular test.

In Figure 6.11, the propeller wake is registered almost immediately upon starting, and as the pod is started with the carriage, there is a surge in voltage before stabilization occurs.

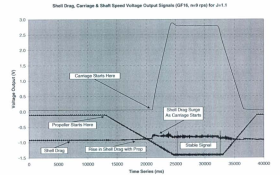

Figure 6.11 – Shell drag voltage output trace from RUN8, n=9 rps, J=1.1.

As with the thrusts, torque, carriage & shaft speed signals, the shell drag signal stabilizes for all runs. Figure 6.12 is the same plot as 6.11, but with only the shell drag signal displayed.

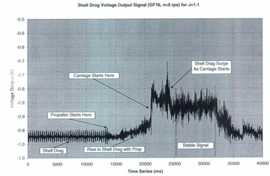

Figure 6.12 – Shell drag voltage output only, from RUN 8, n=9 rps, J=1.1.

Figure 6.13 is from RUN 11. Here the shaft speed is 12 rps and advance speed is 0.7. The response pattern is nearly identical to the previous figures in this section.

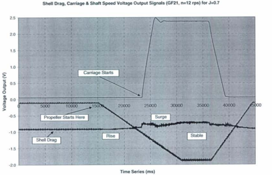

Figure 6.13 – Shell drag voltage output trace from RUN11, n=12 rps, J=0.7.

The discussion now turns to the unit dynamometer.

6.3.4 Unit Dynamometer (X-axis only)

As indicated in chapter 4, the focus for the unit dynamometer was the x-axis load cell reading only. During the process of analyzing the results, it became apparent that the unit thrust was differing significantly from the pod thrusts. There are several possibilities for this. The most likely reason is the haste with which the author completed the installation and adjustment of the wave shroud. As a result, the pod instrumentation could have been mechanically grounded against the wave shroud. Another possibility is an accidental change in excitation voltage and/or gain setting on the data acquisition cards, or indeed a mistake in the calibration process or a combination of all factors mentioned. One plot is provided for viewing in figure 6.14. The dynamometer does respond in a way that is indicative of correct responsive behavior for such type of instrumentation.

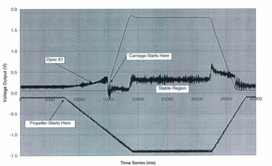

Figure 6.14 – Unit dynamometer X axis only voltage trace, from RUN 10, n=9 rps, J=0.7.

It is worth mentioning that this instrumentation was successfully used in work that followed that of the author. It is left to reader to investigate further.

The discussion now switches to pressure transducers.

6.3.5 Pressure Transducers

This section presents voltage signal traces for the pressure transducers for several runs. It was obvious while viewing the voltage outputs that these transducers are subject to influences from a number of sources. One was mechanical and electrical triggers, such as releasing the carriage brakes and starting the carriage and propeller motors, which sometimes greatly shifted the voltages for all five sensors at different and unpredictable times. This caused great difficulty in determining a suitable region of stable data for tare and steady state regions of each test. Another influence was due to the possibility of entrapped air bubbles that delayed the registration or release of pressures either at the start, during or end of a test. This influence exists despite all the care taken during design and setup of the pressure instrumentation. Finally, at one point there was a small water leak into the cavity of the atmospheric pressure chamber, through which the gauge vents entered. This was noticed early however, and the cause determined to be a hose clamp that didn't quite seal the clear tubing to the spigot through which all wiring exited to the strut. The water was evacuated and the seal fixed. Although the chamber did not fill completely with water, it is difficult to assess whether or not this leak affected the sensors. There are times at which it seems the voltage seems to have gone to an extreme, as can be seen in the data, but voltage may have changed due to other undetermined reasons.

Figure 6.15 shows a plot of the carriage and propeller shaft speeds, from RUN 6 with GF=01, J=0.9. This plot is to be used with figure 6.16, appearing on the page following.

It is a series of all 5 pressure transducer voltage outputs. One can see how the pressure responses align with the changes in the two speed parameters.

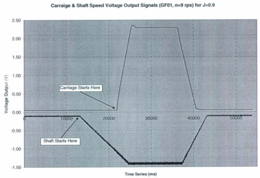

Figures 6.15 – Shaft and Carriage Speed voltage signals, from RUN 6, for J=0.9.
This plot is used for timing for pressure transducer outputs in figures 6.16.

Figure 6.16 – Pressure transducer voltages, from RUN 6 with GF=01, J=0.9.
(Appear on next page.)

Pressure Transducer #1 Voltage Output Signal (GF01, n = 9 rps) for J=0.9

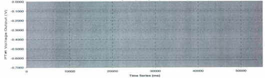

Pressure Transducer #2 Voltage Output Signal (GF01, n = 9 rps) for J=0.9

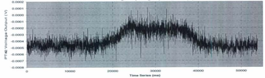

Pressure Transducer #3 Voltage Output Signal (GF01, n = 9 rps) for J=0.9

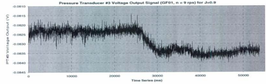

Pressure Transducer #4 Voltage Output Signal (GF01, n = 9 rps) for J=0.9

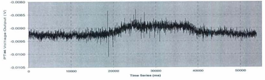

Pressure Transducer #5 Voltage Output Signal (GF01, n = 9 rps) for J=0.9

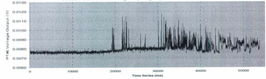

Looking at the output for pressure transducer #1, it appears that water, an electrical problem, or air bubbles, has caused the voltage to stay perfectly constant. This was a typical kind of signal style. Pressure transducers #2 and #4 and 5 to some degree have a response style similar to the other channels. Pressure transducer #5 has extra noise in the signal, which could be from the previously mentioned causes. Pressure transducer #3 exhibits another style that was typical in these experiments, and highlights how the voltage takes on an absolute shift and does not return to the start value.

Figure 6.17 on the next page is a series of pressure transducer responses from RUN 8, with GF=16, J=0.8. Here the voltage shift is universal across all 5 sensors, indicating something electrical is the cause. A problem with this type of response is that it is difficult to obtain a tare value, or trust that the stable area of the test has not been shifted.

Figure 6.17 – Pressure transducer voltages, from RUN 8 with GF=16, J=0.8.
(Appear on next page.)

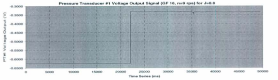
Pressure Transducer #1 Voltage Output Signal (GF 16, n=9 rps) for J=0.8
PT#1 Voltage Output (V)
Time Series (ms)

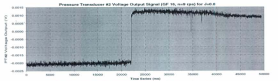
Pressure Transducer #2 Voltage Output Signal (GF 16, n=9 rps) for J=0.8
PT#2 Voltage Output (V)
Time Series (ms)

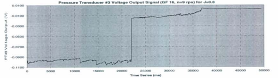
Pressure Transducer #3 Voltage Output Signal (GF 16, n=9 rps) for J=0.8
PT#3 Voltage Output (V)
Time Series (ms)

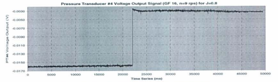
Pressure Transducer #4 Voltage Output Signal (GF 16, n=9 rps) for J=0.8
PT#4 Voltage Output (V)
Time Series (ms)

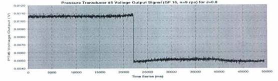
Pressure Transducer #5 Voltage Output Signal (GF 16, n=9 rps) for J=0.8
PT#5 Voltage Output (V)
Time Series (ms)

The sample plots in figure 6.18 on the following page are from RUN 5, GF=06 and J=0.9. This set of plots indicate a more typical behavior of the transducers as installed in these experiments.

Figure 6.18 – Pressure transducer voltages, from RUN 5 with GF=06, J=0.9.
(Appear on next page.)

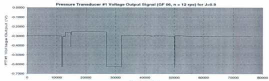
Pressure Transducer #1 Voltage Output Signal (GF 06, n = 12 rps) for J=0.9
PT#1 Voltage Output (V)
Time Series (ms)

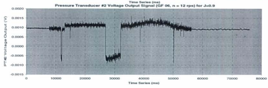
Pressure Transducer #2 Voltage Output Signal (GF 06, n = 12 rps) for J=0.9
PT#2 Voltage Output (V)
Time Series (ms)

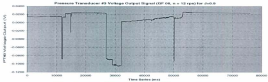
Pressure Transducer #3 Voltage Output Signal (GF 06, n = 12 rps) for J=0.9
PT#3 Voltage Output (V)
Time Series (ms)

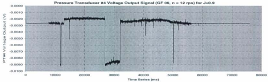
Pressure Transducer #4 Voltage Output Signal (GF 06, n = 12 rps) for J=0.9
PT#4 Voltage Output (V)
Time Series (ms)

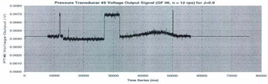
Pressure Transducer #5 Voltage Output Signal (GF 06, n = 12 rps) for J=0.9
PT#5 Voltage Output (V)
Time Series (ms)

The sample plots in figure 6.19 through to 6.23 are from RUN 4, GF=06 and J=0.7. These plots are presented individually to capture the magnitude of the voltage response. The large spike is due to release of the carriage brakes.

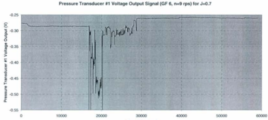

Figure 6.19 – Pressure transducer #1 voltage output from RUN 4, GF=06, J=0.7.

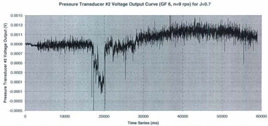

Figure 6.20 – Pressure transducer #2 voltage output for RUN4, GF=06, J=0.7.

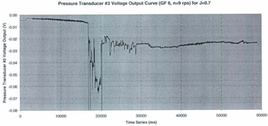

Figure 6.21 – Pressure transducer #3 voltage output for RUN 4, GF=06, J=0.7.

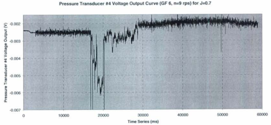

Figure 6.22 – Pressure transducer #4 voltage output for RUN 4, GF=06, J=0.7.

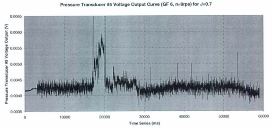

Figure 6.23 – Pressure transducer #5 voltage output for RUN 4, GF=06, J=0.7.

The discussion now turns to summary plots.

6.4 Summary Test Data

The following tables present the entire test program data in a format that is easy to understand. After the individual run data is presented, some comparison tables are presented, along with their corresponding plots.

RUN 1 GF 11 Shaft speed 3.5 rps

DATA Files

n1_b_gf11.txt n1_c_gf11.txt n1_d_gf11.txt n1_e_gf11.txt

CHANNEL	ADVANCE COEFFICIENT J											
	0.1	0.2	0.3	0.4	0.5	0.6	0.7	0.8	0.9	1	1.1	1.2
Pressure Transducer #1 (Pa)	-90.575	-120.689	-240.118	331.885	448.712	345.673	267.318	302.433	-242.372	133.687	61.749	609.659
Pressure Transducer #2 (Pa)	-1.707	-1.058	-2.715	7.557	11.003	10.656	7.913	9.155	7.368	9.454	8.696	9.951
Pressure Transducer #3 (Pa)	482.345	615.824	565.887	697.924	743.932	720.389	-717.732	-685.445	-712.869	-936.839	-881.078	-1277.182
Pressure Transducer #4 (Pa)	0.097	8.376	5.434	40.324	46.751	40.494	24.660	24.475	3.433	14.700	13.720	32.822
Pressure Transducer #5 (Pa)	2.962	2.845	7.344	-18.799	-23.146	-20.332	-17.504	-17.998	9.453	-2.262	-2.538	-170.931
Shell Drag Force (N)	0.899	0.875	0.652	0.662	0.665	0.522	-0.178	0.094	0.032	0.040	0.180	0.160
Propeller Torque, Q (Nm)	1.208	1.129	1.064	0.986	0.898	0.813	0.679	0.574	0.494	0.342	0.232	0.080
Thrust from Propeller Hub, T_{PROP} (N)	24.109	23.858	22.144	21.015	19.228	17.350	15.208	12.602	9.981	-8.391	-11.045	-7.346
Thrust from Pod Unit, T_{POD} (N)	31.952	29.683	26.844	23.918	21.205	18.022	12.336	9.206	6.045	0.740	-2.603	-3.648
Unit Thrust (Dyno X1) (N)	52.283	48.551	44.707	40.757	35.815	30.614	21.361	16.699	10.437	0.184	-5.943	-13.779
	26.1413	24.27533	22.3533	20.37857	17.90733	15.307	10.6805	8.349707	5.218525	0.09199	-2.971273	-6.88933751
Shaft Speed	3.558	3.559	3.560	3.562	3.563	3.563	3.564	3.566	3.567	3.567	3.568	3.569
Carriage Speed	0.095	0.183	0.282	0.377	0.473	0.566	0.661522	0.757	0.852	0.947	1.044	1.137
Advance Coefficient, J	0.099	0.191	0.293	0.392	0.491	0.588	0.687374	0.786	0.885	0.984	1.084	1.180
Thrust Coefficient, $K_{T,PROP}$	0.358	0.354	0.329	0.312	0.285	0.257	0.225	0.187	0.148	-0.124	-0.163	-0.109
Thrust Coefficient, $K_{T,POD}$	0.475	0.441	0.398	0.355	0.314	0.267	0.183	0.136	0.089	0.011	-0.038	-0.054
Unit Thrust Coefficient, $K_{T,UNIT}$	0.777	0.721	0.664	0.605	0.531	0.454	0.316	0.247	0.154	0.003	-0.088	-0.204
Propeller Efficiency, η_{PROP}	0.08495	0.173229	0.262445	0.359532	0.451879	0.539573	0.661189	0.741023	0.768207	-1.03796	-2.21926	-4.64958028
Propeller Efficiency, η_{POD}	0.112585	0.215524	0.318151	0.409188	0.498331	0.560471	0.536322	0.54134	0.465307	0.091579	-0.523057	-2.30913951
Torque Coefficient (x10), 10 K_Q	0.665	0.621	0.585	0.542	0.493	0.446	0.373	0.315	0.271	0.187	0.127	0.044

Table 6.2 - Summary Data for RUN 1

RUN 2 GF 11 Shaft speed 7 rps

DATA Files

n2_a_gf11.txt n2_b_gf11.txt n2_c_gf11.txt n2_d_gf11.txt
n2_e_gf11.txt n2_f_gf11.txt n2_g_gf11.txt n2_h_gf11.txt

CHANNEL	ADVANCE COEFFICIENT J											
	0.1	0.2	0.3	0.4	0.5	0.6	0.7	0.8	0.9	1	1.1	1.2
Pressure Transducer #1 (Pa)	-7.902	-243.473	-28.409	113.759	98.026	99.063	14.93252	-24.284	78.320	4.228	-233.986	110.852
Pressure Transducer #2 (Pa)	8.194	7.709	9.194	10.967	10.969	13.954	13.9514	9.193	12.283	13.731	7.447	17.705
Pressure Transducer #3 (Pa)	-1900.729	-1679.678	-1649.796	-886.940	183.267	252.856	-395.755	-53.429	-57.4442	213.873	271.208	162.130
Pressure Transducer #4 (Pa)	8.918	2.816	9.129	16.152	8.019	6.743	1.066	2.132	17.89271	2.471	6.335	10.314
Pressure Transducer #5 (Pa)	13.853	17.901	16.619	10.183	14.716	15.129	10.29148	22.451	15.972	19.122	28.375	14.364
Shell Drag Force (N)	6.954277	7.080073	6.977772	6.00786	5.850751	5.097635	4.949134	4.831537	4.709811	5.052148	5.346853	5.844757
Propeller Torque, Q (Nm)	4.733	4.439337	4.110131	3.792695	3.444911	3.060687	2.619564	2.231705	1.805838	1.28534	0.803443	0.224305
Thrust from Propeller Hub, T_{PROP} (N)	85.53174	78.49639	69.67835	59.23345	50.24199	38.07257	32.24097	26.22181	18.45896	8.194917	5.965558	-6.317799
Thrust from Pod Unit, T_{POD} (N)	116.990	107.9399	98.34237	88.48947	78.13284	69.2448	56.84683	48.58898	36.27337	22.00218	6.980912	-8.765216
Unit Thrust (Dyno X1) (N)	235.133	225.1246	211.4907	194.3783	152.4355	125.5672	100.774	65.94874	37.46447	-5.340206	-46.84308	-83.56986
Shaft Speed	7.110	7.114038	7.118173	7.120887	7.122505	7.126228	7.13071	7.134628	7.137413	7.141243	7.146355	7.151048
Carriage Speed	0.184	0.375767	0.567	0.758	0.945891	1.142263	1.32654	1.517779	1.710854	1.899	2.088499	2.275
Advance Coefficient, J	0.095736	0.195631	0.294855	0.394368	0.491863	0.593666	0.689007	0.787904	0.887786	0.984974	1.082395	1.178289
Thrust Coefficient, $K_{T,PROP}$	0.318	0.292	0.259	0.220	0.186	0.141	0.119	0.097	0.068	0.030	0.022	-0.023
Thrust Coefficient, $K_{T,POD}$	0.435	0.401	0.365	0.328	0.290	0.257	0.210	0.180	0.134	0.081	0.026	-0.032
Unit Thrust Coefficient, $K_{T,UNIT}$	0.875	0.837	0.785	0.721	0.565	0.465	0.373	0.244	0.138	-0.020	-0.173	-0.308
Propeller Efficiency, η_{PROP}	0.074348	0.148646	0.214801	0.26467	0.30826	0.317337	0.364407	0.397817	0.389961	0.269858	0.345355	-1.426145
Propeller Efficiency, η_{POD}	0.101693	0.204403	0.303165	0.395394	0.479385	0.577158	0.642518	0.737155	0.766305	0.724531	0.404136	-1.978612
Torque Coefficient (x10), 10 K_Q	0.652	0.611	0.565	0.521	0.473	0.420	0.359	0.306	0.247	0.176	0.110	0.031

Table 6.3 - Summary Data for RUN 2

RUN 3 GF 11 Shaft speed 9 rps

DATA Files

n3_a_gf11_b.txt n3_a_gf11_c.txt n1_c_gf11.txt n1_d_gf11.txt n1_e_gf11.txt
n3_f_gf11.xls n3_g_gf11.txt n3_h_gf11.txt n3_i_gf11.txt

CHANNEL	ADVANCE COEFFICIENT J											
	0.1	0.2	0.3	0.4	0.5	0.6	0.7	0.8	0.9	1	1.1	1.2
Pressure Transducer #1 (Pa)	729.950	1064.697	843.079	548.929	824.527	32121.220	-2632.328	-2062.658	-9364.830	-166.273	377.556	404.993
Pressure Transducer #2 (Pa)	38.961	42.086	42.150	41.252	27.241	168.041	24.13981	28.301	-30.975	58.498	47.986	40.330
Pressure Transducer #3 (Pa)	423.046	455.485	528.192	611.151	-196.647	3997.470	237.2255	-150.241	-332.450	1084.517	213.831	68.570
Pressure Transducer #4 (Pa)	47.860	51.037	47.095	37.365	52.001	675.491	-19.36992	-2.104	-134.663	64.494	45.058	49.936
Pressure Transducer #5 (Pa)	28.211	20.438	32.360	38.249	41.973	-593.035	113.856	94.593	213.137	83.836	75.365	49.106
Shell Drag Force (N)	15.70058	14.56019	13.37119	12.21658	10.25223	9.621127	10.00735	9.578536	9.584767	9.574018	10.0227	10.02781
Propeller Torque, Q (Nm)	7.863232	7.319778	6.835	6.302	5.754	5.039	4.368793	3.728	3.026	2.283	1.361	0.369
Thrust from Propeller Hub, T_{PROP} (N)	144.4231	132.5724	119.9876	105.8069	79.44365	42.71637	44.11945	37.5371	17.5248	15.75043	-4.006505	-17.73181
Thrust from Pod Unit, T_{POD} (N)	194.600	176.718	159.254	141.587	129.459	110.560	88.42734	73.678	49.446	31.210	11.963	-18.645
Unit Thrust (Dyno X1) (N)	399.0927	393.3056	361.0105	325.3576	275.075	222.5249	182.7122	134.661	84.185	35.46853	-28.1689	-92.51554
Shaft Speed	9.133668	9.139267	9.146	9.151	9.159	9.161	9.164898	9.171	9.179	9.185	9.193	9.202
Carriage Speed	0.248	0.495	0.732	0.973	1.219	1.466	1.710106	1.955	2.198	2.442	2.688	2.934
Advance Coefficient, J	0.100602	0.200531	0.296575	0.393922	0.492839	0.592525	0.691085	0.789592	0.887029	0.98481	1.082885	1.181
Thrust Coefficient, $K_{T,PROP}$	0.326	0.299	0.270	0.238	0.178	0.096	0.099	0.084	0.039	0.035	-0.009	-0.039
Thrust Coefficient, $K_{T,POD}$	0.439	0.398	0.358	0.318	0.290	0.248	0.198	0.165	0.110	0.070	0.027	-0.041
Unit Thrust Coefficient, $K_{T,UNIT}$	0.900	0.886	0.812	0.731	0.617	0.499	0.409	0.301	0.188	0.079	-0.063	-0.206
Propeller Efficiency, ηPROP	0.079401	0.15607	0.223725	0.2842	0.292389	0.21586	0.299905	0.341663	0.220751	0.291961	-0.136941	-2.441367
Propeller Efficiency, ηPOD	0.106987	0.208041	0.29694	0.380305	0.47647	0.558694	0.601092	0.670617	0.622841	0.578538	0.408894	-2.567046
Torque Coefficient (x10), 10 K_Q	0.657	0.611	0.569	0.524	0.478	0.418	0.362	0.309	0.250	0.189	0.112	0.030

Table 6.4 - Summary Data for RUN 3

RUN 4 GF 06 Shaft speed 9 rps												
	DATA Files											
	n3_a_gf06.txt		n3_b_gf06.txt		n3_c_gf06.txt		n3_d_gf06.txt		n3_e_gf06.txt		n3_f_gf06.txt	
	n3_g_gf06.txt		n3_h_gf06.txt		n3_i_gf06.txt							
CHANNEL	ADVANCE COEFFICIENT J											
	0.1	**0.2**	**0.3**	**0.4**	**0.5**	**0.6**	**0.7**	**0.8**	**0.9**	**1**	**1.1**	**1.2**
Pressure Transducer #1 (Pa)		1866.740	1926.395	1487.898	562.789	43459.911	2889.914	1075.903	49300.587	3098.866	243.439	5517.878
Pressure Transducer #2 (Pa)		15.418	20.883	17.585	0.674	261.395	49.48658	39.241	322.833	39.968	35.241	54.132
Pressure Transducer #3 (Pa)		-1635.212	-1642.845	-1882.292	-584.753	3798.119	-2807.064	3944.738	15712.376	785.614	1545.635	-2261.508
Pressure Transducer #4 (Pa)		47.405	46.167	35.300	14.419	723.850	68.88687	19.971	943.939	74.813	48.913	119.139
Pressure Transducer #5 (Pa)		27.118	27.777	33.597	42.237	-359.019	12.21124	27.784	-485.863	8.804	26.500	-8.526
Shell Drag Force (N)		3.32061	2.778378	2.154632	2.349219	10.437	4.401091	1.500019	0.763	0.287	0.676379	0.676884
Propeller Torque, Q (Nm)		7.387	6.817	6.274	5.690	5.125	4.459452	3.740	3.010	2.227	1.331	0.291
Thrust from Propeller Hub, T_{PROP} (N)		129.914	110.4063	89.82068	74.08204	69.856	53.03037	31.30065	12.649	1.998	-4.137268	-19.34273
Thrust from Pod Unit, T_{POD} (N)		179.370	160.772	143.778	125.843	112.712	87.7322	77.734	55.927	36.467	14.374	-15.265
Unit Thrust (Dyno X1) (N)		411.9954	367.9544	327.2746	286.4462	242.672	191.2263	140.0713	84.239	29.212	-27.57447	-98.30153
Shaft Speed		9.157	9.162	9.169	9.169	9.172	9.182168	9.188	9.196	9.200	9.209	9.218
Carriage Speed		0.482	0.726	0.975	1.218	1.463	1.706954	1.951	2.197	2.442	2.688	2.932
Advance Coefficient, J		0.194949	0.29332	0.393724	0.492	0.591	0.688514	0.786474	0.885	0.983	1.081135	1.178
Thrust Coefficient, $K_{T,PROP}$		0.292	0.248	0.201	0.166	0.156	0.118	0.070	0.028	0.004	-0.009	-0.043
Thrust Coefficient, $K_{T,POD}$		0.403	0.360	0.322	0.282	0.252	0.196	0.173	0.124	0.081	0.032	-0.034
Unit Thrust Coefficient, $K_{T,UNIT}$		0.925	0.825	0.733	0.641	0.543	0.427	0.312	0.187	0.065	-0.061	-0.218
Propeller Efficiency, ηPROP		0.147337	0.204129	0.242204	0.275348	0.3458993	0.351836	0.282863	0.159828	0.037893	-0.144377	-3.36962
Propeller Efficiency, ηPOD		0.203426	0.297248	0.387702	0.467734	0.5581044	0.582069	0.702482	0.706667	0.691775	0.501607	-2.659168
Torque Coefficient (x10), 10 K_Q		0.614	0.566	0.520	0.472	0.425	0.369	0.309	0.248	0.183	0.109	0.024

Table 6.5 - Summary Data for RUN 4

RUN 5 GF 06 Shaft speed 12 rps												
	DATA Files n3_a_gf06_b.txt											
CHANNEL	ADVANCE COEFFICIENT J											
	0.1	0.2	0.3	0.4	0.5	0.6	0.7	0.8	**0.9**	1	1.1	1.2
Pressure Transducer #1 (Pa)									64.689			
Pressure Transducer #2 (Pa)									51.950			
Pressure Transducer #3 (Pa)									-405.6589			
Pressure Transducer #4 (Pa)									61.82997			
Pressure Transducer #5 (Pa)									82.535			
Shell Drag Force (N)									4.858117			
Propeller Torque, Q (Nm)									5.255027			
Thrust from Propeller Hub, T_{PROP} (N)									62.84006			
Thrust from Pod Unit, T_{POD} (N)									96.16787			
Unit Thrust (Dyno X1) (N)									166.8023			
Shaft Speed									12.25721			
Carriage Speed									2.930424			
Advance Coefficient, J									0.885473			
Thrust Coefficient, $K_{T,PROP}$									0.079			
Thrust Coefficient, $K_{T,POD}$									0.120			
Unit Thrust Coefficient, $K_{T,UNIT}$									0.209			
Propeller Efficiency, η_{PROP}									0.45501			
Propeller Efficiency, η_{POD}									0.696329			
Torque Coefficient (x10), 10 K_Q									0.244			

Table 6.6 - Summary Data for RUN 5

RUN 6 GF 01 Shaft speed 9 rps												
	DATA Files											
	n3_a_gf01.txt		n3_b_gf01.txt		n3_c_gf01.txt		n3_d_gf01.txt		n3_e_gf01.txt		n3_f_gf01.txt	
	n3_g_gf01.txt		n3_h_gf01.txt		n3_i_gf01.txt							
CHANNEL	ADVANCE COEFFICIENT J											
	0.1	0.2	0.3	0.4	0.5	0.6	0.7	0.8	0.9	1	1.1	1.2
Pressure Transducer #1 (Pa)			1511.361	1054.990	8798.942	0.000	0	0.000	0.000	0.000	0.000	0.000
Pressure Transducer #2 (Pa)			36.220	30.962	35.040	55.293	52.65401	42.851	42.164	40.629	33.531	19.901
Pressure Transducer #3 (Pa)			825.938	764.200	260.375	-284.054	-295.736	181.023	-155.9833	-333.130	-36.787	-316.312
Pressure Transducer #4 (Pa)			44.729	34.700	56.549	61.343	-108.690	47.843	42.95456	42.993	37.195	38.968
Pressure Transducer #5 (Pa)			25.815	28.600	50.823	65.270	63.90255	48.675	64.357	57.670	57.828	50.640
Shell Drag Force (N)			3.437745	2.722977	2.380317	10.04801	2.679403	2.310862	0.953342	0.877893	0.926767	0.59692
Propeller Torque, Q (Nm)			6.80926	6.230645	5.661725	5.031	4.3894	3.65919	2.960	2.178	1.305794	0.269047
Thrust from Propeller Hub, T_{PROP} (N)			142.6195	123.3796	106.5763	78.20501	58.5291	42.34192	32.84778	22.19825	8.275336	-8.378872
Thrust from Pod Unit, T_{POD} (N)			163.152	143.857	126.878	106.274	88.49627	70.825	49.968	33.418	10.252	-8.811
Unit Thrust (Dyno X1) (N)			361.5458	319.3187	275.5122	236.1492	179.8305	127.9841	76.36233	23.43463	-36.69295	-103.6655
Shaft Speed			9.145372	9.153604	9.160354	9.163	9.168563	9.176027	9.182	9.190	9.196551	9.204033
Carriage Speed			0.725	0.974	1.219	1.466	1.710544	1.953	2.199	2.441	2.688	2.936105
Advance Coefficient, J			0.293676	0.394133	0.492663	0.592558	0.690986	0.7884	0.886951	0.98375	1.082512	1.181489
Thrust Coefficient, $K_{T,PROP}$			0.321	0.277	0.239	0.175	0.131	0.095	0.073	0.049	0.018	-0.019
Thrust Coefficient, $K_{T,POD}$			0.367	0.323	0.285	0.238	0.198	0.158	0.112	0.074	0.023	-0.020
Unit Thrust Coefficient, $K_{T,UNIT}$			0.716	0.632	0.544	0.466	0.355	0.252	0.150	0.046	-0.072	-0.203
Propeller Efficiency, η_{PROP}			0.264321	0.33538	0.398516	0.395823	0.395932	0.392027	0.422945	0.430876	0.2948	-1.581142
Propeller Efficiency, η_{POD}			0.302374	0.391043	0.47443	0.537891	0.59865	0.655739	0.64339	0.648656	0.365219	-1.662776
Torque Coefficient (x10), 10 K_Q			0.567	0.518	0.470	0.418	0.364	0.303	0.245	0.180	0.108	0.022

Table 6.7 - Summary Data for RUN 6

RUN 7 GF 01 Shaft speed 12 rps

DATA Files

n4_a_gf01.txt n4_b_gf01.txt n4_c_gf01.txt

CHANNEL	ADVANCE COEFFICIENT J											
	0.1	0.2	0.3	0.4	0.5	0.6	**0.7**	**0.8**	**0.9**	1	1.1	1.2
Pressure Transducer #1 (Pa)							-911.979	300.496	165.150			
Pressure Transducer #2 (Pa)							-265.6037	23.322	30.586			
Pressure Transducer #3 (Pa)							-282.418	302.218	85.59764			
Pressure Transducer #4 (Pa)							-904.116	2.566	6.593985			
Pressure Transducer #5 (Pa)							656.2074	92.113	71.040			
Shell Drag Force (N)							3.586717	2.287984	3.412923			
Propeller Torque, Q (Nm)							7.721919	6.468721	5.345426			
Thrust from Propeller Hub, T_{PROP} (N)							141.0035	104.2052	70.41484			
Thrust from Pod Unit, T_{POD} (N)							162.4435	127.8835	95.12724			
Unit Thrust (Dyno X1) (N)							327.3807	232.5065	167.597			
Shaft Speed							12.22239	12.23409	12.25115			
Carriage Speed							2.278821	2.606274	2.929			
Advance Coefficient, J							0.690543	0.789014	0.885344			
Thrust Coefficient, $K_{T,PROP}$							0.178	0.131	0.088			
Thrust Coefficient, $K_{T,POD}$							0.205	0.161	0.119			
Unit Thrust Coefficient, $K_{T,UNIT}$							0.412	0.292	0.210			
Propeller Efficiency, η_{PROP}							0.541851	0.546186	0.501162			
Propeller Efficiency, η_{POD}							0.62424	0.670294	0.677047			
Torque Coefficient (x10), 10 K_Q							0.360	0.301	0.248			

Table 6.8 - Summary Data for RUN 7

RUN 8 GF 16 Shaft speed 9 rps

DATA Files

n3_a_gf16.txt	n3_b_gf16.txt	n3_c_gf16_b.txt	n3_d_gf16.txt	n3_e_gf16.txt	n3_f_gf16.txt
n3_g_gf16.txt	n3_h_gf16.txt	n3_i_gf16.txt			

CHANNEL	ADVANCE COEFFICIENT J											
	0.1	0.2	0.3	0.4	0.5	0.6	0.7	0.8	0.9	1	1.1	1.2
Pressure Transducer #1 (Pa)				40112.865	-24516.553	0.000	40271.9	38851.640	45580.860	-7183.132	756.006	4242.410
Pressure Transducer #2 (Pa)				590.377	17407.305	107.397	145.6575	565.464	699.888	61.847	30.034	76.672
Pressure Transducer #3 (Pa)				9844.955	14776.257	170.036	-7593.242	14383.803	12540.35	1635.304	-1141.683	-1288.567
Pressure Transducer #4 (Pa)				1795.437	10182.404	93.101	242.901	1677.137	2018.892	-62.934	38.752	107.501
Pressure Transducer #5 (Pa)				-992.183	15481.344	137.897	25.116	-953.297	-1175.096	117.103	33.211	-0.477
Shell Drag Force (N)				11.85671	11.51515073	11.01328	10.79412	10.88057	10.8389	11.10244	11.41747	11.16881
Propeller Torque, Q (Nm)				6.148178	5.611985852	5.061998	4.361315	3.545763	2.86184	2.187224	1.306951	0.28477
Thrust from Propeller Hub, T_{PROP} (N)				124.2172	108.2626373	88.18189	67.23434	48.83072	35.1555	23.50367	5.010502	-11.53011
Thrust from Pod Unit, T_{POD} (N)				145.7747	129.7116987	109.595	90.96907	70.7553	53.376	33.592	9.886271	-13.53526
Unit Thrust (Dyno X1) (N)				324.7011	281.1285861	231.8464	182.0824	130.5829	78.72165	29.87345	-34.28393	-96.46366
Shaft Speed				9.150002	9.153888361	9.167522	9.175192	8.547475	9.180118	9.187338	9.19286	9.198213
Carriage Speed				0.976	1.217	1.464	1.70941	1.953	2.198	2.442	2.686	2.932
Advance Coefficient, J				0.394921	0.49254039	0.591273	0.690029	0.846339	0.886665	0.984284	1.082266	1.180436
Thrust Coefficient, $K_{T,PROP}$				0.279	0.243	0.197	0.150	0.126	0.078	0.052	0.011	-0.026
Thrust Coefficient, $K_{T,POD}$				0.328	0.291	0.245	0.203	0.182	0.119	0.075	0.022	-0.030
Unit Thrust Coefficient, $K_{T,UNIT}$				0.730	0.631	0.457	0.358	0.296	0.155	0.067	-0.076	-0.215
Propeller Efficiency, η_{PROP}				0.34287	0.408308243	0.442619	0.457115	0.500855	0.46805	0.454514	0.178295	-2.053838
Propeller Efficiency, η_{POD}				0.402374	0.489202528	0.550099	0.618483	0.725735	0.710636	0.649605	0.351796	-2.411012
Torque Coefficient (x10), 10 K_Q				0.512	0.467	0.420	0.361	0.338	0.237	0.181	0.108	0.023

Table 6.9 - Summary Data for RUN 8

RUN 9 GF 16 Shaft speed 12 rps

DATA Files

n4_a_gf16.txt n4_b_gf16.txt n4_c_gf16.txt

CHANNEL	ADVANCE COEFFICIENT J											
	0.1	0.2	0.3	0.4	0.5	0.6	**0.7**	**0.8**	**0.9**	**1**	**1.1**	**1.2**
Pressure Transducer #1 (Pa)							2580.912	49272.314	3557.742			
Pressure Transducer #2 (Pa)							53.74593	657.524	76.016			
Pressure Transducer #3 (Pa)							-922.198	5909.465	-2830.258			
Pressure Transducer #4 (Pa)							61.184	1969.815	88.9191			
Pressure Transducer #5 (Pa)							37.96259	-1052.901	39.921			
Shell Drag Force (N)							19.39987	18.8959	19.0248			
Propeller Torque, Q (Nm)							7.750442	6.438122	5.358785			
Thrust from Propeller Hub, T_{PROP} (N)							133.7389	99.09041	64.62675			
Thrust from Pod Unit, T_{POD} (N)							166.527	131.9506	98.47856			
Unit Thrust (Dyno X1) (N)							349.3253	238.6653	157.3982			
Shaft Speed							12.22612	12.23229	12.24706			
Carriage Speed							2.275234	2.603841	2.927			
Advance Coefficient, J							0.689245	0.788393	0.885248			
Thrust Coefficient, $K_{T,PROP}$							0.168	0.125	0.081			
Thrust Coefficient, $K_{T,POD}$							0.210	0.166	0.124			
Unit Thrust Coefficient, $K_{T,UNIT}$							0.440	0.300	0.197			
Propeller Efficiency, η_{PROP}							0.51108	0.521434	0.45877			
Propeller Efficiency, η_{POD}							0.636379	0.694351	0.699076			
Torque Coefficient (x10), 10 K_Q							0.361	0.300	0.249			

Table 6.10 - Summary Data for RUN 9

RUN 10 GF 21 Shaft speed 9 rps

DATA Files

n3_a_gf21.txt	n3_b_gf21.txt	n3_c_gf21.txt	n3_d_gf21.txt
n3_e_gf21.txt	n3_f_gf21.txt	*n3_g_gf21.txt	n3_h_gf21.txt

* NOT USED

CHANNEL	ADVANCE COEFFICIENT J											
	0.1	0.2	0.3	0.4	**0.5**	**0.6**	**0.7**	**0.8**	**0.9**	**1**	**1.1**	1.2
Pressure Transducer #1 (Pa)					44704.908	45279.472	45793.14	44211.103	43875.606	44008.304	36943.439	
Pressure Transducer #2 (Pa)					515.182	501.428	592.348	583.475	543.040	535.319	553.376	
Pressure Transducer #3 (Pa)					4834.422	5058.372	8373.547	6652.801	6627.898	-1112.999	10200.439	
Pressure Transducer #4 (Pa)					1667.119	1480.524	1741.611	1906.335	1735.216	1757.921	1771.597	
Pressure Transducer #5 (Pa)					-873.148	-823.294	-1008.143	-1004.238	-901.026	93.120	-922.047	
Shell Drag Force (N)					11.86901	11.44661	11.45048	11.49351	11.56753	11.54899	11.952	
Propeller Torque, Q (Nm)					5.649334	4.950492	4.317637	3.631895	2.878449	2.053494	1.205862	
Thrust from Propeller Hub, T_{PROP} (N)					102.8871	87.03446	66.22537	50.9112	34.04307	25.40074	3.960924	
Thrust from Pod Unit, T_{POD} (N)					127.2212	108.0639	90.36293	71.79925	51.09979	30.962	8.849804	
Unit Thrust (Dyno X1) (N)					281.8251	231.8406	183.8457	134.4801	79.5822	26.49798	-34.49846	
Shaft Speed					9.154517	9.160489	9.168254	9.170906	9.180269	9.18836	9.193133	
Carriage Speed					1.218	1.464	1.707311	1.950812	2.196005	2.441	2.686	
Advance Coefficient, J					0.492589	0.591768	0.689703	0.787842	0.88596	0.983893	1.081985	
Thrust Coefficient, $K_{T,PROP}$					0.231	0.195	0.148	0.114	0.076	0.057	0.009	
Thrust Coefficient, $K_{T,POD}$					0.286	0.242	0.202	0.161	0.114	0.069	0.020	
Unit Thrust Coefficient, $K_{T,UNIT}$					0.633	0.520	0.412	0.301	0.178	0.059	-0.077	
Propeller Efficiency, η_{PROP}					0.385507	0.447073	0.454595	0.474574	0.450266	0.52298	0.152723	
Propeller Efficiency, η_{POD}					0.476685	0.555096	0.620284	0.669284	0.675864	0.637491	0.341226	
Torque Coefficient (x10), 10 K_Q					0.470	0.411	0.358	0.301	0.238	0.170	0.099	

Table 6.11 - Summary Data for RUN 10

RUN 11 GF 21 Shaft speed 12 rps

DATA Files

n4_a_gf21.txt n4_b_gf21.txt n4_c_gf21.txt

CHANNEL	ADVANCE COEFFICIENT J											
	0.1	0.2	0.3	0.4	0.5	0.6	**0.7**	**0.8**	**0.9**	1	1.1	1.2
Pressure Transducer #1 (Pa)							47283.4	0.000	39166.982			
Pressure Transducer #2 (Pa)							591.0507	437.176	450.118			
Pressure Transducer #3 (Pa)							5164.035	16391.771	475.2962			
Pressure Transducer #4 (Pa)							1869.623	1093.841	1462.344			
Pressure Transducer #5 (Pa)							-958.5289	-387.215	-732.458			
Shell Drag Force (N)							20.48512	19.95531	19.86487			
Propeller Torque, Q (Nm)							7.628622	6.468937	5.293474			
Thrust from Propeller Hub, T_{PROP} (N)							140.4581	102.1413	65.60551			
Thrust from Pod Unit, T_{POD} (N)							162.6538	128.7172	95.72889			
Unit Thrust (Dyno X1) (N)							327.7577	238.8211	149.896			
Shaft Speed							12.22217	12.23463	12.24778			
Carriage Speed							2.278424	2.602764	2.930791			
Advance Coefficient, J							0.690434	0.787916	0.886265			
Thrust Coefficient, $K_{T,PROP}$							0.177	0.128	0.082			
Thrust Coefficient, $K_{T,POD}$							0.205	0.162	0.120			
Unit Thrust Coefficient, $K_{T,UNIT}$							0.413	0.300	0.188			
Propeller Efficiency, η_{PROP}							0.54627	0.534605	0.472006			
Propeller Efficiency, η_{POD}							0.632594	0.673702	0.688732			
Torque Coefficient (x10), 10 K_Q							0.356	0.301	0.246			

Table 6.12 - Summary Data for RUN 11

6.4.1 Tables & Plots from Summary Data

Tables 6.13 to 6.17 are from the summary data tables in the previous section. The values from the runs with the highest shaft speed (n=12 rps) were used as this decreases the percentage magnitude of mechanical effects. Only the J-values common to all runs were used. One can see that the results in these tables represent repeats, as the only parameter that changes is the gap setting. Any effect of changing the gap is not likely to be discernable for these tests that are essentially a break-in trial for the experimentation.

Table 6.13 compares the torque coefficient ($10K_Q$) for 4 gap settings. Table 6.14 compares the thrust coefficient (K_T) from the thrust as measured in the pod instrumentation. Table 6.15 compares K_T from the thrust as measured in the hub instrumentation.

Comparison of 10KQ for Shaft Speed = 12 rps				
RUN	GF	10KQ (at J=0.7)	10KQ (at J=0.8)	10KQ (at J=0.9)
7	1	0.36024	0.30120	0.24820
5	6	n/a	n/a	0.24377
9	16	0.36135	0.29986	0.24899
11	21	0.35590	0.30118	0.24593

Table 6.13 – Comparison or 10KQ for shaft speed = 12 rps and J=0.7, 0.8 and 0.9.

Comparison of KT_{POD} for Shaft Speed = 12 rps				
RUN	GF	KT_{POD} (at J=0.7)	KT_{POD} (at J=0.8)	KT_{POD} (at J=0.9)
7	1	0.20461	0.16077	0.11926
5	6	n/a	n/a	0.12045
9	16	0.20963	0.16594	0.12354
11	21	0.20489	0.16181	0.12008

Table 6.14 – Comparison of KT_{POD} for shaft speed = 12 rps and J=0.7, 0.8 and 0.9.

Comparison of KT_{PROP} for Shaft Speed = 12 rps				
RUN	GF	KT_{PROP} (at J=0.7)	KT_{PROP} (at J=0.8)	KT_{PROP} (at J=0.9)
7	1	0.17761	0.13101	0.08828
5	6	n/a	n/a	0.07870
9	16	0.16835	0.12461	0.08108
11	21	0.17693	0.12840	0.08229

Table 6.15 – Comparison of KT_{PROP} for shaft speed = 12 rps and J=0.7, 0.8 and 0.9.

Tables 6.16 and 6.17 compare the propeller efficiency, derived from the thrust in the pod unit and propeller hub respectively.

Comparison of η_{POD} for Shaft Speed = 12 rps				
RUN	GF	η_{POD} (at J=0.7)	η_{POD} (at J=0.8)	η_{POD} (at J=0.9)
7	1	0.62424	0.67029	0.67705
5	6	n/a	n/a	0.69633
9	16	0.63638	0.69435	0.69908
11	21	0.63259	0.67370	0.68873

Table 6.16 – Comparison of η_{POD} for shaft speed = 12 rps and J=0.7, 0.8 and 0.9.

Comparison of η_{PROP} for Shaft Speed = 12 rps				
RUN	GF	η_{PROP} (at J=0.7)	η_{PROP} (at J=0.8)	η_{PROP} (at J=0.9)
7	1	0.54185	0.54619	0.50116
5	6	n/a	n/a	0.45501
9	16	0.51108	0.52143	0.45877
11	21	0.54627	0.53460	0.47201

Table 6.17 – Comparison of η_{PROP} for shaft speed = 12 rps and J=0.7, 0.8 and 0.9.

Table 6.18 displays the various performance coefficients for RUN 1. A plot of the data is presented in Figure 6.24 below.

J	10KQ	KTPROP	KTPOD	η_{PROP}	η_{POD}
0.099	0.665	0.358	0.475	0.08495	0.112585
0.190725	0.621	0.354	0.441	0.173229	0.215524
0.293381	0.585	0.329	0.398	0.262445	0.318151
0.392434	0.542	0.312	0.355	0.359532	0.409188
0.491349	0.493	0.285	0.314	0.451879	0.498331
0.588318	0.446	0.257	0.267	0.539573	0.560471
0.687374	0.373	0.225	0.183	0.661189	0.536322
0.786067	0.315	0.187	0.136	0.741023	0.54134
0.885094	0.271	0.148	0.089	0.768207	0.465307
0.983704	0.187	-0.124	0.011	-1.03796	0.091579
1.083681	0.127	-0.163	-0.038	-2.21926	-0.523057
1.180403	0.044	-0.109	-0.054	-4.64958	-2.30914

Table 6.18 – Performance coefficients for RUN 1, GF=11, n=3.5 rps.

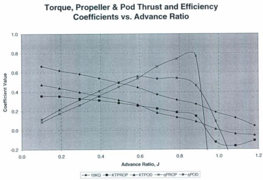

Figure 6.24 – Performance coefficients vs. J for RUN 1, GF=11, n=3.5rps.

Table 6.19 displays the various performance coefficients for RUN 2. A plot of the data is presented in Figure 6.25 below.

J	10KQ	KTPROP	KTPOD	η_{PROP}	η_{POD}
0.096	0.652	0.318	0.435	0.074348	0.101693
0.195631	0.611	0.292	0.401	0.148646	0.204403
0.294855	0.565	0.259	0.365	0.214801	0.303165
0.394368	0.521	0.220	0.328	0.26467	0.395394
0.491863	0.473	0.186	0.290	0.30826	0.479385
0.593666	0.420	0.141	0.257	0.317337	0.577158
0.689007	0.359	0.119	0.210	0.364407	0.642518
0.787904	0.306	0.097	0.180	0.397817	0.737155
0.887786	0.247	0.068	0.134	0.389961	0.766305
0.984974	0.176	0.030	0.081	0.269858	0.724531
1.082395	0.110	0.022	0.026	0.345355	0.404136
1.178289	0.031	-0.023	-0.032	-1.426145	-1.978612

Table 6.19 – Performance coefficients for RUN 2, GF=11, n=7 rps.

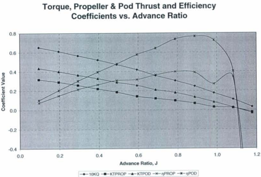

Figure 6.25 – Performance coefficients vs. J for RUN 2, GF=11, n=7 rps.

Table 6.20 displays the various performance coefficients for RUN 3. A plot of the data is presented in Figure 6.26 below.

J	10KQ	KTPROP	KTPOD	η_{PROP}	η_{POD}
0.101	0.657	0.326	0.439	0.079401	0.106987
0.200531	0.611	0.299	0.398	0.15607	0.208041
0.296575	0.569	0.270	0.358	0.223725	0.29694
0.393922	0.524	0.238	0.318	0.2842	0.380305
0.492839	0.478	0.178	0.290	0.292389	0.47647
0.592525	0.418	0.096	0.248	0.21586	0.558694
0.691085	0.362	0.099	0.198	0.299905	0.601092
0.789592	0.309	0.084	0.165	0.341663	0.670617
0.887029	0.250	0.039	0.110	0.220751	0.622841
0.98481	0.189	0.035	0.070	0.291961	0.578538
1.082885	0.112	-0.009	0.027	-0.136941	0.408894
1.180903	0.030	-0.039	-0.041	-2.441367	-2.567046

Table 6.20 – Performance coefficients for RUN 3, GF=11, n=9 rps.

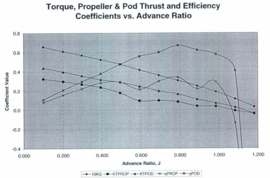

Figure 6.26 – Performance coefficients vs. J for RUN 3, GF=11, n=9 rps.

Table 6.21 displays the various performance coefficients for RUN 4. A plot of the data is presented in Figure 6.27 below.

J	10KQ	KTPROP	KTPOD	η_{PROP}	η_{POD}
0.000	0.000	0.000	0.000	0	0
0.194949	0.614	0.292	0.403	0.147337	0.2034255
0.29332	0.566	0.248	0.360	0.204129	0.2972484
0.393724	0.520	0.201	0.322	0.242204	0.3877018
0.492109	0.472	0.166	0.282	0.275348	0.4677336
0.590569	0.425	0.156	0.252	0.345899	0.5581044
0.688514	0.369	0.118	0.196	0.351836	0.5820692
0.786474	0.309	0.070	0.173	0.282863	0.7024823
0.88493	0.248	0.028	0.124	0.159828	0.7066673
0.98303	0.183	0.004	0.081	0.037893	0.6917747
1.081135	0.109	-0.009	0.032	-0.144377	0.5016074
1.17819	0.024	-0.043	-0.034	-3.36962	-2.659168

Table 6.21 – Performance coefficients for RUN 4, GF=06, n=9 rps.

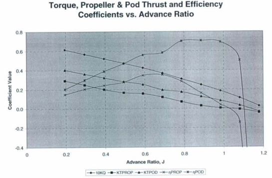

Figure 6.27 – Performance coefficients vs. J for RUN 4, GF=06, n=9 rps.

Table 6.22 displays the various performance coefficients for RUN 6. A plot of the data is presented in Figure 6.28 below.

J	10KQ	KTPROP	KTPOD	η_{PROP}	η_{POD}
0.000	0.000	0.000	0.000	0	0
0	0.000	0.000	0.000	0	0
0.293676	0.567	0.321	0.367	0.264321	0.302374
0.394133	0.518	0.277	0.323	0.33538	0.391043
0.492663	0.470	0.239	0.285	0.398516	0.47443
0.592558	0.418	0.175	0.238	0.395823	0.537891
0.690986	0.364	0.131	0.198	0.395932	0.59865
0.7884	0.303	0.095	0.158	0.392027	0.655739
0.886951	0.245	0.073	0.112	0.422945	0.64339
0.98375	0.180	0.049	0.074	0.430876	0.648656
1.082512	0.108	0.018	0.023	0.2948	0.365219
1.181489	0.022	-0.019	-0.020	-1.581142	-1.662776

Table 6.22 – Performance coefficients for RUN 6, GF=01, n=9 rps.

Torque, Propeller & Pod Thrust and Efficiency Coefficients vs. Advance Ratio

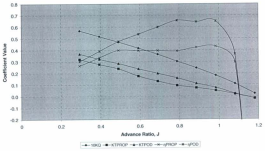

Figure 6.28 – Performance coefficients vs. J for RUN 6, GF=01, n=9 rps.

Table 6.23 displays the various performance coefficients for RUN 8. A plot of the data is presented in Figure 6.29 below.

J	10KQ	KTPROP	KTPOD	η_{PROP}	η_{POD}
0.000	0.000	0.000	0.000	0	0
0	0.000	0.000	0.000	0	0
0	0.000	0.000	0.000	0	0
0.394921	0.512	0.279	0.328	0.34287	0.402374
0.49254	0.467	0.243	0.291	0.408308	0.489203
0.591273	0.420	0.197	0.245	0.442619	0.550099
0.690029	0.361	0.150	0.203	0.457115	0.618483
0.846339	0.338	0.126	0.182	0.500855	0.725735
0.886665	0.237	0.078	0.119	0.46805	0.710636
0.984284	0.181	0.052	0.075	0.454514	0.649605
1.082266	0.108	0.011	0.022	0.178295	0.351796
1.180436	0.023	-0.026	-0.030	-2.053838	-2.411012

Table 6.23 – Performance coefficients for RUN 8, GF=16, n=9 rps.

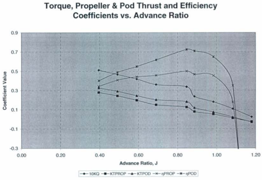

Figure 6.29 – Performance coefficients vs. J for RUN 8, GF=16, n=9 rps.

Table 6.24 displays the various performance coefficients for RUN 10. A plot of the data is presented in Figure 6.30 below.

J	10KQ	KTPROP	KTPOD	η_{PROP}	η_{POD}
0.000	0.000	0.000	0.000	0	0
0	0.000	0.000	0.000	0	0
0	0.000	0.000	0.000	0	0
0	0.000	0.000	0.000	0	0
0.492589	0.470	0.231	0.286	0.385507	0.476685
0.591768	0.411	0.195	0.242	0.447073	0.555096
0.689703	0.358	0.148	0.202	0.454595	0.620284
0.787842	0.301	0.114	0.161	0.474574	0.669284
0.88596	0.238	0.076	0.114	0.450266	0.675864
0.983893	0.170	0.057	0.069	0.52298	0.637491
1.081985	0.099	0.009	0.020	0.152723	0.341226
0	0.000	0.000	0.000	0	0

Table 6.22 – Performance coefficients for RUN 10, GF=21, n=9 rps.

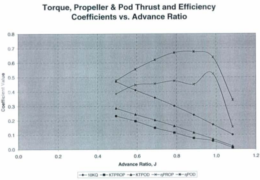

Figure 6.30 – Performance coefficients vs. J for RUN 10, GF=21, n=9 rps.

This now end the results section. Conclusions and recommendations for future work are stated in the next chapter.

CHAPTER 7 – CONCLUSIONS & RECOMMENDATIONS FOR FUTURE WORK

INTRODUCTION

This section outlines some conclusions and recommendations for future work.

7.1 Conclusions & Recommendations on Equipment Function

Overall, the equipment did produce results that were in keeping with similar type tests. Propeller opens testing is routinely carried out to produce characteristic curves such as those displayed in chapter 6. The propeller torque and pod thrust yielded results typical of such tests. The more novel instrumentation setups such as gap pressure, shell drag and propeller hub thrust yielded results that indicate more investigation and development are required to fine tune any measurements. The gap distance setting mechanism and ability to change the outer shell geometry worked as intended.

The wave shroud assembly was most likely not working as intended, and seems to have interfered with the functioning of the unit dynamometer. It was recommended by the author after the commissioning tests that a new wave shroud design be implemented. This was carried out by others using the equipment in subsequent testing.

The belt drive system was successful, despite some limitations during the initial testing. After the initial tests, the author carried out a survey of the alignment surfaces of the gearbox mounts and determined that these caused the belt problems. It was fixed and alignment issues with the belt solved. Some time after, for another set of tests, the drive case was redesigned to lower the bending stress of the belt as it passed over the lower pinch rollers. The entrance and exit angles were reduced and the roller diameter was increased. These changes increased the belt life.

Other general conclusions are listed below:

1. The pressure transducers should be moved out of the pressure sensing plate and farther up the strut, connected by stainless steel refrigeration system grade tubing with silver soldered joints. Alternatively, the pressure sensor setup may benefit from the selection of a type that doesn't require an atmospheric vent at all.

2. The use of an off-the-shelf load cell may not have been the best choice for the hub instrumentation. It was good for the thrust measurement in the pod assembly, but caused much grief during the design phase. Had a strain gauged element been used, water proofing would have been as relatively simple as with the torque. In general, the task of fitting a sensor and isolating the required forces, while applying torque to the assembly, with the additional problem of supplying power and obtaining a voltage signal was very difficult to accomplish. Keeping water out of this assembly added another level of complexity. Designing the hub assembly as a single block with strain gauged sections might be considered for the future.

3. Although given a great deal of attention during the design phase, wiring considerations in future designs must be given even more attention. It might be possible to use EDM processes to minimize impact on the design if the tooling required to produce a part is not such a consideration, especially in the propeller shaft.

4. The instrumentation must be run-in to allow all mechanical settling to occur.

7.2 Conclusions & Recommendations on Calibrations

An accurate calibration procedure is necessary to obtain useful data from any experiment. Some conclusions on these tests include the following:

1. In the future, in-situ calibrations might be carried out after all subassemblies have been calibrated. This will involve the design and fabrication of extra jigs and frames to provide the correct loading to the test apparatus.
2. Dynamic calibrations might also be considered.
3. A full and accurate calibration of the unit dynamometer will allow the pod thrusts and torque to be cross checked, in addition to allowing an understanding of the shell drag response and functionality.

7.3 Conclusions & Recommendations on Data Collection & Processing

One main conclusion the author makes on data collection and processing is that it is essential to derive an automated method of processing collected data from experiments. This will make it possible to display some diagnostic plots of the test just conducted as a way of gauging whether or not there are any problems. A specific example of this is in the response time of the hub thrust signals. A possible and probable reason for this is the fact that the space between the end of the propeller hub and the hub taper angle adapter was filled with excess grease. During assembly the author proceeded on the side of caution and decided not to remove the excess grease from this space. The effect of this was not discovered until after the experiments had been clued up. It is recommended that LabView™ or a similar software package be used in future work utilizing a test package of this complexity and number of data channels.

Two other general recommendations are:

1. Consider using one data channel to sample the excitation voltages. Monitoring the excitation voltage will help in determining whether voltage drift is due to changing excitation voltages or other reason.

2. One might also consider running pressure transducers, or indeed the entire set of instrumentation on batteries to minimize electrical noise.

CLOSING REMARKS

The design of an experimental apparatus to carry out new research is time consuming and requires the help of a great number of skilled persons to accomplish. The author was fortunate to have been involved in such a project and to have worked with a talented group of people capable of carrying it out. The projects goals as set forth in section 1.3 were mainly met over the course of this thesis work and the testing that was carried out by others using the instrumentation in subsequent research.

REFERENCES

[1] Dynamic Positioning Committee, Dynamic Positioning Conference, Matilla, M., Ylitalo (ABB Finland) & Soles, J. (GlobalSantaFe), [September 17-18, 2002], *SEMISUBMERSIBLE RIG "The Reliable Solution with Minimal Thrust Losses"*

[2] [Online], URL http://evolution.skf.com/zino.aspx?pageID=27&articleID=589&image=2 (1 of 5)

[3] [Online],URL http://evolution.skf.com/zino.aspx?pageID=27&articleID=589&image=2 (3 of 5)

[4] [Online], URL http://evolution.skf.com/zino.aspx?pageID=27&articleID=589&image=2 (2 of 5)

[5] [Online],URL http://www.rollsroyce.com/products/propulsion/electrical_pod/default.jsp

[6] Macneill, Andrew, [April 14-16, 2004], *Personal notes #1 written during the course of TPOD, The First Internation Conference on Technological Advances in Podded Propulsion, University of Newcastle, UK.*

[7] Macneill, Andrew, [April 14-16, 2004], *Personal notes #2 written during the course of TPOD, The First Internation Conference on Technological Advances in Podded Propulsion, University of Newcastle, UK.*

[8] Macneill, Andrew, [April 14-16, 2004], *Personal notes #3 written during the course of TPOD, The First Internation Conference on Technological Advances in Podded Propulsion, University of Newcastle, UK.*

[9] Macneill, Andrew, [April 14-16, 2004], *Personal notes #4 written during the course of TPOD, The First Internation Conference on Technological Advances in Podded Propulsion, University of Newcastle, UK.*

[10] Ship Propulsion and Railway Traction Systems Conference, Feudale, F., Bordignon, P., Ferrero, C., and Castangia, P., [October 4-6, 2005], *ASIROBICON: TRADITION AND INNOVATION IN SHIP ELECTRICAL COMPONENTS AND SYSTEMS*, pp. 17-22.

[11] VAISALA News 160/2002, "On-line Measurement of Oil Gives Up-to-date Information for Operators", Issue 160, September 17, 2002, pp. 14-16.

[12] Jessup, S. Bose, N., Dugué, C., Esposito, P.G., Holtrop, J., Lee, J.T., Mewis, F., Pustoshny, A., Salvatore, F., Shirose, Y. 2002. *Report of the propulsion committee. 23rd International Towing Tank Conference*.

[13] ITTC - Recommended Procedures: Propulsion, Performance; *Podded Propulsor Tests and Extrapolation*. (7.5-02-03-01.3), 2002.

[14] Personal communications with Dr. B. Veitch, 2002.

[15] Personal communications with Dr. N. Bose, 2002.

[16] Personal conversation with Mr. F. Mewis, April 2002.

[17] Personal conversation with Mr. J. Holtrop, April 2002.

[18] Macneill, Andrew,et al, "DESIGN OF A MODEL POD TEST UNIT", *TPOD, The First Internation Conference on Technological Advances in Podded Propulsion, University of Newcastle, UK.*, April 14-16, 2004.

[19] Personal communication with Thordon bearings Ltd., 2003.

[20] Personal conversations with Mr. Howard Mesh, IOT, 2004.

BIBLIOGRAPHY

White, Frank M., "Fluid Mechanics"] University of Rhode Island McGraw-Hill Publishing Company 1986, pp. 26,271-276, 291-293.

Appendix A – Factory Load Cell Specifications

The first set of specifications is for the propeller hub thrust and pod thrust respectively (#2199 and #2198).

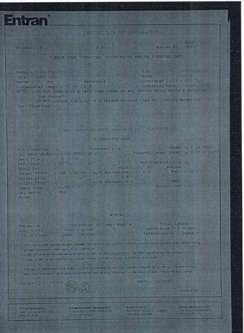

Entran

CERTIFICATE OF CALIBRATION

42617

Property of : P.O. : Entran PO :

PLEASE READ OPERATING INSTRUCTIONS BEFORE POWERING UNIT

Model : S/N :
Type : LOAD CELL Mode :
Range : Reference : Overrange limit :
Compensated temp. : Operating temp. :
NOTE : DO NOT load with a ball type press or any device which makes a point or line contact.
DO NOT torque the body of a thread mounted load cell during mounting.
Specifications :

Other characteristics according to :

CALIBRATION DATA

Non-linearity : Hysteresis : CNLAH :
Th. zero shift : Thermal Sens. Shift :
Zero (typ.) :
Ref. Temp. : Non-repeatability :
Shunt Cal : with : across :
Output "FSO" : with Excitation : Max. :
Tested with : S/N :
Output "FSO" : with Excitation : Max. :
Input ohms : Output ohms :
Cal Equip. : M66
Notes :

WIRING

Connector : Transducer to Comp. Module : Total length :
+In. : red +Out. : green Common mode : V output
-In. : black -Out. : white referenced to - Input -

Date :

Propeller hub thrust load cell specifications.

Entran®

CERTIFICATE OF CALIBRATION

42617

Property of : P.O. : Entran PO : 26938

PLEASE READ OPERATING INSTRUCTIONS BEFORE POWERING UNIT

Model : ELHS-T1E-200L S/N : Y02192
Type : LOAD CELL *Mode : T/C
*Range : 200 lbs Reference : Overrange limit : 300 lbs
Compensated temp. : 70 to 170°F Operating temp. : 0 to 170°F
NOTE : DO NOT load with a ball type press or any device which makes a point or line contact.
DO NOT torque the body of a thread mounted load cell during mounting.
Specifications :

Other characteristics according to : ELHSSDS10-PC

CALIBRATION DATA

*Non-linearity : ± *Hysteresis : ± *CNL&H : ± 0.50 %FSO
*Th. zero shift : ± 1.00 %FSO/100°F *Thermal Sens. Shift : ± 2.50 %/100°F
*Zero (typ.) : ± 10 mV
Ref. Temp. : 22 °C (72°F) *Non-repeatability : ±
Shunt Cal : with : KΩ across :
Output "FSO" : 194.0 mV/FS with Excitation : 15.0 V Max. : 18.0 V
Tested with : S/N :
Output "FSO" : with Excitation : Max. :
Input ohms : 1566 Ω Output ohms : 544 Ω
Cal Equip : M66
Notes :

WIRING

Connector : Transducer to Comp. Module : Total length :
+In. : red +Out. : green Common mode : V output
-In. : black -Out. : white referenced to - Input =

*The calibrated values do not exceed the data sheet specifications, value shown is the data sheet value unless purchase order specifies otherwise.
*Load cells must be loaded with load on center and parallel to the flat surface of the device.
*Value given by manufacturing design unless purchase order specifies otherwise.

The above instrument has been calibrated against a working standard which is directly traceable to a National Standard. All data interpreted per Entran Instruction Manuals unless otherwise indicated.

Control : S. COSTE Date : 12/06/02

ENT QC3

8 Q.C.

DOQ3179_US

Entran Devices, Inc. FAIRFIELD, NJ 07004 - USA
Entran European Headquarters F-78340 LES CLAYES-SOUS-BOIS
Entran Limited WATFORD - England
Entran Sensoren GmbH D-6700 LUDWIGSHAFEN

Pod thrust load cell specifications.

This data sheet is for the 50 lb shell drag load cell.

Entran®

CERTIFICATE OF CALIBRATION

Property of : P.O.# Entran FO#: 43057

PLEASE REVIEW OPERATING SPECIFICATIONS BEFORE POWERING UNIT
CAUTION: DO NOT PRESS OR LOAD THE SENSITIVE AREA WITH A SHARP OR POINTED OBJECT

S/N : 03B03A27-Y14

Model	: ELFS-T3E-50L-/M0.166F				
Type	: LOAD CELL			[4] Mode	: COMPRESSION/TEN
[4] Range	: 50 LBS	Reference	: N/A	Do Not Exceed	: 75 LBS
Temperature Range		Compensated	: 70 TO 170°F	Operating	: -40 TO 250°F

NOTE: Exceeding Installation Torque of may damage unit

CALIBRATION DATA

[1] CNL&H	:	[1] Hysteresis	: +/- 1%FSO	[1] Non-linearity	: +/- 1%FSO
[1] Zero	:	Thermal Zero Shift	: +/- 2.5mV/100°F	[2] Thermal Sens Shift	: +/- 2 1/2%/100°F
Ref. Temp	: 75°F			[2] Non-repeatability	:
Shunt Cal	:	with	:	across	:
Sensitivity	: 222.07 mV/FS	with Excitation	: 15 Vdc	Max. Excitation	: 18 Vdc
Tested with	:			S/N	:
Sensitivity	:	[5] with Excitation	:	Max. Excitation	:
[3] Input ohms	: 1490	[3] Output ohms	: 896		
Cal Equip.	: DWT 2729005	DVM 0690077			
Notes	:				

WIRING

Sensor : Total : 5'

+ In : RED + Out: GREEN

- In : BLACK - Out: WHITE

Connector : Mate:

[5] Electronics : Signal In Connector: Mate:

+ Sensor Power: + Signal In:

- Sensor Power: - Signal In:

Amp out Connector: Mate:

+ Supply : + Signal Out: Common:

- Supply : - Signal Out:

Notes :

[1] If calibrated data equals or exceeds data sheet specifications, value shown is the data sheet value unless purchase order specifies actual calibrated value. CNL&H is combined non-linearity and hysteresis. [2] Value given is by manufacturing design and not calibrated unless purchase order specifies actual calibrated value. [3] Input/Output impedance recorded for sensor alone if separate item from electronics. [4] Load cells must be loaded with load on-center and perpendicular to the flat surface of the device. The load must be equally distributed over the load bearing surface. DO NOT load with a ball type press or any device which makes a point of the contact. DO NOT load only one edge or unevenly. DO NOT torque the body of a thread mounted load cell during mounting. [5] For +/- 15V input, DO NOT USE unipolar 30V power supply.

The above instrument has been calibrated against a working standard which is directly traceable to a National Standard. All data interpreted per Entran catalogs and Instruction Manuals unless otherwise indicated.

Entran® by: SH Calibration Date: 2/19/2003 QC : B Q.C.

Fairfield, NJ, USA Garston, Watford Herts, UK Les Clayes-sous-Bois, France

Factory load cell calibration data for **Global Dynamometer load cell 1**

COOPER
INSTRUMENTS & SYSTEMS

P.O. Box 3048 * Warrenton, Virginia 20188 * Phone: (540) 349-4746 * Fax: (540) 347-4755

CERTIFICATE OF CALIBRATION

Transducer Model:	LPM 530		
Serial Number:	951008		
Capacity:	1000	LBS	
Calibration Date:	4/16/2003		
Excitation:	10	VDC	
Calibration Factor:	1.945	MV/V	Tension
Input Resistance:	353	Ohms	
Output Resistance:	353	Ohms	
Temperature Range:	60-160	Degrees F	

An output of 1.490 MV/V is induced when a shunt resistor of 59K ohms is applied across (-) Excitation and (-) Signal.

Special Instructions:

Wiring Code	RED	**(+)Excitation**
	BLACK	**(-) Excitation**
	WHITE	**(+)Signal**
	GREEN	**(-) Signal**

This is to certify that the following instrument was calibrated using loading equipment traceable to NIST through one or more of standards. The unit was found to meet or exceed all published sales literature accuracy specifications.

Date of Shipment: 5/14/2003 Re-Calibration Date: 1 year after Shipment Date

www.cooperinstruments.com * email: sales@cooperinstruments.com

Factory load cell calibration data for **Global Dynamometer load cell 2**

COOPER
INSTRUMENTS & SYSTEMS

CERTIFICATE OF CALIBRATION

Transducer Model:	LPM 530		
Serial Number:	951009		
Capacity:	1000	LBS	
Calibration Date:	4/16/2003		
Excitation:	10	VDC	
Calibration Factor:	1.945	MV/V	Tension
Input Resistance:	353	Ohms	
Output Resistance:	353	Ohms	
Temperature Range:	60-160	Degrees F	

An output of 1.489 MV/V is induced when
a shunt resistor of 59K ohms is applied across (-) Excitation and (-) Signal.

Special Instructions:

Wiring Code	RED	**(+)Excitation**
	BLACK	**(-) Excitation**
	WHITE	**(+)Signal**
	GREEN	**(-) Signal**

This is to certify that the following instrument was calibrated using loading equipment traceable to NIST through one or more of standards. The unit was found to meet or exceed all published sales literature accuracy specifications.

Date of Shipment: 5/14/2003 Re-Calibration Date: 1 year after Shipment Date

www.cooperinstruments.com • email: sales@cooperinstruments.com

P.O. Box 3048 • Warrenton, Virginia 20188 • Phone: (540) 349-4746 • Fax: (540) 347-4755

Factory load cell calibration data for **Global Dynamometer load cell 3**

COOPER
INSTRUMENTS & SYSTEMS

P.O. Box 3048 • Warrenton, Virginia 20188 • Phone: (540) 349-4746 • Fax: (540) 347-4755

CERTIFICATE OF CALIBRATION

Transducer Model:	LPM 530		
Serial Number:	951011		
Capacity:	1000	LBS	
Calibration Date:	4/16/2003		
Excitation:	10	VDC	
Calibration Factor:	2.029	MV/V	Tension
Input Resistance:	353	Ohms	
Output Resistance:	353	Ohms	
Temperature Range:	60-160	Degrees F	

An output of **1.492** **MV/V** is induced when a shunt resistor of 59K ohms is applied across (-) Excitation and (-) Signal.

Special Instructions:

Wiring Code	RED	**(+)Excitation**
	BLACK	**(-) Excitation**
	WHITE	**(+)Signal**
	GREEN	**(-) Signal**

This is to certify that the following instrument was calibrated using loading equipment traceable to NIST through one or more of standards. The unit was found to meet or exceed all published sales literature accuracy specifications.

Date of Shipment: 5/14/2003 Re-Calibration Date: 1 year after Shipment Date

www.cooperinstruments.com • email: sales@cooperinstruments.com

Factory load cell calibration data for **Global Dynamometer load cell 4**

COOPER
INSTRUMENTS & SYSTEMS

CERTIFICATE OF CALIBRATION

Transducer Model:	LPM 530		
Serial Number:	951012		
Capacity:	1000	LBS	
Calibration Date:	4/16/2003		
Excitation:	10	VDC	
Calibration Factor:	1.950	MV/V	Tension
Input Resistance:	353	Ohms	
Output Resistance:	353	Ohms	
Temperature Range:	60-160	Degrees F	

An output of 1.492 MV/V is induced when a shunt resistor of 59K ohms is applied across (-) Excitation and (-) Signal.

Special Instructions:

Wiring Code	RED	**(+)Excitation**
	BLACK	**(-) Excitation**
	WHITE	**(+)Signal**
	GREEN	**(-) Signal**

This is to certify that the following instrument was calibrated using loading equipment traceable to NIST through one or more of standards. The unit was found to meet or exceed all published sales literature accuracy specifications.

Date of Shipment: 5/14/2003 Re-Calibration Date: 1 year after Shipment Date

www.cooperinstruments.com • email: sales@cooperinstruments.com

P.O. Box 3048 • Warrenton, Virginia 20188 • Phone (540) 349-4746 • Fax (540) 347-4755

Factory load cell calibration data for **Global Dynamometer load cell 5**

COOPER
INSTRUMENTS & SYSTEMS

P.O. Box 3048 • Warrenton, Virginia 20188 • Phone (540) 349-4746 • Fax (540) 347-4755

CERTIFICATE OF CALIBRATION

Transducer Model:	LPM 530		
Serial Number:	951013		
Capacity:	1000	LBS	
Calibration Date:	4/16/2003		
Excitation:	10	VDC	
Calibration Factor:	1.987	MV/V	Tension
Input Resistance:	353	Ohms	
Output Resistance:	353	Ohms	
Temperature Range:	60-160	Degrees F	

An output of 1.490 MV/V is induced when a shunt resistor of 59K ohms is applied across (-) Excitation and (-) Signal

Special Instructions:

Wiring Code	RED	**(+)Excitation**
	BLACK	**(-) Excitation**
	WHITE	**(+)Signal**
	GREEN	**(-) Signal**

This is to certify that the following instrument was calibrated using loading equipment traceable to NIST through one or more of standards. The unit was found to meet or exceed all published sales literature accuracy specifications.

Date of Shipment: 5/14/2003 Re-Calibration Date: 1 year after Shipment Date

www.cooperinstruments.com • email: sales@cooperinstruments.com

Factory load cell calibration data for **Global Dynamometer load cell 6**

COOPER
INSTRUMENTS & SYSTEMS

CERTIFICATE OF CALIBRATION

Transducer Model:	LPM 530		
Serial Number:	951016		
Capacity:	1000	LBS	
Calibration Date:	4/16/2003		
Excitation:	10	VDC	
Calibration Factor:	1.963	MV/V	Tension
Input Resistance:	352	Ohms	
Output Resistance:	352	Ohms	
Temperature Range:	60-160	Degrees F	

An output of 1.487 MV/V is induced when a shunt resistor of 59K ohms is applied across (-) Excitation and (-) Signal.

Special Instructions:

Wiring Code	RED	**(+)Excitation**
	BLACK	**(-) Excitation**
	WHITE	**(+)Signal**
	GREEN	**(-) Signal**

This is to certify that the following instrument was calibrated using loading equipment traceable to NIST through one or more of standards. The unit was found to meet or exceed all published sales literature accuracy specifications.

Date of Shipment: 5/14/2003 Re-Calibration Date: 1 year after Shipment Date

P.O. Box 3048 • Warrenton, Virginia 20188 • Phone: (540) 349-4746 • Fax: (540) 347-4755

Appendix B – Material Properties

303 Stainless Steel

Physical Properties Metric English Comments
Density 8.00 g/cc 0.289 lb/in³

Mechanical Properties Metric English Comments
Hardness, Brinell 160 160
Hardness, Knoop 180 180 Converted from Brinell hardness.
Hardness, Rockwell B 83.0 83.0 Converted from Brinell hardness.
Hardness, Vickers 167 167 Converted from Brinell hardness.
Tensile Strength, Ultimate 620 MPa 89900 psi
Tensile Strength, Yield 240 MPa 34800 psi at 0.2% offset
Elongation at Break 50.0 % 50.0 % in 50 mm
Modulus of Elasticity 193 GPa 28000 ksi tension
Poissons Ratio 0.250 0.250 Calculated
Fatigue Strength 240 MPa 34800 psi annealed
330 MPa 47900 psi 25% hardened
Shear Modulus 77.2 GPa 11200 ksi

Electrical Properties Metric English Comments
Electrical Resistivity 0.0000720 ohm-cm 0.0000720 ohm-cm
Magnetic Permeability 1.008 1.008 at RT

440C Stainless Steel

Physical Properties Metric English Comments
Density 7.80 g/cc 0.282 lb/in³

Mechanical Properties Metric English Comments
Hardness, Rockwell C 58.0 58.0
Tensile Strength, Ultimate 1750 MPa 254000 psi
Tensile Strength, Yield 1280 MPa 186000 psi
Elongation at Break 4.00 % 4.00 %
Modulus of Elasticity 200 GPa 29000 ksi
Charpy Impact 19.0 J 14.0 ft-lb

Thermal Properties Metric English Comments
CTE, linear 20°C 10.2 µm/m-°C 5.67 µin/in-°F from 0-100°C (32-212°F)
Specific Heat Capacity 0.460 J/g-°C 0.110 BTU/lb-°F from 0-100°C (32-212°F)
Maximum Service Temperature, Air 760 °C 1400 °F Continuous Service
815 °C 1500 °F Intermittent Service

17-4 H900

Physical Properties Metric English Comments
Density 7.80 g/cc 0.282 lb/in³

Mechanical Properties Metric English Comments
Hardness, Rockwell C 45.0 45.0
Tensile Strength, Ultimate 1448 MPa 210000 psi
Tensile Strength, Yield 1379 MPa 200000 psi 0.2% YS
Elongation at Break 7.00 % 7.00 % in 2 inches

Electrical Properties Metric English Comments
Electrical Resistivity 0.0000770 ohm-cm 0.0000770 ohm-cm

Thermal Properties Metric English Comments
CTE, linear 20°C 10.8 µm/m-°C 6.00 µin/in-°F 21 to 93°C
11.7 µm/m-°C 6.50 µin/in-°F to 427°C
Specific Heat Capacity 0.460 J/g-°C 0.110 BTU/lb-°F
Thermal Conductivity 17.9 W/m-K
@Temperature 149 °C 124 BTU-in/hr-ft²-°F
@Temperature 300 °F
22.6 W/m-K
@Temperature 482 °C 157 BTU-in/hr-ft²-°F
@Temperature 900 °F

Appendix C – Strain Gauge Specifications

The gauges used in this project are specifically designed to measure strains due to torsion loading. Each gauge element has two separate gauges, thus two are used for a full bridge configuration. Specifications are given below.

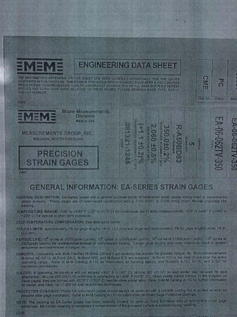

ENGINEERING DATA SHEET

THE INFORMATION APPEARING ON THIS SHEET HAS BEEN COMPILED SPECIFICALLY FOR THE GAGES CONTAINED IN THIS PACKAGE. THIS FORM IS PRODUCED WITH ADVANCED EQUIPMENT & PROCEDURES WHICH PERMIT COMPREHENSIVE QUALITY ASSURANCE VERIFICATION OF ALL DATA SUPPLIED HEREIN. SHOULD ANY QUESTIONS ARISE RELATIVE TO THESE GAGES, PLEASE MENTION GAGE TYPE, BATCH AND LOT NUMBER.

H001

Final QA	Check	Batch
CME	PC	S183091

Micro-Measurements Division

Made in USA

MEASUREMENTS GROUP, INC.

RALEIGH, NORTH CAROLINA

PRECISION STRAIN GAGES

F007

TYPE	EA-06-062TV-350
OPTION	
QUANTITY	5
LOT NUMBER	R-A50BD83
RESISTANCE IN OHMS AT 24°C	350.0±0.2%
GAGE FACTOR AT 24°C	2.060 ±0.5%
TRANSVERSE SENSITIVITY AT 24°C	(+1.1 ±0.2)%
CODE	081321-1245

EA-06-062TV-350

GENERAL INFORMATION: EA-SERIES STRAIN GAGES

GENERAL DESCRIPTION: EA-Series gages are a general-purpose family of constantan strain gages widely used in experimental stress analysis. These gages are of open-faced construction with a 1 mil [0.001 in (0.03) mm]] tough, flexible polyimide film backing.

TEMPERATURE RANGE: -100° to +350° F (-75° to +175°C) for continuous use in static measurements. -320° to +400° F (-195° to +205° C) for special or short-term exposure.

SELF-TEMPERATURE COMPENSATION: See data curve below.

STRAIN LIMITS: Approximately 5% for gage lengths 1/8 in. (3.2 mm) and larger and approximately 3% for gage lengths under 1/8 in. (3.2 mm).

FATIGUE LIFE: 10^8 cycles at ±1200µin/in (µm/m); 10^6 cycles at ±1500µin/in (µm/m); 10^5 cycles at ±1800µin/in (µm/m); 10^3 cycles at 2800µin/in (µm/m) for unidirectional tension or compression loading. Longer gage lengths and lower resistance result in greater endurance and less scatter in fatigue life.

CEMENTS: Compatible with M-M Certified M-Bond 200 but it will normally not provide the greatest fatigue life. Micro-Measurements M-Bond AE-10/15, M-Bond GA-2, M-Bond 600, and M-Bond 610 are excellent. M-Bond 610 is the best choice over the entire operating range. Refer to M-M Catalog A-110 for information on bonding agents, and Bulletins B-127, B-130, and B-137 for installation procedures.

SOLDER: If operating temperature will not exceed +300° F (+150° C), M-Line 361 (63-37) tin-lead solder may be used for lead attachment. M-Line 450 (95-5) tin-antimony is satisfactory to +400° F (+205° C). When solder turrets (Option S) are supplied on these gages, they are formed with +570° F (+300° C) lead-tin silver solder alloy. Refer to M-M Catalog A-110 for further information on solder, and Tech Tip TT-609 for lead attachment techniques.

PROTECTIVE COATINGS: These EA open-faced gages should always be protected with a suitable coating that is applied as soon as possible after gage installation. Refer to M-M Catalog A-110 for information on Strain Gage Protective Coatings.

NOTE: The backing on EA-Series gages has been specially treated for optimum bond formation with all appropriate strain gage adhesives. No further cleaning is necessary if contamination of the prepared surface is avoided during handling.

G023

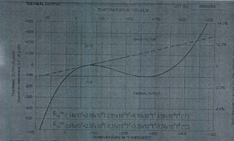

TESTED ON: 1018 STEEL TEST PATTERN: T004R CODE: 51116 ENG: GU

TEST PROCEDURES USED BY MICRO-MEASUREMENTS

OPTICAL DEFECT ANALYSIS . . . . M-M Procedures and Standards
GAGE RESISTANCE AT 24°C AND 50% RH . . . . M-M Procedure, Direct NIST Traceability on Resistance Standards
GAGE FACTOR AT 24°C & 50% RH (UNIAXIAL STRESS FIELD - POISSON'S RATIO - 0.285) . . . . ASTM E-251 (Constant Stress Cantilever Method)
TEMPERATURE COEFFICIENT OF GAGE FACTOR . . . . ATSM E-251 (Step Deflection Method)
THERMAL OUTPUT . . . . ASTM E-251 (Slow Heating Rate, Continuously Recorded)
TRANSVERSE SENSITIVITY AT 24°C AND 50%H . . . . ASTM E-251
FATIGUE LIFE . . . . NAS-942 (Modified)
STRAIN LIMITS . . . . NAS-942 (Modified)
GAGE THICKNESS . . . . M-M Procedure
CREEP AND DRIFT . . . . M-M Procedure (Similar to NAS 942 Method)

NOTE: Gage resistance, gage factor, temperature coefficient of gage factor, thermal output, and transverse sensitivity testing and information presentation are in compliance with OIML International Recommendation NO. 62, "Performance characteristics of metallic resistance strain gages." Other tests are not included in I.R. NO. 62.

T001

Appendix D – Factory Pressure Transducer Specifications

These are the factory specifications for the pressure transducers (R=1, 2, 3, 4 & 5 respectively).

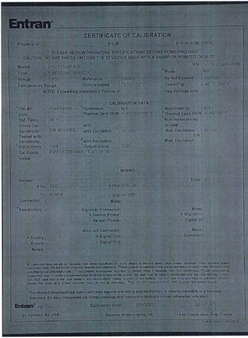

Entran

CERTIFICATE OF CALIBRATION

Property of : P.O.# Entran FO#: 42908

PLEASE REVIEW OPERATING SPECIFICATIONS BEFORE POWERING UNIT
CAUTION: DO NOT PRESS OR LOAD THE SENSITIVE AREA WITH A SHARP OR POINTED OBJECT

S/N : 03B03B10-W09

Model : EPE-T11-5P-/L5F
Type : PRESSURE SENSOR
[4] Mode : N/A
[4] Range : 5 PSI Reference : GAUGE Do Not Exceed : 100 PSI
Temperature Range Compensated : 70 TO 170° F Operating : -40 TO 250° F
NOTE: Exceeding Installation Torque of may damage unit.

CALIBRATION DATA

[1] CNL&H	: +/-3/4%FSO	[1] Hysteresis	: N/A	[1] Non-linearity	: N/A
[1] Zero	:	Thermal Zero Shift	: +/-3%FSO/100° F	[2] Thermal Sens.Shift	: +/-4%/100° F
Ref. Temp	: 74° F			[2] Non-repeatability	:
Shunt Cal	:	with	:	across	:
Sensitivity	: 278.49 mV/FS	with Excitation	: 10 Vdc	Max. Excitation	: 12 Vdc
Tested with	:			S/N	:
Sensitivity	:	[5] with Excitation	:	Max. Excitation	:
[3] Input ohms	: 1045	[3] Output ohms	: 1034		
Cal Equip.	: DVM US37016561 DWT 57175				
Notes	:				

WIRING

Sensor : Total : 5'
+ In : RED + Out: GREEN
- In : BLACK - Out: WHITE
Connector : Mate:
[5] Electronics : Signal In Connector: Mate:
+ Sensor Power: + Signal In:
- Sensor Power: - Signal In:
Amp out Connector: Mate:
+ Supply : + Signal Out: Common:
- Supply : - Signal Out:
Notes :

[1] If calibrated data equals or exceeds data sheet specifications, value shown is the data sheet value unless purchase order specifies actual calibrated value. CNL&H is combined non-linearity and hysteresis. [2] Value given is by manufacturing design and not calibrated unless purchase order specifies actual calibrated value. [3] Input/Output impedance recorded for sensor alone if separate item from electronics. [4] Load cells must be loaded with load on center and perpendicular to the flat surface of the device. The load must be equally distributed over the load bearing surface. DO NOT load with a ball type press or any device which makes a point or line contact. DO NOT load only one edge or unevenly. DO NOT torque the body of a thread mounted load cell during mounting. [5] For +/- 15V input, DO NOT USE unipolar 30V power supply.

The above Instrument has been calibrated against a working standard which is directly traceable to a National Standard. All data interpreted per Entran catalogs and Instruction Manual's unless otherwise indicated.

Entran by: CU Calibration Date: 2/21/2003 QC :

Fairfield, NJ, USA   Garston, Watford Herts, UK   Les Clayes-sous-Bois, France

Pressure transducer #1 (R=15.875 mm (0.625")).

Entran®

CERTIFICATE OF CALIBRATION

Property of : P.O # Entran FO#: 42906

PLEASE REVIEW OPERATING SPECIFICATIONS BEFORE POWERING UNIT
CAUTION: DO NOT PRESS OR LOAD THE SENSITIVE AREA WITH A SHARP OR POINTED OBJECT

Model	: EPE-T11-5P-/L5F			S/N :	03C03B10-W
Type	: PRESSURE SENSOR			[4] Mode	:N/A
[4] Range	: 5 PSI	Reference	: GAUGE	Do Not Exceed	: 100 PSI
Temperature Range		Compensated	: 70 TO 170° F	Operating	: -40 TO 250° F

NOTE: Exceeding Installation Torque of may damage unit.

CALIBRATION DATA

[1] CNL&H	: +/-3/4%FSO	[1] Hysteresis	: N/A	[1] Non-linearity	: N/A
[1] Zero	:	Thermal Zero Shift:	+/- 3%FSO/100° F	[2] Thermal Sens.Shift:	+/- 4%/100° F
Ref. Temp	: 74° F			[2] Non-repeatability	:
Shunt Cal	:	with	:	across	:
Sensitivity	: 259.21 mV/FS	with Excitation	: 10 Vdc	Max. Excitation	: 12 Vdc
Tested with	:			S/N	:
Sensitivity	:	[5] with Excitation	:	Max. Excitation	:
[3] Input ohms	: 1087	[3] Output ohms	: 1077		
Cal Equip.	: DVM US 37016661 DWT 67175				
Notes	:				

WIRING

Sensor : Total : 5'

+ In : RED + Out: GREEN

- In : BLACK - Out: WHITE

Connector : Mate:

[5] Electronics : Signal In Connector: Mate:

+ Sensor Power: + Signal In:

- Sensor Power: - Signal In:

Amp out Connector: Mate:

+ Supply : + Signal Out: Common:

- Supply : - Signal Out:

Notes :

[1] If calibrated data equals or exceeds data sheet specifications, value shown is the data sheet value unless purchase order specifies actual calibrated value. CNL&H is combined non-linearity and hysteresis. [2] Value given is by manufacturing design and not calibrated unless purchase order specifies actual calibrated value. [3] Input/Output impedance recorded for sensor alone if separate item from electronics. [4] Load cells must be loaded with load on-center and perpendicular to the flat surface of the device. The load must be equally distributed over the load bearing surface. DO NOT load with a ball type press or any device which makes a point or line contact. DO NOT load only one edge or unevenly. DO NOT torque the body of a thread mounted load cell during mounting. [5] For +/- 15V input, DO NOT USE unipolar 30V power supply.

The above instrument has been calibrated against a working standard which is directly traceable to a National Standard. All data interpreted per Entran catalogs and Instruction Manuals unless otherwise indicated.

Entran® by: SH Calibration Date: 3/13/2003 QC :

• Fairfield, NJ, USA ○ Garston, Watford Herts, UK ☐ Les Clayes-sous-Bois, France

Pressure transducer #2 (R=20.6325mm (0.8125"))

Entran®

CERTIFICATE OF CALIBRATION

Property of : P.O.# Entran FO#: 42008

PLEASE REVIEW OPERATING SPECIFICATIONS BEFORE POWERING UNIT
CAUTION: DO NOT PRESS OR LOAD THE SENSITIVE AREA WITH A SHARP OR POINTED OBJECT

Model	: EPE-T11-5P-/L5F			S/N :	03B03B10-W05
Type	: PRESSURE SENSOR			[4] Mode	: N/A
[4] Range	: 5 PSI	Reference	: GAUGE	Do Not Exceed	: 100 PSI
Temperature Range		Compensated	: 70 TO 170° F	Operating	: -40 TO 250° F

NOTE: Exceeding Installation Torque of may damage unit.

CALIBRATION DATA

[1] CNL&H	: +/-3/4%FSO	[1] Hysteresis	: N/A	[1] Non-linearity	: N/A
[1] Zero	:	Thermal Zero Shift:	+/-3%FSO/100° F	[2] Thermal Sens.Shift:	+/-4%/100° F
Ref. Temp	: 74° F			[2] Non-repeatability	:
Shunt Cal	:	with	:	across	:
Sensitivity	: 281.98 mV/FS	with Excitation	: 10 Vdc	Max. Excitation	: 12 Vdc
Tested with	:			S/N	:
Sensitivity	:	[5] with Excitation	:	Max. Excitation	:
[3] Input ohms	: 1063	[3] Output ohms	: 1063		
Cal Equip.	: DVM US37016651 DWT 67175				
Notes	:				

WIRING

Sensor : Total : 5'

+ In : RED + Out: GREEN

- In : BLACK - Out: WHITE

Connector : Mate:

[5] Electronics : Signal In Connector: Mate:

+ Sensor Power: + Signal In:

- Sensor Power: - Signal In:

Amp out Connector: Mate:

+ Supply : + Signal Out: Common:

- Supply : - Signal Out:

Notes :

[1] If calibrated data equals or exceeds data sheet specifications, value shown is the data sheet value unless purchase order specifies actual calibrated value. CNL&H is combined non-linearity and hysteresis. [2] Value given is by manufacturing design and not calibrated unless purchase order specifies actual calibrated value. [3] Input/Output impedance recorded for sensor alone if separate item from electronics. [4] Load cells must be loaded with load on-center and perpendicular to the flat surface of the device. The load must be equally distributed over the load bearing surface. DO NOT load with a ball type press or any device which makes a point or line contact. DO NOT load only one edge or unevenly. DO NOT torque the body of a thread mounted load cell during mounting. [5] For +/-15V input, DO NOT USE unipolar 30V power supply.

The above instrument has been calibrated against a working standard which is directly traceable to a National Standard. All data interpreted per Entran catalogs and Instruction Manuals unless otherwise indicated.

Entran® by: CU Calibration Date: 2/21/2003 QC :

Fairfield, NJ, USA ○ Garston, Watford Herts, UK ○ Les Clayes-sous-Bois, France

Form No: CAL-PL-UNIV REV. 3

Pressure transducer #3 (R=25.4mm (1.000"))

Entran®

CERTIFICATE OF CALIBRATION

Property of : P.O.# Entran FO#: 42908

PLEASE REVIEW OPERATING SPECIFICATIONS BEFORE POWERING UNIT
CAUTION: DO NOT PRESS OR LOAD THE SENSITIVE AREA WITH A SHARP OR POINTED OBJECT

Model	: EPE-T11-5P-/L5F			S/N :	03C03B10-W04
Type	: PRESSURE SENSOR			[4] Mode	: N/A
[4] Range	: 5 PSI	Reference	: GAUGE	Do Not Exceed	: 100 PSI
Temperature Range		Compensated	: 70 TO 170° F	Operating	: -40 TO 250° F

NOTE: Exceeding Installation Torque of may damage unit

CALIBRATION DATA

[1] CNL&H	: +/-3/4%FSO	[1] Hysteresis	: N/A	[1] Non-linearity	: N/A
[1] Zero	:	Thermal Zero Shift:	+/-3%FSO/100° F	[2] Thermal Sens.Shift:	+/-4%/100° F
Ref. Temp	: 74° F			[2] Non-repeatability	:
Shunt Cal	:	with	:	across	:
Sensitivity	: 281.87 mV/FS	with Excitation	: 10 Vdc	Max. Excitation	: 12 Vdc
Tested with	:			S/N	:
Sensitivity	:	[5] with Excitation	:	Max. Excitation	:
[3] Input ohms	: 1067	[3] Output ohms	: 1061		
Cal Equip.	: DVM US 37016661 DWT 67175				
Notes	:				

WIRING

Sensor			:		Total : 5'
+ In :	RED	+ Out:	GREEN		
- In :	BLACK	- Out:	WHITE		
Connector :		Mate:			
[5] Electronics :		Signal In Connector:		Mate:	
		+ Sensor Power:		+ Signal In:	
		- Sensor Power:		- Signal In:	
		Amp out Connector:		Mate:	
+ Supply :		+ Signal Out:		Common:	
- Supply :		- Signal Out:			
Notes :					

[1] If calibrated data equals or exceeds data sheet specifications, value shown is the data sheet value unless purchase order specifies actual calibrated value. CNL&H is combined non-linearity and hysteresis. [2] Value given is by manufacturing design and not calibrated unless purchase order specifies actual calibrated value. [3] Input/Output Impedance recorded for sensor alone if separate item from electronics. [4] Load cells must be loaded with load on-center and perpendicular to the flat surface of the device. The load must be equally distributed over the load bearing surface. DO NOT load with a ball type press or any device which makes a point or line contact. DO NOT load only one edge or unevenly. DO NOT torque the body of a thread mounted load cell during mounting. [5] For +/-15V input, DO NOT USE unipolar 30V power supply.

The above instrument has been calibrated against a working standard which is directly traceable to a National Standard. All data interpreted per Entran catalogs and instruction Manuals unless otherwise indicated.

Entran® by: SH Calibration Date: 3/13/2003 QC : 9 Q.C.

• Fairfield, NJ, USA ○ Garston, Watford Herts, UK ○ Les Clayes-sous-Bois, France

Form No. QCAL PL-UNIV REV. 3

Pressure transducer #4 (R=30.1625 (1.1875"))

Entran®

CERTIFICATE OF CALIBRATION

Property of : P.O.# Entran FO#: 42908

PLEASE REVIEW OPERATING SPECIFICATIONS BEFORE POWERING UNIT
CAUTION: DO NOT PRESS OR LOAD THE SENSITIVE AREA WITH A SHARP OR POINTED OBJECT

S/N : 03C03B10-W08

Model	: EPE-T11-5P-/L5F				
Type	: PRESSURE SENSOR			[4]Mode	: N/A
[4]Range	: 5 PSI	Reference	: GAUGE	Do Not Exceed	: 100 PSI
Temperature Range		Compensated	: 70 TO 170° F	Operating	: -40 TO 250° F

NOTE: Exceeding installation Torque of may damage unit.

CALIBRATION DATA

[1]CNL&H	: +/- 3/4%FSO	[1]Hysteresis	: N/A	[1]Non-linearity	: N/A
[1]Zero	:	Thermal Zero Shift:	+/- 3%FSO/100° F	[2]Thermal Sens.Shift:	+/- 4%/100° F
Ref. Temp	: 74° F			[2]Non-repeatability	:
Shunt Cal	:	with	:	across	:
Sensitivity	: 248.73 mV/FS	with Excitation	: 10 Vdc	Max. Excitation	: 12 Vdc
Tested with	:			S/N	:
Sensitivity	:	[5]with Excitation	:	Max. Excitation	:
[3]Input ohms	: 1590	[3]Output ohms	: 1573		
Cal Equip.	: DVM US 37016661 DWT 67175				
Notes	:				

WIRING

Sensor : Total : 5'

+ In : RED + Out: GREEN

- In : BLACK - Out: WHITE

Connector : Mate:

[5]Electronics :

Signal In Connector: Mate:
+ Sensor Power: + Signal In:
- Sensor Power: - Signal In:

Amp out Connector: Mate:
+ Supply : + Signal Out: Common:
- Supply : - Signal Out:
Notes :

[1]If calibrated data equals or exceeds data sheet specifications, value shown is the data sheet value unless purchase order specifies actual calibrated value. CNL&H is combined non-linearity and hysteresis. [2]Value given is by manufacturing design and not calibrated unless purchase order specifies actual calibrated value. [3]Input/Output impedance recorded for sensor alone if separate item from electronics. [4]Load cells must be loaded with load on-center and perpendicular to the flat surface of the device. The load must be equally distributed over the load bearing surface. DO NOT load with a ball type press or any device which makes a point or line contact. DO NOT load only one edge or unevenly. DO NOT torque the body of a thread mounted load cell during mounting. [5]For +/- 15V input, DO NOT USE unipolar 30V power supply.

The above instrument has been calibrated against a working standard which is directly traceable to a National Standard. All data interpreted per Entran catalogs and Instruction Manuals unless otherwise indicated.

Entran® by: SH Calibration Date: 3/14/2003 QC : 8 Q.C.

Fairfield, NJ, USA Garston, Watford Herts, UK Les Clayes-sous-Bois, France

Pressure transducer #5 (R=47.625 (1.375"))

Appendix E – Renshape 460 Properties

REN SHAPE® 460

MODELING BOARD

Ren Shape 460 is a higher-density precision modeling board and features a lower coefficient of thermal expansion
to provide enhanced dimensional stability over a broader temperature range than other modeling materials. Ren
Shape 460 provides the same excellent definition and accuracy for which the Ren Shape® family of materials is
well known. Machinable with carbide cutters, Ren Shape 460 features properties including:
? Ultra-fine surface finish ? Outstanding resistance to shrinkage and warping
? Superior reproduction of intricate detail
Applications include temporary and throwaway master models, styling and visual models, prototypes and
prototype foundry patterns and vacuum-form molds, architectural and automotive die models, tooling
aids and fixtures, and other applications requiring fast machining and good model surfaces.

ACCESSORIES Matched Adhesive Repair Paste
Ren-Weld® 103
or RP 6465 UltraFast
TDT 177-113 R/H
or Ren Patch® 440

TYPICAL PROPERTIES* ASTM Method Cure Value
Color Visual Light brown
Density, lb./ft3 (g/cm3) D-792 48 (0.77)
Hardness, Shore D D-2240 64
Ultimate Flexural Strength, psi D-790 3,700
Flexural Modulus, psi D-790 185,000
Ultimate Tensile Strength, psi D-638 1,800
Tg by DMA, E", °F(°C) D-4065 219 (104)
Compressive Strength, 0.2% offset, psi D-695 2,200
Compressive Modulus, psi D-695 181,000
Coefficient of Thermal Expansion D-3386
-22° to 86°F, in/in/°F 29.9 x 10-6
-30° to 30°C, in/in/°C 53.8 x 10-6
* Tested @ 77°F (25°C) unless otherwise noted.

NOTE: These physical properties are reported as typical test values obtained by our test laboratory. If assistance is needed in establishing product
specifications, please consult with our Product Management Department.

MACHINING Roughing Speed Roughing Feed Finishing Speed Finishing Feed
1,600 RPM 40 IPM 10,000 RPM 100 IPM
Cutters: Roughing - 1" Hog Ball End Mill 4-Flute HS Steel 8% Cobalt
Finishing - 5/8" Ball End Mill 2-Flute Carbide
Depth: Roughing - varied from 1/4" to 2-1/2" deep with a 40% stepover
Finishing - 1/8" deep leaving 0.002" scallop height

SAFETY: Do not use or handle this product until the Material Safety Data Sheet has been read and understood.
IMPORTANT: The following supercedes Buyer's documents. **SELLER MAKES NO REPRESENTATION OR WARRANTY, EXPRESS OR
IMPLIED, INCLUDING OF MERCHANTABILITY OR FITNESS FOR A PARTICULAR PURPOSE.** No statements herein are to be construed as
inducements to infringe any relevant patent. Under no circumstances shall Seller be liable for incidental, consequential, or indirect damages for

alleged negligence, breach of warranty, strict liability, tort, or contract arising in connection with the product(s). Buyer's sole remedy and Seller's sole
liability for any claims shall be Buyer's purchase price. Data and results are based on controlled or lab work and must be confirmed by Buyer by
testing for its intended conditions of use. The product(s) has not been tested for, and is therefore not recommended for, uses for which prolonged
contact with mucous membranes, abraded skin, or blood is intended; or for uses for which implantation within the human body is intended.

REN®

Modeling & Styling Boards

distributed by Freeman Mfg & Supply Co. 800-321-8511

Appendix F – Retaining compound specifications

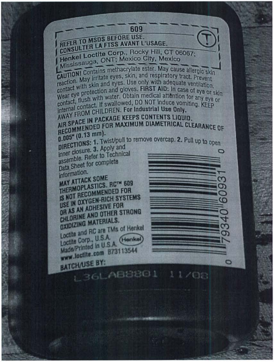
609
REFER TO MSDS BEFORE USE.
CONSULTER LA FTSS AVANT L'USAGE.
Henkel Loctite Corp., Rocky Hill, CT 06067;
Mississauga, ONT; Mexico City, Mexico
CAUTION! Contains methacrylate ester. May cause allergic skin reaction. May irritate eyes, skin, and respiratory tract. Prevent contact with skin and eyes. Use only with adequate ventilation. Wear eye protection and gloves. FIRST AID: In case of eye or skin contact, flush with water. Obtain medical attention for any eye or internal contact. If swallowed, DO NOT induce vomiting. KEEP AWAY FROM CHILDREN. For Industrial Use Only.
AIR SPACE IN PACKAGE KEEPS CONTENTS LIQUID.
RECOMMENDED FOR MAXIMUM DIAMETRICAL CLEARANCE OF 0.005" (0.13 mm).
DIRECTIONS: 1. Twist/pull to remove overcap. 2. Pull up to open inner closure. 3. Apply and assemble. Refer to Technical Data Sheet for complete information.
MAY ATTACK SOME THERMOPLASTICS. RC™ 609 IS NOT RECOMMENDED FOR USE IN OXYGEN-RICH SYSTEMS OR AS AN ADHESIVE FOR CHLORINE AND OTHER STRONG OXIDIZING MATERIALS.
Loctite and RC are TMs of Henkel
Loctite Corp., U.S.A.
Henkel
Made/Printed in U.S.A.
www.loctite.com 873113544
0 79340 60931 0
BATCH/USE BY:
L36LAB8801 11/08

Appendix G – 5 hp Baldor Motor Specifications

Product Overview: M3615T

Click for Larger Image

Catalog Number:	M3615T
Description:	5HP,1750RPM,3PH,60HZ,184T,3632M,TEFC,F1
Ship Weight:	79 lbs.
List Price:	$546
Multiplier Symbol:	LS

View Specifications | View Operation Manual

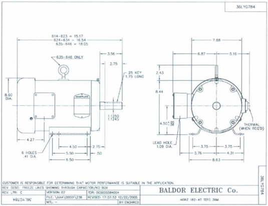

AC Motors | General Purpose |

Specifications: M3615T

Catalog Number:	M3615T
Specification Number:	36G784T846H1
Horsepower:	5
Voltage:	208-230/460
Hertz:	60
Phase:	3
Full Load Amps:	15.4-14.2/7.1
Usable at 208 Volts:	N/A
RPM:	1750
Frame Size:	184T
Service Factor:	1.15
Rating:	40C AMB-CONT
Locked Rotor Code:	K
NEMA Design Code:	B
Insulation Class:	F
Full Load Efficiency:	87.5
Power Factor:	75
Enclosure:	TEFC
Baldor Type:	3633M
DE Bearing:	6206
ODE Bearing:	6205
Electrical Specification Number:	36WGT846
Mechanical Specification Number:	36G784
Base:	RG
Mounting:	F1

* For certified information, contact your local Baldor office.

Appendix H – Gearbox & Lubrication Specifications

The gearbox chosen is a Hub City Gearbox. The part number is 0221-05041.

This gearbox had to be ordered with a vertical input shaft, and thus this shaft has its own set of sealed and lubricated bearings. Maintenance of the gearbox includes application of grease via the grease nipple, as well as topping up the main gearbox lubrication reservoir with gear oil of the type specified below. The drive ratio is 2:1.

APPENDIX I – Drive Belt Specifications

The drive belt selected is of type T5, polyurathane steel cord reinforced. The belt ordered is a 400 tooth 1 inch wide custom belt. Company is Stock Drive Products.

METRIC — Timing Belts - T5 mm Pitch

■ TRUE METRIC® PROFILE ■ POLYURETHANE ■ 6, 10 & 16 mm WIDE

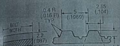

NOTE: Dimensions in ( ) are inch size.

CATALOG NUMBER DESIGNATION:

A 6T35M □□□□□□

No. of Grooves (See tables below) — Width Code (See right)

Width Code	Belt Width	Equivalent Inch Width
060	6 mm	.236
100	10 mm	.394
160	16 mm	.630

Example: A 6T35M068100 is a 68 Groove 10 mm Wide Belt.

MATERIAL: Polyurethane – Translucent, Reinforced with Steel Tensile Cords
BREAKING STRENGTH (Min.): 118 N/mm (84 lbs. per 1/8") Belt Width
TEMPERATURE RANGE: -18°C to +82°C (0°F to 180°F)

No. of Grooves	Pitch Length mm	Pitch Length Inch
33	165	6.496
37	185	7.283
40	200	7.874
43	215	8.465
44	220	8.661
45	225	8.858
49	245	9.646
50	250	9.843
51	255	10.039
52	260	10.236
54	270	10.630
55	275	10.827
56	280	11.024
59	295	11.614
60	300	11.811
61	305	12.008
65	325	12.795
66	330	12.992
68	340	13.386
70	350	13.780
71	355	13.976
73	365	14.370

No. of Grooves	Pitch Length mm	Pitch Length Inch
78	390	15.354
80	400	15.748
82	410	16.142
84	420	16.535
85	425	16.732
90	450	17.717
91	455	17.913
93	465	18.307
95	475	18.701
96	480	18.898
100	500	19.685
102	510	20.079
105	525	20.669
109	545	21.457
110	550	21.654
112	560	22.047
115	575	22.638
120	600	23.662
122	610	24.016
124	620	24.409
126	630	24.803
128	640	25.197

No. of Grooves	Pitch Length mm	Pitch Length Inch
130	650	25.591
132	660	25.984
138	690	27.165
139	695	27.362
140	700	27.559
144	720	28.346
150	750	29.528
156	780	30.709
163	815	32.087
168	840	33.071
170	850	33.465
180	900	35.433
198	990	38.976
200	1000	39.370
215	1075	42.323
220	1100	43.307
243	1215	47.835
276	1380	54.331
280	1400	55.118
288	1440	56.693

TIMING BELTS 1

1-27

APPENDIX J – Bearing Specifications

Main drive gear bearings are part number JA-030-CP0, from Kaydon Bearings.

Sealed Bearing Selections

Type C
Radial Contact

JHA SERIES (DOUBLE SEALED)

Kaydon Bearing Number	Dimensions in Inches				Radial Capacity (lbs.)①		Limiting Speeds (RPM*)	Torque Max. No Load (Oz-In)④	Weight in Pounds
	Bore	Outside Diameter	Dia. L_1	Dia. L_2	Static②	Dyn.			
JHA10CL0	1.000	1.375	1.108	1.274	290	150	6110	5	.035
JHA15CL0	1.500	1.875	1.608	1.774	400	180	4300	5	.052
JHA17CL0	1.750	2.125	1.858	2.024	460	200	3750	6	.060

③F = .015
Bearing corners are normally chamfered

JA SERIES (DOUBLE SEALED)

Kaydon Bearing Number	Dimensions in Inches				Radial Capacity (lbs.)①		Limiting Speeds (RPM*)	Torque Max. No Load (Oz-In)④	Weight in Pounds
	Bore	Outside Diameter	Dia. L_1	Dia. L_2	Static②	Dyn.			
•JA020CP0	2.000	2.500	2.148	2.356	680	320	3,220	6	.10
•JA025CP0	2.500	3.000	2.648	2.856	830	360	2,630	8	.12
•JA030CP0	3.000	3.500	3.148	3.356	990	410	2,230	12	.14
•JA035CP0	3.500	4.000	3.648	3.856	1,140	450	1,930	16	.17
•JA040CP0	4.000	4.500	4.148	4.356	1,290	485	1,700	20	.19
•JA042CP0	4.250	4.750	4.398	4.606	1,370	500	1,510	24	.20
•JA045CP0	4.500	5.000	4.648	4.856	1,440	520	1,520	28	.21
JA047CP0	4.750	5.250	4.898	5.106	1,520	540	1,450	32	.22
JA050CP0	5.000	5.500	5.148	5.356	1,590	560	1,380	36	.23
JA055CP0	5.500	6.000	5.648	5.856	1,750	590	1,260	44	.25
JA060CP0	6.000	6.500	6.148	6.356	1,900	630	1,160	52	.28
JA065CP0	6.500	7.000	6.648	6.856	2,050	660	1,070	61	.30

③F = .025
Bearing corners are normally chamfered

① Capacities listed are not simultaneous. For combined loading see discussion of Bearing Selection and Load Analysis. Dynamic capacities are based upon (1.0 million revolutions) of L10 life.
② Static capacities are non-brinell limits based on rigid support from the shaft and housing.
③ "F" is the maximum shaft or housing fillet radius the bearing corners will clear.
④ Torque figures shown are for single bearings with standard lubricant at room temperature and under 5 pounds thrust load.
Limited availability.
* Values apply to bearings loaded up to 20% of their dynamic capacity.
• Available from stock—check for availability of other sizes.

APPENDIX K – Tachometer Generator Specifications

The tachometer selected is TYPE SB-740A-7. See catalogue page below.

SERVO-TEK®

1086 Goffle Road • Hawthorne, NJ 07506 • sales@servotek.com
Phone (973) 427-3100 • Fax (973) 427-4249 • www.servotek.com

A-Series
1 to 10 volts/1000 RPM

SA-757A-2 and SA-740A-2

SN-783A-2

A-Series Tachometer Generators

Instrument Type:
- 0.120 inch shaft diameter
- Small in size
- Ideally suited to instrumentation applications

Industrial Type:
- 0.187 inch shaft diameter
- Special front-end bearings for radial loads
- Ideal for pulley and belt drive applications

B-Series
11 to 24 volts/1000 RPM

SB-757B-1 and SU-73460-1

B-Series Tachometer Generators

As is the case with the A-Series DC tachometer generator, the B-Series also comes in instrument and industrial configurations. Depending on the unit, the output voltage ranges between 11 and 24 V/1000 RPM. Electrical characteristics, ripple, linearity and temperature effects are the same as the A-Series.

Other shaft sizes and mounting configurations are available for most Servo-Tek generators.

A-Series and B-Series Specifications

Model Number	Mounting	Weight (Approx.)	Inertia (Approx.) oz-in-sec²	V/1000 RPM	RPM (max)	Armature Resistance (dynamic)	Armature Inductance (henrys)	Outline Dimensions	Mounting Dimensions	Shaft Size (in.)
SA-740A-7	Face	3.0 oz	1.32×10^{-4}	2.6v	12,000	40Ω	0.024h	Fig. 10	Fig. 1	.120
SB-740A-7	Flange	3.0 oz	1.32×10^{-4}	2.6v	12,000	40Ω	0.024h	Fig. 10	Fig. 2	.120
SA-740A-2	Face	3.0 oz	1.32×10^{-4}	7.0v	12,000	350Ω	0.18h	Fig. 10	Fig. 1	.120
SB-740A-2	Flange	3.0 oz	1.32×10^{-4}	7.0v	12,000	350Ω	0.18h	Fig. 10	Fig. 2	.120
SA-757A-2	Face	3.0 oz	1.32×10^{-4}	7.0v	12,000	350Ω	0.18h	Fig. 11	Fig. 1	.187
SB-757A-2	Flange	3.0 oz	1.32×10^{-4}	7.0v	12,000	350Ω	0.18h	Fig. 11	Fig. 2	.187
SA-740B-1	Face	4.0 oz	2.27×10^{-4}	20.8v	8,000	1000Ω	0.56h	Fig. 10	Fig. 1	.120
SB-740B-1	Flange	4.0 oz	2.27×10^{-4}	20.8v	8,000	1000Ω	0.56h	Fig. 10	Fig. 2	.120
SA-757B-1	Face	4.0 oz	2.27×10^{-4}	20.8v	8,000	1000Ω	0.56h	Fig. 11	Fig. 1	.187
SB-757B-1	Flange	4.0 oz	2.27×10^{-4}	20.8v	8,000	1000Ω	0.56h	Fig. 11	Fig. 2	.187

Maximum Driving Torque for A-Series and B-Series is 0.25 oz-in
Most units listed above are normally in stock

APPENDIX L – Slip Ring Specifications

An 8 conductor slip ring and one piece brush block was selected. Part number 1908.

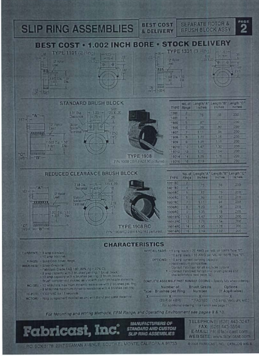

TYPE	No. of Rings	Length "A" Inches	Length "B" Inches	Length "C" Inches
1201	2	.75	.58	.200
1401	4			
1905	5	.87	.70	.200
1906	6	.99	.82	.200
1907	7	1.11	.94	.200
1908	8	1.23	1.06	.200
1909	9	1.35	1.18	.200
19010	10	1.47	1.30	.200
19012	12	1.71	1.54	.200
19014	14	1.95	1.78	.200
19016	16	2.19	2.02	.200

TYPE	No. of Rings	Length "A" Inches	Length "B" Inches	Length "C" Inches
1201RC	2	.75	.58	.220
1401RC	4			
1905RC	5	.87	.70	.200
1906RC	6	.99	.82	.200
1907RC	7	1.11	.94	.200
1908RC	8	1.23	1.06	.200
1909RC	9	1.35	1.18	.200
19010RC	10	1.47	1.30	.200
19012RC	12	1.71	1.54	.200
19014RC	14	1.95	1.78	.200
19016RC	16	2.19	2.02	.200

CHARACTERISTICS

CURRENT: • 5 amp standard • 10 amp optional
RINGS: • Solid Coin Silver Rings
BRUSHES: • Silver Graphite • Fabricast Grade FAG 180 (80% Ag – 20% C) • 5 amp capacity with 2 brushes per ring (1 brush block) • 10 amp capacity with 4 brushes per ring (2 brush blocks) • Brush complement molded as unit with diallyl phthalate dielectric
NOISE: • 10 Milliohms maximum dynamic resistance with 2 brushes per ring • 5 Milliohms maximum dynamic resistance with 4 brushes per ring
HI-POT: • 1000 VAC for 15 seconds
ROTOR: • Ring complement molded as unit with diallyl phthalate dielectric

ROTOR LEADS: • 5 amp leads – 20 AWG per MIL-W-16878 Type "E" • 10 amp leads – 16 AWG per MIL-W-16878 Type "E"
OPTIONS: • 10 amp current carrying capacity • Hard vacuum compatible • Consult Fabricast for all available options • Consult Fabricast for optional brush grades and characteristics (see page 32)

COMPLETE ASSEMBLY PART NUMBER CODING – Specify fully when ordering:

Type X — Number of Brushes per Ring X (2BR or 4BR) — Brush Grade Number X *(FAG180 — Options (If Applicable) X (10 amp, Vacuum, etc.)

For additional ordering information see page 11.

For Mounting and Wiring Methods, RPM Range, and Operating Environment see pages 9 & 10.

Fabricast, Inc.® MANUFACTURERS OF STANDARD AND CUSTOM SLIP RING ASSEMBLIES
TELEPHONE: (626) 443-3247
FAX: (626) 443-5594
E-MAIL: info@fabricast.com
WEB SITE: www.fabricast.com
P.O. BOX 3178 · 2517 SEAMAN AVENUE, SOUTH EL MONTE, CALIFORNIA 91733
© 2005 FABRICAST, INC. CATALOG 905 S

APPENDIX M

INSTRUMENTATION MANUFACTURE

INSTRUMENTATION MANUFACTURE

INTRODUCTION

This document presents the fabrication of many of the parts of the instrumentation package pictorially. It represents an enormous effort in scheduling and adherence to geometric tolerances in a relatively short time period to produce the vast number of intricate parts required. The order depicted doesn't represent the chronological order of parts manufacture but rather an order as related to each subassembly, starting with those of the global dynamometer and ending with some of the more interesting parts of the pod instrumentation.

1 Global Dynamometer & Associated Parts Fabrication

The main structures of the global dynamometer were made from commonly available mild steel plate, solid round bar and box tubing. Mild steel is easy to weld and machine and exhibits high strength and good corrosion resistance when properly prepared before painting. Lightening holes were included to offset its relatively high density. Aluminum plate and various solid sections were used to fabricate some components where strength was of less concern.

1.1 Inner Pod Strut Manufacture

Figures 1 to 25 show the various stages of manufacturing the inner pod strut. This component connects the pod unit instrumentation to the dynamometer live end masts and is composed of separate steel pieces welded together and then machined as an assembly. Some pre-machining was carried out before welding to complete several of the part features. After machining, the strut was sandblasted and coated with an industrial corrosion inhibiting paint, given that this component will be immersed in water for extended periods of time.

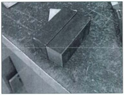

Figure 1 – Steel blocks for idler pulley mounts.

Figure 2 – Gearbox mounting plate, squared and ready to have other features machined.

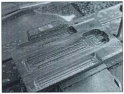

Figure 3 – Main features nearly finished.

Figure 4 – Test fit-up to inner strut tube. (Note drive belt and gearbox side mounting plate test fit.)

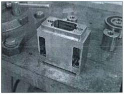

Figure 5 – Completed main pod mount and pulley tensioner blocks. (Note installed idler bearing).

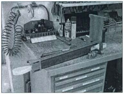

Figure 6 – Test fit-up of main strut components.

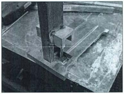

Figure 7 – Tack welding of idler pulley pivot points and main plate to strut tube.

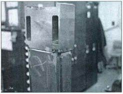

Figure 8 – Tack welding of main pod mount to strut tube.

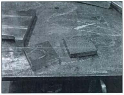

Figure 9 – Main strut tube stiffener plates.

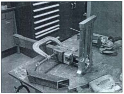

Figure 10 – Main strut gusset fit-up.

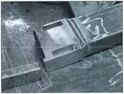

Figure 11 – Completed main pod mount weld.

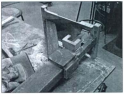

Figure 12 – Ready to finish welding on assembly.

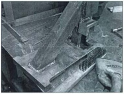

Figure 13 – Welding of tubes to gearbox plates complete.

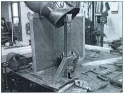

Figure 14 – Completed pod strut assembly.

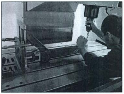

Figure 15 – First machining step, checking alignment of machining envelope with stock available. Sometimes welding will warp the assembly, as was the case here.

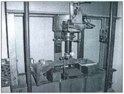

Figure 16 – A 30 ton press was used to correct the misalignment before final machining.

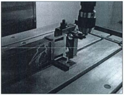

Figure 17 – Dialing in the reference point for final machining.

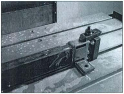

Figure 18 – Reference marks machined to allow coordinates to be picked up in subsequent set-ups.

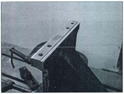

Figure 19 – Alignment faces and mounting holes completed. These will ensure that all distances from the propeller to the dynamometer load cells are exact and thus load calculations can be carried out accurately.

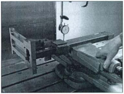

Figure 20 – Part rotated, picking up reference marks for the next machining operation. Note that the mounting holes and surfaces for the gearbox mount have been already machined. This was a mistake and caused a belt misalignment and partial failure during equipment commissioning. These holes and surfaces were fixed at a later date.

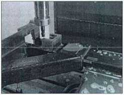

Figure 21 – Finish machining of the belt tensioner pivot points. Note that most of the material had been removed prior to welding to strut assembly.

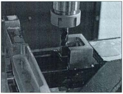

Figure 22 – A close-up of this operation.

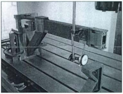

Figure 23 – Final machining set-up to complete mounting holes, faces and pivot shaft holes.

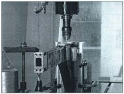

Figure 24 – Center drilling mounting holes. note support in foreground to prevent vibrations during machining.

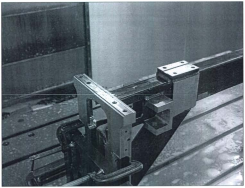

Figure 25 – Completed Piece

As noted in figure 20 the mounting holes and surfaces for the gearbox mounting plates were mistakenly machined prior to welding. This caused a slight misalignment between the axes of the gearbox output shaft and the propeller shaft. Upon starting the drive system for the first time this slight misalignment allowed the teeth of the drive belt to ride up on the teeth of the gearbox output shaft gear. Because the belt is a high strength steel strand reinforced polyurethane construction, the momentary effective increase in pulley center-to-center distance caused several of the strands to break, thus limiting the torque that could be applied during the initial testing.

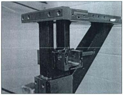

Figure 26 – After machining, the pivot shafts were test fit in their bores.

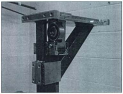

Figure 27 – The tensioner blocks and pulley were test fit next.

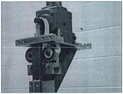

Figure 28 – The gearbox and belt test fit next.

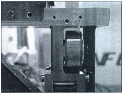

Figure 29 – Unlike the gearbox, both pulleys are aligned correctly.

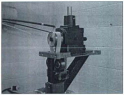

Figure 30 – Finally the drive gear pulley and belt are test fit.

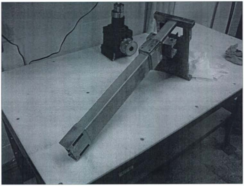

Figure 31 – Completed inner pod strut.

Figures 26 to 30 show the finished piece being test fit with various components of the drive belt system. Figure 31 depicts the part after sandblasting. It was painted shortly afterwards to ensure there was a good bond between the paint and steel surfaces.

1.2 Strut Support Masts

The next components to be discussed are the two masts allowing the inner pod strut to be connected to the live end of the global dynamometer as well as the motor mount plate and bracing. The mast subassemblies are constructed of steel because they must carry the bending loads induced on the dynamometer as the pod unit moves through the water in the test tank. The many lightening holes are drilled to reduce the mass that must be carried by vertical (Z-direction) load cells in the dynamometer. The small x-brace frames that form the rigid structure surrounding the motor increase the moment of inertia of the main masts without adding a significant amount of weight to the system.

Figures 32 to 43 show the mast fabrication details while figure 44 shows a test fit of the main mast and strut. These subassemblies were also welded first then machined after.

Figure 32 – Setting the reference for the 3" x 3" x 1/8" steel tubing that forms the main mast structure.

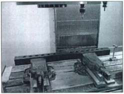

Figure 33 – The first set of lightening Holes milled in top surface.

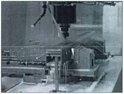
Figure 34 – Plenty of coolant ensures an exact cut.

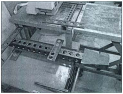
Figure 35 – All parts for both masts after machining.

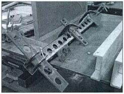
Figure 36 – Fit-up of parts prior to welding.

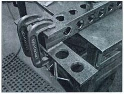
Figure 37 – Welding nearly complete.

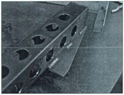

Figure 38 – Welding at the base. This plate increases the bending strength of the inner pod strut.

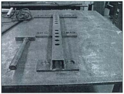

Figure 39 – Completely welded support mast.

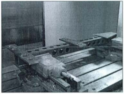

Figure 40 – Setup of the main mast for milling.

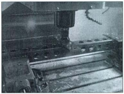

Figure 41 – Facing the mounting surfaces.

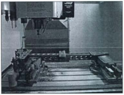

Figure 42 – First side of main mast finished and checked for flatness. Face machining of plate structures can release stresses causing bending of the structure.

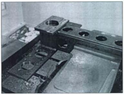

Figure 43 – The final machining of the main mast completed.

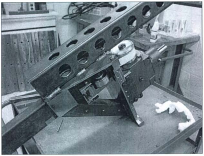

Figure 44 – Test fitting the main mast to the inner pod strut.

1.3 Motor Mount Plate

The two masts act as supports for the motor base plate. This plate is made of aluminum and contributes to the weight savings of the structure.

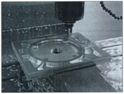

Figure 45

Figures 45 and 46 show the machining of the plate.

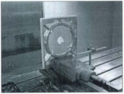

Figure 46

Figure 47 shows the motor test fit, figure 48 shows the plate supported by the masts.

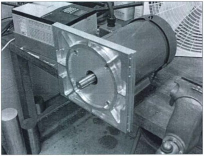

Figure 47 – Motor test fit.

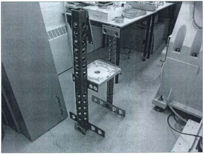

Figure 48 – Test fit of motor plate to masts.

1.4 Mast Base Plate & Supports

Completing the connection of the pod support structures to the live end of the dynamometer is the mast base plate and supports, center azimuth spacer and the azimuth angle setting plate. Figure 49 shows the plate stock for the mast base plate and mast mounts.

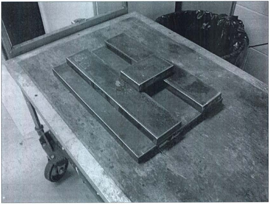

Figure 49 – Steel plate stock.

Figures 50 to 53 show the various stages of producing the mast mount plates. Figure 54 and 55 show the completed mast base plate. All these components were face milled with an insert holding face milling cutter to produce the finish.

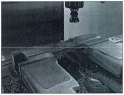

Figure 50 – Facing the mast mounts.

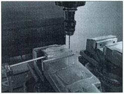

Figure 51 – Drilling mounting holes.

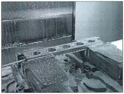

Figure 52 – Milling lightening holes.

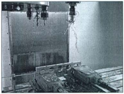

Figure 53 – Milling screw head counter-bores.

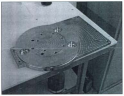

Figure 54 – Completed mast base plate top view.

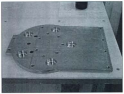

Figure 55 – Bottom view.

Figures 56 and 57 show the stock used to machine the mast center azimuth spacer and live end center spacer respectively. Large pieces were used to allow adequate bolting of the joints and extra material in the event of needing to modify the structure to accommodate bearings for dynamic azimuth motion of the pod unit.

Figures 58 to 62 show the turning of the live end center spacer. Both spacers were manufactured on a CNC lathe in the same way. Reliefs are to reduce weight.

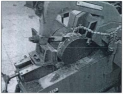

Figure 56 – Steel round stock for the mast azimuth center spacer.

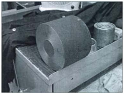

Figure 57 – Steel round stock for the dynamometer live end center spacer.

Figure 58 – Boring the internal diameter.

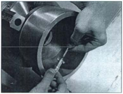

Figure 59 – Checking the internal bore diameter.

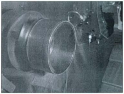

Figure 60 – Turning the outer diameter to size.

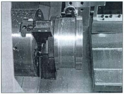

Figure 61 – Machining the reliefs.

Figure 62 – Both spacers completed except for threaded mounting holes.

Figure 63 shows a test fitting of the center spacer. Figures 64 to 66 depict tapping the threaded mounting holes. Figures 67 and 68 show a test fit of the mast mounts to the base plate. After this step, all components were sandblasted and painted to protect them from corrosion. Figure 69 shows a test assembly of the painted components

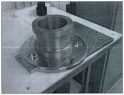

Figure 63 – Test fit of spacer to base plate.

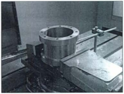

Figure 64 – Set-up to drill and tap mount holes.

Figure 65 – Bottom tapping holes after starting with CNC tapping head attachment. Deep tapping in steel with a tapping head runs the risk of breaking the tap. Finishing by hand prevents (reduces) this risk.

Figure 66 – Tapping completed on live end spacer.

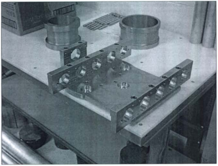

Figure 67 – Test fit of mast mounts to base plate.

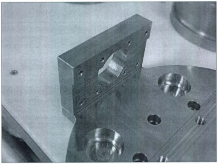

Figure 68 – A close-up of the fit before mounting holes drilled.

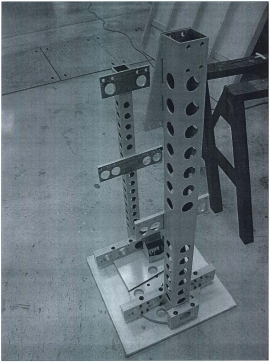

Figure 69 – Test assembly of masts and base plate after painting.

The last component of the mast support structure to be manufactured was the azimuth angle setting plate, shown in figure 70.

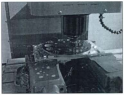

Figure 70 – Machining the azimuth angle setting plate. This plate also supports the weight of the entire pod unit assembly.

1.5 Dynamometer Live Plate Components

Next, the global dynamometer live end component fabrication is discussed. Figure 71 shows the ½" thick steel plate stock that is used for both the upper and lower live plates. The hold down slots in the table of the CNC milling machine were measured during the design phase so that a hold down pattern could be incorporated into the plate design, thus making the plate also serve as its own machining jig (these holes are also to be used in the future should a drive system be installed for a dynamic azimuthing system). To fabricate this part, first the hole pattern was machined complete with a shallow counterbore. This allowed a cylindrical stand-off spacer to be placed on the table and then the plate placed over the set of stand-offs. This prevented any natural deviations in the plate from inducing any stress during later assembly, given that the counter-bores were machined with the plate in a relaxed state. These steps are important in producing an accurate dynamometer. Figure 72 shows a side view of the support stand-offs.

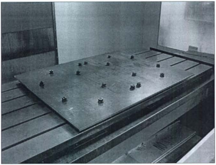

Figure 71 – Live upper/lower plate mounting details.

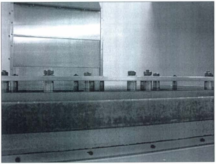

Figure 72 – Stand-offs form part of the machining jig for this part production.

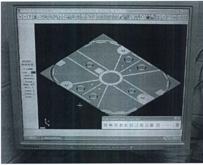

Figure 73 – The live plate as viewed in MasterCAM™ toolpath generation software.

Figure 73 shows a typical display seen while a part machining program is being generated. Figures 74 and 75 show the machining in-progress. Essentially this operation mills a series of surfaces to which all other components are attached. Because the plate is firmly attached to the bed of the milling machine, all elevations are extremely accurate. The symmetrical nature of the jig design also ensures that the elevations of the plate are accurate from one side to the other, a task that can at first seem trivial but in practice is difficult to carry out on flexible members or subassemblies. Figure 76 shows the completed lower live plate. The upper live plate was machined in the same manner. Figure 77 shows the plate stock. Figures 78 and 79 show the milling of lightening holes in the upper live plate. Helical milling was used here by the addition of a Z-feed command in the NC code program. This drastically reduced milling time.

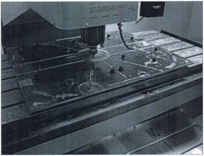

Figure 74 – All elevations machined, awaiting the hole cutouts.

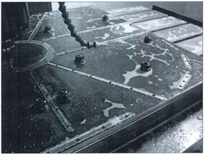

Figure 75 – A close-up of above.

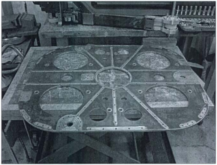

Figure 76 – The completed lower live plate.

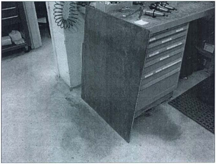

Figure 4.77 – Stock for the upper live plate.

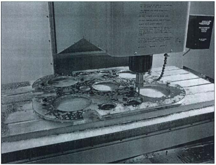

Figure 78 – Machining lightening holes in the plate.

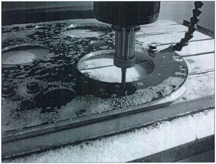

Figure 79 – Close-up of above.

When both plates were finished, the surfaces were cleaned and then painted. The edges of all holes were painted first, then the top and bottom surfaces. Figure 80 shows the edges after being painted, figure 81 shows the completed paint coating.

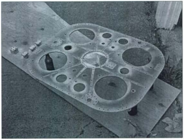

Figure 80 – Painting of the edges of the holes.

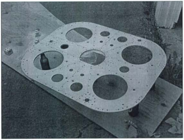

Figure 81 – Final coat of paint added.

The live plates are separated by aluminum spacers. These components of the live end separate the steel plates thereby increasing the moment of inertia of this assembly. As with the steel parts, as much material as possible was removed to reduce the weight carried by the Z-direction load cells. Figures 82 and 83 show the stock from which all stiffeners were manufactured. The material is T6061 ½" aluminum plate.

Figure 82 – Aluminum plate stock.

Figure 83 – Aluminum plate stock.

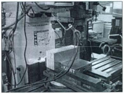

Figure 84 – Preparing the machining blanks.

Figure 84 shows the first operation in preparing machining blanks for the stiffeners. The edges are being squared up with a fly cutter using power feed on the manual milling machine. Note the hydraulic vise and air/mist cooling of the cutter tip, a very effective and efficient machining method. All blanks of each type were machined in one set-up to save time and ensure that all pieces had the same height. Figure 85 shows a stiffener in the CNC milling machine. The stiffener designs were kept to four variations to save time in the machining stage: only 4 sets of programs had to be produced to make all 22 parts.

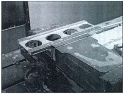

Figure 85 – CNC stage of stiffener fabrication.

These parts also afforded the opportunity to tweak the cutting tool feedrates to decrease the time required for each stiffener.

Figure 86 – Finishing threaded holes with an automatic tapping head attachment. Note the long steel stand-off to the left of the tapping head. This allows a driving torque to be developed for the tap and prevents the part from rotating should it be grabbed by the tool.

Figure 86 depicts the thread finishing. The pilot holes were completed in the CNC milling machine. Figure 87 shows the test fitting of nearly all the stiffeners.

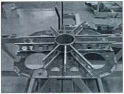

Figure 87 – Test fit of stiffeners.

The last component to connect the upper and lower plates of the live dynamometer assembly is the flex link cage. This aluminum component adds stiffness and protects the lower end of the flex link from accidental bumping. Figures 88, 89 and 90 show the production of these 3 pieces. When finished, all of these aluminum parts were painted with a clear coat to protect them from the high humidity levels of the test tank.

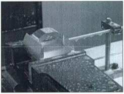

Figure 88 – Milling a cut-out to allow access to the bolts of the flex link mounts.

Figure 91 shows nearly all aluminum parts in a test fit with both steel plates. Screws were tried in random hole positions to ensure that the assembly could proceed when all parts had been painted.

Figure 89 – Two milled pieces and blank for third.

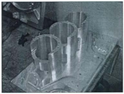

Figure 90 – Completed with tapped holes.

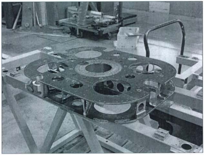

Figure 91 – Test fitting aluminum pieces between steel plates.

1.6 Flex Links

The discussion now turns to the production of the flex links and their mounts. These components ensure exact placement of the axis through which the forces act on the dynamometer load cells as well as their loading limit. Dimensional checks were even more stringent during the fabrication of these components. Figure 92 shows the 17-4 PH stainless steel blanks with the force transducer mounting threads machined. A class H2 fit was employed with these threads to prevent vibrations due to excessive clearance between the load cell mounting stud and the threads. Extra care was taken to ensure that no debris from the tapping operation remained in the hole. This prevents binding of the mating parts due to the sticky nature of stainless steel threaded components. Figure 93 shows the machining setup that produces the flats allowing a wrench to be used in the adjustment and final tightening of the flex link. Figure 94 shows the completed hex head on the load cell end of the flex link.

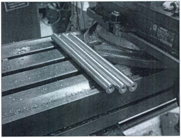

Figure 92 – Flex Link Blanks

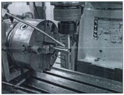

Figure 93 – Milling wrench flats using a manual indexing head.

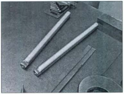

Figure 94 – Completed hex head on load cell end of flex link.

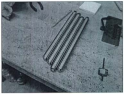

Figure 95 – Stud end hex completed.

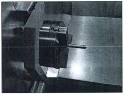

Figure 96 – Setup in the CNC lathe to turn the adjustment stud end of the flex link.

Shown in figure 95 is the completed adjustment stud hex. Having a nut form on each end of the flex link allows installation without stressing this component or the load cell body in torsion, which is important for longevity and preventing incorrect loading that could lead to premature or unexpected catastrophic failure. This completes the manual aspect of preparing the flex link blank for final machining. Figure 96 highlights the relative placement of the blank in the chuck of the CNC lathe. Stability while machining a flex link is always a problem, it results from the one or two small diameter areas of the component and minimizing the overhang is of the utmost importance. Figures 97 and 98 indicate the close proximity of the tool holder to the chuck jaws during the threading and neck down operations. Note also the tailstock in figure 97.

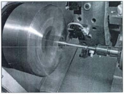

Figure 97 – Minimum part overhang ensures maximum stability during machining.

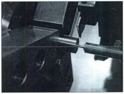

Figure 98 – The diameter of the necked down area of the flex link is critical.

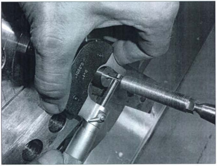

Figure 99 – Checking the critical diameter.

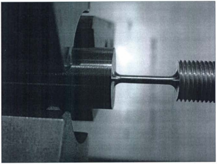

Figure 100 – The completed stud end.... Perfection!

Micrometers were used extensively during the manufacture of all flex links as shown in figure 99. A close-up of a completed neck down area is shown in figure 100. Note the exceptionally smooth transitions between the threaded length, radii and necked down areas. Figure 101 shows several flex links prior to machining the second necked down area. Note the nut used to test the threads. Figures 102 and 103 show the load cell mounting end of the load cell and the dimensional check of the necked down area. Note that high percentage of scrap pieces would result from using manual methods to produce such a piece and that no parts were discarded during the machining of the 12 flex links for this project. Shown in figure 104 is the jig (being removed) used to prevent damage to the stud end of the flex link as the load cell mount end is machined. The delrin disk was machined to a diameter slightly smaller than the bore in the chuck and then mounted to the stud before being inserted into the chuck's stock receiving tube. Figure 105 shows the completed flex link being test fitted to one of the dynamometer's six 1000 lb (4448.2 N) button load cells.

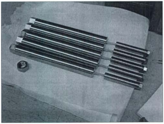

Figure 101 – Flex links ready for last machining operation.

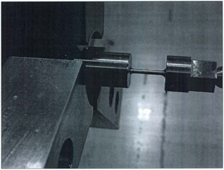

Figure 102 – Load cell necked down end.

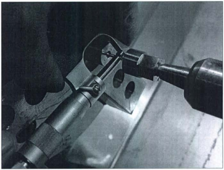

Figure 103 – Checking the critical diameter.

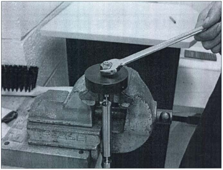

Figure 104 – Flex link machining jig.

Figure 105 – Completed flex link mounted to 1000 lb (4448.2 N) button load cell.

1.7 Heat Treatment of Flex Links

Figures 106 to 110 show the heat treatment process of the flex links, which is the final step in their production. The heat treatment was carried out to H-900 specifications, which is heating to 900° F for 1 hour then allowing to air cool at room temperature.

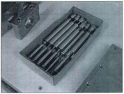

Figure 106 – Flex Links prior to heat treatment.

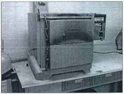

Figure 107 – The heat treatment oven located in the materials lab, Faculty of Engineering and Applied Science.

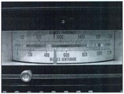

Figure 108 – The temperature specified for an H-900 heat treatment of 17-4 PH stainless steel is 900° F.

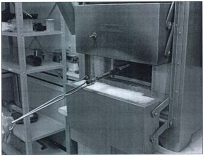

Figure 109 – Removing the first flex link to allow air cooling at room temperature.

Figure 110 – Two complete flex link sets after heat treatment.

After heat treatment, a hardness test was carried out on two test samples. One sample was subjected to the same heat treatment procedure as the flex links. The test samples were taken from the same stock as the flex links. Figure 111 shows the sample and the indenter used in the Rockwell hardness test. Figures 112 and 113 show the sample and reading of the test on the 'as-received' sample. Figures 114 and 115 show the heat treated sample and hardness reading. These results indicated that the components had been successfully increased in strength.

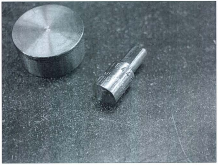

Figure 111 – Sample and indenter for the Rockwell hardness test for 17-4 PH SS.

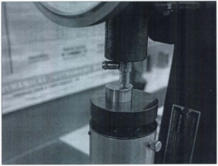

Figure 112 – Hardness testing of the non heat treated test sample.

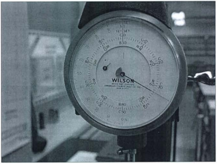

Figure 113 – Hardness reading for the "C" scale.

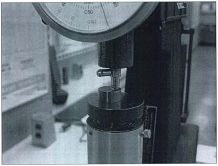

Figure 114 – Hardness testing of the heat treated sample.

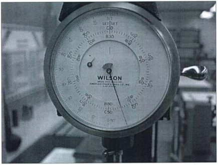

Figure 115 – Hardness reading for the “C” scale

1.8 Flex Link & Load Cell Mounts

The fabrication of the flex link and load cell mounts will now be discussed. These parts were manufactured using the CNC lathe. The following photos show the parts at various stages beginning with figure 116, which shows the hexagonal bar stock used in the manufacture of the load cell mounts for the X, Y and Z reference frame positions. Where-ever possible the component's design utilized available stock material sizes, in this case it was hexagonal bar stock. This kept manufacturing time to a minimum. Figure 117 shows a close-up of the nearly completed load cell mount. Figure 118 depicts all six completed load cell mounts. Figure 119 displays a y-axis flex link with load cell and its mount. Figure 120 shows thread checking using the three wire technique. This method was used on all component threads.

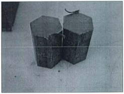

Figure 116 – Hex steel bar stock.

Figure 117 – Z-load cell mount nearly completed.

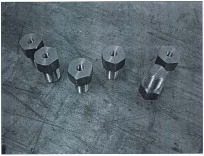

Figure 118 – Completed Load Cell Mounts

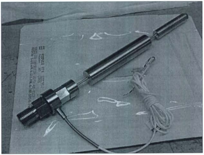

Figure 119 – Y- Axis load cell, mount and flex link

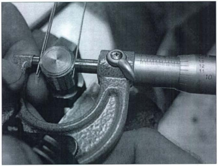

Figure 120 – Thread checking using the 'three wire' technique.

This marks the end of the discussion on the fabrication of the global dynamometer. The discussion now shifts to the pod instrumentation manufacture.

2 Pod Instrumentation Component Manufacture

The fabrication of some of the major instrumentation package components is now discussed. These components were machined with relative ease, but generally required more set-up time because of their intricacy.

2.1 Propeller Shaft Manufacture

As stated in the chapter on design, the propeller shaft material is type 303 stainless steel. This material was chosen because its ease of machining would facilitate the number of machining operations that had to be carried out, in addition to the type, especially the deep drilling of the passageway through the shaft's center.

Manufacturing began with turning the shaft blank from the 76.2 mm (3") diameter round stock. During the first setup the shaft length, gauge area, wiring passageway, o-ring seal mounting groove and threads for the attachment of the propeller hub instrumentation features were machined. After this step the seal area of the shaft was polished with a super fine wet sanding paper and then a polishing compound. This step was carried out while the part was still in the lathe. Figure 121 shows the seal end of the propeller shaft blank. The drive surfaces for the transmission of torque were machined next. This operation was completed on the CNC mill while the part was mounted in a three jaw chuck. After this step the shaft was re-mounted so that the features in the opposite end could be completed. Figure 122 shows the arrangement for the mounting. The chuck had to be elevated from the table to allow several tool indexes to be carried out.

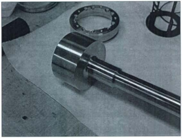

Figure 121 – Propeller shaft blank.

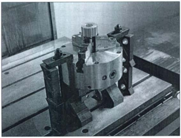

Figure 122 – Setup to allow machining on the opposite end of the blank.

In this setup the mounting holes for the hardened and ground stainless steel rods that allow the torque to be transmitted from the drive gear to the shaft were drilled and reamed to size. The clearance slots for the balls and ball cage were also milled in this setup. This step was carried out last, and completed with an end mill. Figure 123 shows drilling of the rod holes. Figure 124 shows the part after the ball clearance slots have been milled. Note the dot used for timing the last steps of the shaft manufacture.

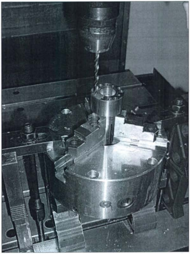

Figure 123 – Drilling of the rod mounting holes.

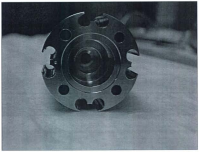

Figure 124 – Completed rod mounting holes & ball clearance slots.

The next series of steps to be carried out finished the propeller shaft. The holes that allowed the wiring to pass from one location to another were machined. The 6.35 mm (1/4") hole through the center of the shaft had been competed during manufacture of the blank. To complete this passageway the entrances and exits intersecting this central passageway had to be completed. Figure 125 shows the setup for this operation. The angles of the intersecting holes were selected to be integer numbers during the design phase to allow an easier setup procedure. The angled table was set up to the correct value and then the shaft center line dialed in. Figure 126 shows this operation. Several points were selected to ensure that the shaft was mounted on a plane parallel to the X-axis of the manual milling machine. When the setup was complete an end mill was used to produce a flat face that would allow a center drill to be used to produce the hole for the propeller thrust signal cable entrance and torque gauge wiring. Figures 127 to 129 show this series of steps.

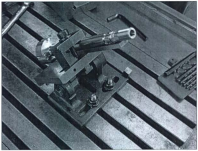

Figure 125 – Setup for drilling the wiring exits and entrances to the central passageway.

Figure 126 – Locating the shaft center line.

Figure 127 – Using an end mill to produce a flat surface for center-drilling.

Figure 128 – Centre-drilling the hole location.

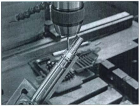

Figure 129 – Final hole drilling.

The next operation on the propeller shaft was drilling the wiring exits from the central passageway. The shaft was removed from angle plate and mounted in an indexing head that had adjustment in angle from the bed and rotation of the chuck. The dot machined earlier in production was used as the reference point before rotation. The same procedure for drilling the holes as before was carried out and is depicted in figure 130 to 132. Figures 133 and 134 show the completed holes. Figure 135 shows the completed propeller shaft. The hub instrumentation manufacture is discussed next.

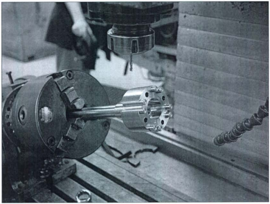

Figure 130 – Shaft mounted in an angled indexing head for milling of the starting flat.

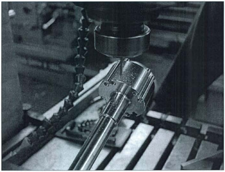

Figure 131 – Milling the flat to allow starting the drill.

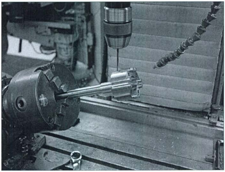

Figure 132 – Final drilling of the hole. Note this procedure was repeated at 180°.

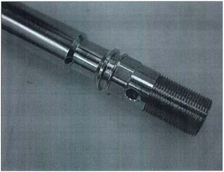

Figure 133 – Final wiring entrance holes.

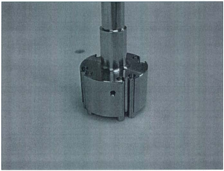

Figure 134 – Final wiring exit holes.

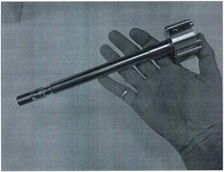

Figure 135 – Completed propeller shaft.

2.2 Propeller Hub Thrust Instrumentation Manufacture

The propeller hub thrust instrumentation assembly consists of 7 major components, listed below:

- seal adaptor
- hub taper angle adaptor
- reference base
- ball cage
- propeller mounting adaptor (live end)
- drive rods
- retaining nut

Several of these had several challenging aspects to their manufacture which had to be accounted for during the design process to ensure a successful part manufacture. For example, the revolved profile of the sealing section of the reference base had to be composed of arcs and lines to make maximum use of the CNC lathe's controller to ensure a smooth and accurate o-ring sealing surface. Consideration of the tooling available was key in the development of this aspect of the design. A similar consideration was made when designing the drive faces, which are internal in the case of the reference base. It had to be ensured that the tooling could be utilized in such a small space and at such depths to get the required fillet radius between faces. The remaining difficulty was in utilizing multiple setups. Care was taken to ensure that orientation changes during machining were minimized. As another example, achieving the desired dimensions in some materials is not so trivial, given a certain desired geometry and the method used to produce it. This became evident with the ball cage, which has the important function of allowing installation of the drive balls to occur. Without this component there would be almost no procedure to facilitate this action. To allow this function, the holes had to be tight enough to hold the balls, but yet not so tight as to induce friction in the system. The author sought to produce a design that allowed this very light grip that would allow holding of the balls to occur, yet also allow the relative positioning of the balls when installed so as to correctly distribute the load without introducing excess friction. To allow this to happen, some experimentation had to occur as the delrin material used in this component does not yield the size of hole of the drill bit used to make it. In this case, using a 6.4 mm (0.252") drill bit was successful in producing a hole with the slightly smaller than 6.35 mm (0.250") diameter required. The smaller hole is a result of the material being deflected slightly during processing. In the end, the desired result was produced. The ball cage held the ball elements quite well, but did not add a considerable magnitude of friction to the system.

The depiction of the part manufacture begins with the seal adaptor. Figure 136 shows the seal adaptor as it is being parted off from the stock from which it was made. Figure 137 shows the part being set up to finish the other side of the blank. Figures 138 and 139 show both sides of the finished piece. Note the smooth finish on the inner bore that will become the sealing surface for the inner part of the propeller.

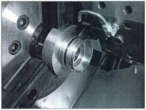

Figure 136 – Parting off operation.

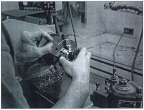

Figure 137 – Setup for the back face.

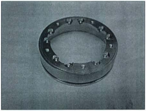

Figure 138 – Mating face side of the seal adaptor.

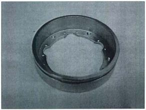

Figure 139 – Seal bore side of the seal adaptor.

Next to be discussed is the hub taper angle. As discussed in the design chapter, this component is made from bronze and facilitates the isolation of any effects the gap pressure may have on other readings. Figure 140 shows the initial setup of the turning operation of this part's manufacture. Figure 141 and 142 show the completion of the blank. Figure 143 and 144 show the setup and nearly completed mounting hole pattern. The countersinks for the #4-40 screws were completed last.

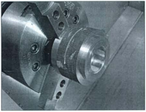

Figure 140 – Initial blank turning setup.

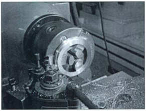

Figure 141 – Completion of the mounting face of the blank.

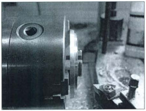

Figure 142 – A side view of the completed blank.

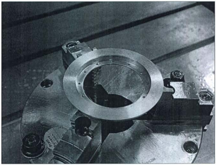

Figure 143 – Setup for drilling the mounting holes.

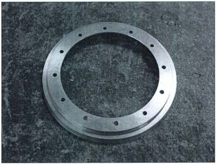

Figure 144 – The completed hub taper angle adaptor, except for the countersinks.

The next component of the hub instrumentation manufacture to be shown is the reference base. The utmost care was taken in machining this component as the smoothness of the thrust decoupling joint depended upon the accuracy of all features in this part. The first step consisted of turning the outer diameter of the 303 stainless steel round stock to a known and true cylindrical surface. This blank was then mounted to the bed of the CNC milling machine in a three jaw chuck. The first operation in this setup consisted of drilling and reaming the holes for the drive rods. Then clearance slots for the balls and ball cage assembly were milled. Figure 145 shows the blank in the milling machine setup during the drilling cycle. Figure 146 shows the milling of the clearance slots. After this step, the part was setup in the CNC lathe. The seal holding grooves, inner bore for the propeller shaft and retaining nut, as well as the remaining outer diameters for the hub taper angle mounting surfaces were machined in this setup. Figure 147 shows a check of the retaining nut bore diameter.

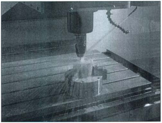

Figure 145 – Drilling the rod mounting positions in the reference base blank.

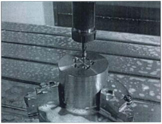

Figure 146 – Milling the clearance slots for the drive cage and ball elements.

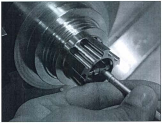

Figure 147 – Checking the bore diameter of the retaining nut mounting location.

After this step the reference base was parted off and the back face completed to give a smooth finish, as this face will form part of the fixed face of the propeller hub facing the end of the pod. At this point the fit of the stainless steel rods was checked in each position, as shown in figure 148. The fit of the hub taper angle adaptor was also tried as shown in figure 149.

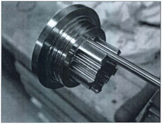

Figure 148 – Checking the fit of the drive rod stock.

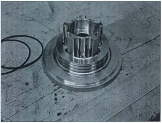

Figure 149 – Checking the fit of the hub taper angle adaptor.

At this time the o-rings were fabricated and test installed, then the seal adaptor was installed and tested for ease of motion. This is shown in figure 150 and 151.

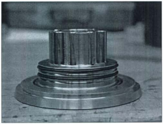

Figure 150 – Test installation of the o-rings used to seal the hub instrumentation.

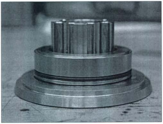

Figure 151 – Test installation of the seal adaptor.

At this point the reference base was again mounted into the milling machine in a three jaw chuck and the final drive features machined into the back face, as shown in figure 152. The o-ring installation taper was also machined at this time. This piece was then flipped over and mounted one final time in the 3 jaw chuck. In this setup, the threaded mounting holes for the hub taper angle adaptor were machined, as was the clearance slot for the thrust load cell wiring, as seen in figure 153. This completed the reference base.

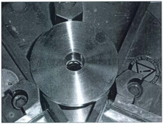

Figure 152 – Machining the drive faces in the reference base.

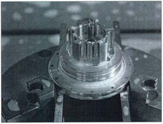

Figure 153 – Completed part after milling the wiring clearance slots and drilling the threaded mounting holes for the hub taper angle adaptor.

A discussion on the ball cage manufacture now follows.

Machining the ball cage commenced by turning and facing a suitably sized piece of Delrin® material. The blank was then mounted in the 3 jaw chuck on the CNC milling machine. The individual mounting arms of the cage were machined as pockets, then the component was parted off in a manual lathe. The holes were then drilled using as 6.4 mm (0.252") diameter drill bit to produce the required fit for holding the drive ball elements, as discussed earlier. This completed the part. Figures 154 through to 158 show the manufacturing process.

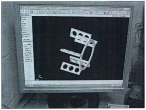

Figure 154 – The ball cage as viewed on MasterCAM™.

Figure 155 – The milling of the ball cage holders.

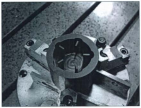

Figure 156 – The nearly completed part.

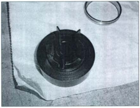

Figure 157 – Part ready for drilling.

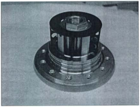

Figure 158 – Test fit of completed ball cage on reference base.

The next component of the hub instrumentation to be depicted is the propeller mounting adaptor. This is the live end of the instrumentation sub-assembly to which the propeller is mounted as well as the live end of the thrust load cell. Manufacture of this component started with turning a blank of type 303 stainless steel on the CNC lathe, then finishing on the CNC milling machine. As with the reference base, alignments between setups were critical to ensure the successful operation of the thrust decoupling joint and smooth transfer of torque to the propeller. Figures 159 through to 164 show the manufacture of the part.

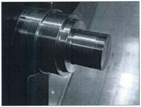

Figure 159 – Turning the blank for the reference base.

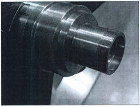

Figure 160 – Machining the counter-bore face that holds the load cell jam nuts.

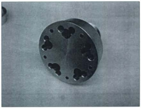

Figure 161 – Part with drive rod, ball element clearance slot and fastener holes.

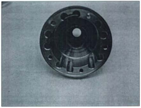

Figure 162 – Part with all counter-bores completed.

Figure 163 – Test fit of the seal adaptor on the propeller mount adaptor.

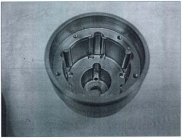

Figure 164 – Completed part with wiring space slots, and a test fit of drive rods.

The last two components of the hub instrumentation to be discussed are the drive rods and retaining nut. The drive rods were simply cut to length and then modified by the addition of a #4-40 threaded hole in one end. This allows the rod to be extracted easily by threading in a screw and then pulling the rod out. During the parting off operation, the rod was mounted in a lathe equipped with a collet chuck to prevent damage to the rod surface.

The retaining nut was machined from bronze by first turning it the CNC lathe. The threads were then completed in the chuck using the tailstock to keep the tap parallel to the nut center axis. The part was then mounted in a dividing head to complete the milling of the hex flats. Note that the flange retains the drive rods in the reference base as well as keeping the reference base attached to the propeller shaft. The generous fillet under the flange compensates for its thinness. Figures 165 and 166 show the details of the completed retaining nut.

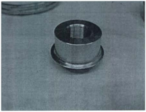

Figure 165 – Underside of completed retaining nut.

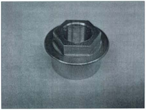

Figure 166 – Hex side of completed retaining nut.

2.3 Drive Gear Manufacture

The next major component to be discussed is the drive gear. This component complements the propeller shaft as this component is in direct contact with it via the drive ball elements. There is a ball cage between the two that locate the ball elements, and this component was manufactured in the same manner as the drive ball cage for the propeller hub instrumentation.

The drive gear was started by turning an aluminum blank on a manual lathe. Once completed, the timing belt teeth used by the drive belt to apply torque to the drive system were machined. For this operation the blank was placed in a dividing head on the CNC milling machine. The tooth profile was programmed manually and then copied in a word processor to allow the toolpath to traverse across the tooth face. After each tooth milling, the gear was rotated by the correct pitch angle. After this operation the drive rod holes and ball element clearance slots were machined while mounted in the 3 jaw chuck of the CNC milling machine. Completing the part consisted of milling the PC board mounting pockets in the back face of the drive gear. Figure 167 shows the part after the teeth have been completed. Figure 168 shows the part before completing the last step of milling the PC board mounts. Note that there is a groove machined on each side of the gear teeth. This is to allow the tooth to be completely formed. The belt guide rings are mounted in these slots to complete the geometry required for correct belt tracking, as discussed in the chapter on design. Figure 169 shows the completed drive gear, complete with a test fit of the belt guide rings, support bearings and blade position sensor, which was not used in the end due to time constraints.

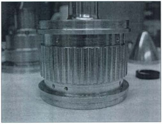

Figure 167 – Drive gear with teeth machined.

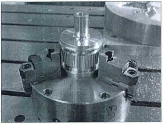

Figure 168 – Drive gear mounted for completing operations.

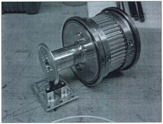

Figure 169 – Completed drive gear.

2.4 Drive Case Manufacture

The next component to be discussed is the drive case manufacture. There are two similar parts and a middle section to this major component. The function of this case is to act as a water-tight container to house the drive system assembly and to act as a base to which all other subassemblies can mount.

Each end plate of the drive case is an aluminum component into which one of the two drive gear support bearings mount, and two of the four idler pulley bearings mount. Manufacture of the end plate began with an aluminum blank that had been milled to an exact size to facilitate mounting in the hydraulic vise of the CNC milling machine. Having all faces milled as orthogonal before fabrication allowed part orientation changes to take place with a minimal chance for error. Figure 170 shows the drive case segment to which the slip ring brushes mount. In this figure the clearance bore for the slip-rings, as well as the idler pulley bearing bores and bolt pattern that keep the case components together have been machined.

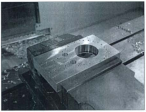

Figure 170 – Initial machining of drive gear housing.

After this step the final drive gear bearing bore and its relief were machined, as shown in figure 171. The part orientation was then changed and the top mounting details that allow the pod unit to the attached to the lower strut assembly completed, as shown in figure 172. The screw holes that allow the fasteners to hold the assembly together were

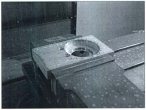

Figure 171 – Completed drive gear bearing bore and installation relief.

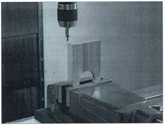

Figure 172 – Machining the pod mounting features.

then finish tapped. The holes were partially tapped in the milling machine, but finished by hand to prevent a tap from breaking. This step is shown in figure 173. Next the face to which the brush block mounts was machined and then finally the outer profile was completed. The part was then checked as shown in figure 174. The final part is shown in figure 175.

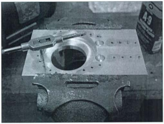

Figure 173 – Finish tapping the holes by hand.

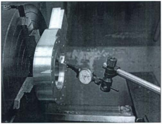

Figure 174 – Checking the concentricity of the circular features.

The opposite cover was manufactured in a similar manner. The middle section was fabricated by first drilling the through holes into the thick aluminum block. The profile was then machined on the inside of the part and finally the outside. Next the pod shell manufacture is discussed.

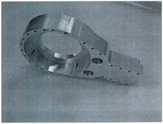

Figure 175 – Completed drive gear housing component.

3 Pod Shell Manufacture

The pod shell assembly consists of the following components:

- pod shell body
- ring adaptor
- pressure plate adaptor
- gap adjustment ring adaptor
- gap filler
- pod body end cone

These components were machined exclusively using a combination of the CNC milling machine and CNC lathe, with some finishing steps using a manual milling machine. The pod shell body was machined from renshape 460. Prior to machining the shell, there were two blocks of material glued together to form a laminated block that was 101.6 mm (4") thick. This formed the stock from which one half of the pod body was machined. The first step consisted of milling out the interior clearance volume (the design of which is discussed in chapter 3) as shown in figures 176 and 177. Then using a jig plate to mount the material, the block was flipped over and the outside form machined. The second half was produced by mirroring the toolpath and machining a second block. The process was the same for each block.

The ring adaptor and gap adjustment ring adaptor were machined from 316 stainless steel on the CNC lathe. These were simply machined from one solid length of round stock. Figures 178 through to 180 show the process used for removing the bulk of the material in the center of the part. Figure 181 shows the finished adaptor and figure 182 shows a test fit in the pod shell.

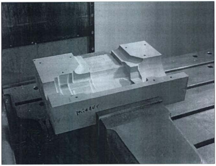

Figure 176 – Milled out interior space.

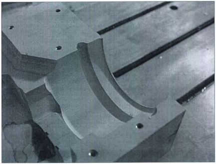

Figure 177 – Milled out space for the ring adaptor.

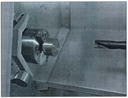

Figure 178 – Start of the material removal process in the part center.

Figure 179 – Turning in progress.

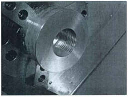

Figure 180 – Ring adaptor with center roughing finished.

Figure 181 – The completed ring adaptor.

Figure 182 – A test fit of the part in the pod shell.

The pressure plate adaptor and gap fillers were machined as two separate pieces for each assembly. This was necessary because their assembly to the instrumentation required that each half mount on the assembly as a separate piece. This meant that the joint between the two parts had to essentially have zero thickness, or no gap. To produce such a feature, two identical parts were produced and then each half had most of one side cut away with two bandsaw cuts. The edges were then finished on a manual milling machine. Figure 183 shows a finished gap filler ring. Figure 184 shows the pod shell, ring adaptor and one piece of a gap filler and pressure plate adaptor set.

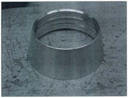

Figure 183 – A completed gap filler half.

Figure 184 – Pod shell, ring adaptor and gap filler set halves.

The milling process to finish the edges of the gap fillers and pressure plate adaptors was the same. The setup is shown in figure 185. A test fit of the gap filler installation on the pod shell, complete with pressure plate adaptor and rolling o-ring seal is shown in figure 186. A similar test fit was carried out on the pressure sensing plate, as shown in figure 187. The pod end cone and ring adaptor used to access the gap adjustment mechanism was similarly machined and a test fit of these components is shown in figure 188. This ends the discussion on the pod shell manufacture.

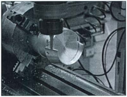

Figure 185 – Milling process for gap filler and pressure plate adaptor pieces.

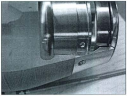

Figure 186 – Test fit of gap filler components with shell.

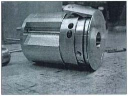

Figure 187 – A similar test fit of gap filler components on pressure sensing plate.

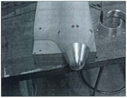

Figure 4.188 – Test fit of pod end cone and ring adaptor with shell.

4 Propeller Manufacture

The propeller manufacture consisted of first machining a blank that had the interior features of the hub design and mounting locations, as well as the jacking screw threads. Next the blank was mounted to the trunion of the 4^{th} and 5^{th} axis attachment of the HAAS milling machine. The first side of the propeller was then machined to completion. This is shown in figures 189, 190 and 191. The resulting cavity was then filled with a fast

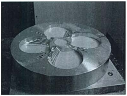

Figure 189 – Roughing operation of the propeller.

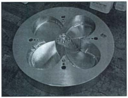

Figure 190 – The completed first side of the propeller.

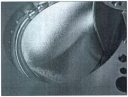

Figure 191 – A close-up view of the surface finish, before completion by hand.

curing polyurethane filler resin which was machined flat when hard. Note that the propeller blade surface of the cavity to be filled was waxed to keep the resin from adhering to the surface permanently. The procedure of using resin reduced any potential vibrations while the second side of the propeller was machined. The end result is shown in figure 192. The partially finished propeller was then remounted in the milling machine and the second side completed. After completion the polyurethane resin was then removed. The finish of the hub and blade surfaces was then completed by a hand sanding and polishing operation, carried out by technicians at the model making shop at IOT. The final propeller finish is shown in figure 193. After completing the blade finish, the o-ring seal entrance taper was machined. This type of operation is best carried out on a lathe, and is shown in figure 194.

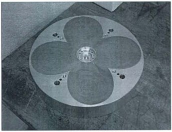

Figure 192 – The resin filled first side of the propeller has been milled flat for mounting.

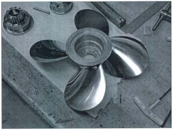

Figure 193 – Polished blade.

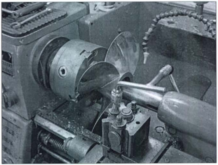

Figure 194 – Turning the o-ring seal entrance taper.

To complete the propeller manufacture, the nose cap was completed. As discussed in chapter 3, the nose cap was designed to have no interruptions on the outer surface. This part was completely machined on the CNC lathe. Figure 195 and figure 196 show the threaded portion and outer surface finish respectively. The smooth outer surface of the nose cap results from designing and modeling the CAD part with arc segments. When CNC code on a lathe is produced from arc generating entities, the end NC code utilizes the machine tool's circular interpolation function which produces superior surfaces, as shown in figure 196. A test fit of the finished propeller and nose cap is shown in figure 197.

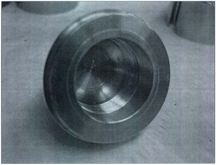

Figure 195 – Threaded section of the nose cap interior.

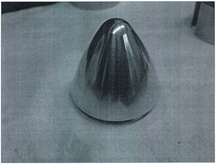

Figure 196 – Outer surface of the nose cap.

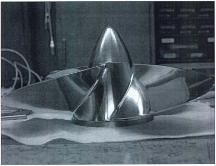

Figure 197 – Test fit of the propeller with nose cap and hub taper angle adaptor.

This marks the end of the discussion on the manufacture of the pod unit. Note that there were a significant number more parts manufactured that are not discussed. At numerous times throughout the manufacturing process for all components and subassemblies, checks on dimensions were carried out as well as check test assemblies. Figure 198 shows a test fit of every major subassembly prior to final assembly.

The author wishes to acknowledge the fact that every machinist who had a part in fabricating the pieces of this assembly did so with great enthusiasm and skill. Without their help (and patience, especially when listening to advise and instructions, or moving out of the way for another great shot), this aspect of the project's endeavor could never have happened, period.

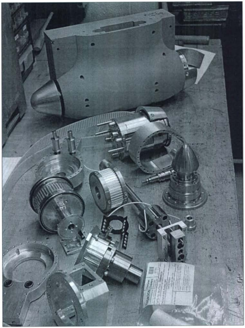

Figure 198 – Test fit of all major components at the end of manufacture of the pod unit.

APPENDIX N

EXPERIMENTAL SETUP

EXPERIMENTAL SETUP

INTRODUCTION

This document outlines the steps taken to assemble the experimental apparatus in preparation for running a series of tests to commission the instrumentation. It is segmented into two main discussions, one on the assembly of the apparatus and the other on the setup of the data acquisition system. Each main discussion is subdivided as required.

The following discussion should serve as a reference text for any future work that requires the use of this instrumentation package.

1 Apparatus Setup

The apparatus setup consisted of assembling the two main subassemblies: the pod instrumentation and the global dynamometer. During this phase the mechanical and electrical systems were put together and adjusted to give correct performance. The forward thinking during the design phase regarding the installation of wiring allowed for a successful assembly.

1.1 Pod Instrumentation Assembly

The pod instrumentation assembly started with the propeller shaft and progressed outward from this part.

1.1.1 Propeller Shaft Torque Sensing Gauges

The finished propeller shaft and torsion strain gauges are shown in figure 1. These components make up the transducer that allows torque to be measured at the propeller hub, free of any frictional effects from seals and bearings. The transducer is set up in a full bridge configuration to maximize output, given that the torque signal was not pre-amplified. Positions indicating the mounting location of the gauges had been accurately placed on the propeller shaft after all other machining operations were finished. Figure 2 shows the intersecting scribe lines on the gauge area of the propeller shaft. The gauges were installed by an external contractor using bonding agents and procedures recommended on the strain gauge information sheet. The reader is referred to **Appendix**

D, line items 6 thru 8 for further information on gauges, installation procedures and protective coatings.

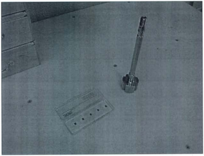

Figure 1 – Propeller shaft and torque strain gauges.

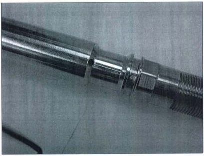

Figure 2 – Gauge position marks.

Prior to installation of the gauges, a check was first carried out to ensure that the two signal cables for propeller torque and thrust could be installed in the propeller shaft and that the propeller shaft, complete with its cabling, could be installed in both the drive gear unit and propeller hub thrust reference base. Figures 3 through 5 show the wiring route through the propeller shaft. Figures 6 through 8 show the wiring route though the drive gear. Figures 9 through 11 show the wiring route through the propeller hub thrust reference base. Note the slot milled along the threaded portion of the shaft in figure 9. This allows the propeller thrust signal cable to lie below the ID of the hub reference base when the propeller shaft is inserted into the bore. Once the hub base is in place the wire is moved to a clearance slot in the ID of the reference base and the bronze retaining nut threaded into position. Note that a pre-planned procedure consisting of milling a final clearance slot in the retaining nut during the final assembly stages of the propeller thrust unit to allow the cable to be installed in the propeller mounting base was carried out later. Section 1.1.6 explains this detail. Figure 12 shows the completed test installation of the propeller thrust signal cable. Figure 13 shows the completed gauge installation, complete with soldered signal cable connections.

Once installation of the gauges was complete a sealant was applied to keep water and other contaminants away from the gauges as well as out of the hollow center section of the propeller shaft. A jig was used to allow a silicone based sealant to be squeezed into the strain gauge area shaft relief as well as the shaft center. Once cured, the jig was removed to reveal a smooth surface whose contours matched the shaft outer profile.

Figure 14 illustrates the sealant installation process. The jig was made from UHMW (polyethylene) to prevent the sealant from sticking to it.

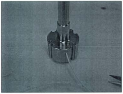

Figure 3 – Wiring exit for propeller thrust signal cable.

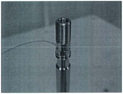

Figure 4 – Wiring entrance for propeller thrust signal cable.

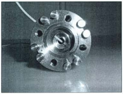

Figure 5 – Bottom view of cable route. Note that torque cable exits 180° from thrust cable.

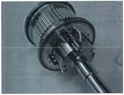

Figure 6 – Cable test installation into drive gear.

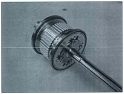

Figure 7 – Prop shaft fully installed into position.

Figure 8 – Torque and thrust cables successfully test installed in drive gear.

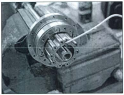

Figure 9 – Cable test installation into propeller hub reference base.

Figure 10 – Installation of retaining nut, wire moved to ID clearance slot.

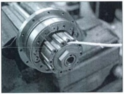

Figure 11 – Retaining nut fully installed.

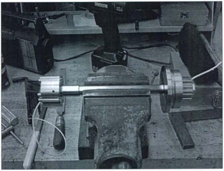

Figure 12 – Finished thrust cable test installation for entire shaft.

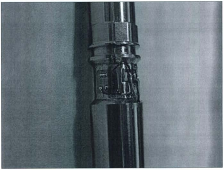

Figure 13 – Finished gauge installation.

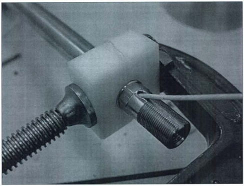

Figure 14 – Sealant installation jig.

1.1.2 Drive Assembly

Completing the drive assembly consisted of final assembly of the propeller shaft mechanical and electrical parts and inserting it into the drive gear with the drive ball cage. The strain gauged propeller shaft subassembly was completed by first pressing in the radial roller bearing that keeps the thrust shaft aligned with the propeller shaft axis of rotation. Figure 15 shows the radial roller bearing installation operation. Note that a brass installation tool was machined to prevent bearing damage during assembly. Next the thrust bearing installation height had to be set before installation. Figure 16 shows how the thrust keeper portion of the thrust bearing is fitted to the thrust shaft. Figure 17

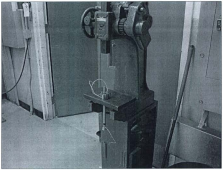

Figure 15 – Press installation of thrust shaft radial roller bearing.

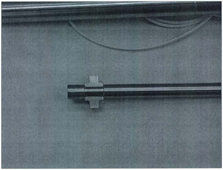

Figure 16 – Thrust shaft keeper mounted to thrust shaft.

shows both thrust keepers with the thrust bearing washers and roller cages installed. The thrust washers hold the keepers in place around the thrust shaft. The final height of the thrust bearings and washers were adjusted to the final depth of the bore in the end of the propeller shaft (minus acceptable running clearances) by using a surface grinder to reduce the thickness of one washer. The final thickness was measured to give 0.0005" (0.0127 mm) clearance in the thrust direction. The dimensions of the pocket for these bearings had been designed with this operation in mind to ensure that material could be removed from the thrust washers to achieve the correct running tolerances. Figure 18 shows the final thickness of the thrust bearing assembly while figure 19 shows all parts in a test fit on the thrust shaft prior to installation into the propeller shaft.

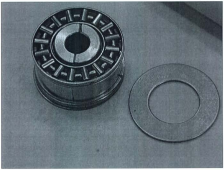

Figure 17 – Thrust shaft keepers, washers and roller bearing cages.

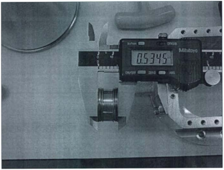

Figure 18 – Final thrust bearing assembly thickness.

Figure 19 – Final assembly of thrust bearing on thrust shaft prior to shaft insertion.

As a final preparation for the torque and thrust signal cables, the ends were tinned with solder and solid wire leads soldered in place as well. This aided in keeping the cable conductor strands together while installing into the terminal blocks of the drive gear and propeller thrust unit. It also allowed the minute manipulations with needle nose pliers required to align the lead with the miniature terminal block connector lug. The outer insulation and shielding layers were removed at the drive gear end of the cable as an additional preparation. This allowed for the strain relief loops to be formed upon insertion into the drive gear insulation tubes. These loops were necessary to prevent cable damage during relative movement between the propeller shaft and drive gear during gap distance setting and normal pod unit thrust movement. Figures 20 and 21 show the cable ends of the drive gear end and prop thrust end respectively.

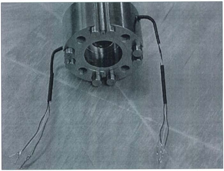

Figure 20 – Drive gear end cable termination details.

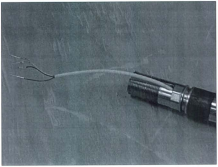

Figure 21 – Prop hub thrust end cable termination details.

Completing the drive gear subassembly to allow integration with the propeller shaft required installing and setting up the slip rings and brush block that allow the thrust and torque signals to be transmitted across the rotating connection. First the printed circuit boards that serve as insulated mounts for the terminal blocks were soldered to the slip ring assembly. Figures 22 and 23 show two views of this completed step.

Next the slip rings were pressed installed over the spigot of the drive gear and the thin roller bearings and brass belt guide rings installed. The assembly was then pressed into the aft gear housing and the brush block was installed. The sliding fit at this joint allowed the ring set to be easily adjusted to locate the brushes on the center of the ring width. Figure 24 shows the drive gear, slip rings and brush block ready for final adjustment.

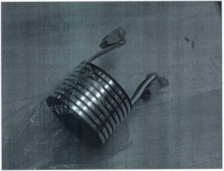

Figure 22 – Slip rings with miniature terminal block PC boards in place.

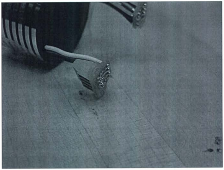

Figure 23 – Close-up of underside of terminal block.

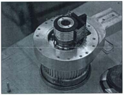

Figure 24 – Drive gear installed to allow slip ring position adjustment.

Figure 25 – Adhesive applied to perimeter of slip ring-to-spigot interface.

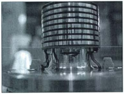

Figure 26 – Adhesive at wire exit end of slip rings.

Shown in figures 25 and 26 are the aft and forward views of the slip rings sealed with silicone adhesive. This adhesive secures the position of the slip rings and allows easy removal for replacement or readjustment in the future.

Once the setup steps had been carried out on the thrust bearing assembly thickness and the slip ring position, the final assembly sequence could be carried out. Figure 27 shows the nearly inserted nylon drive gear insulation tubes. These were inserted such that their lengths aligned with the depth of the cable passageway bores in the drive gear. The thrust shaft and cover were then installed complete with seal and gasket on the fully prepped propeller shaft. The cover and its seal are shown in figure 28. The fully installed thrust shaft is depicted in figure 29.

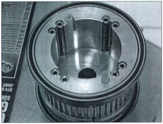

Figure 27 – Installation of drive gear insulation tubes.

Next, to allow the propeller shaft to be inserted into the drive gear, the delrin ball cage was assembled by snapping in each ball element into its positioning hole and then coating the assembly with lubricant. The cage was then slipped into position on the completed propeller shaft subassembly. Figure 30 shows the ball cage with ball elements installed. Figure 31 shows the lubricated ball cage assembly mounted on the propeller shaft. Shown in figure 32 is the propeller shaft partially installed into the drive gear.

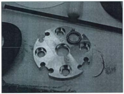

Figure 28 – Propeller shaft end cover and seal.

Figure 29 – Fully installed thrust shaft.

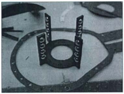

Figure 30 – Drive assembly ball cage with elements installed.

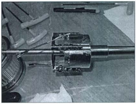

Figure 31- Cage in position.

Figure 32 – Start installation into gear.

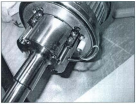

Figure 33 – Start strain relief loop.

Figure 34 – Complete loop.

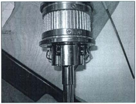

Figure 35 – Top view.

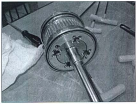

Figure 36 – Fully inserted.

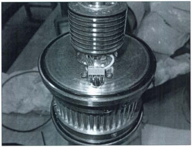

Figure 37 – Cable ends installed into terminal blocks.

Figures 33 and 34 depict the formation of the stain relief loop. Figure 35 is a top view of the assembly while 36 shows the fully inserted propeller shaft. At this point the shaft was firmly pressed entirely into the gear to allow the ball cage end to positively contact the bottom of the drive gear bore. The dimensions of the cage have been designed such that when assembled in this manner the ball positions will be correctly located for all positions of the propeller shaft as adjustment of the gap setting is carried out during testing. Figure 37 shows the cable leads installed into the terminal block. This completed the drive gear assembly.

1.1.3 Drive Gear Housing

Assembly of the drive gear housing started with fabrication of the gaskets required to seal the interfaces between the forward and aft drive gear housing plates with the center section. All gaskets were fabricated by printing a 1:1 scale profile of the outline and then carefully cutting the gasket out from 1/32" (0.794 mm) rubber impregnated gasket paper sheet stock.

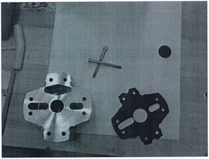

Figure 38 – Gasket making form, gasket and part.

Following gasket manufacture was installation of the radial roller bearings. These were installed using a manual press and the brass installation tool used to install the bearing in the propeller shaft. Note that the bearings only have a seal on one side. The seal side was installed towards the interior of the drive housing. This keeps grease from contaminating the drive belt and other interior surfaces as well as keeping the bearing permanently lubricated. The bearings are lubricated at the factory and none was added. Figure 39 shows the bearing and one drive housing before installation. Note that the same procedure was carried out on both plates composing the drive gear housing. Figure 40 shows the bearing and installation tool aligned, ready to press the bearing in. Figure 41 shows the bearing partially installed. Figure 42 shows both bearings fully installed. The bearings were pressed in until they fully contacted the bottom of the bearing bores in the plates as the depth was designed to locate the rollers in the correct location when installed in this manner.

Figure 39 – Radial bearing.

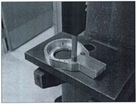

Figure 40 – Bearing ready to install.

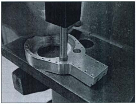

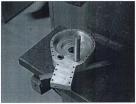

Figure 41 – Bearing partially installed. Figure 42 – Both bearings installed.

Following bearing installations, the propeller shaft seals in the drive gear plate facing the propeller were installed. Two seals were incorporated in the design for redundancy. These were pressed in by hand until they made positive contact with the seal bore bottom. At this point the top of the outermost seal was just below the internal type stainless steel retaining clip groove, shown in figure 43. Installation of the retaining clip was completed using the proper installation pliers, shown in figure 44.

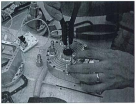

Figure 43 – Seals installed. Figure 44 – Installing retaining clip.

Installation of bearings and seals, as well as fabricating the gaskets, completed the pre-assembly work required to put together the drive gear housing. The main components, shown prior to the final assembly sequence, appear in Figure 45. To start the final assembly sequence, the propeller shaft seals were lightly lubricated with general purpose grease, and the drive assembly inserted into the propeller shaft side drive gear housing plate. This is illustrated in figures 46 though 52.

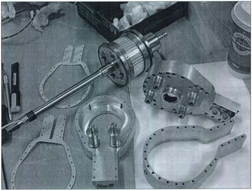

Figure 45 – Main components of the drive gear housing, shown with drive assembly.

Figure 46 – Applying grease to seals.

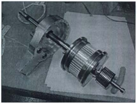

Figure 47 – Start with propeller side cover.

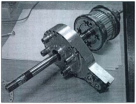

Figure 48 – Inserting shaft.

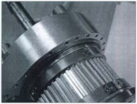

Figure 49 – Bearing enters relief first.

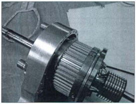

Figure 50 - Bearing fully installed.

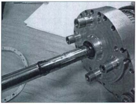

Figure 51 – View from seal side.

During the insertion of the bearing into its bore (figures 49 and 50) a machined relief made the task easy until the final 0.250" (6.35 mm). A minimal effort was required to insert the bearing all the way into the bore due to the relaxed bearing fit. This was done to make disassembly in the future much easier. The fit between the bearing outer race and the cover bearing bore tightens when then unit is immersed in water due to the differing rates of contraction between the aluminum housing and the steel bearing race. This allows for ample heat dissipation from the bearing during normal operation.

Next the gasket, belt and the two idler pulleys were placed over the drive gear as shown in figure 52. The center section was then placed over the drive assembly until the gasket was fully flat as in figures 53, 54 and 55. Note that the ends of the center section were spread apart slightly to allow it to slide over the out bearing races. Several of the #6-32 diameter cover screws were then inserted into the counter-bored holes until they passed through the center section as shown in figures 56 and 57. These acted to 'hold' the second gasket when installed over the protruding screw ends as shown in figure 58. The second cover was then positioned over the bearing of the drive assembly. This is shown in figure 59. Note at this time the 2 magnesium based sacrificial anodes on the stem of the cover. There are two of these on each cover near the intersection with the steel strut tube to hinder the rate of corrosion of the aluminum parts.

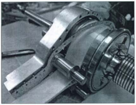

Figure 52 – Gasket, belt and idler pulleys.

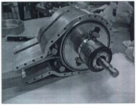

Figure 53 – Install center section next.

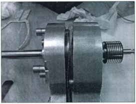

Figure 54 – Compress gasket until flat.

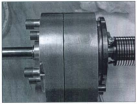

Figure 55 – Gasket fully seated.

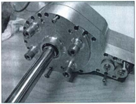

Figure 56 – Install several 'holding' screws.

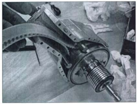

Figure 57 – Push until protruding.

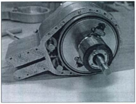

Figure 58 – Place gasket over screws.

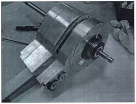

Figure 59 – Install second housing.

Using the previously installed 'holding' screws each fastener was gently threaded into the second cover and pulled over the second bearing until the gasket was flat and all three components had made positive contact. The screws were tightened using an alternating pattern. First using figure 63 as a guide, the pattern (approximately) 1 – 2 – 21 – 22 was repeated until the gasket was flat. Then using 63 for the complete sequence, the pattern was 1 thru to 27 until each screw was tight enough to cause the long handle allen wrench to twist slightly without fastener rotation. The correct torque value for a #6-32 stainless steel fastener is approximately 10 in-lbs. This completes the assembly.

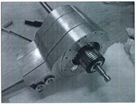

Figure 60 – Draw covers tight with screws.

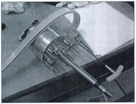

Figure 61 – Install remaining screws.

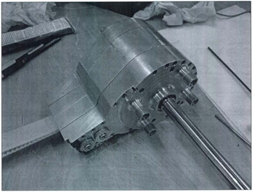

Figure 62 – Drive gear housing fully assembled.

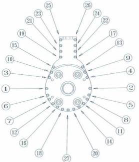

Figure 63 – Screw tightening sequence guide.

1.1.4 Strut Tube & Drive Gear Housing Assembly

To allow ease in the ensuing assembly steps, the drive gear housing and strut tube were connected to allow the unit to be mounted on the calibration frame. This acted as a suitable "platform" to allow the remaining components and subassemblies to be connected to the main pod instrumentation unit.

To start the assembling process, the four 5/16" diameter socket head cap screws were positioned into their respective filling slots and inserted into the through holes, as illustrated in figure 64. This allowed the gasket to be installed such that it was held by the threads as shown in figure 65. Next the drive belt was inserted as shown in 66. The drive gear housing was supported on the strut tube to make this step easier. Once the belt had been inserted nearly all the way, the drive gear housing was lifted and positioned such that is could be used to push the belt into the strut tube all the way, as shown in figure 67. When the belt was in and the top of the drive gear housing was near the mounting end of the strut tube, each of the 5/16" bolts were engaged with the threaded holes in the top of the drive gear housing. This was done using a ball-head tee-handle allen wrench. Each of the bolts was threaded in until the gasket was slightly compacted between the two machined faces of the joint, as shown in 68. Figure 69 gives an overall view to this step. Note that the center to center distance for the two sets of holes are different so that the drive gear can only be mounted on the strut tube one way. For future assembly attempts ensure that the relative positioning of the strut tube and drive gear are as shown in figure 70.

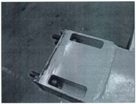

Figure 64 – Insert 5/16 diameter screws.

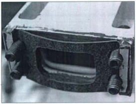

Figure 65 – Install gasket.

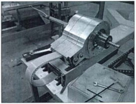

Figure 66 – Insert drive belt into tube.

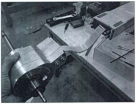

Figure 67 – Complete belt installation.

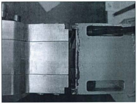

Figure 68 – Compressing gasket.

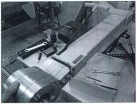

Figure 69 – Tee-handle Allen wrench.

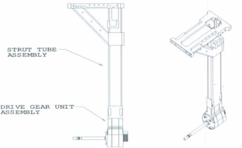

Figure 70 – Orientation of strut tube-to-drive gear housing.

During the next phase of assembly, a small amount of gasket sealant was then applied to both sides of the gasket. The installation tube supplied with the silicone gasket material tube was cut with a utility knife to allow a 1/16" (1.5 mm) diameter bead to be deposited in the joint area. This step ensures that any voids not filled by gasket material will be positively sealed. Generally, this is not normal practice. Note also that the gasket in this case is cut from 1/16" (1.5 mm) thick gasket sheet stock. Figure 71 illustrates application of gasket sealant. Gasket sealant is a sensor safe RTV type silicone sealant. After sealant application, the screws were tightened in succession until the excess gasket sealant squeezed out of the joint, as shown in figure 72. At this point all external joints were coated with gasket sealant as depicted in figures 73 and 74. This was done as a sealing redundancy to ensure that no leaks occurred.

Figure 71 – Applying sealant to joint.

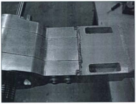

Figure 72 – Tightened joint.

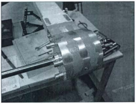

Figure 73 – Completed installation, with all joints sealed.

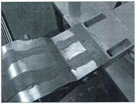

Figure 74 – Close-up of completed installation.

1.1.5 Propeller Gap Pressure Sensing Plate

The pressure sensing plate assembly started with the installation of the water lubricated propeller shaft bearing. This bearing was manufactured to be installed using liquid nitrogen. Using liquid nitrogen caused the bearing to shrink so that its outer diameter was smaller than the bore diameter in the pressure sensing head. Installation was a simple matter of dropping the bearing into the bore using a stainless steel shaft as an installation tool. The pressure sensing plate was designed such that the bore had a smaller diameter at the bottom to stop the bearing at the correct location during installation. Once the bearing heated up it was fixed permanently into position. Figure 75 depicts the pressure transducer sensing plate and atmospheric pressure chamber, water lubricated bearing and water anti-flow seal. Figure 76 shows the bearing immersed in liquid nitrogen. Installation temperature was realized when boiling off of nitrogen ceased. The completed bearing installation is shown in figure 77.

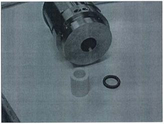

Figure 75 – Pressure sensing plate, atmospheric chamber, seal and bearing.

Figure 76 – Cooling the bearing to shrink.

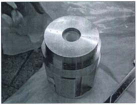

Figure 77 – Fully installed bearing.

After installing the bearing, the pressure transducers were installed. This was done prior to the calibration procedure as described in **Appendix O**. First the transducer was carefully removed from its package and the protective cap removed, as shown in figures 78 and 79. Next the transducer body was grasped and the adjoining cable gently wound in the opposite direction of the threading installation direction to prevent the cable from becoming tangled when the transducer was threaded into its respective hole. After the transducer's o-ring seal had contacted the machined surface of the pressure sensing plate, a ¼" (6.35 mm) wrench was used to gently tighten the transducer. This is shown in figures 80 and 81.

Each transducer was installed in the above manner until all five were in place. The serial number of each transducer location was then recorded such that the data acquisition system could be configured correctly. Figure 82 shows all transducers as installed. Note that the installation procedure was carried out while the pressure sensing plate was installed in the calibration tower.

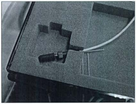

Figure 78 – Pressure transducer.

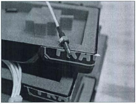

Figure 79 – Protective cap removed.

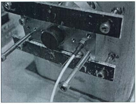

Figure 80 – First transducer threaded into position.

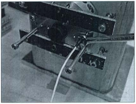

Figure 81 – Tightening transducer body.

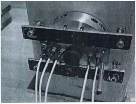

Figure 82 – All transducers installed.

To complete the installation of the pressure transducers, it was necessary to fill the passageways from the open end of the transducers to the opening of the pressure sensing orifice with silicone based oil. The transducers were ordered from the supplier without screens in anticipation of using them with oil. This allows a reduced chance of air entrapment hindering the operation of the transducer. Oil is necessary to prevent the transducer pressure sensing element from direct contact with water, which would destroy the transducer. To allow this operation to take place, a method of purging air from the passageway was developed and implemented as part of the pressure sensing plate design. A filler port was fitted at 90° to the passageway leading to the orifice and is shown in the cutaway of figure 83. The air purging screw allows oil to be added to the passageways until all air has been pushed out and then tightened to prevent air from returning.

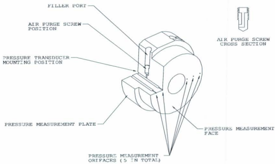

Figure 83 – Pressure measurement plate air purging system details.

All air purging screws were loosely installed with an allen wrench and then oil added using a sterile glass syringe. The air purging screws were then tightened and the excess oil wiped away from the face of the pressure sensing plate. The orifices were then observed for a period of time to ensure that there were no slow leaks that would allow the oil to leak out (or water leak in during operation). These steps are shown in figures 84 and 85. Once the author was satisfied the installation had been successfully carried out, the next step commenced. Note that the procedure was carried out one port at a time.

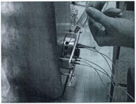
Figure 84 – Adding silicone oil.

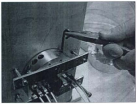
Figure 85 – Tightening air purging screw.

The atmospheric pressure chamber was the next part to be assembled to the pressure sensing head. This container allows the gauges to vent the opposite side of the diaphragm to atmospheric pressure for correct operation. First the required gasket was cut out of 1/32" thick gasket sheet stock and placed into position. Next the cables leading from the pressure transducers were inserted into the correct opening of the atmospheric pressure chamber allowing it to be positioned in contact with the pressure sensing plate. These steps are shown in figures 86 and 87. Figure 88 shows a view into the chamber,

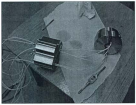

Figure 86 – Gasket installed, inserting cables through chamber.

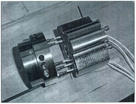

Figure 87 – Parts aligned for installing screws.

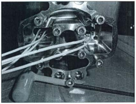

Figure 88 – View into back end of chamber.

one can see the aligned screw holes at the bottom. All screws were then coated with a ceramic anti-seize compound and installed to connect the pressure sensing plate to the chamber. Anti-seize was used in this joint because both the threaded holes in the pressure sensing plate component as well as the fasteners were manufactured from stainless steel, which opens the possibility of creating stuck or broken fasteners in the threaded hole during assembly or removal. The corresponding gasket for the chamber end cover was then positioned and the cables were then inserted into the single outlet hole spigot. The screws for this joint were then coated in anti-seize, installed and tightened. Figure 89 shows the screw tightening guide for both joints. Figure 90 shows the chamber with its cover installed and outer cable trunk hose fitted. The hose acts to

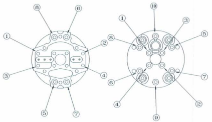

Figure 89 – Screw tightening sequences for pressure sensing system components.

continue the chamber space up to and above the water surface, allowing the pressure transducers to be exposed to atmospheric pressure on the vented side of the diaphragm. It is made from clear PVC. Once all cables had been pulled through the hose, the 10 pin connecters were soldered in place and strain relief kits installed. The strain relief kits prevent the cable from being accidentally pulled from the connector body, thereby preventing a short or open circuit to the data acquisition system. Once the assembly of the pressure sensing system components was complete, it was installed on the main pod unit assembly.

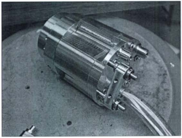

Figure 90 – Pressure sensing system components fully assembled, note that propeller end shell mount installation progress is shown in this photo.

Assembly of the pressure sensing system onto the main pod instrumentation unit started with a pre-assembly of the propeller end shell mount floats. These components allow the outer shell components to be fitted to the pod unit and form part of the shell drag measurement system, the assembly of which is described in 1.1.7. Assembly of each shell mount float started by inserting each stainless steel linear bearing into the bore of the shell mount and fixing its position by the installation of the external retaining clips on each end of the bearing. Next a piece of stainless steel hardened and ground rod was inserted into the bearing center until an equal length protruded from each side of the assembly. This is illustrated in figure 91. The two free-floating propeller end shell mounts were assembled in the above manner and then inserted into the corresponding mounting holes in the atmospheric pressure chamber cover (as shown previously in figure 90). The entire assembly was then carefully placed over the propeller shaft on the main pod unit, ensuring that the cable for the propeller thrust made it all the way through the water lubricated bearing. The four spigots of the chamber cover were located on the drive unit cover as were the free ends of the shell mount rods. The 4 stainless steel socket head cap screws were then placed into their respective filling slots and tightened using a ball end tee-handle allen wrench. Anti-seize compound was also used on these screws.

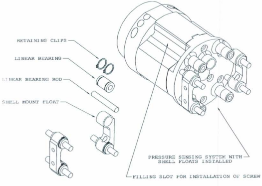

Figure 91 – Shell mount float assembly illustration.

Figure 92 shows the completed installation of the pressure sensing system onto the pod unit. To complete the assembly thus far, a seal was installed where the propeller shaft exits the pressure sensing face. The purpose of this seal is not to seal the inner space between the instrumentation's exterior and pod shell's interior, but to stop the flow of water in or out of the propeller gap area around the propeller shaft. This prevents contamination of the gap pressure measurements caused by flows other than those at the periphery of the rotating propeller hub and pod end. The seal chosen is a hydraulic piston seal because of its soft material. The seal was modified before installation by removing the central o-ring portion that normally keeps the seal edges in contact with a hydraulic piston. This reduces the friction at the shaft interface and ensures that the seal will stay in place due to the friction of its installation into the pressure plate bore. Figure 93 shows the shaft exit through the pressure sensing face prior to seal installation. Figure 94 shows the seal prior to modification. Figure 95 shows the seal with the o-ring center removed. Figures 96 though to 98 show the seal installation in stages.

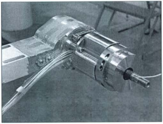

Figure 92 – Completed pressure sensing system and propeller end shell mount floats.

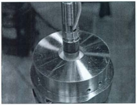

Figure 93 – Shaft exit view.

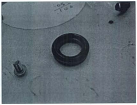

Figure 94 – Shaft water anti-flow seal.

Figure 95 – Seal with o-ring removed.

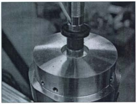

Figure 96 – Seal installation start.

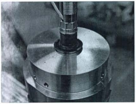

Figure 97 – Seal before pressing in bore.

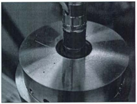

Figure 98 – Final seal installation.

1.1.6 Propeller Hub Thrust

The next step in the instrumentation assembly process was the propeller hub thrust measurement assembly and setup. First the main hub o-ring seal was fabricated and installed in position on the propeller shaft. The installed o-ring is shown in figure 99. To fabricate all o-rings in the project, a suitable length of o-ring chord stock was cut from a roll (in this case 0.070" (1.78 mm) diameter) and glued using cyanoacrylate, which is commonly known as "super-glue". Next the propeller reference base was prepared for installation over the propeller shaft. First, the o-ring seal taper was lightly sanded with 2000 grit sandpaper to remove the last traces of any burrs that could damage the seal during installation. The taper length was carefully calculated during the design phase to allow full engagement of the seal before being compressed into the groove on the propeller shaft. Figure 100 shows the taper on the back side of the propeller reference base. Next, the drive rods were installed into their respective positions as shown in figure 101. Note the threaded holes in the rod ends. This allows the rods to be extracted and replaced in the event of damage. Grease was then installed over the o-ring on the propeller shaft as shown in figure 102. This is not normal practice, usually only a small amount of o-ring lubricant is used during the assembly of such designed joints, however the design of the reference base bore taper allows the grease to fill all of the groove volume and acts to hydraulically compress the seal very tightly as the propeller shaft is inserted into the reference. As the reference base was installed, it was ensured that the position of the thrust signal cable was aligned with its holding slot in the reference base

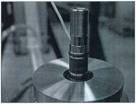

Figure 99 – O-ring seal installed.

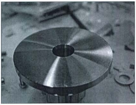

Figure 100 – Bore taper in reference base.

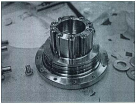

Figure 101 – Drive rods installed.

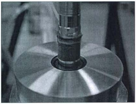

Figure 102 – Grease installed on o-ring.

retaining nut bore. This is shown in figures 103 and 104. Next the propeller reference base retaining nut was installed. During installation care was taken to ensure that the torque exerted by the wrench in completing the final tightening did not pass through the drive balls and rods in the drive assembly. To do so could cause potential damage. The reference base was grasped by a gloved hand to provide the reaction torque required to tighten the nut. The fine pitch of the propeller shaft threads made this step easy. Figures 105 and 106 show the tightened nut installation. The position of the nut relative to the thrust signal cable was then marked with a pencil. It was then removed and a final clearance slot milled in the rod retaining rim portion. It was then re-installed thus completing the installation, as shown in figure 107.

The next component to be installed was the propeller shaft seal adaptor. This has several important functions relating to sealing the hub thrust system. It creates a seal between the propeller hub thrust interior space and the exterior while allowing the relative movement the propeller experiences during thrust loading. It also seals the inner bore of the

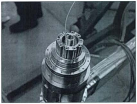

Figure 103 – Reference base in position.

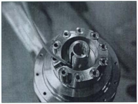

Figure 104 – Cable position details.

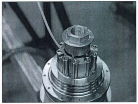

Figure 105 – Nut threaded onto shaft.

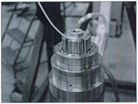

Figure 106 – Nut fully tightened.

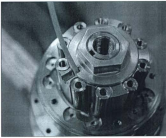

Figure 107 – Nut final installation with cable clearance slot.

propeller hub to form an integral part of the overall sealing system. Both sealed joints use o-rings. In the latter case the o-ring installation and operation is typical of most o-ring applications. The former case is not of standard practice and thus extra care was taken during this assembly case.

The installation of the seal adaptor started with fabricating the o-rings using the same procedure as before however extra care was taken to ensure that the length of the chord stock for the two inner seal o-rings was exact and that the face of the cut on each end was flat and free of surface defects. A brand new knife blade was used for this operation. When gluing the ends together, only a very small drop of glue was used so that excess was minimal and it was ensured that the ring ends were not twisted about its central axis when the faces were pressed together. After the ring ends had bonded, a piece of clean lint free cloth was used to absorb the small traces of glue that had squeezed out of the joint. This procedure was carried out on all three o-rings for this component. The extra care was important because the amount of squeeze that each o-ring is subjected to is significantly less than standard design practice. This allows the ring to act as a bearing as well as a seal. The amount of squeeze is 10% (versus 30%) and was determined experimentally, as mentioned in section 3.2. Figure 108 shows a cut away view of the seal installation configuration. Figure 109 shows the fabricated seals installed into the shallow grooves on the propeller reference base. A double seal provides redundancy to compensate for the reduced installation squeeze and both o-rings act to dampen any motion of the propeller about an axis normal to its axis of rotation due to the relatively short length of the drive rod and ball arrangement. The seals were installed by carefully rolling them over the outer diameter of their installation locations so as not to stretch them.

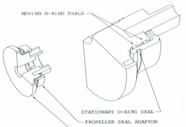

Figure 108 – O-ring seal arrangement for hub thrust reference base.

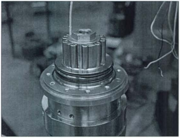

Figure 109 – O-rings installed on reference base.

To install the propeller seal adaptor it was placed over the reference base such that the first seal was resting in the chamfer of the entrance to the inner bore diameter of the seal adaptor. Then, using a twisting and pushing motion together the adaptor was moved into position. The motion was the same as if threading the parts together in the absence of threads. This allowed the o-rings to settle into place without being wedged into the smaller space between the two seal grooves. When the adaptor had been fully pushed over the reference base as far as it would go and then allowed to be pulled off slightly the installation was complete. Now the adaptor could be easily moved in the thrust direction as the o-rings rolled between the two faces. Figure 110 shows the installed seal adaptor. Note that the propeller hub taper angle adaptor is also present in this photo. This adaptor was installed using only 4 of the installation screws to allow final setup of the thrust instrumentation. It was then removed to allow the shell drag instrumentation to be set up.

The next step in the hub assembly was installing the drive ball and cage subassembly. The balls were snapped into position and then grease applied. The cage was then placed over the drive rods of the reference base. After this step, the 200 lb (889.6 N) load cell was threaded into the end of the propeller shaft. Ceramic anti-seize was applied to the threads. The load cell was threaded all the way into its mounting hole and then backed out until the wiring exit on the load cell body was 180° from the cable exiting the reference base. Note that the reference end of the load cell must be installed into the propeller shaft. Figure 111 shows the installed drive ball and cage subassembly as well as the load cell. Note that at this point the spring strain relief for the cable exiting the load cell was carefully cut off to allow a tighter bending radius of the cable. This allowed the cable to be installed in the propeller reference mount. The spring was cut using a high speed cut-off tool with a miniature cutting disk attachment. Care was taken not to cut the individual wire conductors inside the sheathed cable of the load cell. After installing the load cell, a jam nut was threaded over the stud on the live end of the load cell. This nut determines the installation clearance between the propeller hub and the hub taper angle adaptor. Ceramic anti-seize was used here are well. The installed jam nut is shown in figure 112. Next the propeller reference mount was installed over the load cell and drive balls. Prior to its installation, the drive rods were installed by pressing them

Figure 110 – Propeller seal adaptor installed.

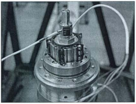

Figure 111 – Load cell and drive cage with balls installed.

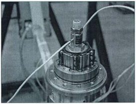

Figure 112 – Load cell jam nut installed.

into their respective bores. The location of the jam nut will determine how far the propeller mount can be installed over the reference base. Also, the two cables were pulled through the exit holes in the end of the propeller reference mount while installing. The installed propeller mount is depicted in figure 113. Care was taken not to wind the two cables around each other as the mount was installed. After the initial fitting into position, the relative position of the assembly had to be set up. This was done by first rotating the installed jam nut by inserting a small flat tipped screwdriver into the round access hole in the load cell mounting portion of the propeller mount to lower it until it contacted the seal adaptor. Then the seal adaptor was pulled out slightly to allow its spigot to fit into the relief in the end of the propeller mount. The assembly was then lowered again by rotating the nut with a screwdriver through the access port. The five installation screws were then installed and tightened to hold the seal adaptor to the propeller mount. At this point a feeler gauge was inserted between the end of the seal

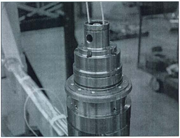

Figure 113 – Installed propeller mount.

adaptor and the top of the hub taper angle adaptor, temporarily installed earlier. The lowering process continued until the thickness of the space was 0.010" (0.25 mm). This is shown in figure 114.

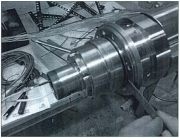

Figure 114 – Checking installed gap with feeler gauge.

When the final gap thickness had been achieved the second jam nut was installed on the outside of the load cell threaded stud. It was tightened gently while holding the propeller mount with the other hand. After tightening, the threads at the end of the load cell were sealed with silicone adhesive to prevent the outer nut from vibrating loose during operation. Figure 115 shows where the sealant was applied, in addition to the location of the access hole for adjusting the inner jam nut position.

When the sealant had been applied, the printed circuit board was installed and the two cable ends connected to the terminal blocks. Figure 116 shows the connection and wire colour designations. The conductor path is straight across from the input terminal block to the output terminal block. It doesn't matter which block acts as input or output. The wire colour designations are typical of all transducers used in this instrumentation package. Connecting the cables completed the hub thrust assembly process.

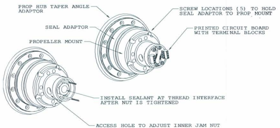

Figure 115 – Sealant, adjuster hole and printed circuit board installation locations.

Figure 116 – Connection details – *Cable in* connected directly across to *cable out*.

1.1.7 Slip Ring Case

Assembling the slip ring case to the main pod instrumentation unit consisted of first fabricating the three gaskets. Next the wiring was installed that carries the propeller torque and thrust signals out of the brush block assembly. The individual rings on the slip ring assembly had been recorded previously and the wiring on the brushes was colour coded to have the same typical designation as all the transducers in the instrumentation package. One can refer again to figure 116 for the colour coding designation.

Figure 117 shows the completed brush block wiring. Once the wiring was complete the

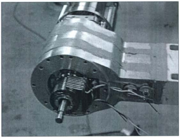

Figure 117 – Brush block wiring completed.

slip ring case was positioned with the gasket in place between it and the drive gear housing. Care must be taken to ensure that the slip ring case is positioned with the brush block clearance cutout in the correct orientation. Attempting to install it with the incorrect orientation could cause damage to the wiring and makes it impossible to install the fasteners. Figure 118 shows the correct orientation used.

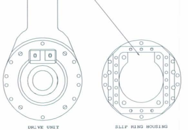

Figure 118 – Orientation of slip ring case to drive unit.

To attach the slip ring case, 8 stainless steel socket head cap screws were used on the sides of the case, while the top and bottom fasteners were 2 stainless steel countersunk philips head screws. These fasteners were used to provide a flush mounting surface for the top wiring exit cover and the bottom inspection/blade position & sensor cover. Figure 119 shows the completed slip ring case installation. Note that there are 4 unused holes in the slip ring cover. These are the result of a mounting hole pattern change to accommodate clearance for the brush block wire mounting solder tabs. These holes are blanked by the gasket and thus will not affect sealing or operation of the unit.

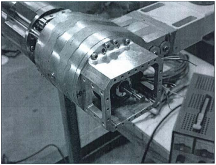

Figure 119 – Slip ring case installed.

1.1.8 Pod Thrust Block & Gap Adjuster Mechanism

This subassembly serves to allow the axial positioning of the propeller that determines the width of the propeller gap as well as decoupling the torsion forces from the load cell as the propeller is loaded in the thrust direction. To start the assembly the thrust block has its miniature stainless steel linear bearings installed. These are installed by applying a small amount of retaining compound (specifications found in **Appendix 'G'**) to the linear bearing outer perimeter and then inserting the bearings into the bores of the thrust block. This method of bearing installation was chosen during the design phase because it absolutely does not apply any forces that will alter the operation of the bearing. The holes had been reamed during assembly to allow a sliding fit and the retaining compound fills the space between the two components, curing to positively lock the bearing into position. Next the thrust shaft retainers were installed into the thrust block by inserting the two stainless steel socket head cap screws into the counter-bored holes and threading the retainers over the protruding ends of the screws. Figure 120 shows the installation details for the bearings and retainers. Next the linear races were installed into the thrust block linear race mount, as shown in figure 121. Following this step the load cell was installed by first threading a stainless steel jam nut over the reference end stud of the transducer body. Then the load cell was coated with ceramic anti-seize and installed into the threaded mounting hole of the thrust block. It was threaded in all the way and then backed out to allow the wire exit point on the transducer body to align with the block as depicted in figure 122, which shows the thrust block installed over the linear races.

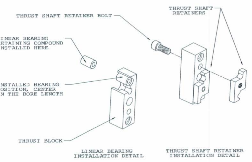

Figure 120 – Linear bearing and thrust shaft retainer details.

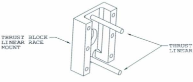

Figure 121 – Linear races mounted in thrust block linear race mount.

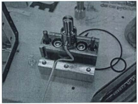

Figure 122 – Load cell installed in thrust block – Note wire alignment.

After installing the load cell and aligning the wire, a strain relief loop was formed before proceeding to the next step. This is also shown in figure 522. The jam nut was then gently tightened. Next the live end of the load cell was coated with anti-seize and the thrust link was installed by threading over the stud. It was threaded all the way on until it stopped and then backed off so that it appears as shown in figure 123. Then the thrust block, along with the linear race mount and load cell was carefully put into position on the load cell housing and the 6 screws installed to keep the subassembly together. Figures 124 and 125 show this step. Figure 126 shows a screw tightening guide.

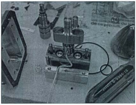

Figure 123 – Thrust link installed.

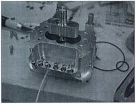

Figure 124 – Load cell housing in position.

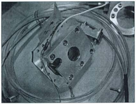

Figure 125 – View from opposite side, all screws installed.

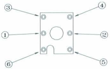

Figure 126 – Screw tightening guide.

Next the subassembly was connected to the main pod unit. Prior to this step it was ensured that the thrust shaft retainers were in the open position. Figure 127 shows the retainers as closed. Figure 128 depicts the retainers opened. The gasket was then fabricated and placed into position and the thrust block was then mounted over the thrust shaft. The retainers were then moved to the closed position by rotating them using a suitable tool (in the author's case it was a tee-handle allen wrench). The partially installed subassembly is shown in figure 129. The screws were then installed and tightened using the guide shown in figure 130. At this point it should also be noted that

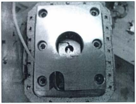

Figure 127 – Retainers closed .

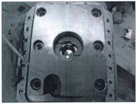

Figure 128 – Retainers opened.

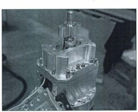

Figure 129 – Subassembly mounted in position on main pod unit.

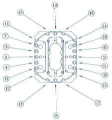

Figure 130 – Screw tightening guide.

it was necessary that the subassembly be installed in the correct orientation to the drive unit. Figure 131 shows the correct orientation.

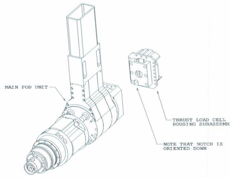

Figure 131 – Installation orientation of pod thrust components.

To complete the installation of the subassembly to the pod unit the thrust shaft had to be positively locked into position with the thrust block. This was accomplished by holding one of the retainers in the closed position (the other will stay closed automatically) while the retainer screws were tightened with a ball end tee-handle allen wrench. This step is shown in figure 132.

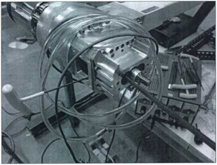

Figure 132 – Locking the thrust shaft to the thrust block.

After this step the position shaft o-rings were fabricated and installed in the shaft grooves. The threads of the thrust link were then lubricated with grease and the position shaft threaded onto it. Grease was used instead of anti-seize because these components would be subjected to frequent relative motion during testing. It is the rotation of this shaft that determines the gap distance setting. Figure 133 shows the position shaft installed. Nearing the completion of the pod unit and gap distance mechanism assembly is the installation of the adjuster housing. Note that only two of the 6 screws were installed at this point because the other four are part of the shell mounting and drag force measurement system. The gasket was fabricated and the adjuster housing was slipped over the position shaft taking care not to damage the previously installed o-ring seals. Figure 134 shows the installed adjuster housing. To bring the assembly to completion was the installation of the gap position lock nut. The last o-ring seal was fabricated and installed under the rim of the nut. Figure 135 shows the installed lock nut.

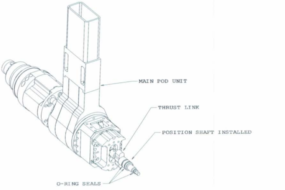

Figure 133 – Position shaft installed.

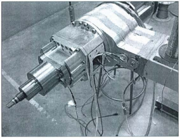

Figure 134 – Adjuster housing installed over position shaft.

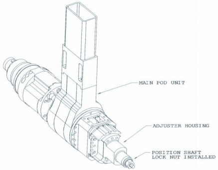

Figure 135 – Position shaft lock nut installed.

1.1.9 Shell Drag Load Cell & Shell Float

There were two aspects to the assembly and setting up of the shell drag instrumentation to allow it to function properly. The first was the completion of the installation of the remaining two of four shell mounts, one of which was instrumented to measure the drag load. The first two shell mounts were installed when the gap pressure sensing instrumentation components were installed on the main pod unit, see section 1.1.5. The second aspect of this system's assembly was the gap filler components installation and its role in setting up the shell drag load cell. Note that although the instrumentation was designed with symmetrical installation locations for the shell drag load cell only one is necessary for most types of anticipated measurements and only one was installed for the first set of tests.

To complete the installation of the two remaining shell floats, first the load cell was threaded into its mounting position. Care was taken during the threading in process to ensure that the wires exiting the load cell canister did not become pinched between the load cell canister and the load cell housing wall as noted in figure 136. Also, to prevent the load cell from water damage, the laser welded construction of the sensor was taken advantage of by applying a small amount of silicone sealant around the wiring exit. This created a leak-proof device. The temperature compensation module was also sealed with silicone sealant. Next the drag link was threaded onto the live end of the load cell as depicted in figure 137. It was threaded all the way onto the stud, but not tightly as it would be backed off slightly during the adjustment process. Following this step the shell mount floats were pre-assembled prior to installation. Assembly consisted of installing the stainless steel linear bearings into the shell mount. Installation of these bearings utilized a liquid retaining compound instead of retaining clips, which was the case with the shell mounts in section 1.1.5. A small amount (several drops) of retaining compound was placed on the surface of the bearing before installation. Installation was carried out with a slight twisting motion as it was inserted into the bore. Figure 138 shows the instrumented shell mount float bearing installation details. Once the bearings were installed, the linear race rods were inserted into the linear bearing bores and these subassemblies were then positioned on the main pod unit such that the race rods were inserted into the two mounting pockets of the load cell housing. At this point the reader should note that although the two mounts are identical, one is connected to the load cell and one is free to move on its linear race rods. Figure 139 shows the installation step in progress for the instrumented shell mount float. The shell mount was pushed towards the

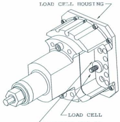

Figure 136 – Load cell position noting installation caution.

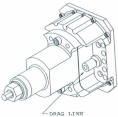

Figure 137 – Installation position of drag link.

drag link until the pan head screw was installed, but not tightened completely. Figure 140 depicts the installed screw. Note the wiring position.

The wiring was routed out behind the lower race rod and across the face of the slip ring housing. The sealed temperature compensation module was then taped to this face using

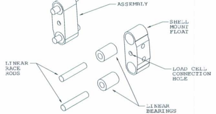

Figure 138 – Shell mount float assembly detail

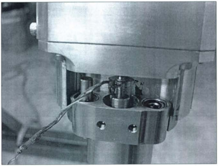

Figure 139 – Installed load cell and drag link, installing shell mount float.

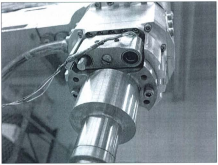

Figure 140 – Installed shell mount float load cell screw.

vinyl water proof tape. The shell drag signal cable was then routed up and into a clear ¼" (6.35mm) diameter PVC hose which acts as a mechanical shield during shell installation.

To allow completion of the shell mount floats it was next necessary to install the gap filler components. These parts allow the gap between the back face of the propeller hub and the flat face of the pod end (where the pressure transducer orifices are) to be changed in such a manner that the pod's outer surface is tangent to the propeller hub taper angle across the gap for specific distance settings. These parts also allow the relative movement of the shell as it is loaded in the direction of its flow in water as well as creating a barrier to prevent any flow rate of water in or out of the volume between the exterior of the main pod unit and the interior of the shell. Installation of these parts was required to allow the axial position of the shell relative to the main pod unit to be adjusted to give proper operating clearances.

Figure 141 shows the 4 components that make up the gap filler system. To start the assembly process the ring adaptor was placed over the main pod unit, as shown in figure 142. Note that the propeller hub taper adaptor, temporarily installed in section 1.1.6, was first removed. The pressure plate adaptor was next installed. This component is composed of two halves which are held onto the pressure sensing plate by 6 stainless steel screws, 3 in each half. These were installed by first placing the o-ring seal over the pressure sensing plate and then placing each half into position on the pressure sensing plate underneath the o-ring seal. This avoided having to stretch the o-ring over the larger diameter of the positioned pressure plate adaptor pieces. The screws were then carefully installed using ceramic anti-seize, given that both the screws and pressure sensing plate are made from stainless steel. The installed ring adaptor, pressure plate adaptor and o-

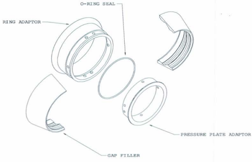

Figure 141 – Gap filler system components.

ring seal are shown in figure 143. One outer shell half was then placed over the ring adaptor to rough in its relative position with the rest of the pod unit. One of the two stainless steel socket head cap screws was installed into the instrumented shell mount float and both screws for the propeller end shell mount float were installed to keep the shell in position. Figure 144 shows the pod unit with one shell half installed. Note that the load cell is now keeping the shell in position in the axial direction. Figure 145 shows a close-up photo of the seal installation position at this point in the assembly.

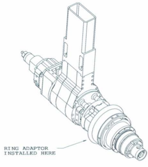

Figure 142 – Installation position of ring adaptor.

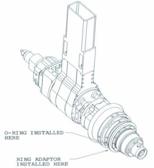

Figure 143 – Installation positions of o-ring and pressure plate adaptor.

Next a gap filler adaptor was installed. This part is also composed of two halves and held into position on the ring adaptor with 6 stainless steel screws. Care was taken to ensure

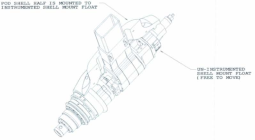

Figure 144 – Pod unit with shell half installed on instrumented shell mount float.

Figure 145 – Close-up of gap filler o-ring seal, ring adaptor and pressure plate adaptor.

Figure 146 – Gap filler installed, note position of its o-ring seal.

that the o-ring seal was positioned in the center of gap filler seal recess, as is shown in figure 146. Note that propeller hub taper angle adaptor is now again in place. The process of setting up the proper operating clearances was then carried out next.

To set the proper operating clearances it was necessary to adjust the position of the instrumented shell float to achieve a gap of 0.010" (0.254 mm) between the opposing faces of the end of the gap filler and the pressure plate adaptor. Figure 147 shows the position of the correct clearance. To adjust the position of the instrumented shell float the slotted retaining screw was loosened and the thrust link moved in the axial direction by rotating with a small standard screwdriver inserted in the space between the load cell housing and the shell mount float. Once a new position was reached, the slotted retaining screw was re-tightened and the clearance gap checked. This process took several iterations until the correct gap was achieved. Note that all critical clearances are 0.010"

(0.254 mm). This makes future setup work simpler with only one value to use. Figure 148 shows all gap filler components installed and set at the correct spacing.

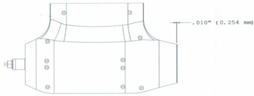

Figure 147 – Gap filler clearance position and value.

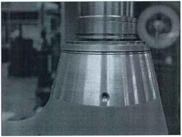

Figure 148 – Completed clearance setup of gap filler components.

With the shell drag load cell correctly positioned, the shell half used in the setup process was removed and the instrumented shell mount float linear race rod ring mount was installed by inserting and tightening four #10-24 x 0.75" screws using the remaining four threaded holes in the position shaft housing. Figure 149 shows a view of the installed

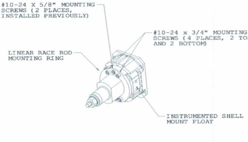

Figure 149 – Installed linear race rod mounting ring.

ring. Next the position shaft and gap filler lock nut access cone cover and its threaded adapter were positioned on the main pod unit and the shell half reinstalled. General clearance was checked for between the exterior of the main pod unit and the interior of the shell. Minimum design clearance was 0.078" (2.00 mm) all around. Figures 150 through to 152 show all internal clearance areas.

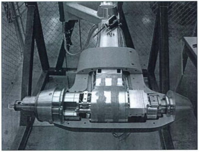

Figure 150 – Overall view of clearances between exterior of pod unit and interior of pod shell.

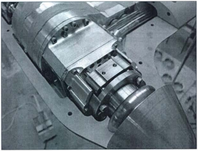

Figure 151 – View of clearances at instrumented shell mount float end.

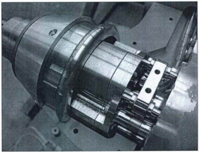

Figure 152 – View of clearances at propeller shell mount float end.

1.1.10 Final Wiring Installation & Pod Enclosure

To complete the enclosure of the main pod unit and create a water tight vessel, the wiring and access hatches were installed. This step also acted to complete the electrical connection between the pod unit and the main wiring harness that allowed the signals to be carried to the data acquisition system. Figure 153 shows a view of the internal pod wiring terminations. The gasket has already been installed at this point. Note the tinned tips that aided the insertion into the terminal blocks on the printed circuit board of the wiring access hatch, shown in figure 154.

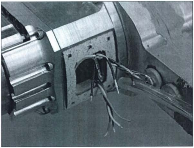

Figure 153 – Wiring terminations from main pod torque and thrust transducers.

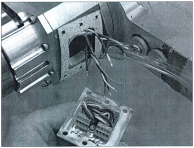

Figure 154 – Wiring access hatch with PCB mounted terminal blocks.

Before final connection of the signal cables, each channel was tested for both continuity, electrical isolation from chassis ground and correct sensor resistance. Figure 155 shows the resistance test for part of the torque bridge circuit.

Figure 155 – Testing the torque bridge circuit (and all others).

After each channel had been tested, the cable ends were inserted into the corresponding terminal block and tightened. Figure 156 shows the finished connections. Note that the cables exiting the hatch have been installed into a clear PCV hose, which acts as a water-tight mechanical shield as well as a passageway to carry dry air to the pod interior. This aspect is discussed in section 7.2. Figure 157 depicts the hatch after being fully installed with the stainless steel socket head cap screws tightened. Note that again the use of ceramic anti-seize was required to prevent breakage or stripping of the fasteners as they are installed or removed at a later date from the aluminum slip ring housing.

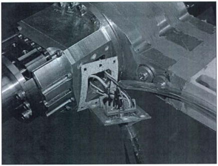

Figure 156 – Cables fully connected.

When the wiring hatch installation was complete, the hose carrying the cables were taped to the pod strut with water-proof vinyl tape. This was done to ensure that no part of the main wiring harness interfered with the operation of the shell drag movement. Figure 158 shows a view of the taped hoses passing through the clearance passageways machined into the pod outer shell and extension. The hose carrying the cables for the pressure transducers was also secured with tape in the same manner on the opposite side of the strut.

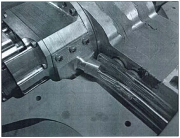

Figure 157 – Wiring hatch fully installed with cables installed in PVC hose.

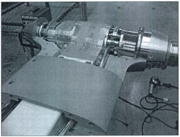

Figure 158 – Secured cable hoses and clearance passageways.

The final step in assembly of the main pod instrumentation unit is now discussed before moving on to the global dynamometer assembly.

1.1.11 Belt Separator, Idler Tensioner Blocks & Gear Box

The propeller drive system was completed by the installation of the Teflon belt separator and the right angled gear box. The belt separator prevents the teeth of opposing sides of the drive belt from interlocking at high propeller speeds. It was inserted into the strut tube by first gently twisting the top loop of the drive belt where it exits the strut tube to allow the belt separator to be inserted. There were slots machined into the top of the bottom strut mount block prior to welding it to the strut tube to allow the belt separator to stay in position during operation. There were also features machined into the belt separator to allow it to fit exactly into the top of the strut tube and gearbox mounting plate. Figure 159 shows the belt separator fully inserted into the strut tube.

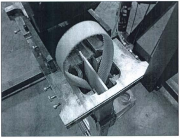

Figure 159 – Inserted belt separator.

The belt separator retaining bracket was next installed to keep this component stationary. This is shown in figure 160. Next the gearbox was mounted after having been filled with the proper quantity and type of lubricant. See **Appendix 'I'** for lubrication specification.

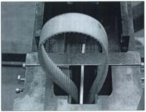

Figure 160 – Belt separator retaining bracket.

To mount the gearbox, first the gearbox mounting plates were installed and then the gearbox laid into position between the plates. Two screws were threaded into position on the end opposite the drive pulley (installed prior to lifting the gearbox into position). This allowed the gearbox to be tilted into position and achieve an initial tensioning of the drive belt. This step is depicted in figure 161. Note that the screws were not tightened at this time. Next the belt tensioner idler pulley blocks were installed in their pivot positions and the drive belt placed over the drive pulley. The gearbox was then lifted to allow an initial tension to be set-up. This is shown in figure 162. The two remaining screws were installed at this time and tightened slightly until the entire unit was installed onto the test carriage. This ends the discussion on the main pod unit assembly and setup.

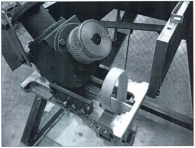

Figure 161 – Gearbox and its mounting plates installed to allow gearbox pivoting.

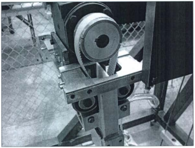

Figure 162 – Gearbox mounted into preliminary position prior to carriage mounting (Note the idler pulleys installed in their pivot points).

1.2 Global Dynamometer Assembly

The global dynamometer assembly started with the live end assembly and progressed outward from this subassembly.

1.2.1 Upper & Lower Live Plate Assembly

The live end of the global dynamometer was designed to be accurately produced and when put together, dimensionally stable under all loading conditions. Assembly consisted of bolting all the components of the live plate together and then proceeding to attach the load points.

The first step consisted of laying the lower live plate assembly on the carriage frame. The plate was positioned on the machined surfaces that were to be used during the initial setup of the flex link and load cell assemblies. This assembly location was utilized because of its flatness and thus would allow the structure to be bolted together in a flat condition. After positioning the lower live plate, each of the stiffeners as well as the center spacer was placed into its machined groove in the lower live plate. One or more screws were installed loosely to keep the stiffeners in place. Figures 163 and 164 show this progression. When all parts were in position the upper live plate was positioned on top of the assembly. This is shown in figure 165.

Next all screws were installed to connect the components together. The installation tightening sequence is shown in figure 166. For each position in the sequence, a screw was installed in both the top and bottom plates. This allowed the tightening force to

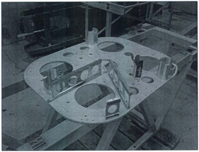

Figure 163 – Lower live plate sitting on carriage frame machined points.

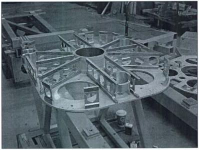

Figure 164 – All stiffeners in place.

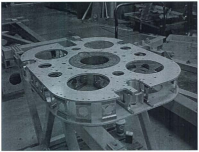

Figure 165 – Upper live plate positioned over assembly.

radiate outwards from the center of the structure as the as assembly progressed. All the fasteners used in this step were ¼ UNC low head socket head cap screws. This choice allowed for a compact fastening method. In the case of the screws connecting the center spacer, the heads were modified by making the thickness of the heads shorter. This compensates for the thinner plate section at this location while still allowing for a counterbore. Figure 167 and 168 show this detail.

Once the live plate components had been fastened together, the load adapters were installed. First the X direction load adapter was connected then the two Y direction load adapters. The Z direction load adapters were installed when the flex links were installed, as their design differed from the X and Y. Figure 169 shows the positioned X load adapter while 170 shows one of the positioned Y load adapters.

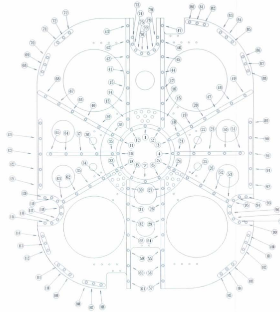

Figure 166 – Fastener tightening sequence for top and bottom live plates.

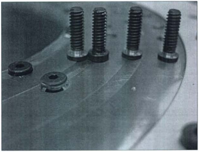

Figure 167 – Modifications to centre spacer screws.

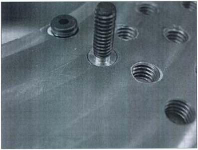

Figure 168 – Test fit of modified fastener head into plate counterbore.

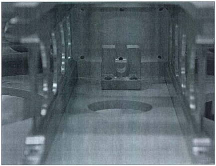

Figure 169 – Positioned X load adapter.

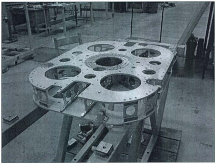

Figure 170 – Positioned Y load adapter.

1.2.2 Positioning the Live Plate Assembly w.r.t. the Reference Frame

As mentioned in the section of the thesis on the design of the dynamometer, one of the key features of an accurate dynamometer is ensuring that the live end is positioned accurately relative to the reference end. To carry this out, the dynamometer was designed to allow the live and reference ends to be positioned such that any of the six load cell and flex link subassemblies could independently be installed or removed without interfering with the others or the overall dynamometer assembly process. This section outlines briefly the procedure used to position the live plate assembly with respect to the reference end of the dynamometer and accurately set the distance between them.

After assembly of the live plate, it was removed and a series of safety studs installed into the tapped holes on the machined pads of the carriage frame. These studs serve two purposes. The first purpose is to prevent the dynamometer live plate from rolling out of position during assembly. The second is to prevent the live end of the dynamometer from uncontrolled movements in the event of a complete flex link failure during use. By using the safety studs, if one or more flex links should fail, the studs will restrain the movement of the live plate preventing further equipment damage or injury to test carriage personal. Figure 171 shows a safety stud installed in the threaded machined pad used for setting the relative distance between the live and reference ends of the dynamometer.

The next step consisted of positioning two ¼" (6.35 mm) diameter steel dowel pins onto the machined pad as depicted in figure 172. These act as rollers. Next, a machined shim was installed onto the rollers at each of the four machined pad locations, as shown in figure 173. Next a ¼" (6.35 mm) diameter roller was placed on top of the shim as shown in figures 174 and 175. Note the placement of the shim's slot in the figures.

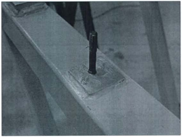

Figure 171 – Safety stud.

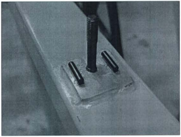

Figure 172 – First two locating rollers installed into position.

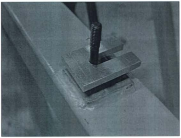

Figure 173 – Installed spacer shim.

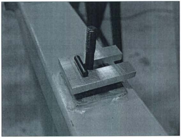

Figure 174 – Top roller.

This allowed the shim to be pulled out when all flex link and load cell assemblies had been added to the assembly.

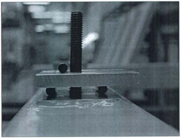

Figure 175 – Side view of all rollers and shim.

All four safety studs, shims and rollers are shown as installed in figure 176. The assembled live plate was then placed over the safety studs such that the top roller in each location contacted the corresponding machined surface on the underside of the lower live plate. Figure 177 shows the positioned live plate assembly sitting in place. Figure 178 shows a close-up of the roller and shim arrangement between the two dynamometer components. The positioning of the reference frame is discussed in the next section.

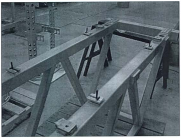

Figure 176 – All four sets of positioning components installed.

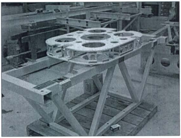

Figure 177 – Live plate assembly installed with correct height set.

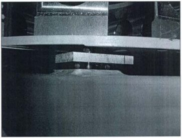

Figure 178 – Close-up of shim and roller assembly between dynamometer components.

1.2.3 Reference Frame and Carriage Frame Assembly

The reference frame serves two major functions in the overall dynamometer assembly. First it is the object with which all forces react against during instrumentation use. Its second function is to serve as a platform that can be raised when adjustments, changes, installation or removal of the pod unit must be carried out. It was necessary (as presented in the section on its design) therefore to make the rigid attachment and removal of this component to the carriage frame relatively easy. The assembly of these two components consisted of placing the reference frame into position on the carriage frame and aligning the four attachment bolt holes. The four retaining bolts were then installed and tightened. No other alignment was necessary to continue onto the next step of installing the load cells and flex links. Figure 179 shows the reference frame positioned over the carriage frame. Figure 180 shows the attachment bolt locations.

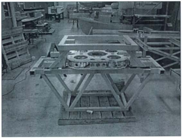

Figure 179 – Reference frame positioned.

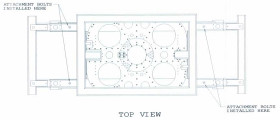

Figure 180 – Attachment bolt locations.

1.2.4 Flex Link & Load Cell Assembly & Installation

The global dynamometer is designed to allow each of the flex link and load cell assemblies to be installed independently of the others. Thus, to start the assembly, each of the load cells was screwed into position on the reference frame using the appropriate adaptor. Figure 181 shows the load cell adaptor for the X, Y and Z directions. Note that the X-direction required two adaptors to allow load cell installation as there was limited space available in this location of the dynamometer. The X-direction load cell and its adaptor were both installed on the 90° adaptor before bolting all three components to the reference frame.

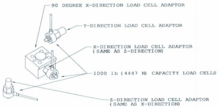

Figure 181 – Load cell adaptors.

Installing the load cells with the adaptors minimizes risk of damaging the load cell due to cross threading or applying too much torque to the body of the load cell. Also, in the event of a catastrophic failure due to collision in the test tank or other scenario, the adaptor can always be unscrewed even if the load cell threads in the adaptor are damaged as the strength of the adaptor makes it unlikely to be damaged. Figure 182 depicts one of the Y-direction load cell adaptor installed on the reference frame (note that photo was taken during QA of the adaptor and before dynamometer assembly), the Z setup is similar and is shown in figure 183. Once all load cells had been installed the flex links were

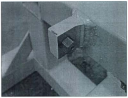

Figure 182 – Y-Dir load cell adaptor.

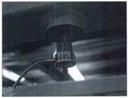

Figure 183 – Z-Dir load cell & adaptor.

then added by threading them over the live end stud of the load cell. The installation of the Z-direction flex links are discussed first.

The design of the Z-direction setup was such that it was simple to tilt the flex link into position and thread it over the load cell stud. This is due to the over-sized hole in the lower live plate. Figure 184 is a photo showing a test fit of a Z-direction flex link installation (note the stud end of the flex link in the over-sized hole). Next the Z-direction load adaptor was placed into position after the flex link was installed. To complete this step first one ½" UNF nut was threaded over the flex link stud. Next a flat washer was installed, then the Z-direction load adaptor was pushed on over the stud and up through the hole in the lower live plate. A second flat washer then a second nut was installed. The position of the Z-direction load adaptor was adjusted using the two nuts until it just contacted the plate. Six ¼" UNC low head socket cap screws were then installed but not fully tightened. Next each of the two fine thread nuts previously

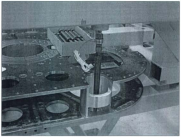

Figure 184 – A test installation photo of a Z-direction flex link. Note the oversized hole in the lower live plate to facilitate easy flex link installation.

installed on the flex link stud was loosened to give about 1 mm (0.040") clearance between it and the adjacent face of the Z-direction load adaptor. Then the 6 screws securing the live plate adaptor were tightened fully. The two flex link stud nuts were then tightened only until contact with the adaptor was made. This procedure was followed to avoid lifting the live plate away from the top roller installed on the positioning shim. Figure 185 shows a view looking up at the bottom of the lower live plate and installed load adaptor for the Z-direction flex link. Figure 186 shows a view of the entire installation of a Z-direction load cell, flex link and load adaptor. Final tightening is discussed in section 1.2.5.

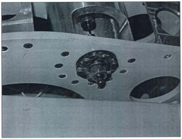

Figure 185 – Installed but not yet tightened load adaptor for a Z-Direction flex link.

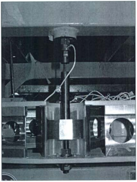

Figure 186 – Complete load cell and flex link installation for Z-direction.

To install the X and Y direction flex links, first one ½-UNF nut needed to be threaded all the way onto the stud end of the flex link and a flat washer pushed on over the stud after nut installation. This allowed the stud to be linked to the live plate load adaptor and adjusted as described in section 1.2.5. Each of the X and Y direction flex links was then maneuvered into position and the stud end dropped into the slot of the live plate load adapter, making sure the previously installed nut was not contacting the adjacent face. The ¼-UNF threaded hole of the flex link was then threaded over the live end of the previously installed load cell. Once installed, a second washer and the second nut were threaded onto the flex link studs of the X and both Y flex links, but again not fully tightened. Figure 185 shows one of the two installed Y-direction load cells with the flex link installed while figure 186 shows the live plate load adapter with the flex link stud installed in the slot and both nuts and washers contacting the faces.

Figure 187- Installed Y-direction load cell and flex link.

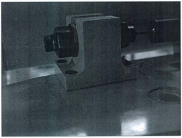

Figure 188 – Live plate load adapter with flex link, washers and nuts installed.

1.2.5 Adjusting the Flex Links

Note that to complete this step the data acquisition system was partially set-up to allow the voltage outputs from the load cells to be monitored. The complete procedure for setting up the data acquisition system is outlined in section 2.

Adjustment of the flex links served two purposes. The first was to ensure that the assembly was aligned correctly in the X-Y plane and the second was to ensure that the assembly did not contain an excessive amount of tension or compression preload in the force measurement system. Ideally a dynamometer should only register the mass of the live portion of the assembly (unless counter-weighted), the magnitude of which is factored into the load capacity of the individual load cells. If a dynamometer is poorly adjusted then a large portion of the load capacity can be wasted in system preload. This leads to a situation where one or more channels can be saturated when the dynamometer is placed into service and a slight load is encountered on a channel that has a high degree of preloading.

The data acquisition system had been partially assembled at this point in time, and was functional for this procedure. All six load cell cables were connected to two data acquisition signal conditioning cards. The signal gain for each channel was set to allow a reading to be seen on the screen in metering mode, which is a continuous voltage monitoring mode of operation. Figure 189 shows a typical screen display of the data acquisition system in metering mode.

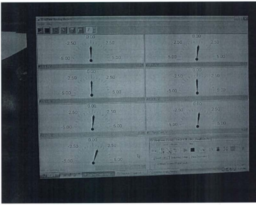

Figure 189 – Metering mode display of all six load cells in the dynamometer.

To start the dynamometer adjustment process, the X-Y alignment was carried out first. Figure 190 shows a locating diagram used to measure the relative dimensions between the machined faces of the live end load point adaptors and the corresponding reference frame load cell mounting positions. A set of digital calipers was used to measure both relative dimensions. Next the average of both values was calculated and thus became the target distance value used in the adjustment process. The adjustment was made by carefully loosening the nut on the flex link stud that was closest to the direction desired to move the live plate assembly, and then tightening the other nut to carry out the movement in the desired direction. These adjustments were carried out until the computed average target value was met for both Y-direction loading positions.

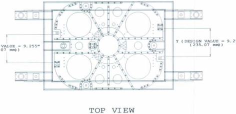

Figure 190 – Location for measuring relative distances between live & reference faces.

When the X-Y alignment was complete, a final tightening of the flex links was carried out. This was accomplished by first noting the voltage output of each of the X and Y-direction load cell channels. The two nuts on each flex link stud were backed off slightly to allow the load cell to relax. The zero load voltage was viewed and used as the value to aim for when tightening the two nuts. The nuts were progressively tightened by first tightening one, then tightening the opposite nut an equal amount while viewing the voltage output. For each pair of tightening turns, the voltage was maintained to the no load voltage. This procedure was carried out all three flex links in the X-Y plane were fully tightened. Note that to accomplish the tightening, two open end wrenches were used (and are the best tools for this operation). A ¾" (19.05 mm) wrench was used on the nut, while a 3/8" (9.525 mm) wrench was used to hold the stud stationary. The 3/8" (9.525 mm) hex at the bottom of the flex link stud is to prevent the necked down region of the flex link from being loaded in torsion by acting as a point to apply a reaction torque. Figure 191 illustrates the two wrenches in use. When fully tightened, the target distance value was checked again. Once this value had been verified, the Z-direction flex link tightening commenced. Note that for reference purposes, the design value for the XY distance is 9.255 inches (235.07 mm).

For the Z-direction, the procedure was slightly different. As in the case of the X and Y voltages, they were first observed, but then each bottom flex link nut was turned in a direction so as to increase the flex link load (clockwise (CW) if viewed from the bottom, counter-clockwise (CCW) if viewed from the top) until it was just supporting its portion of the live assembly mass. This point was realized when the voltage change stopped. Note that again the stud was prevented from rotating by using two wrenches. The nut was then rotated back in the opposite direction until the voltage just started to change.

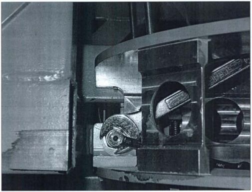

Figure 191 – Using two wrenches for final Y-direction flex link tightening.

The voltage at this point was observed and used as the target voltage for final tightening. At this point the top nut was tightened (CW looking down, CCW looking up) and then the bottom nut was tightened by the same amount. These steps were carried out in a progressive pattern until all three Z-direction flex links were secured. As with the Y-direction flex links, a 3/8" (9.525 mm) wrench was used to prevent the stud of the flex link from turning, as illustrated in figure 192. After adjusting in this manner, the flex links were "just" supporting the mass of the dynamometer and the previously installed shims were not carrying a significant amount of load.

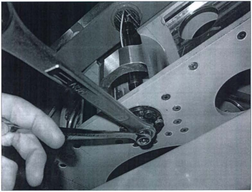

Figure 192 – Using two wrenches for final Z-direction flex link tightening.

The last flex link to be adjusted was the one for the X-direction. In this case, the nuts on the stud were backed off and the no-load voltage noted as the target value. Both nuts were then adjusted as in the previous directions so as to not change the no-load condition. Note that all voltages were monitored during this last phase to ensure that off-axis voltages were not significantly changed. At this point the dynamometer was ready to have its shims and roller removed.

1.2.6 Removal of Spacer Locating Shims and Rollers

When all adjustments on the load cells had been completed the spacer shims and rollers were removed. To carry out this last step the shim was simply grasped by two edges and pulled out in a direction parallel to the slot. The rollers made it easy to pull the shim out. The dynamometer was now ready for calibrations. This procedure is discussed in **Appendix O**. A discussion on the setup of the data acquisition system now follows.

2 Data Acquisition Setup

To allow the newly assembled instrumentation to be calibrated and then used, the data acquisition system had to be electrically connected and interfaced correctly. The author had originally intended to use LabVIEW as the software for the data acquisition process. This program can be configured to allow plotting and analysis of data in engineering units after each experimental run. This allows a summary of each experiment to be produced nearly immediately after a run and when viewed, gives an indication of whether or not the experiment, instrumentation, or both are proceeding in a manner that makes sense, depending on the insight of the experimenter. However, because of a limited availability of time during testing, the author had to use DaqView as the acquisition software package. All data was therefore acquired in volts and analyzed much later. This is generally not good practice but had to be accepted given the tank time constraints of the experimentation.

2.1 Electronics Assembly and Card Channel Selection

The first step in the electrical interfacing of the instrumentation sensors and the data acquisition system was the assembly of the data acquisition electronics and the card channel selections. The author is indebted to the efforts of Mr. Jonathon Fleming for carrying out this important task, as well as soldering together all connectors and cabling for the system.

Assembly of the electronics consisted of inserting each sensor system card into the chassis box that had been ordered for the project, and connecting all of them together with a parallel ribbon cable. Selecting a channel for each card consisted of placing a jumper switch over the correct two pin set of the channel to be selected. Figure 193 shows a DBK-45 signal conditioning card. Note the channel assignment jumper pin sets. The channel assignment had no bearing on the data acquisition operation with the exception of the DBK-45 cards, which has the requirement of not being set to the lowest channel number.

In addition to the card channel, there was a port assignment (sub-channel) for each particular card. As a result, each sensor was identifiable by a card and port channel number. The card and port channel number was labeled in the data acquisition software to identify the channels of data that were collected during the experiments.

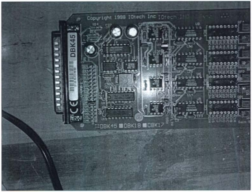

Figure 193 – Typical channel assignment jumper switch setting.

2.2 Gain Selection for Transducers

The gain value for each set of instrumentation systems was set to achieve a final amplified voltage of as close to approximately ± 4 volts as possible without going over. A range of ± 4 volts was chosen to minimize the possibility of channel saturation by having a contingency of ± 1 volt. As an example, for the dynamometer load cells, the output from the sensor is approximately 1.94 mV per volt of excitation at the maximum rated load capacity (1000 lbs or 4448.2 N). The excitation voltage is 10 VDC, therefore the maximum expected voltage from the sensor at a loading of 1000 lbs is approximately 19.4 mV. If one divides 4000 mV by 19.4 the result is approximately 206. The closest gain value available from the selector jumper switches on the DBK-45 signal conditioning card is 200. Thus the gain value used was 200. Most load cells can handle a certain amount of overload (typically 10%), thus by having a gain of 200 it is unlikely that the channel would have a voltage input to the card that exceeds the maximum ± 5 volts the card is capable of measuring. The trade-off for this gain value however is a loss of resolution at lower loading conditions for the dynamometer. After some experience with the instrumentation, it would be possible to alter the gain value if one was sure the maximum sensor voltage would not exceed ± 5 volts at the higher levels of loading. Thus the next gain value of 500 could be used. Alternatively, one could calculate the resistance of a gain resistor that would allow the sensor to yield ± 5 volts at full load. This resistance is calculated by the formula: $R_{GAIN} = [40000 / (GAIN - 1)] - 50\ \Omega$. Once calculated, the resistor is soldered directly into the correct location on the PC board of the DBK45 card.

In the case of the shell drag, hub assembly and pod assembly thrust load cells, the output from the sensor is considered to be high output since at full scale loading the output is approximately 200 mV. Thus the gain value was set to a value of 10 to prevent channel saturation. As in the case of the dynamometer load cells, the next gain value of 100 could be used if one was sure that the loading was at the lower end of the load cell's range, or a specific gain resistance calculated and soldered onto the PC board.

In the case of the test carriage speed, the gain was set to 1, as the output from this transducer is approximately 1 VDC for every 1 m/s velocity.

In the case of the pressure transducers and propeller shaft tachometer generator, the gain level was 1 by default, as these devices were connected to the DBK80 data acquisition card, which has unity gain.

For the propeller torque signal, setting the gain required following a procedure set forth in the IOTech manual on the DBK16, which is a 2 channel strain gauge amplifier. Essentially, the procedure was followed to allow setting 10 VDC as the excitation voltage and ±4 V for the maximum design torque of 34 N·m.

2.3 Labeling of Channels in DAQVIEW

Labeling was carried out to reflect the sensor connections to the data acquisition cards. These labels appeared in the final data files collected during testing.

2.4 Wiring the Connectors

With the exception of the propeller shaft speed and test carriage speed tachometer generators, each sensor needed 4 conductors to function. This resulted in a need for 64 conductors to carry all excitation voltages and signals between the instrumentation package and the data acquisition system. To carry this out, the author sourced a shielded cable with 25 individual conductors. Each conductor was colour coded with the combination of a solid colour and stripe colour. A wiring key was developed to allow the distribution box to be set up with each connector positively identified. The cable was then cut into 3 lengths (as short as possible) that made up the main wiring bundle for the electrical system. This provided enough conductors with 11 to spare. Again, Mr. Jonathon Fleming carried out the tedious task of following the wiring key in soldering the connectors to the wiring bundle to allow all sensors to function correctly.

2.5 Selecting the Cable Routes

The last detail in setting up the data acquisition system was in the selection of the cable routes. The data acquisition cable was run in such a manner as to maximize its distance from the drive motor, power and control cables. The cable route was also set out to provide the movement necessary as the lift elevator raised and lowered the instrumentation package.

This ends the discussion on experimental setup.

APPENDIX O

CALIBRATIONS

CALIBRATIONS

INTRODUCTION

This document presents the calibration process for the various instrumentation systems.

1 Calibration Fixture Setups

Calibration of the instrumentation started with planning the loading scheme for each system. In the case of the global dynamometer, thrust and drag portions of the pod instrumentation, fixtures were set up to allow forces to be applied to the sensors in the correct orientation. In the case of propeller torque, a moment arm was designed to allow the accurate application of torque. The relative twist in the shaft as well as any stretch in the belt which would occur during torsion loading was accounted for by machining a radius on the end of the moment arm used in the application of torque. This radius ensured that the moment arm remained constant throughout the angle of rotation of the shaft. For the pressure transducers, a hollow square tube with marked water depths was fabricated. The entire pressure sensing assembly was installed and all transducers calibrated under the same conditions. In all cases where required, the system was leveled to ensure that the loading axis was parallel with the movement axis of the instrumentation.

2 Propeller and Pod Propeller Thrust Calibrations

To calibrate the thrust instrumentation of the pod unit, a simple calibration jig was designed and fabricated. This jig consists of two thin walled square aluminum tubes and two threaded rods. These components allow the thrust to be calibrated in both pull (tractor) mode and push mode. One tube connects to the hub instrumentation utilizing the threaded propeller mounting holes. The other tube connects to a weight hanger on which weights of known mass are placed during the calibration procedure. The threaded rods connect the two tubes in such a manner that the pod unit does not obstruct the thrust line in the case of push mode calibrations. Figure 1 shows the setup for tractor mode (system in tension), while figure 2 shows the setup for push mode (system in compression). Note that the shell can be installed or omitted from the instrumentation during thrust calibrations.

To start the calibration procedure, the load cells for the two thrust measuring systems were tested in the un-installed condition. This was to establish a linear calibration constant that was checked against the factory calibration constant as well as to establish a base line slope that could be compared to the installed calibration constant. This would be the first indication as to the mechanical functioning of the thrust measurement systems. Each load cell was calibrated by first mounting a pull point on each stud of the device and then hanging it from a suitable frame that could carry the 889.64 N (200 lb) test load force. The load cell was then hard-wired to the data acquisition system using a spare channel with the gain (x10) appropriately set. The excitation voltage was then set and verified with an external digital multi-meter. Note that the power supply was allowed several hours to warm up and stabilize, given that it was an analogue unit. The test of the load cell was conducted by hanging known weights, in an increasing fashion, on the device for at least ten seconds at each step. Then the load cell was unloaded by

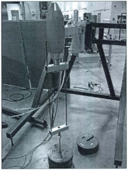

Figure 1 – Pull configuration calibration set-up.

Figure 2 – Push configuration calibration set-up.

removing weights and allowing it to stabilize for at least ten seconds at each step. A time series plot was then created to allow the stable regions of test data to be identified. These stable regions then had an average voltage computed in Excel, a spreadsheet software package. Figure 3 shows the time series plot for the propeller hub thrust load cell (#2199). Table 1 contains the resulting stable region voltage average values, along with their corresponding loading mass, for loading condition and unloading conditions. The values in table 1 are plotted separately in figures 4 and 5. These are the calibration plots for loading and unloading of the load cell and show the computed slope that resulted from fitting a linear trendline in each case. The slight variances in slope between loading and unloading portions of the test may be due to transient forces sustained during placement or removal of the weights, however the author was careful to select the data regions outside any noticeable transient voltages at the beginning or end of a stable region for each calibration weight addition/removal. The difference in intercept values is due to hysterisis.

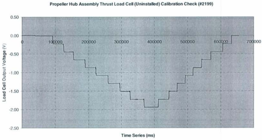

Figure 3 – Time series plot for the calibration of the propeller hub assembly thrust load cell.

(#2199) CALIBRATION SUMMARY DATA FOR LOADING/UNLOADING					
Weight #	Individual Mass (kg)	Total Added Mass (kg)	Thrust (N)	Vavg (V)	Vavg x -1 (Wiring Corrected*)
0	0	0	0	0.00872	-0.00872
Weight Hook	0.7876	0.7876	7.7264	-0.00801	0.00801
1	10.0036	10.7912	105.8617	-0.22515	0.22515
2	9.9936	20.7848	203.8989	-0.44277	0.44277
3	10.0012	30.786	302.0107	-0.65942	0.65942
4	10.0046	40.7906	400.1558	-0.87239	0.87239
5	10.0198	50.8104	498.4500	-1.08407	1.08407
6	10.0056	60.816	596.6050	-1.29728	1.29728
7	10.00505	70.82105	694.7545	-1.51331	1.51331
8	10.01805	80.8391	793.0316	-1.72870	1.72870
9	10.0079	90.847	891.2091	-1.94005	1.94005
8	10.01805	80.8391	793.0316	-1.72809	1.72809
7	10.00505	70.82105	694.7545	-1.51209	1.51209
6	10.0056	60.816	596.6050	-1.29708	1.29708
5	10.0198	50.8104	498.4500	-1.08474	1.08474
4	10.0046	40.7906	400.1558	-0.87493	0.87493
3	10.0012	30.786	302.0107	-0.65760	0.65760
2	9.9936	20.7848	203.8989	-0.44084	0.44084
1	10.0036	10.7912	105.8617	-0.22404	0.22404
Weight Hook	0.7876	0.7876	7.7264	-0.00648	0.00648
0	0	0	0	-0.00710	0.00710

Table 1 – Average voltage values of stable regions of *loading & unloading* portions of time series plot (Propeller **hub** assembly thrust load cell, **uninstalled**).

*NOTE: indicates that result was multiplied by -1 to account for wiring polarity (this is the only case requiring such a correction for all experiments).

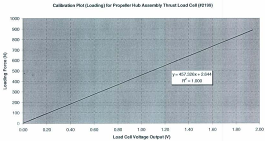

Figure 4 – Calibration plot for *loading* condition of uninstalled hub load cell. (Data from table 1)

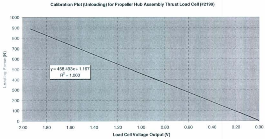

Figure 5 – Calibration plot for *unloading* condition of uninstalled hub load cell. (Data from table 1)

The correlation coefficient for both calibrations is included in the plots. A value of 1.000 indicates a good calibration.

Figure 6 shows the time series plot for the pod unit propeller thrust load cell (#2198). Table 2, along with figures 7 and 8, show the calibration result complete with correlation coefficient. Note that the slopes and correlation coefficients have been calculated using all points in the calibration process.

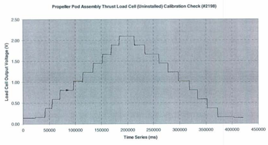

Figure 6 – Times series plot for the calibration of the propeller pod assembly thrust load cell.

(#2198) CALIBRATION SUMMARY DATA FOR LOADING/UNLOADING				
Weight #	Individual Mass (kg)	Total Added Mass (kg)	Thrust (N)	Vavg (V)
0	0	0	0	0.13923
Weight Hook	0.7876	0.7876	7.7264	0.15626
1	10.0036	10.7912	105.8617	0.37291
2	9.9936	20.7848	203.8989	0.58851
3	10.0012	30.786	302.0107	0.80430
4	10.0046	40.7906	400.1558	1.02029
5	10.0198	50.8104	498.4500	1.23602
6	10.0056	60.816	596.6050	1.45181
7	10.00505	70.82105	694.7545	1.66889
8	10.01805	80.8391	793.0316	1.88355
9	10.0079	90.847	891.2091	2.09854
8	10.01805	80.8391	793.0316	1.88246
7	10.00505	70.82105	694.7545	1.66602
6	10.0056	60.816	596.6050	1.45047
5	10.0198	50.8104	498.4500	1.23458
4	10.0046	40.7906	400.1558	1.01881
3	10.0012	30.786	302.0107	0.80289
2	9.9936	20.7848	203.8989	0.58597
1	10.0036	10.7912	105.8617	0.37072
Weight Hook	0.7876	0.7876	7.7264	0.15533
0	0	0	0	0.13906

Table 2 - Average voltage values of stable regions of *loading & unloading* portions of time series plot (Propeller **pod** assembly thrust load cell, **uninstalled**).

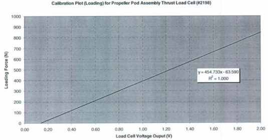

Figure 7 – Calibration plot for *loading* condition of uninstalled pod load cell (Data from table 2).

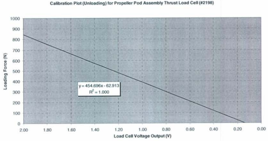

Figure 8 – Calibration plot for *unloading* condition of uninstalled pod load cell (Data from table 2).

At this point the calculated slopes were compared to the factory slopes specified at the full scale output of the sensor devices (see **appendix A**). Table 3 compares the two sets of slopes. Note that units are Newtons/Volt. The difference between the two might be accounted for by the voltage drops across the signal cables, the extra resistances in the plugs and error in the excitation voltage setting, given that the unit is an analogue unit set by a potentiometer. Without justification the author averaged the loading/unloading experimental calibration constant for the comparison to the factory slope. Note also that the percent difference between loading/unloading of the hub and pod load cells is approximately 0.25% and 0.08% respectively. The values of 97.2% and 99.2% indicate that the load cells were functioning correctly and had a high degree of agreement with the factory value.

Newtons/Volt	Hub Load Cell (#2199)	Pod Load Cell (#2198)
Factory Slope	*470.960*	*458.580*
Calibration Slope (loading)	457.326	454.733
Calibration Slope (unloading)	458.493	454.696
Average Calibration Slope	*457.910*	*454.715*
Calibration Slope as % of Factory Slope	**97.2**	**99.2**

Table 3 – Comparison of factory specified slope to experimental calibration slope.

Following calibration of the load cells in the uninstalled state was the required assembly and installation procedure to integrate the load cells into the complete instrumentation package. The reader is referred to **Appendix M** for these details.

Referring again to figures 1 and 2, the completed pod unit subassembly was calibrated in both push and tractor (pull) mode. At this point in time, it was decided to test the unit in tractor mode only. The reason was a looming time restraint. There was only time for testing in one of the two modes of propulsion in the time frame allowed. Thus, having to make a choice, testing in tractor mode was selected to conduct the initial series of tests with an un-obstructed inflow to the propeller.

The calibration procedure started with mounting the assembled pod unit to a frame that was specifically designed for this task. After the frame and pod unit had been leveled, the calibration jig and weight hook were attached to the propeller mounting face on the hub instrumentation. Next the weights were added in succession as the data was collected. Note that both thrust load cells were calibrated at the same time during this exercise. Without justification, the added calibration mass totaled 60 kg (132.28 lb), less than the 90 kg (198.42 lb) used on the load cells in the uninstalled state. The anticipated propeller thrust was such that a 60 kg (132.28 lb) calibration was deemed adequate, thus avoiding subjecting the instrumentation to excessive forces. As each weight was added, the drive system was rotated clockwise and counter-clockwise to reduce the frictional effect that the seals and bearings would have on the thrust measurement system. Friction in such a system tends to reduce the effective load reaching the load cells and must be reduced as far as possible by rotating the components fitted with seals and bearings. The effect of this slight rotation can be seen as a settling of the output voltage in figure 9 and figure 10 time series plots of the calibration procedure for the pod unit in tractor mode.

Of particular interest is the fact that upon close examination of these two plots, the pod thrust settling is more pronounced than the hub thrust (almost none), with the voltage output increasing/decreasing by approximately 25-35% during loading/unloading (a visual estimate) after the slight agitation of the system. This result is to be expected because the thrust instrumentation mechanical system in the pod unit is more complicated, having more seals and bearing elements than the hub thrust instrumentation mechanical system.

The load cell results are presented in individual plots to allow detailed viewing of the data traces and an understanding/insight into the instrumentation operating characteristics.

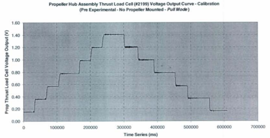

Figure 9 – Times series plot for the calibration of the installed propeller hub assembly thrust load cell (Pull Mode).

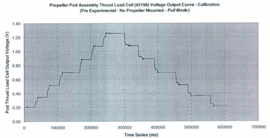

Figure 10 – Time series plot for the calibration of the installed propeller pod assembly thrust load cell (Pull Mode).

Derived from the time series plots are the average voltages for the stable regions, presented in tables 4 (hub load cell), and 5 (pod load cell). The calibration plots from this data are shown in figures 11 through to 14, along with the computed slopes and correlation coefficients.

(#2199) CALIBRATION SUMMARY DATA FOR LOADING/UNLOADING				
Weight #	Individual Mass (kg)	Total Added Mass (kg)	Thrust (N)	Vavg (V)
Cal Jig & Hook	2.4940	2.494	24.4661	0.15066
1	10.0036	12.4976	122.6015	0.36000
2	9.9936	22.4912	220.6387	0.56718
3	10.0012	32.4924	318.7504	0.77627
4	10.0046	42.497	416.8956	0.98476
5	10.0198	52.5168	515.1898	1.19745
6	10.0056	62.5224	613.3447	1.40854
5	10.0198	50.8104	498.4500	1.20325
4	10.0046	40.7906	400.1558	0.99478
3	10.0012	30.786	302.0107	0.78702
2	9.9936	20.7848	203.8989	0.57366
1	10.0036	10.7912	105.8617	0.37043
Cal Jig & Hook	2.4940	0.7876	7.7264	0.16407

Table 4 - Average voltage values of stable regions of *loading & unloading* portions of time series plot.
(Propeller **hub** assembly thrust load cell, **installed pull mode**)

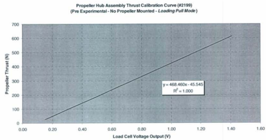

Figure 11 – Calibration plot for *loading* condition of Hub Assembly (Data from table 3).

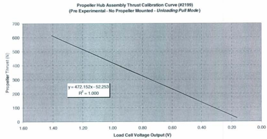

Figure 12 – Calibration plot for *unloading* condition of Hub Assembly (Data from table 3).

In the case of the hub thrust calibration, the correlation of the data is good with a change in slope of 3.692 N/V (about 0.79%) from the loading case to the unloading case. Next is the result from the pod thrust calibration. Referring to table 5, one can immediately see that the amount of retained registering voltage is more pronounced for the installed pod load cell, indicating a higher degree of friction as the components involved are reversed in loading.

(#2198) CALIBRATION SUMMARY DATA FOR LOADING/UNLOADING				
Weight #	Individual Mass (kg)	Total Added Mass (kg)	Thrust (N)	Vavg (V)
Cal Jig & Hook	2.4940	2.494	24.4661	0.20215
1	10.0036	12.4976	122.6015	0.34638
2	9.9936	22.4912	220.6387	0.51472
3	10.0012	32.4924	318.7504	0.69936
4	10.0046	42.497	416.8956	0.88400
5	10.0198	52.5168	515.1898	1.07112
6	10.0056	62.5224	613.3447	1.25462
5	10.0198	50.8104	498.4500	1.08013
4	10.0046	40.7906	400.1558	0.89225
3	10.0012	30.786	302.0107	0.69903
2	9.9936	20.7848	203.8989	0.51958
1	10.0036	10.7912	105.8617	0.36211
Cal Jig & Hook	2.4940	0.7876	7.7264	0.21877

Table 5 - Average voltage values of stable regions of *loading & unloading* portions of time series plot.
(Propeller **pod** assembly thrust load cell, **installed pull mode**)

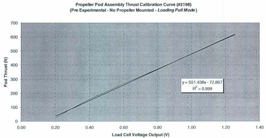

Figure 13 – Calibration plot for *loading* condition of Pod Unit (Data from table 4).

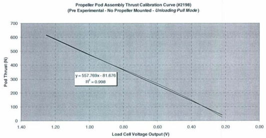

Figure 14 – Calibration plot for *unloading* condition of Pod Unit (Data from table 4).

In the case of the pod thrust calibration, the correlation of the data is good with a change in slope of 6.331 N/V (about 1.15%) from the loading case to the unloading case. Note that the correlation has dropped slightly however. If one plots the data while omitting the lowest point, the correlation goes up and the change in slope drops to 4.569 N/V as indicated in figure 15 and figure 16 (about 0.85%). Note also that the overall apparent stiffness seems to drop by omitting the lowest data point. This is an indication that friction dominates the operation of the instrumentation located in the pod at lower magnitudes of thrust loading.

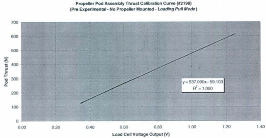

Figure 15 – Calibration plot for *loading* condition of Pod Unit with lowest data point omitted (Data from table 5).

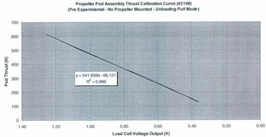

Figure 16 – Calibration plot for *unloading* condition of Pod Unit with lowest data point omitted (Data from table 5).

Note also that if you compare the slopes from the tests of the load cells in the installed case to the uninstalled case, there is a larger degree of stiffness increase for the pod thrust instrumentation than in the hub thrust instrumentation, as seen in table 6. This result was predictable given the extra complexity of the pod thrust instrumentation.

	Uninstalled Load Cells		*Installed Load Cells*	
Newtons/Volt	Hub Load Cell (#2199)	Pod Load Cell (#2198)	Hub Load Cell (#2199)	Pod Load Cell (#2198)
Calibration Slope (loading)	457.326	454.733	468.46	537.09
Calibration Slope (unloading)	458.493	454.696	472.152	541.659
Average Calibration Slope	*457.910*	*454.715*	*470.306*	*539.375*
% Increase (Uninstalled-Installed loading)	2.43	18.11		
% Increase (Uninstalled-Installed unloading)	2.98	19.13		
% Increase Average (Uninstalled-Installed)	2.71	18.62		

Table 6 – Comparison of uninstalled to installed calibration constants, pull mode.

Although not tested, the pod instrumentation was calibrated in the pusher configuration as the author was interested in the calibration characteristics in this direction. The pod unit was reoriented and the calibration jig changed to suit this direction (see figure 2). In this configuration the load cells were loaded in compression. Calibration of the uninstalled load cells was not carried out in compression prior to installation because this would have required that two more loading jigs be designed and manufactured. Loading an uninstalled load cell in compression is slightly more difficult and time did not permit this task. Figure 17 and figure 18 show the time series plots for the calibration operation in pusher mode.

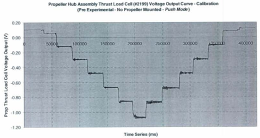

Figure 17 – Times series plot for the calibration of the installed hub unit propeller thrust load cell (Push Mode).

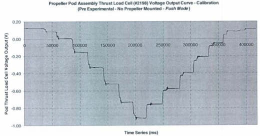

Figure 18 – Time series plot for the calibration of the installed pod unit propeller thrust load cell (Push Mode).

An interesting point visible when one observes these two plots is that the hub assembly load cell exhibits a more oscillatory motion in push configuration than in pull configuration. This is not the case with the pod assembly load cell, which is dampened in both modes of calibration. Tables 7 and 8 display the calibration data for the installed load cells in push mode. These values were derived from the average values of the stable regions of the time series plots. Plotted in figures 19 through to 22 are the loading and unloading calibration lines, with slope and correlation coefficients. Note that again some data points were omitted to arrive at these slopes.

When one looks at these plots in comparison to those from pull mode it is observable that the stiffness increase is higher in the hub assembly load cell in push configuration than in pull configuration. The stiffness increase in push mode for the pod assembly load cell is about that same as that for pull mode. This could be due to the fact that at this point in time the instrumentation had not been operated. The author decided that a post calibration would thus be of interest after the experiments were finished. This result also indicates that a dynamic calibration would be useful to carry out as the continued motion would tend to settle any components subject to the effects of friction.

Table 9 summarizes the calibration constants for both pull and push mode for the loading and unloading conditions.

(#2199) CALIBRATION SUMMARY DATA FOR LOADING/UNLOADING				
Weight #	Individual Mass (kg)	Total Added Mass (kg)	Thrust (N)	Vavg (V)
Cal Jig & Hook	2.4940	2.494	24.4661	0.05964
1	10.0036	12.4976	122.6015	-0.11790
2	9.9936	22.4912	220.6387	-0.29041
3	10.0012	32.4924	318.7504	-0.47397
4	10.0046	42.497	416.8956	-0.66802
5	10.0198	52.5168	515.1898	-0.85358
6	10.0056	62.5224	613.3447	-1.07350
5	10.0198	52.5168	515.1898	-0.86548
4	10.0046	42.497	416.8956	-0.67636
3	10.0012	32.4924	318.7504	-0.47658
2	9.9936	22.4912	220.6387	-0.28992
1	10.0036	12.4976	122.6015	-0.10056
Cal Jig & Hook	2.4940	2.494	24.4661	0.08463

Table 7 - Average voltage values of stable regions of *loading & unloading* portions of time series plot.
(Propeller **hub** assembly thrust load cell, **installed push mode**)

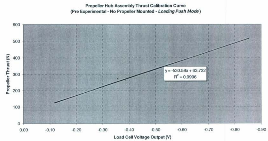

Figure 19 – Calibration plot for *loading* condition of Hub Assembly in push mode with lowest data point omitted (Data from table 7).

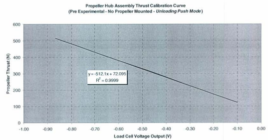

Figure 20 – Calibration plot for *unloading* condition of Hub Assembly in push mode with lowest data point omitted (Data from table 7).

(#2198) CALIBRATION SUMMARY DATA FOR LOADING/UNLOADING				
Weight #	Individual Mass (kg)	Total Added Mass (kg)	Thrust (N)	Vavg (V)
Cal Jig & Hook	2.4940	2.494	24.4661	0.08192
1	10.0036	12.4976	122.6015	0.00345
2	9.9936	22.4912	220.6387	-0.15489
3	10.0012	32.4924	318.7504	-0.33503
4	10.0046	42.497	416.8956	-0.52227
5	10.0198	52.5168	515.1898	-0.73111
6	10.0056	62.5224	613.3447	-0.91736
5	10.0198	52.5168	515.1898	-0.75542
4	10.0046	42.497	416.8956	-0.57645
3	10.0012	32.4924	318.7504	-0.39787
2	9.9936	22.4912	220.6387	-0.20788
1	10.0036	12.4976	122.6015	-0.05126
Cal Jig & Hook	2.4940	2.494	24.4661	0.08415

Table 8 - Average voltage values of stable regions of *loading & unloading* portions of time series plot.
(Propeller **pod** assembly thrust load cell, **installed push mode**)

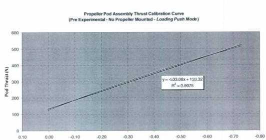

Figure 21 – Calibration plot for *loading* condition of Pod Assembly in push mode with lowest data point omitted (Data from table 8).

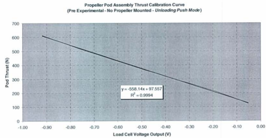

Figure 22 – Calibration plot for *unloading* condition of Pod Assembly in push mode with lowest data point omitted (Data from table 8).

After testing, a post calibration was hurriedly carried out to see if running the equipment had an effect on calibration, but unfortunately due to time constraints only in push mode, which was not the mode tested. Because of an insight into the performance of the hub instrumentation the post calibration was carried out with the propeller installed to see the effect on calibration. Ultimately the lack of time and accessibility to hardware (screws and other brackets) caused the author to abandon the attempt to calibrate the pod unit in pull mode with the propeller installed, which was not possible with the setup as it was. Also, there was the pressure of having to fix the belt misalignment before the next test program, the solution of which was thought about during the course of the first set of experiments by the author. After testing, the strut was removed, mounted in a CNC milling machine, measured to determine which faces needed correcting, and then re-machined to fix the problem. Testing following the corrections verified that the alignment issue had been fixed and that the belt drive system was functioning correctly.

	*Installed Load Cells - **Pull Mode***		*Installed Load Cells - **Push Mode***	
Newtons/Volt	Hub Load Cell (#2199)	Pod Load Cell (#2198)	Hub Load Cell (#2199)	Pod Load Cell (#2198)
Calibration Slope (loading)	468.46	537.09	-530.58	-533.08
Calibration Slope (unloading)	472.152	541.659	-512.10	-558.14
Average Calibration Slope	***470.306***	***539.375***	*-521.340*	*-545.610*

Table 9 – Summary of calibration constants for both modes of propulsion.

The result of the post calibration for thrust is presented in table 10. As one can see there was a significant drop in stiffness for push mode. The author believes that as the pod unit receives more use, the calibration slopes will assume values much closer to the uninstalled calibration slopes for both the hub and pod instrumentation.

For the set of experiments carried out by the author, the true calibration constant lies somewhere between the two sets of values in table 6. As an afterthought, perhaps if time had allowed, it might have been a good idea to allow instrumentation to run for a significant length of time before collecting any data. Also, had the belt not been damaged, completing a bollard pull at regular intervals would have given a good insight as to the wearing in of the mechanical systems and any resulting change in system stiffness.

	POST CALIBRATION - PUSH MODE			
	Installed Load Cells - ***No Prop***		*Installed Load Cells* - ***Prop Installed***	
Newtons/Volt	Hub Load Cell (#2199)	Pod Load Cell (#2198)	Hub Load Cell (#2199)	Pod Load Cell (#2198)
Calibration Slope (loading)	-500.31	-485.13	-518.71	-477.97
Calibration Slope (unloading)	-490.73	-481.24	-500.64	-482.96
Average Calibration Slope	*-495.520*	*-483.185*	*-509.675*	*-480.465*

Table 10 – Post experimental calibration values.

As a result of these procedures in the calibration of the thrust instrumentation, it was decided to use the installed average slope of 470.306 N/V for the hub thrust and the installed average slope of 539.375 N/V for the pod thrust.

The calibration of torque is discussed next.

3 Propeller Torque Calibrations

The calibration procedure for propeller torque was straight forward. Several calibration weights were obtained and their masses determined and recorded. Next the newly manufactured calibration moment arm was mounted to the hub and the calibration procedure started. This is shown in figure 23 and 24.

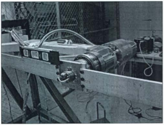

Figure 23 – Propeller torque calibration arm – note the level.

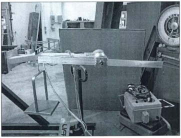

Figure 24 – A view with the weight pan attached.

Each weight was added and the system and then allowed to stabilize for as long as possible. The time series plot for the LH rotation propeller torque calibration is shown in figure 25. The average voltages for the stable regions of the time series plot is shown in table 11. One should note that when viewing the pod unit as a pulling unit using the LH 15° hub taper angle pulling propeller, the shaft has to be loaded in a clockwise (CW) rotation fashion during calibration in this reference frame of viewing to represent the reaction torque as a result of the LH propeller loading the shaft in torsion. In this case the voltage output is positive.

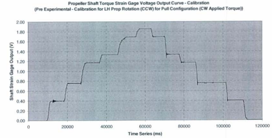

Figure 25 – Time series plot for the LH Rotation Propeller calibration procedure.

A calibration plot of the loading case for a LH propeller on the pod configured as pull unit is shown in figure 26. The results were very linear, which is to be expected because there are no sources of mechanical loss present. Because of the good linear characteristics of this transducer, the result for the loading and unloading cases is presented in tabular form only, in table 12. Because of the way the propeller was loaded during testing, the final calibration slope for the pull configuration pod unit with a LH prop was averaged.

(TORQUE) CALIBRATION SUMMARY DATA FOR LOADING/UNLOADING (CCW)				
WEIGHT #	Indiviual Mass (Kg)	Total Added Mass (kg)	Torque (Nm) (using 0.500 m Moment Arm)	Strain Gage Output Voltage (Vavg) (mV)
0	0	0	**0.000**	**0.000176**
Weight Pan	1.1208	1.1208	**5.498**	**0.398068**
1	1.0001	2.1209	**10.403**	**0.753478**
2	1.171	3.2919	**16.147**	**1.169324**
3	0.4572	3.7491	**18.389**	**1.331509**
4	1.0009	4.75	**23.299**	**1.689624**
5	0.4503	5.2003	**25.507**	**1.851909**
4	1.0009	4.75	**23.299**	**1.692304**
3	0.4572	3.7491	**18.389**	**1.335809**
2	1.171	3.2919	**16.147**	**1.173438**
1	1.0001	2.1209	**10.403**	**0.757116**
Weight Pan	1.1208	1.1208	**5.498**	**0.402314**
0	0	0	**0.000**	**0.005483**

Table 11 - Average voltage values of stable regions of *loading & unloading* portions of time series plot.
(Propeller shaft **torque** strain gage voltage output, **LH Prop pull mode**)

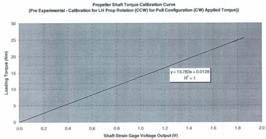

Figure 26 – Calibration plot for the *loading* case for a **LH propeller** with pod configured as **pull** unit.

	All Data Points	R^2	Lowest/Highest Omitted	R^2
SLOPE (loading)	13.7826251	0.9999980	13.78937353	0.9999987
SLOPE (unloading)	13.8099845	0.9999996	13.80000926	0.9999997
% Difference	0.199		0.077	

Average of Loading/Unloading Slopes Calculated with Highest/Lowest Values Omitted
13.795 Nm/V

Table 12 – Summary of slope calculations, the final calibration slope value for a **LH Prop** on a ***pull*** configuration pod unit.

Although not tested by the author, the torque instrumentation was calibrated as a RH pull unit as well to see the functioning of the system in the reverse direction. Figure 27 shows the time series plot for this configuration. Table 13 shows the final averaged calibration constant for this mode of operation.

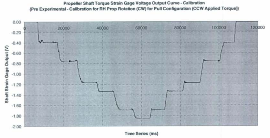

Figure 27 – Time series plot for the RH Rotation Propeller calibration procedure.

	All Data Points	R^2	Lowest/Highest Omitted	R^2
SLOPE (loading)	-13.78758909	-0.9999993	-13.78120981	-0.9999991
SLOPE (unloading)	-13.821008	-0.9999997	-13.83171159	-0.9999999
% Difference	0.242		0.366	

Average of Loading/Unloading Slopes Calculated with All Data Points
-13.804 Nm/V

Table 13 – Summary of slope calculations, the final calibration slope value for a **RH Prop** on a ***pull*** configuration pod unit.

Note the high degree of agreement between LH and RH (CCW and CW) propeller rotation. The calibration constant used in the data analysis is thus 13.795 Nm/V. The calibration of the propeller speed is discussed next.

4 Propeller Rotation Speed Calibration

Calibrating the propeller rotation speed consisted of using a hand held tachometer unit to accurately measure the speed of the propeller shaft while collecting voltage output data at each speed. During the speed calibration process the speed setting was entered in steps using the controller software for the Allen Bradley AC motor controller. The speed set points used in the process are shown in table 14. At each speed step the actual speed was determined using the hand held tachometer unit. The speed was determined by this machine by counting the rate of shaft revolution utilizing a reflected light beam. An adhesive backed reflector tape was affixed to the coupling connecting the motor to the input shaft of the gearbox to allow the beam reflection to occur during this process. Figure 28 shows the time series plot for the speed calibration. Referring again to table 14, the averaged stable region data for the speed calibration process is shown. Figure 29 shows the resulting calibration plot along with the slope and correlation coefficient. As a result of this process the speed calibration constant was determined to be -6.533 rps/volt. The carriage speed calibration is discussed next.

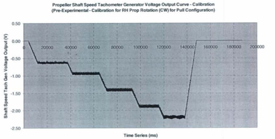

Figure 28 – Time series plot for speed calibration process.

Desired Calibration Speed (rps)	Calculated CFN[1]	Tachometer Output[2] (rpm)	Propeller Speed[3] (rpm)	Propeller Speed (rps)	Propeller Shaft Tach Gen Voltage Ouput (V)
0	0	0	0	0	0.00293934
4	16.457	490	245.0	4.083	-0.621997244
6	24.686	737	368.5	6.142	-0.936642775
9	37.029	1106	553.0	9.217	-1.408659488
12	49.371	1477	738.5	12.308	-1.881093514
14	57.600	1725	862.5	14.375	-2.1971195

[1] Defined in 7.4.1.3
[2] Handheld unit aimed at motor coupling
[3] Motor speed / 2 (Gearbox ratio)

Table 14 – Average voltage values from stable regions of figure 28.

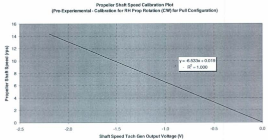

Figure 29 – Shaft rotation speed calibration plot.

5 Carriage Speed Calibration

This procedure was carried out by using the equipment that normally is mounted at all times on the carriage. The carriage speed was set using the speed input dial on the carriage motor speed controller shown in figure 30. After accelerating to the set speed, the readout on the frequency counter, shown in figure 31, was recorded to correspond to the acquired voltage from the frequency to voltage converter, shown in figure 32. The frequency counter is set up to express the number of counts/revolution of the track encoder shown in figure 6.33, in decimeters/second.

Figure 34 shows the time series plot for the carriage speed calibration procedure. The resulting stable data regions are shown in table 15. The final carriage speed calibration plot is shown in figure 35. The calibration constant from figure 35 is 0.982 m/s/Volt.

The pressure transducer calibration process is discussed next.

Figure 30 – Speed controller for the MUN test carriage.

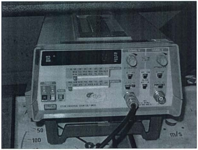

Figure 31 – Frequency counter.

Figure 32 – Frequency to voltage converter.

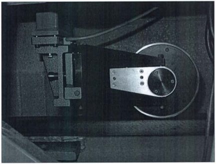

Figure 33 – Track speed encoder.

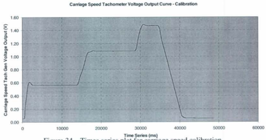

Figure 34 – Times series plot for carriage speed calibration.

Measured Carriage Speed (m/s)	Carriage Speed Tachometer Generator Voltage Ouput (V)
0.000	0.0556750
0.501	0.5643918
1.006	1.0809262
1.388	1.4690893

Table 15 – Average voltage values from stable regions of figure 34.

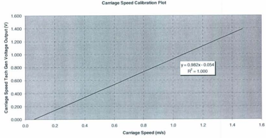

Figure 35 – Carriage speed calibration plot.

6 Pressure Transducer Calibration

To allow the calibration of the pressure transducers for this project, a calibration device had to be designed and manufactured in a short period of time. This calibration device consisted of a section of aluminum square tubing that had several holes drilled at distances corresponding to 1.5 D_P, 1.75 D_P and 2.0 D_P. These holes allowed a pressure head to be developed when the tube was filled with water. A bottom was manufactured from a piece of aluminum plate. The bottom was attached to the tower portion by applying a bead of silicone sealant to the joint area before connecting the two parts, and then allowing it to set over night. To allow the installation of the assembled gap pressure sensing plate, a hole was machined into the tube, as shown in figure 36, along with several threaded holes. Two brackets were then fabricated to allow the pressure sensing plate to be clamped into position with an o-ring installed between it and the face of the tube. Figure 37 shows the pressure sensing plate installed with the o-ring and clamps. The assembly was then leveled while in position by placing a level across two screws installed in the plate. This is shown in figure 38. Figure 39 shows a close-up of the leveled plate. Once leveled, the pressure transducers were installed and connected to the data acquisition system. Silicone oil was then added to the internal passageways and the air purged from each sensor. For more on this procedure the reader is referred to **Appendix N** section 1.1.5. Once the required setup had been completed, the calibration commenced.

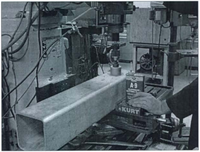

Figure 36 – Machining the pressure sensing plate installation hole for the calibration tower.

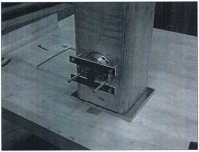

Figure 37 – Installed pressure sensing plate. Note the rubber plug at the propeller shaft bearing location.

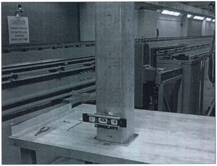

Figure 38 – Leveling the calibration setup.

Figure 39 – Close-up view of the leveled plate.

The calibration procedure consisted of adding water to the setup until it flowed out of the hole corresponding to the desired depth. Initially, the water was added carefully from the bottom up by holding the filling hose at the very bottom to avoid introducing air bubbles and general turbulence. This is shown in figure 40. Paper towels were taped to the side of the tower just below the hole to keep any drips from falling on the instrumentation below. When the desired depth had been reached, the voltage output corresponding to this depth was acquired by the data acquisition system.

Figure 40 – Filling the apparatus with water.

Figures 41 through to 46 show the time series plots for pressure transducers 1 through to 5, for the depths of 0 D_P (Atmospheric pressure, gauge),1.50 D_P, 1.75 D_P and 2.0 D_P, beginning with pressure transducer #1.

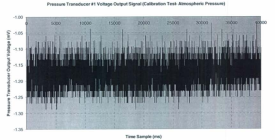

Figure 41 – Pressure Transducer #1 at **P = 0 D_P**.

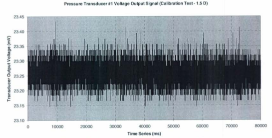

Figure 42 – Pressure Transducer #1 at **P = 1.5 D_P**.

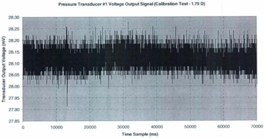

Figure 43 – Pressure Transducer #1 at **P = 1.75 D_P**.

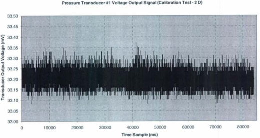

Figure 44 – Pressure Transducer #1 at **P = 2.0 D_P**.

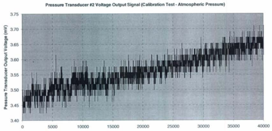

Figure 45 – Pressure Transducer #2 at **P = 0 D$_P$**.

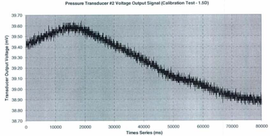

Figure 46 – Pressure Transducer #2 at **P = 1.5 D$_P$**.

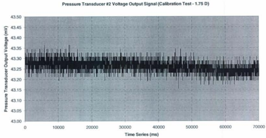

Figure 47 – Pressure Transducer #2 at **P = 1.75 D$_P$**.

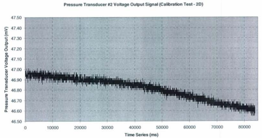

Figure 48 – Pressure Transducer #2 at **P = 2.0 D$_P$**.

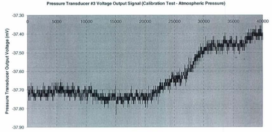

Figure 49 – Pressure Transducer #3 at **P = 0 D$_P$**.

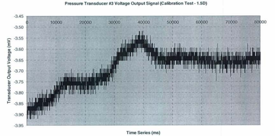

Figure 50 – Pressure Transducer #3 at **P = 1.5 D$_P$**.

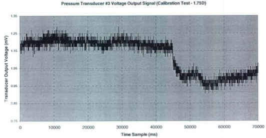

Figure 51 – Pressure Transducer #3 at **P = 1.75 D$_P$**.

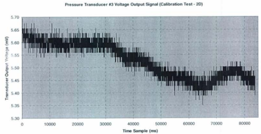

Figure 52 – Pressure Transducer #3 at **P = 2.0 D$_P$**.

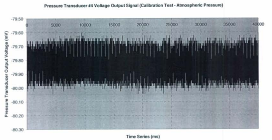

Figure 53 – Pressure Transducer #4 at **P = 0 D$_P$**.

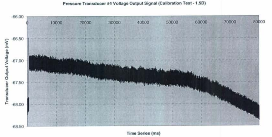

Figure 54 – Pressure Transducer #4 at **P = 1.5 D$_P$**.

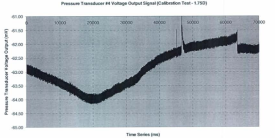

Figure 55 – Pressure Transducer #4 at **P = 1.75 D_P**.

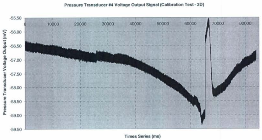

Figure 56 – Pressure Transducer #4 at **P = 2.0 D_P**.

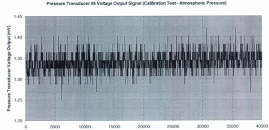

Figure 57 – Pressure Transducer #5 at **P = 0 D$_P$**.

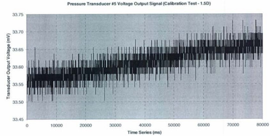

Figure 58 – Pressure Transducer #5 at **P = 1.5 D$_P$**.

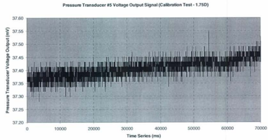

Figure 59 – Pressure Transducer #5 at **P = 1.75 D$_P$**.

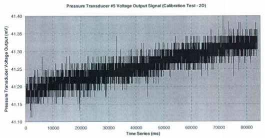

Figure 60 – Pressure Transducer #5 at **P = 2.0 D$_P$**.

At first glance, the variation in output voltage for some transducers from the beginning to the end of the sample period seems to be quite noticeable. However, the range as a percent of the factory full scale pressure voltage output is reasonable, and is presented in table 16 along with the average value for the sample time as a means of gauging variability and drift. **Note however that despite having a channel gain of 1, the variation across the time sample _is_ higher than for the other transducers in this instrumentation package, whose variation for the stable calibration regions of the time series plots is in the range of the smallest resolvable voltage for the analogue to digital (A/D) converter at a resolution of 16 bits.** This variation may be due to drifting of the transducer, vibration, noise or other source of interference. Indeed, the data traces seem to drift quite noticeably in some loading cases at some pressures. For the purposes of developing a calibration constant, the author chose to use the average voltage value calculated from the data set. The average voltages, along with minimum & maximum values, voltage spread, median voltage and standard deviation are presented in table 16, mentioned previously. Appearing in table 17 are the factory calibration constants. Table 18 presents the calibration pressures and average voltages only.

In terms of performance from a calibration point of view, pressure transducers #1 and #5 seem to be the best behaved. Pressure transducers #2 and #3 tend to drift, as does #4 with some additional operational characteristic present. This type of result is typical for the type of pressure transducers used in this application [20].

		Pressure Transducer (With Radius Value) Voltage Ouput (mV) - Calibration				
		PT#1 (W09) R=15.875 mm (0.625 in)	**PT#2 (W06)** R=20.6325 mm) (0.8125 in)	**PT#3 (W05)** R=25.4 mm (1.000 in)	**PT#4 (W04)** R=30.1625 mm (1.1875 in)	**PT#5 (W08)** R=47.625 mm (1.375 in)
Water Depth *	Channel Stats					
0xD (P_{atm})						
	Avg Output	**-1.175**	**3.562**	**-37.630**	**-79.834**	**1.342**
	Min Output	-1.288	3.424	-37.833	-80.043	1.249
	Max Ouput	-1.020	3.729	-37.356	-79.604	1.421
	Δ Output	0.267	0.305	0.477	0.439	0.172
	Δ Output (%FS)[1]	**0.096**	**0.118**	**0.169**	**0.156**	**0.069**
	Median	-1.173	3.557	-37.699	-79.833	1.345
	SD	0.055	0.078	0.610	1.264	0.028
1.5xD						
	Avg Output	**23.255**	**39.251**	**-3.691**	**-67.438**	**33.613**
	Min Output	23.146	38.825	-3.9197	-68.389	33.503
	Max Ouput	23.432	39.645	-3.5191	-66.482	33.732
	Δ Output	0.286	0.82	0.4006	1.907	0.229
	Δ Output (%FS)[1]	**0.103**	**0.316**	**0.142**	**0.677**	**0.092**
	Median	23.26	39.263	-3.6526	-67.378	33.618
	SD	0.260	0.491	0.095	0.837	0.374
1.75xD						
	Avg Output	**28.119**	**43.262**	**1.124**	**-62.851**	**37.407**
	Min Output	27.914	43.154	0.906	-64.174	37.28
	Max Ouput	28.277	43.364	1.2875	-61.007	37.547
	Δ Output	0.363	0.21	0.3815	3.167	0.267
	Δ Output (%FS)[1]	**0.130**	**0.081**	**0.135**	**1.124**	**0.107**
	Median	28.124	43.269	1.173	-62.877	37.413
	SD	0.335	0.514	0.099	1.071	0.444
2.0xD						
	Avg Output	**33.202**	**46.810**	**5.527**	**-57.270**	**41.258**
	Min Output	33.083	46.55	5.3502	-59.367	41.114
	Max Ouput	33.37	47.007	5.6935	-55.533	41.4
	Δ Output	0.287	0.457	0.3433	3.834	0.286
	Δ Output (%FS)[1]	**0.103**	**0.176**	**0.122**	**1.360**	**0.115**
	Median	33.198	46.836	5.5219	-57.078	41.266
	SD	0.363	0.518	0.090	0.934	0.449

*(D=0.270m)

[1](Δ Output (%FS) = (Δ Output/Full Scale Ouput)*100%)

Table 16 – Channel summary data for the 5 pressure transducers.

	#1 FS Output	#2 FS Output	#3 FS Output	#4 FS Output	#5 FS Output
Output in mV *	278.49	259.21	281.98	281.87	248.73

* (Full scale output is for 5 psi (34473.8 Pa))

Table 17 – Factory calibration constants.

Pressure Transducer Calibration Data						
Water Depth* (m)	Pressure Head[1] (Pa)	Pressure Transducer Output (mV)				
		#1	#2	#3	#4	#5
$0.0D_P$	0	**-1.175**	**3.562**	**-37.630**	**-79.834**	**1.342**
$1.5D_P$	3973.05	**23.255**	**39.251**	**-3.691**	**-67.438**	**33.613**
$1.75D_P$	4635.225	**28.119**	**43.262**	**1.124**	**-62.851**	**37.407**
$2.0D_P$	5297.4	**33.202**	**46.810**	**5.527**	**-57.270**	**41.258**

[1] $= \rho g h$

* $D_P = 0.270$ m

Table 18 – Final calibration data.

The plot of the data in table 18 is shown in figure 61.

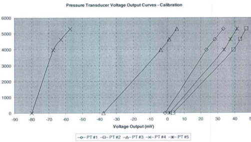

Figure 61 – Calibration plot of all pressure transducers.

After studying the calibration plots and data values, the calibration constants and correlation coefficients were calculated. The slopes were initially calculated with all four points, then recalculated omitting the lowest point. This improved the correlation, and in some cases the agreement with the factory slope. This result is presented in table 19. In some cases the slope agreement with the factory value worsened after the second calculation, however because the correlation improved the author decided to use this value as the calibration constant for the experiments.

	Pressure Transducer Calibration Constants				
	Pressure Transducer				
	#1	#2	#3	#4	#5
Calibration Constant[1] (Pa/mV)	**156.0802**	**118.5881**	**120.8921**	**241.8655**	**129.7587**
Correlation Coefficient[1]	0.9992	0.9972	0.9993	0.9761	0.9983
Calibration Constant[2] (Pa/mV)	*133.1235*	*174.9617*	*143.578*	*129.8302*	*173.232*
Correlation Coefficient[2]	*0.9999*	*0.9994*	*0.9997*	*0.9984*	*1.0000*
Factory Cal (5psi for FS Output)	278.49	259.21	281.98	281.87	248.73
Factory Cal (Pa/mV)	**123.7882**	**132.9956**	**122.2561**	**122.3039**	**138.5992**

[1] Calculated using all points
[2] Calculated omitting first point

Table 19 – Final pressure transducer calibration constants.

The calibration of the shell drag instrumentation is discussed next.

7 Shell Drag Force Calibration

To calibrate the shell drag force instrumentation the pod unit was oriented vertically as shown in figure 62. The shell was installed along with the gap fillers and rolling o-ring seal and a weight pan attached to the shell ring adapter with a piece of twine, utilizing two screws. Weights were then added to the system as the calibration data was acquired. The time series plot is shown in figure 63. The average voltages from the stable regions are presented in table 20. The loading case only is considered because for all tests, the shell is loaded such that the load cell is increasing in tension.

Figure 62 – Calibration of the shell drag instrumentation system.

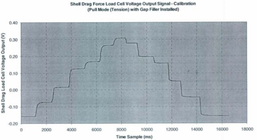

Figure 63 – Time series plot of the shell drag instrumentation.

Shell Drag Load Cell Calibration Data - Loading				
Weight #	Mass (g)	Mass (kg)	Force (N)	Load Cell Output (V)
0	0	0	0	-0.1586
Pan	1105.8	1.1058	10.847898	-0.0736
1	2105.9	2.1059	20.658879	0.0157
2	3276.9	3.2769	32.146389	0.1259
3	3734.1	3.7341	36.631521	0.2314
4	4735	4.735	46.45035	0.2644
5	5185.3	5.1853	50.867793	0.3076

Table 20 – Calibration data for shell drag.

Calculated from the values in table 20 is the slope and correlation coefficient, presented in table 21. The factory calibration constant is expressed in N/V in table 21 as well, for comparison. The calibration plot is shown in figure 64. Note that there is a significant appearance of hysterisis, however its magnitude is not investigated.

Calibration Constant & Correlation Coefficient for Shell Drag - Loading	
Calibration Constant	104.658 (N/V)
Correlation Coefficient	0.9999
Factory Calibration Constant[1]	222.07mV
Factory Calibration Constant[2]	100.16 (N/V)

[1]Voltage for 50 lbs of loading
[2]Voltage for 50 lbs loading expressed in Newtons/Volt

Table 21 – Calibration constant & correlation coefficient for shell drag force.

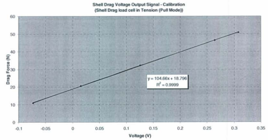

Figure 64 – Calibration plot for shell drag force.

The load cell had been calibrated before installation, as with the propeller thrust load cells, however the results will not be presented. The final value used for the shell drag force calibration is thus 104.66 N/V.

The calibration of the global dynamometer is discussed next.

8 Global Dynamometer Calibrations

The process of calibrating a dynamometer that measures in the X, Y and Z axes simultaneously is time consuming and involves much care. The author chooses to treat the subject quickly however, deciding instead to focus only on resolving the thrust component in the x-direction as means of viewing the functioning of the dynamometer.

To calibrate the assembled dynamometer, it was first placed on a suitably strong and stiff frame and fixed into position with large c-clamps. Another frame was then secured to the first frame to act as a loading point. Loading was accomplished by using several pulleys to align the force developed by large calibration weights that hung from a hook. An in-line load cell that was placed directly at the point of application of the calibration force ensured that no friction losses would affect the process. This load cell had been calibrated prior to the dynamometer calibration process. The time series of this calibration appears in figure 65. The stable region voltage averages and loading mass data, along with the slope and correlation coefficient are presented in table 22. Note that this data is for the loading case only.

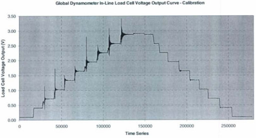

Figure 65 – Time series plot of the calibration in-line load cell.

CALIBRATION DATA for IN-LINE LOAD CELL		
Calibration Mass (kg)	Loading Force (N)	Load Cell Output (V)
0	0	0.095
10	98.1	0.404
20	196.2	0.714
30	294.3	1.025
40	392.4	1.334
50	490.5	1.643
60	588.6	1.953
70	686.7	2.262
80	784.8	2.571
90	882.9	2.882
91	892.71	2.912
Calibration Constant (N/V) = 316.865		
Correlation Coefficient = 1.0000		

Table 22 – Calibration data for in-line load cell.

Once the dynamometer had been secured, the components that complete the strut assembly, as well as the motor and gearbox were added to the apparatus. This was to ensure that the z-direction load cells were loaded with as much as the final mass as possible. Note that the pod instrumentation was not fully assembled at the point in time during which the dynamometer calibrations occurred. Thus, a portion of the drive gear housing was used as the anchor point for the cable applying loading force to the apparatus. Figure 66 depicts the overall test fixture set up for a 0° test with the loading located at the propeller shaft line and parallel to the axis of rotation.

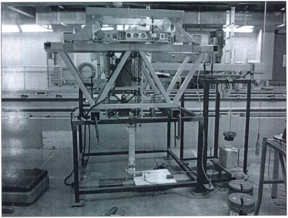

Figure 66 – Calibration jig set up for 0° test pull of the global unit dynamometer.

The individual calibration of the load cells in the global dynamometer was not practical given the 4448 N (1000 lb) range. Assembling the required mass would be difficult in addition to the fact that setting up this much mass for a load cell pull is dangerous and requires the use of special equipment and safety procedures. Given these constraints in addition to time limitation, the calibration process was carried out as quickly as possible.

For each of the 3 axes of measurement, a pull was carried out in that direction to determine the percentage of load that was induced in the off-axis directions, as well as the percentage loss in the direction of the calibration pull. Off axis loads are a result of the stretching of the flex links in the axial direction, causing a slight elongation of the flex links at 90° to the direction of loading, thereby inducing a load. Pulls were also carried out at the loading point for 0°, 5° and 45°. Only the results of the 0° and 5° pulls will be discussed. Essentially, when analyzing the calibration data for the 0° pull at the loading point, it was noticed that at higher loads it seemed as if the dynamometer and loading frame setup was settling. It was thus decided to use the results of the 5° pull to determine a calibration constant for the x-direction. Figure 67 shows a time series plot of the X-axis load cell for the 0 degree pull case. Table 23 shows the data from this calibration pull, along with the slope and correlation coefficient. The data only consists of the first three points. One can see the apparent settling that occurred during the pull. This effect was likely due to slippage of the frames set up for the calibration procedure. Figure 68 and table 24 show the time series plot and calibration data respectively for the 5° pull. Note that the data was corrected for the angle. The time series plot for this case showed expected output values, and an improvement in the correlation coefficient. The final calibration constant for the x-pull is thus -1142.404 N/V.

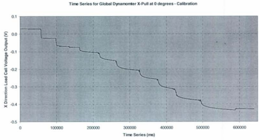

Figure 67 – Time series calibration plot for X-axis load cell (0° pull).

CALIBRATION DATA FOR X-DIRECTION LOAD CELL (0° PULL)			
Load Point	In-Line Load cell Voltage (Volts)	Load from In-Line load cell (N)	X1 Voltage Output (Volts)
0	0.070	22.18	0.03
1	0.093	29.31	-0.02
2	0.401	127.06	-0.08
Calibration Constant (N/V) = -1006.249			
Correlation Coefficient = -0.9264			

Table 23 – Calibration data for the X-axis load cell (0° pull).

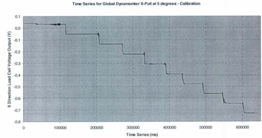

Figure 68 – Time series calibration plot for X-axis load cell (5° pull)

CALIBRATION DATA FOR X-DIRECTION LOAD CELL (5° PULL)				
Load Point	In-Line Load cell Voltage (Volts)	Load from In-Line load cell (N)	Load Corrected for 5 degree pull direction (N)	X1 Voltage Output (Volts)
0	0.0696	22.05	21.97	0.0400
1	0.0920	29.15	29.04	0.0328
2	0.3999	126.72	126.24	-0.0513
3	0.7075	224.18	223.32	-0.1367
4	1.0144	321.42	320.20	-0.2219
5	1.3213	418.69	417.09	-0.3065
6	1.6296	516.36	514.40	-0.3918
7	1.9376	613.95	611.62	-0.4768
8	2.2439	711.03	708.32	-0.5611
9	2.5486	807.58	804.50	-0.6455
10	2.8562	905.01	901.57	-0.7302
Calibration Constant (N/V) = -1142.404 **Correlation Coefficient = -0.9999**				

Table 24 – Calibration data for the X-axis load cell (5° pull).

9 Calibration Constant Summary

Table 25 lists the series of constants resulting from the calibration process. These values allowed the calculation of the parameter values of the various sensor outputs for the series of initial experiments.

Final Calibration Constants for Experimental Data Analysis	
CHANNEL	SLOPE
T_{PROP}	470.306 (N/V)
T_{POD}	539.375 (N/V)
Torque, Q	+13.795 (Nm/V)
Shell Drag	104.658 (N/V)
Pressure Transducer #1	133.123 (Pa/mV)
Pressure Transducer #1	174.961 (Pa/mV)
Pressure Transducer #1	143.578 (Pa/mV)
Pressure Transducer #1	129.830 (Pa/mV)
Pressure Transducer #1	173.231 (Pa/mV)
Propeller Shaft Speed	-6.533 (rps/V)
Carriage Speed	0.982 (m/s/V)
Global Unit Dynamometer (X-Axis Only)	-1142.404 N/V

Table 25 – Summary of calibration constants used for experimental analysis.

This ends the discussion on calibrations.